Beam Asymmetry Measurement from Pion Photoproduction on the Neutron

Daria Sokhan

Department of Physics and Astronomy

University of Edinburgh

A thesis submitted for the degree of

Doctor of Philosophy

August 2009

To Marina, Vladimir and the rest of my family

Acknowledgements

Firstly, I would like to thank Dan Watts, a sterling supervisor, for the expert and tireless guidance in all experimental and theoretical matters over the course of my PhD. Many thanks are due to Ken Livingston and Derek Glazier for guidance in my analysis, a wealth of knowledge about ROOT and help with software trouble-shooting, and to Ken also for the introduction to the Plaza Azteca and life and shifts in JLab. Thanks are due to Derek Branford for the introduction into the project and much advice, and the rest of the Edinburgh Nuclear Physics group for creating a great environment to work in. In particular I must thank Claire Tarbert, for all the help with settling in and for sharing her programming wisdom, to Tom Jude and Mark Sikora for happy physics discussions in and out of the office and for great companionship on the travels.

The deepest thanks are due to everyone I have worked with at JLab — in particular to Chris Keith and James Brock for their patience and guidance, for tirelessly answering millions of questions and for bravely letting me near FROST, to the whole jolly crew of the target group: Dave, Mark, Steve and the rest for teaching me all you have — from soldering to the American way of life — and for making my time in the EEL great. Profound thanks go to Igor Strakovsky for the partial wave analysis and all the advise and theoretical discussions and to Eugene Pasyuk for being an inexhaustible well of knowledge of even the most obscure workings of CLAS and for answering every query so fully. I would like to thank Pawel Nadel-Turonski for helpful suggestions and overseeing the calibration and analysis effort of the g13 experiment and Bill Briscoe and Franz Klein for much fruitful discussion. Thanks are due to Volker Burkert for letting me work on the experiments in the first place, to Joe and Julie and the cats

for a wonderful welcome to JLab and making my time there so much happier. The same thanks go to Raffaella and the Marcos, to Tim and Kalyan for the deep discussions and the happy days and to Chuck, for sharing the early days on FROST.

I am also grateful to all my JLab travelling buddies — Jo and the Glasgow Nuclear Group, in particular Russell for sharing the many happy hours in the EEL building and brightening the day, Craig, Stuart, Neil, my fellow g13-ers, and the rest. Many thanks are due to David Ireland and David Hamilton for being there with enlightening advise at just the right time.

This would be incomplete without deep thanks to Jane Patterson for absolutely wonderful administrative support and for having the answer to seemingly everything! Thanks are of course also due to STFC, formerly EPSRC, for funding my bread in the course of this work.

Most importantly though, I would like to thank my parents — Marina and Vladimir — George and my extended family for incredible support, encouragement and patience, and for all they have done to make my life happier. I could not have done this without them!

Abstract

The resonance spectrum of the nucleon gives direct information on the dynamics and interactions of its constituents. This offers an important challenge to the theoretical models of nucleon structure, including the emerging Lattice QCD predictions, conformal field theories and more phenomenological, QCD-based approaches. Although the various models predict different features for the excitation spectra, the experimental information is currently of too poor quality to differentiate between these models.

Pion photoproduction from the nucleon is a powerful probe of the spectrum as most resonances are expected to couple to the pion decay channel. However, cross-sections alone are not sensitive enough to allow identification of the underlying excitation spectrum, as the resonances have energy widths larger than their separations. A major world effort is underway to additionally measure polarisation observables in the production process. For a model-independent analysis a “complete” set of single- and double-polarisation observables needs to be measured in experiments involving polarised beams, targets and a means of determining recoil nucleon polarisation. In particular, the beam asymmetry is a critical observable for the constraint of partial wave analyses (PWA) used to extract the nucleon excitation spectrum from the data.

Almost all of the available world data on the beam asymmetry has been taken on the proton, with the neutron dataset sparse, containing only three experiments at fixed angles and in a limited photon energy range. The lack of extensive data on the neutron is a major deficiency, as different resonances have very different electromagnetic couplings to the proton and neutron. As a result, the data from the two targets will have very different

relative contributions from, and sensitivities to, the spectrum of nucleon resonances. Moreover, neutron data is essential for the separation of the isoscalar and isovector components of the reaction amplitudes.

This thesis presents a very high statistics measurement of the photon beam asymmetry on the neutron with close-to-complete angular coverage and a wide range of invariant mass (1610 – 2320 MeV) extending over the third resonance region, where the excitation spectrum is particularly ill defined. The experiment was conducted at the Thomas Jefferson National Accelerator Facility (JLab) using a tagged, linearly polarised photon beam, a liquid deuterium target and the CEBAF Large Acceptance Spectrometer (CLAS). The quality and quantity of the data has allowed an invariant mass resolution of 10 MeV and an angular resolution of 0.1 in the cosine of the centre-of-mass pion production angle, θ.

Good agreement is evident in the regions where there is kinematic overlap with sparse previous data. Comparison of the new data is made with the two main partial wave analyses, SAID and MAID. Significant discrepancy is observed at backward θ with SAID (across most of the energy range) and MAID (up to $\sim$ 1750 MeV) and also below $\sim 35^\circ$ in θ with both analyses.

This extensive new dataset will help significantly to constrain partial wave analyses and will be a crucial part of the current world effort to use meson photoproduction to tackle long-standing uncertainties in the fundamental excitation spectrum of the nucleon. As a first step towards this the refitting of the SAID partial wave analysis incorporating the new data was carried out and shows very significant changes in the properties of the magnetic P_{11}, P_{13}, D_{13}, D_{35}, F_{15}, G_{17} and G_{19} partial waves.

Declaration

The data presented in this thesis was obtained in experiments carried out by the CLAS collaboration at Jefferson Laboratory, Virginia, USA. I played a major role in the execution of the experiment and calibration of detectors and the data analysis and interpretation is entirely my own work. Any contributions from colleagues in the CLAS collaboration such as calibrations and the partial wave analysis are explicitly referenced in the text. This thesis was written by myself and the work presented in it has not been submitted in support of another degree or qualification from this or any other university or institute of learning.

Daria Sokhan

Contents

1 Introduction **1**

1.1 Brief history of the hadron . . . 1

1.1.1 A plethora of particles . . . 1

1.1.2 The Quark Model — emerging symmetries . . . 2

1.1.3 Quantum Chromodynamics . . . 5

1.2 Theoretical approaches to the hadron . . . 7

1.2.1 Tools in QCD . . . 8

1.2.1.1 Lattice QCD . . . 8

1.2.1.2 Chiral Perturbation Theory . . . 9

1.2.1.3 Conformal field theories . . . 9

1.2.1.4 Sum Rules . . . 9

1.2.2 Phenomenological Hadron Models . . . 10

1.2.2.1 Constituent Quark Models . . . 10

1.2.2.2 Soliton Models . . . 11

1.2.2.3 QCD exotica . . . 12

1.3 Experimental study of hadronic structure . . . 12

1.3.1 Emergence of the parton model . . . 12

1.3.2 Hadron spectroscopy . . . 14

1.3.2.1 The importance of nucleon resonances . . . 14

1.3.2.2 Experimental challenges . . . 15

1.3.2.3 Electromagnetic and hadronic probes of the nucleon 16

1.3.2.4 Polarisation in meson photoproduction . . . 18

1.4 Measurement of Beam Asymmetry . . . 19

2 Pion Photoproduction **21**
2.1 Introducing the pion . . . 21
2.2 Pion photoproduction . . . 22
2.2.1 Formalism . . . 22
2.2.2 Photoproduction amplitudes . . . 23
2.2.2.1 Momentum representation . . . 23
2.2.2.2 Isospin representation . . . 25
2.2.3 Polarisation observables . . . 27
2.3 Partial Wave Analyses . . . 31
2.3.1 MAID . . . 33
2.3.2 SAID . . . 34
2.4 Summary . . . 35

3 Past Measurements **37**

4 Experimental Facility - Jefferson Lab **41**
4.1 CEBAF . . . 41
4.2 Electron beam . . . 44
4.2.1 Position and intensity . . . 44
4.2.2 Beam profile . . . 44
4.2.3 Polarisation of the electron beam . . . 45
4.3 Techniques for producing photon beams . . . 46
4.3.1 Circularly polarised photons . . . 46
4.3.2 Linearly polarised photons . . . 47
4.3.3 Beam collimation and monitoring . . . 49
4.4 The Photon Tagging Spectrometer . . . 49
4.5 CLAS . . . 51
4.5.1 Torus Magnet . . . 51
4.5.2 Start Counter . . . 54
4.5.3 Drift Chambers . . . 54
4.5.4 Čerenkov Counters . . . 59
4.5.5 Time of Flight system . . . 60
4.5.6 Forward Electromagnetic Calorimeter . . . 61
4.5.7 Large Angle Calorimeter . . . 63

4.6 Targets . . . 64
4.7 Detector electronics and software . . . 64
4.7.1 Trigger . . . 64
4.7.2 Data acquisition . . . 65
4.8 The g13 experiment . . . 66

5 Detector Calibration **67**
5.1 Overview of calibration process . . . 67
5.2 Common features of timing calibration . . . 69
5.2.1 TDC timing calibration . . . 69
5.2.2 Time-walk corrections . . . 69
5.2.3 "Zero time" for the event . . . 70
5.3 Tagger calibration . . . 71
5.4 Start Counter calibration . . . 74
5.4.1 Time for light propagation along the paddle . . . 75
5.4.2 Alignment of the start counter to t_0 . . . 76
5.4.3 Time-walk corrections . . . 79
5.5 Time of Flight system calibration . . . 80
5.5.1 Energy corrections . . . 81
5.5.2 Timing corrections . . . 82
5.6 Drift Chamber calibration . . . 82
5.7 Calorimeter calibration . . . 84

6 Data Analysis I: Event Selection **87**
6.1 Overview . . . 87
6.2 Event reconstruction . . . 88
6.2.1 Charge and momentum . . . 88
6.2.2 Velocity . . . 88
6.2.3 Event vertex . . . 89
6.3 Selecting the p π^- final state . . . 89
6.4 Fiducial Cuts — excluding regions of limited acceptance . . . 94
6.5 Energy loss corrections . . . 99
6.6 Identifying the incident photon . . . 100
6.7 Identifying quasi-free events . . . 104

6.8 Measurements for the extraction of Σ 109

7 Data Analysis II: Beam Asymmetry Extraction 113
7.1 Choice of bin size 113
7.2 Photon polarisation 114
7.3 Removing acceptance effects 116
7.4 Σ extraction method 118
7.5 Optimisation of fit parameters 119

8 Results and Discussion 121
8.1 Quality of fit 121
8.2 Systematic uncertainties in the extraction of Σ 122
8.2.1 Determination of degree of beam polarisation 122
8.2.2 ϕ_0 offset 123
8.2.3 W and $\cos\theta$ 123
8.3 Check of Final State Interaction effects 124
8.4 Results 125

9 Conclusions and Outlook 181

A Frames of measurement 183

References 191

List of Figures

1.1 The two lightest baryon ($B = 1$) multiplets — spin-$\frac{1}{2}$ octet, containing proton and neutron, on the left and spin-$\frac{3}{2}$ decuplet on the right. Image courtesy of *Wikimedia Commons*. 3

1.2 The two lightest meson ($B = 0$) multiplets — spin-0 nonet, containing the three pions, on the left, spin-1 nonet on the right. Image courtesy of *Wikimedia Commons*. 4

1.3 Eightfold Way arrangement of lightest quarks (left) and antiquarks (right). 4

1.4 Strong coupling constant as a function of energy, comparison of world data points from different experiments and QCD calculations (yellow band) [23]. 6

1.5 Artist's impression of a meson showing the valence quarks and quark - anti-quark pairs in the background (Image courtesy of Jefferson Lab). 7

1.6 Feynman diagrams showing multiple loop contributions to the quark-quark interaction. 8

1.7 At high quark momentum, in the perturbative QCD region, quark mass is very small. As quark momentum reduces, however, the "bare" quarks become "dressed" in a gluon cloud, effectively acquiring mass. Constituent quark models operate in this regime. The different curves show scenarios for different "bare" quark masses, m [42]. 10

1.8 The total cross-sections for free proton photoabsorbtion (black data points), showing the three resonance regions. A number of meson channels contributing to the total cross-sections are shown in colour [65]. 16

2.1 Diagram illustrating the kinematics of a reaction with two particles in the initial state (four-momenta k and p_i) and two in the final state (four-momenta q and p_f). 22

3.1 Previous Σ measurement points in the E_γ range 1.0 – 2.3 GeV. 38

4.1 Cartoon showing CEBAF and the three experimental halls. The enlargements are, clockwise from the top: a module in the linac, a steering magnet and a part of the RF separator [101]. 42
4.2 Beam-line components in Hall B [104]. 43
4.3 Example of a beam profile scanned along two perpendicular axes by the harps. The profile indicates a good quality, narrow, circular beam of width ~ 70 μm. 45
4.4 Graph showing degree of circular polarisation as a function of momentum transfer to the bremsstrahlung photon. The two curves are an exact calculation (a) and an approximation (c). The figure was taken from the theoretical treatment by Olsen [106]. 47
4.5 Data and Monte Carlo simulation of the photon intensity spectrum produced by the process of coherent bremsstrahlung [107]. 48
4.6 The tagging spectrometer in cross-section, showing the photon beam, the paths of scattered electrons deflected in the tagger magnetic field and the two planes of the scintillator hodoscope [110]. 50
4.7 Geant 3 visualisation of CLAS showing, symmetrically arranged around the beam axis, the superconducting coils (yellow), three regions of drift chambers (blue), the Čerenkov counters (pink), the shell of time-of-flight scintillation counters (red) and the electromagnetic calorimeters covering the forward angles (green) [104]. 52
4.8 Schematic showing the torus magnet cryostats radially positioned around the beam axis (dashed line) and two regions of the drift chambers. [104]. 53
4.9 Photograph of the torus magnet cryostats, showing one of the two support rings on which they are mounted and the carbon-fibre support rods between neighbouring cryostats (Jefferson Lab Hall B archive). 53
4.10 Start counter with one of the six paddle sectors removed to show the target cell inside [111]. 55
4.11 Cross-section through the start counter, showing the target surrounded by scintillator paddles [111]. 55
4.12 Photograph of CLAS opened up, showing, from the upstream end, the sphere formed by the six sectors of the drift chambers. At the left edge of the photograph and in the bottom right corner (behind the drift chambers), the wrapped scintillator paddles of the time-of-flight system can be seen (Jefferson Lab Hall B archive). 56
4.13 Schematic showing a cross-section through CLAS perpendicular to the beam axis (top) and parallel to it (bottom) [113]. 57

4.14 A section through Region 3 of the drift chamber, showing the two superlayers and the hexagonal array of cells formed by the arrangement of field wires. A possible particle track through the regions is shown as shaded cells where a hit is registered in the sense wire at the centre of each cell [113]. 58

4.15 Schematic showing a segment of a Čerenkov counter and an electron track through it [104]. 60

4.16 A diagram of a ToF sector, showing the scintillation counters arranged, in four panels, perpendicular to the beam line. At both ends of each paddle is a light guide and a PMT [115]. 61

4.17 Diagram showing the layered structure of the electromagnetic calorimeter and the arrangement of scintillation bars inside. The bars are aligned parallel to one of the three long sides of the module. The alignment is rotated for each consecutive layer, forming a grid [116]. 62

4.18 Schematic showing the arrangement of lead, Teflon and scintillator layers inside a LAC module [117]. 63

5.1 Graph showing two signals with identical rise time but different pulse heights. The larger signal will reach a threshold value, shown at a height of 0.6, earlier, by a value of Δt, than the smaller signal. 70

5.2 Neighbouring beam bunches arriving at ~2 ns intervals. The small secondary bumps are from the beam being delivered to one of the neighbouring experimental halls [110]. 71

5.3 Histogram showing alignment of individual T-counters to the RF signal. 72

5.4 Diagram of a start counter paddle from the middle of a sector (not to scale), view from the top. 75

5.5 2-D distribution of Δt vs distance d along the paddle. A plot of the peak positions in each d bin (black points) fitted with Eq. 5.12 (red line) is overlaid. 77

5.6 A GUI panel from the start counter timing calibration process, showing Δt for four paddles in sector 6 of the start counter. The timing of each paddle has been corrected for propagation time of the signal along the scintillators. Average resolution, based on the σ of the Gaussian fits (shown in red) is ~ 300 ps. The buttons underneath each panel allow the individual fit range and limits to be changed for an improved fit. . . 78

5.7 Paddle-by-paddle alignment of Δt. Paddle 9 was damaged during fabrication and typically yields too few data points. 79

5.8 A GUI panel for the time-walk calibration, showing Δt vs ADC channel number histograms for four paddles in a single sector of the start counter. Overlaid is a graph of the Gaussian peak positions for each bin on the ADC axis (black points) and its fit with Eq. 5.13. The fit was performed based on the summed distributions of protons and pions, examples of which from two paddles are shown in the bottom panels. The top panels illustrate the contributions from protons (left) and pions (right) to the hits in the remaining two paddles of the sector. 80
5.9 Drift chamber residuals vs drift time in time-based tracking for a single superlayer. . 84

6.1 Z-position of the reconstructed event vertex showing the target cell and the aluminium exit window of the scattering chamber at $Z = 7$ cm. 90
6.2 Measured β versus momentum for all positive (left) and negative (right) particles in two-particle events. The green line traces the kinematic relation for charged pions, red line that for protons. 91
6.3 Distribution of $\beta_{meas} - \beta_{calc}$, where β_{calc} is calculated based on the particle's assumed mass (left: pion, right: proton). The eventual data cut is shown by red lines. 92
6.4 Projections of $\Delta\beta$ vs momentum, showing the $\Delta\beta$ peak for the proton in a range of momentum bins, as indicated in the histogram titles. A second peak on the right, due to π^+, can be observed. 92
6.5 Edge of $\Delta\beta$ cut used to select π^- events, showing in red an eighth-order polynomial fit. 93
6.6 Mass squared as measured for positive and negative particles showing data remaining after the $\Delta\beta$ cuts shaded in blue. Dashed lines indicate the mass squared values for protons and pions respectively. The small offset of the invariant proton mass peak from its true position is due to larger momentum losses in the drift chambers for particles of higher invariant mass. 93
6.7 β (as measured) vs momentum plots for the identified protons and π^- after a $\Delta\beta$ cut. Dashed black lines trace the theoretical curve for both types of particle. 94
6.8 Angular distributions of π^- showing the sectors of CLAS and statistics depleted torus magnet regions, for a selection of four momentum regions 100 MeV wide. 95
6.9 Angular distributions of protons showing the sectors of CLAS and statistics depleted torus magnet regions, for a selection of four momentum regions 100 MeV wide. . . 96
6.10 An example of half-Gaussian fits to the π^- ϕ-distributions at the edge of a sector, for a range of θ bins. 97

6.11 An example of fits to one sector edge (peak - 2σ) for π^- particles of low momentum (100 – 200 MeV, points and fit in green), high momentum (1500 – 1600 MeV, points and fit in blue) and all momenta (points and fit in red). 98

6.12 Angular distributions for π^- (top) and protons (bottom), summed over all momenta, before and after fiducial cuts have been applied. 99

6.13 Energy loss undergone by protons (red) and π^- (black) on their trajectory through the target, start counter scintillators and beam pipe. 100

6.14 Multiplicity of bremsstrahlung-induced hits in the tagger. 101

6.15 Timing coincidence between π^- and all the "good" γ in the event. Green line traces $\Delta t = 0$. 102

6.16 Timing coincidence between π^- and the γ in the event with the smallest $|\Delta t|$. Green line traces $\Delta t = 0$ for ease of comparison. 103

6.17 "Missing" mass distribution showing the cut position in green lines. Blue line indicates proton mass. 105

6.18 "Missing" momentum of the proton, showing, in green, the position of the cut at 120 MeV. 106

6.19 "Missing" momentum of the proton vs. polar angle θ in the laboratory frame. The red line indicated the position of the cut. 107

6.20 "Missing" momentum of the proton vs. $\Delta\phi$, the difference in azimuthal angles of the proton and π^- in the laboratory frame. A spectator momentum - dependent cut is shown with pink lines. 107

6.21 Difference between the total energy of the reaction calculated using the initial and final state. 108

6.22 Back-to-back angle of proton and π^- direction vectors in CM frame of the initial state. 109

6.23 "Missing" mass distribution, showing the effect of the event selection cuts. The black outline is the distribution before any cuts were applied, yellow the distribution after the missing momentum and coplanarity cut, red the final distribution after an additional α cut. 110

7.1 Energy distribution of photons which were produced in bremsstrahlung from an amorphous radiator, showing the expected $\frac{1}{E_\gamma}$ dependence (overlaid in red). 114

7.2 Enhancement plots showing the energy distribution from data using a diamond radiator oriented to produce a coherent peak at $E_\gamma = 1.7$ GeV, which was divided by the distribution of data obtained with an amorphous radiator to remove the unpolarised contribution. Secondary, smaller coherent peaks at higher energies are also evident from bremsstrahlung off other geometrically equivalent crystal planes in the radiator. The two photon polarisation orientations are shown in different colours and can be seen to agree well. 115

7.3 ϕ distributions in data taken with a parallel (left) and perpendicular (right) beam polarisation ($1735 < W < 1755$ MeV, $0.6 < \cos\theta < 0.8$), strongly dominated by the acceptance of CLAS. The non-fiducial regions due to the magnet coils are clearly seen as gaps in the distribution. 117

7.4 ϕ distributions in data taken with a parallel (left) and perpendicular (right) beam polarisation ($1735 < W < 1755$ MeV, $0.6 < \cos\theta < 0.8$), divided by the amorphous ϕ distribution and fitted with an $A + B\cos\theta$ function. 117

7.5 ϕ distribution for the W range 1.6 – 1.9 GeV and $\cos\theta$ in the range from -0.7 to -0.1 and 0.6 to 0.8, where Σ was always positive. The phase ϕ_0 was extracted from a fit with the function given in Eq. 7.5. 120

8.1 The χ^2 per degree of freedom distribution from fits to ϕ distributions in all W and $\cos\theta$ bins. 121

8.2 A comparison of the beam asymmetry extracted from events where the polarisation ratio was deliberately skewed to its maximum (red) and minimum (black). Any discrepancies in the value of Σ are within the statistical uncertainty. 122

8.3 Σ extracted from a fit with $\phi_0 = -0.047°$ (red) and $\phi_0 = 0.297°$ (black). These values of ϕ_0 are the lower and upper limits of the parameter within its error, $\phi_0 = 0.125° \pm 0.172°$. 124

8.4 A comparison, for a single bin in $\cos\theta$, of the beam asymmetry extracted from events where the momentum of the recoiling proton in the deuteron nucleus is < 30 MeV (black) and 95 – 120 MeV (red). 125

8.5 Beam asymmetry as a function of W, $\cos\theta$ from -0.8 to -0.5 in 0.1 wide bins, overlaid with SAID-09 (blue), MAID-07 (green) and SAID-09-NEW (red) partial wave analysis solutions. 130

8.6 Beam asymmetry as a function of W, $\cos\theta$ from -0.5 to -0.2 in 0.1 wide bins, overlaid with SAID-09 (blue), MAID-07 (green) and SAID-09-NEW (red) partial wave analysis solutions. Previous data from [99] shown with filled triangles. 131

8.7 Beam asymmetry as a function of W, $\cos\theta$ from -0.2 to 0.1 in 0.1 wide bins, overlaid with SAID-09 (blue), MAID-07 (green) and SAID-09-NEW (red) partial wave analysis solutions. Previous data from [97] and [99] shown with open circles and filled triangles respectively. 132

8.8 Beam asymmetry as a function of W, $\cos\theta$ from 0.1 to 0.4 in 0.1 wide bins, overlaid with SAID-09 (blue), MAID-07 (green) and SAID-09-NEW (red) partial wave analysis solutions. Previous data from [99] shown with filled triangles. 133

8.9 Beam asymmetry as a function of W, $\cos\theta$ from 0.4 to 0.7 in 0.1 wide bins, overlaid with SAID-09 (blue), MAID-07 (green) and SAID-09-NEW (red) partial wave analysis solutions. Previous data from [99] and [98] shown with filled triangles and open squares respectively. 134

8.10 Beam asymmetry as a function of W, $\cos\theta$ from 0.7 to 1 in 0.1 wide bins, overlaid with SAID-09 (blue), MAID-07 (green) and SAID-09-NEW (red) partial wave analysis solutions. Previous data from [99] and [98] shown with filled triangles and open squares respectively. 135

8.11 Beam asymmetry as a function of $\cos\theta$ for W 1605 – 1645 MeV, in 10 MeV wide bins, overlaid with SAID-09 (blue), MAID-07 (green) and SAID-09-NEW (red) partial wave analysis solutions. Data points not available in the entire range of W due to limited statistics in several bins. Previous data from [97] and [99] shown with open circles and filled triangles respectively. 136

8.12 Beam asymmetry as a function of $\cos\theta$ for W 1645 – 1685 MeV, in 10 MeV wide bins, overlaid with SAID-09 (blue), MAID-07 (green) and SAID-09-NEW (red) partial wave analysis solutions. Previous data from [99] and [98] shown with filled triangles and open squares respectively. 137

8.13 Beam asymmetry as a function of $\cos\theta$ for W 1685 – 1725 MeV, in 10 MeV wide bins, overlaid with SAID-09 (blue), MAID-07 (green) and SAID-09-NEW (red) partial wave analysis solutions. Previous data from [97] and [99] shown with open circles and filled triangles respectively. 138

8.14 Beam asymmetry as a function of $\cos\theta$ for W 1725 – 1765 MeV, in 10 MeV wide bins, overlaid with SAID-09 (blue), MAID-07 (green) and SAID-09-NEW (red) partial wave analysis solutions. Previous data from [97], [98] and [99] shown with open circles, open squares and filled triangles respectively. 139

8.15 Beam asymmetry as a function of $\cos\theta$ for W 1765 – 1805 MeV, in 10 MeV wide bins, overlaid with SAID-09 (blue), MAID-07 (green) and SAID-09-NEW (red) partial wave analysis solutions. Previous data from [97] and [99] shown with open circles and filled triangles respectively. 140

8.16 Beam asymmetry as a function of $\cos\theta$ for W 1805 – 1845 MeV, in 10 MeV wide bins, overlaid with SAID-09 (blue), MAID-07 (green) and SAID-09-NEW (red) partial wave analysis solutions. Previous data from [97], [98] and [99] shown with open circles, open squares and filled triangles respectively. 141

8.17 Beam asymmetry as a function of $\cos\theta$ for W 1845 – 1885 MeV, in 10 MeV wide bins, overlaid with SAID-09 (blue), MAID-07 (green) and SAID-09-NEW (red) partial wave analysis solutions. Previous data from [99] shown with filled triangles. . . 142

8.18 Beam asymmetry as a function of $\cos\theta$ for W 1885 – 1925 MeV, in 10 MeV wide bins, overlaid with SAID-09 (blue), MAID-07 (green) and SAID-09-NEW (red) partial wave analysis solutions. Previous data from [99] and [98] shown with filled triangles and open squares respectively. 143

8.19 Beam asymmetry as a function of $\cos\theta$ for W 1925 – 1965 MeV, in 10 MeV wide bins, overlaid with SAID-09 (blue), MAID-07 (green) and SAID-09-NEW (red) partial wave analysis solutions. Previous data from [97], [98] and [99] shown with open circles, open squares and filled triangles respectively. 144

8.20 Beam asymmetry as a function of $\cos\theta$ for W 1965 – 2005 MeV, in 10 MeV wide bins, overlaid with SAID-09 (blue), MAID-07 (green) and SAID-09-NEW (red) partial wave analysis solutions. Previous data from [97] and [99] shown with open circles and filled triangles respectively. 145

8.21 Beam asymmetry as a function of $\cos\theta$ for W 2005 – 2045 MeV, in 10 MeV wide bins, overlaid with SAID-09 (blue) and SAID-09-NEW (red) partial wave analysis solutions. Previous data from [97] and [99] shown with open circles and filled triangles respectively. 146

8.22 Beam asymmetry as a function of $\cos\theta$ for W 2045 – 2085 MeV, in 10 MeV wide bins, overlaid with SAID-09 (blue) and SAID-09-NEW (red) partial wave analysis solutions. 147

8.23 Beam asymmetry as a function of $\cos\theta$ for W 2085 – 2125 MeV, in 10 MeV wide bins, overlaid with SAID-09 (blue) and SAID-09-NEW (red) partial wave analysis solutions. Previous data from [97] shown with open circles. 148

8.24 Beam asymmetry as a function of $\cos\theta$ for W 2125 – 2165 MeV, in 10 MeV wide bins, overlaid with SAID-09 (blue) and SAID-09-NEW (red) partial wave analysis solutions. 149

8.25 Beam asymmetry as a function of $\cos\theta$ for W 2165 – 2205 MeV, in 10 MeV wide bins, overlaid with SAID-09 (blue) and SAID-09-NEW (red) partial wave analysis solutions. 150

8.26 Beam asymmetry as a function of $\cos\theta$ for W 2205 – 2245 MeV, in 10 MeV wide bins, overlaid with SAID-09 (blue) and SAID-09-NEW (red) partial wave analysis solutions. 151

8.27 Beam asymmetry as a function of $\cos\theta$ for W 2245 – 2285 MeV, in 10 MeV wide bins, overlaid with SAID-09 (blue) and SAID-09-NEW (red) partial wave analysis solutions. Data points not available in the entire range of W due to limited statistics in several bins. 152

8.28 Beam asymmetry as a function of $\cos\theta$ for W 2285 – 2325 MeV, in 10 MeV wide bins, overlaid with SAID-09 (blue) and SAID-09-NEW (red) partial wave analysis solutions. Data points not available in the entire range of W due to limited statistics in the majority of bins. 153

8.29 Contour plot of SAID-09-NEW beam asymmetry calculation carried out by [130] as a function of photon beam energy and θ overlaid over the grid of measured beam asymmetry points. 154

8.30 Surface plot SAID-09-NEW beam asymmetry calculation carried out by [130] as a function of photon beam energy and θ. 155

8.31 S_{31} and S_{11} electric multipoles for the proton, in units of am, extracted from the SAID-09 (blue), SAID-09-NEW (red) and MAID-07 (green) partial wave analyses by [130]. 156

8.32 S_{11} electric multipoles for the neutron and P_{31} magnetic multipoles for the proton, in units of am, extracted from the SAID-09 (blue), SAID-09-NEW (red) and MAID-07 (green) partial wave analyses by [130]. 157
8.33 P_{11} magnetic multipoles for the proton and neutron, in units of am, extracted from the SAID-09 (blue), SAID-09-NEW (red) and MAID-07 (green) partial wave analyses by [130]. 158
8.34 P_{33} electric and magnetic multipoles for the proton, in units of am, extracted from the SAID-09 (blue), SAID-09-NEW (red) and MAID-07 (green) partial wave analyses by [130]. 159
8.35 P_{13} electric and magnetic multipoles for the proton, in units of am, extracted from the SAID-09 (blue), SAID-09-NEW (red) and MAID-07 (green) partial wave analyses by [130]. 160
8.36 P_{13} electric and magnetic multipoles for the neutron, in units of am, extracted from the SAID-09 (blue), SAID-09-NEW (red) and MAID-07 (green) partial wave analyses by [130]. 161
8.37 D_{33} electric and magnetic multipoles for the proton, in units of am, extracted from the SAID-09 (blue), SAID-09-NEW (red) and MAID-07 (green) partial wave analyses by [130]. 162
8.38 D_{13} electric and magnetic multipoles for the proton, in units of am, extracted from the SAID-09 (blue), SAID-09-NEW (red) and MAID-07 (green) partial wave analyses by [130]. 163
8.39 D_{13} electric and magnetic multipoles for the neutron, in units of am, extracted from the SAID-09 (blue), SAID-09-NEW (red) and MAID-07 (green) partial wave analyses by [130]. 164
8.40 D_{35} electric and magnetic multipoles for the proton, in units of am, extracted from the SAID-09 (blue), SAID-09-NEW (red) and MAID-07 (green) partial wave analyses by [130]. 165
8.41 D_{15} electric and magnetic multipoles for the proton, in units of am, extracted from the SAID-09 (blue), SAID-09-NEW (red) and MAID-07 (green) partial wave analyses by [130]. 166
8.42 D_{15} electric and magnetic multipoles for the neutron, in units of am, extracted from the SAID-09 (blue), SAID-09-NEW (red) and MAID-07 (green) partial wave analyses by [130]. 167

8.43 F_{35} electric and magnetic multipoles for the proton, in units of am, extracted from the SAID-09 (blue), SAID-09-NEW (red) and MAID-07 (green) partial wave analyses by [130]. 168
8.44 F_{15} electric and magnetic multipoles for the proton, in units of am, extracted from the SAID-09 (blue), SAID-09-NEW (red) and MAID-07 (green) partial wave analyses by [130]. 169
8.45 F_{15} electric and magnetic multipoles for the neutron, in units of am, extracted from the SAID-09 (blue), SAID-09-NEW (red) and MAID-07 (green) partial wave analyses by [130]. 170
8.46 F_{37} electric and magnetic multipoles for the proton, in units of am, extracted from the SAID-09 (blue), SAID-09-NEW (red) and MAID-07 (green) partial wave analyses by [130]. 171
8.47 F_{17} electric and magnetic multipoles for the proton, in units of am, extracted from the SAID-09 (blue), SAID-09-NEW (red) and MAID-07 (green) partial wave analyses by [130]. 172
8.48 F_{17} electric and magnetic multipoles for the neutron, in units of am, extracted from the SAID-09 (blue), SAID-09-NEW (red) and MAID-07 (green) partial wave analyses by [130]. 173
8.49 G_{37} electric and magnetic multipoles for the proton, in units of am, extracted from the SAID-09 (blue), SAID-09-NEW (red) and MAID-07 (green) partial wave analyses by [130]. 174
8.50 G_{17} electric and magnetic multipoles for the proton, in units of am, extracted from the SAID-09 (blue), SAID-09-NEW (red) and MAID-07 (green) partial wave analyses by [130]. 175
8.51 G_{17} electric and magnetic multipoles for the neutron, in units of am, extracted from the SAID-09 (blue), SAID-09-NEW (red) and MAID-07 (green) partial wave analyses by [130]. 176
8.52 G_{39} electric and magnetic multipoles for the proton, in units of am, extracted from the SAID-09 (blue), SAID-09-NEW (red) and MAID-07 (green) partial wave analyses by [130]. 177
8.53 G_{19} electric and magnetic multipoles for the proton, in units of am, extracted from the SAID-09 (blue), SAID-09-NEW (red) and MAID-07 (green) partial wave analyses by [130]. 178

8.54 G_{19} electric and magnetic multipoles for the neutron, in units of am, extracted from the SAID-09 (blue), SAID-09-NEW (red) and MAID-07 (green) partial wave analyses by [130]. 179

A.1 Reaction axes convention 184

Chapter 1

Introduction

1.1 Brief history of the hadron

1.1.1 A plethora of particles

The study of the nucleon has occupied fundamental physics for almost a century and played an important role in its history. The discovery of the proton, named perhaps in subconscious anticipation after the Greek word for the "first", emerged in 1919 from Rutherford's scattering experiments [1]. Thought at the time to be a fundamental constituent of the nucleus, it was joined some thirteen years later by the neutron, identified by Chadwick in 1932 [2]. Soon after its discovery, Heisenberg proposed that the similarities in the neutron's and the proton's mass suggest that they are two charge states of a single particle [3], which he called the nucleon, an early indication of a soon-emerging symmetry. This completed a deceptively simple picture of the atom — a nucleus of protons and neutrons surrounded by an electron cloud [4]. Yet it begged the question: what holds the nucleons together? A new force was evidently at play and in 1935 Yukawa quantised the unimaginatively-named "strong" force in terms of the exchange of a new mediator particle, the meson, between nucleons [5]. He calculated its mass based on the short range of the strong force (on the order of 1 fm) to be ~ 150 MeV/c^2, which 12 years later was identified with the pion [6].

The 77 years that followed the Bohr model of the atom, however, proved more turbulent than anyone had anticipated. Early identification of new particles relied primarily on cosmic rays and was therefore limited to relatively long-lived specimen.

However, the development in accelerator technology [7] which started in the 1930's soon allowed intense, focussed beams of particles to be used in fixed-target and, later, collider experiments. As a result, the pantheon of apparently fundamental particles expanded colossally. Significantly, a whole group of "strange" particles appeared on the scene in the late forties, such as the K^0 (1948), K^+ (1949) and the Λ (1950)[1] [9]. Faced with the puzzle of their relatively large creation rate and yet alarmingly slow decay, Gell-Mann [10] and Nishijima [11] both postulated the existence of a new quantum number called "strangeness", S, which had to be conserved in the strong interactions in which the strange particles were created, but could be violated in their weak decay.

By the 1960's the zoo of particles had grown out of all proportion, eliciting from Enrico Fermi the comment to his student "Young man, if I could remember the names of all these particles, I would have been a botanist!" [12]. Particle physics was indeed beginning to look like taxonomy, with proliferating attempts to classify according to mass, charge and other quantum numbers.

1.1.2 The Quark Model — emerging symmetries

A tremendous theoretical breakthrough came in 1961 when Murray Gell-Mann and Yuval Ne'eman independently proposed a way of geometrically arranging the lightest hadrons, recognising their correspondence to members of the SU(3) symmetry group [13]. This discovery was riding on the back of previous attempts to describe the particle reactions in terms of symmetries. Amongst them, Stuckelberg had proposed as early as 1938 the conservation of baryon number (B) to explain the stability of the proton, which, as the lightest baryon, had no other $B = 1$ state to decay into [14]. Heisenberg's identification of a proton and a neutron as two states of a nucleon had led to the introduction of isospin, I, a quantum number by analogy with spin, but pertaining to the state of the nucleon (with proton having $I_3 = \frac{1}{2}$ and neutron $I_3 = -\frac{1}{2}$, of the nucleon's $I = \frac{1}{2}$ isospin). Rotations in isospin space (just as those in spin-space) were thus seen as a representation of the SU(2) symmetry, described by operators analogous to the Pauli matrices.

[1] Given the difficulties, sometimes, of identifying specific "discovery" papers, it is perhaps best to reference Kuhn and his discussion of "discovery" as a process and rarely a single "Eureka!" event [8].

Gell-Mann took this idea further and assembled hadrons of the same baryon number, angular momentum, parity (J^P) and similar masses into super-multiplets, arranging them along axes of strangeness and isospin (Figs. 1.1 and 1.2, where electrical charge Q relates to the isospin via $I_3 = Q - (S + B)/2$). In his Eightfold Way formulation, the lightest known family of $B = 1$ particles formed a hexagonal array with two occupying the $Q = 0$, $S = -1$ point, collectively known as the baryon octet. It belongs to the eight-dimensional representation of the SU(3) group, consisting of a set of SU(2) isospin sub-groups. The lightest mesons ($B = 0$) fall into the corresponding pseudoscalar meson nonet (a combination of an octet and a singlet), with heavier ones forming new super-multiplets. The ten heavier baryons assemble into a triangular decuplet (ten-dimensional SU(3)), the apex of which, the Ω^-, finally brought triumphant verification of the scheme when it was discovered in 1964 [15] based on Gell-Mann's predictions.

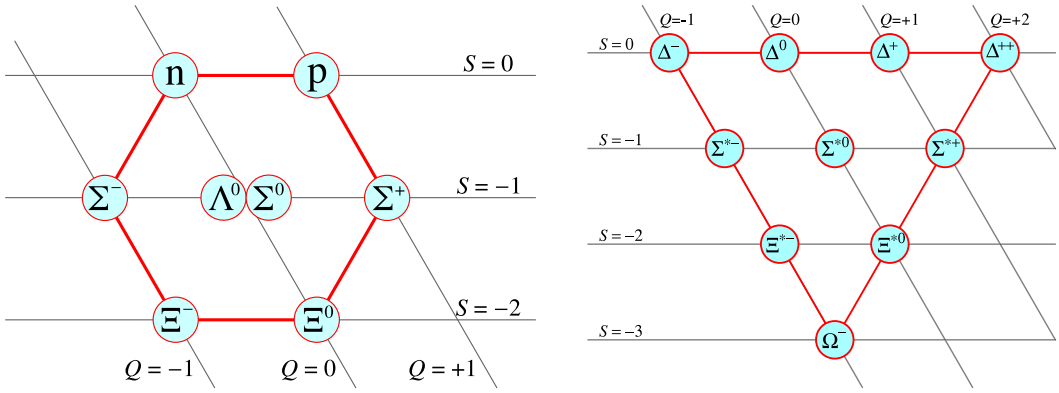

Figure 1.1: The two lightest baryon ($B = 1$) multiplets — spin-$\frac{1}{2}$ octet, containing proton and neutron, on the left and spin-$\frac{3}{2}$ decuplet on the right. Image courtesy of *Wikimedia Commons*.

The arrangement of the hadrons into individual representations of the SU(3) group raised a question about this symmetry's implication. In 1964 Gell-Mann and Zweig [16] both proposed that hadrons were a bound state of fundamental particles called quarks[1], which came in three flavours of "up", "down" and "strange". Rotations in flavour space were then represented by a group of eight matrices in correspondence with SU(3), although the symmetry was not complete due to the small differences in

[1]The name was coined by Gell-Mann, who took the spelling for the sound from the phrase "Three quarks for Muster Mark" which he found in James Joyce's *Finnegans Wake* [17].

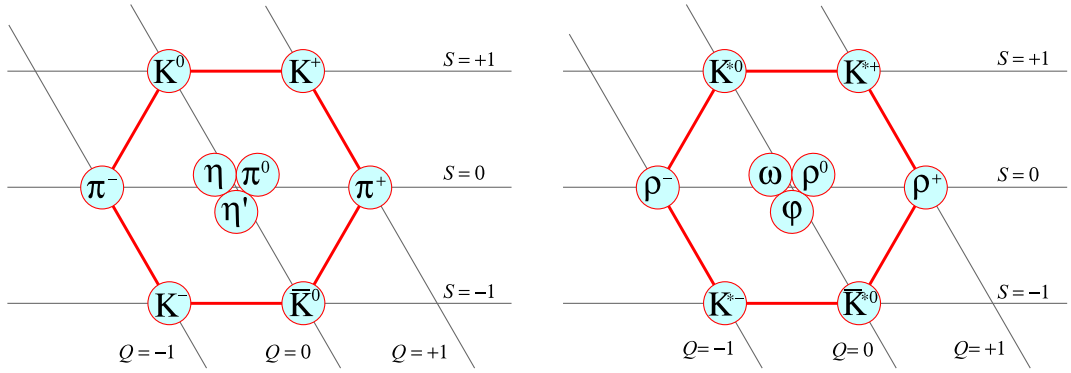

Figure 1.2: The two lightest meson ($B = 0$) multiplets — spin-0 nonet, containing the three pions, on the left, spin-1 nonet on the right. Image courtesy of *Wikimedia Commons*.

the masses of the different flavour quarks. Each quark, it was postulated, carries fractional quantum numbers of charge ($\frac{2}{3}$ for up, $-\frac{1}{3}$ for down and strange), spin ($\frac{1}{2}$) and $\frac{1}{3}$ baryon number, while strangeness is only assigned to the strange quark (with a quantum number of -1). The quark model, as it became known, stated that each baryon was formed of three quarks, each meson of a quark and anti-quark pair. The three quarks and their anti-quarks, arranged into triangles along the same axes of isospin and strangeness as the hadrons, form the fundamental, three-dimensional representation of SU(3) (Fig. 1.3), which in combination leads to the known meson and baryon multiplets.

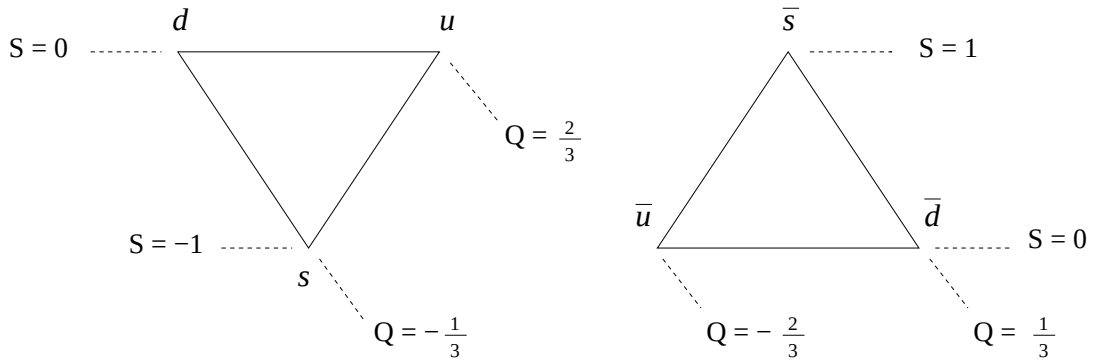

Figure 1.3: Eightfold Way arrangement of lightest quarks (left) and antiquarks (right).

Three heavier flavours of quarks have since been added to the classification: charm,

bottom and top. Evidence for their existence came in the discoveries of the $c\bar{c}$ J/ψ meson (1974) [18], the $b\bar{b}$ Υ (1977) [19] and the observation of top quark decays at Fermilab in 1995 [20]. The symmetry was extended to SU(4), SU(5) and SU(6) with the addition of each new flavour, but became more and more imperfect due to the increasingly large differences in the masses of the quarks — the bare bottom quark mass, for example, is an order of 1000 times greater than the bare up quark mass, while the top quark is some 42 times heavier still [21].

Experimentally, however, the quark model had remained on thin ground for some time. No individual quark had ever been observed and the notion of quark confinement to the only known qqq baryon and $q\bar{q}$ meson bound states bothered experimentalists and theorists alike. Moreover, the fermion nature of the quarks appeared to violate the Pauli Exclusion Principle, for example the Δ^{++} being a uuu combination. This inspired O. Greenberg to propose in 1964 that quarks possess another quantum number, colour, of which there are three choices — red, green and blue [22]. The fact that colour was not experimentally observed in nature implied the condition that only colourless compositions of quarks were allowed. The combination of all three colours, by analogy with optics, results in no colour at all — as must be the case in each baryon. Colour and its corresponding anti-colour also produces a colour-neutral particle (as in a meson). The strong interaction could then be represented by SU(3) rotation matrices and reinterpreted as acting on colour charges.

1.1.3 Quantum Chromodynamics

The field theory of Quantum Chromodynamics (QCD) initially developed along the lines of Quantum Electrodynamics (QED), with the field being mediated via the exchange of gluons, spin 1 bosons, coupling to conserved colour charges. In the simplest form of the interaction, $q \rightarrow q + g$, although the colour of the quark may change, it must be conserved at the vertex. The gluon must therefore carry a colour and anti-colour charge, and can thus couple to other gluons via the strong force. This field theory fits neatly into the SU(3) formalism, where the eight different types of gluons represent the eight generators of rotations in colour space.

The strength of the strong interaction is governed in the theory by the dimensionless coupling constant, α_s. Experimental determination of α_s suggests that, unlike the case

in QED, it depends strongly on the separation of the colour charges (Fig. 1.4, where the energy scale is a measure of the separation achieved), in consequence of which it is known as the running coupling constant.

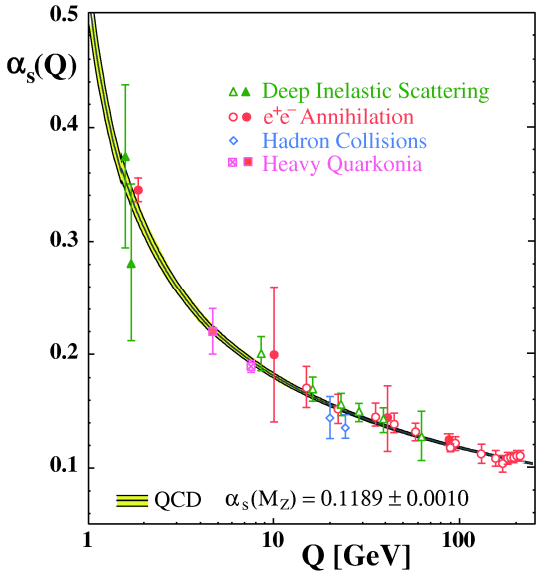

Figure 1.4: Strong coupling constant as a function of energy, comparison of world data points from different experiments and QCD calculations (yellow band) [23].

The QCD picture of the hadron is more complex than one consisting of only the valence quarks (which determine the type of the particle), and includes significant contributions from the "sea" of gluon-gluon interactions and quark - anti-quark pairs popping in and out of existence (Fig. 1.5). The important role of these is evident in the mass difference of a hadron and its valence quarks, the latter accounting for only $\sim 1\%$ of the hadron's mass.

The quark-quark interaction possibilities are illustrated by the Feynman diagrams in Fig. 1.6, where a quark emits a gluon, which can then emit and absorb more quark - antiquark pairs and gluons before being itself absorbed by another quark, resulting in a vacuum anti-screening effect. The probability of more loops being involved in the interaction rises with the particle separation and each additional pair of vertices contributes another factor of α_s. Higher orders can therefore no longer be ignored (as in the treatment of QED with its small coupling constant of $\sim \frac{1}{137}$), which results in the

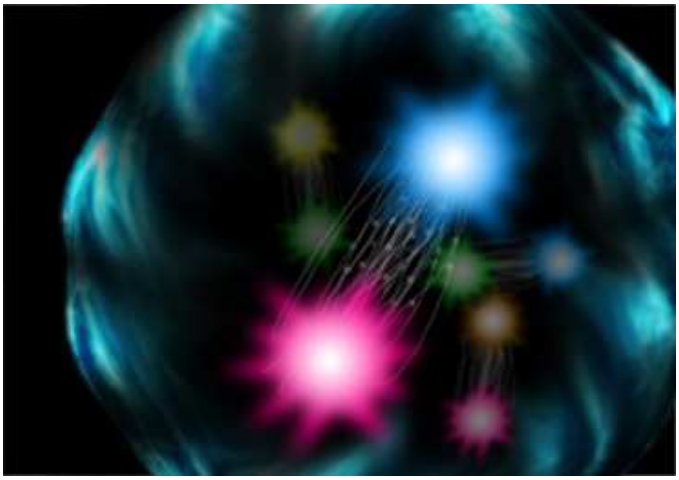

Figure 1.5: Artist's impression of a meson showing the valence quarks and quark - anti-quark pairs in the background (Image courtesy of Jefferson Lab).

phenomenon of asymptotic freedom, where the strong force is weak deep inside the hadrons but rises very sharply as interaction distance increases.

Bound combinations of more than three quarks are theoretically possible within QCD and experimental searches for exotic combinations of four, five or six quarks (called tetraquarks, pentaquarks and hexaquarks) have been carried on for decades. These, however, have not been established.

The study of quantum chromodynamics therefore splits naturally into the high energy, very short distance regime, where Feynman calculus and perturbation theory is applicable, and the world of the low energy region of confinement in the bound states — baryons and mesons. Hadron structure poses a formidable challenge for both theorists and experimentalists alike, while holding the key to our understanding of how QCD manifests itself in the non-perturbative regime.

1.2 Theoretical approaches to the hadron

Theoretically, the phenomenon of confinement cannot be solved in terms of non-perturbative QCD. The hadron is a complicated composite object and its description presents a considerable theoretical challenge. Approaches are separated into QCD-based calculations (such as those on the lattice), where ways have to be found to yield

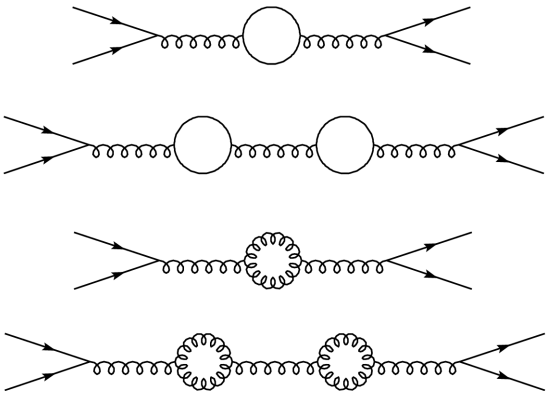

Figure 1.6: Feynman diagrams showing multiple loop contributions to the quark-quark interaction.

testable predictions about the behaviour of the hadrons and phenomenological, QCD-inspired models where the hadron is described in terms of constituent quarks. This section outlines the basic theoretical tool kit of non-perturbative QCD.

1.2.1 Tools in QCD

1.2.1.1 Lattice QCD

Some significant success in describing the hadron has been had with Lattice QCD (LQCD) calculations, where space-time is quantised in terms of a grid along which gluons and valence and sea quarks are allowed to propagate. Realistic predictions about their behaviour can then be extracted by letting the grid spacing tend to zero. This approach is incredibly intensive in terms of computational power and it is only recently that supercomputers large enough to yield testable predictions have been built. Very good precision has been obtained for systems containing heavy quarks (c, b and t) [24], however, computational power increases dramatically with a decreasing quark mass and LQCD becomes particularly difficult for the light quarks. Nevertheless, LQCD has been successful in calculating the masses of ten light hadrons [25], along with other properties of hadronic structure, such as the decay rates of the π^- and K mesons [26]. Predictions for both ground and some excited state properties of the nucleon have also been made in the recent years [27], [28], [29]. Great advances in this approach are

expected in the next decade.

1.2.1.2 Chiral Perturbation Theory

An effective theory which has provided some promising results is Chiral Perturbation theory, a reformulation of QCD in which the fundamental degrees of freedom are hadrons rather than quarks [30]. Based on chiral symmetry, it assumes massless quarks and can therefore only realistically be expected to describe the interaction of hadrons based on the lightest quark set (up, down and strange). Since individual quarks do not figure as degrees of freedom in the theory it is also silent on the matter of hadron resonances, but has been used effectively to describe three-nucleon forces and some aspects of the hadronic interaction [31], [32], [33].

1.2.1.3 Conformal field theories

Some rather successful predictions, to within 10 – 20% accuracy, in the low-energy regime have also come out of the AdS/QCD formulation [34], [35]. It consists of a series of models built up on the AdS/CFT correspondence, yielding calculations on the conformal boundary of a multi-dimensional anti - de Sitter space, where mesons are identified with multi-dimensional strings and baryons with solitonic excitations similar to the Skyrme model [36].

1.2.1.4 Sum Rules

A method which interpolates between the analytical high-energy perturbative limit of QCD and the low energy non-perturbative region, where degrees of freedom are hadrons, is based on the sum rule approach. This relies on the use of dispersion relations, in which a nucleon correlator, related to the quark current, is used to determine the spectral function of hadron excitations [37]. The Gerasimov-Drell-Hearn sum rule [38], [39], for example, directly relates differences in polarised cross-sections to the mass and magnetic moment of the resonance. There is a current series of experimental efforts to establish and look for deviations from these sum rules [40].

1.2.2 Phenomenological Hadron Models

1.2.2.1 Constituent Quark Models

Many of the experimentally testable predictions about the structure of the hadron have been the result of phenomenological models based on the distinguishing characteristics of QCD, such as confinement, asymptotic freedom and constituent quarks. The group of non-relativistic constituent quark models (CQM) treat the hadron as consisting of just the valence quarks. The individual "bare" quark masses from QCD predictions are very small for the lightest set of $SU(3)_f$ quarks (a few MeV/c^2 for the u and d, $\sim$ 100 MeV/c^2 for the strange [21]) and inconsistent with the observed masses of their bound states. The basis of constituent quark models rests on resolving this inconsistency by assigning "effective" mass values to the quarks, which add up to form the masses of the lightest hadron octet and decuplet (Fig. 1.7). This approach is remarkably successful, and even the simplest models show good agreement with data on the magnetic moments of the nucleons [41].

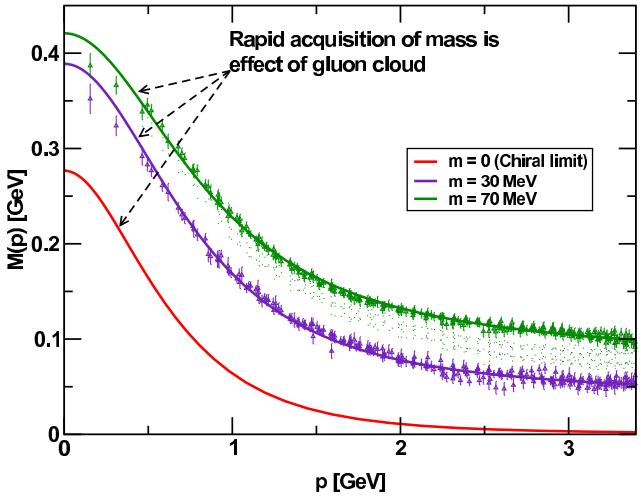

Figure 1.7: At high quark momentum, in the perturbative QCD region, quark mass is very small. As quark momentum reduces, however, the "bare" quarks become "dressed" in a gluon cloud, effectively acquiring mass. Constituent quark models operate in this regime. The different curves show scenarios for different "bare" quark masses, m [42].

The earliest of the constituent quark models have been constructed in the 1960's and were based on a simple harmonic oscillator potential which resulted in a non-

relativistic Hamiltonian expressed, in internal co-ordinates of the quarks, as two independent oscillators. This model formed the basis of constituent models to follow [43]. The de Rujula, Georgi and Glashow (DGG) model [44] was a dynamical extension of the potential model with three quarks, and derived the quark mass formulae based on a short-range one-gluon exchange (OGE) interaction between them and a long-range confining potential. This was very successful in explaining the hyperfine splitting of the Δ - N masses. A few years later, Isgur and Karl [45] extended the harmonic oscillator model to include an anharmonic perturbation and a hyperfine term in the Hamiltonian, which resulted in improved calculations of the masses and widths in the spectrum, but suffered from too many degrees of freedom, resulting in many more nucleon resonances being predicted than were observed.

Recently, models which describe the quark in terms of two degrees of freedom based on a quark and diquark picture have been revisited [46]. The motivation for reducing the number of degrees of freedom comes in the effort to resolve the discrepancy between the greater number of resonances predicted by most models than are observed experimentally. The diquark formulation has seen some success in calculating masses of low-lying resonances [47].

1.2.2.2 Soliton Models

A conceptually different approach was to construct soliton models of the hadron, which focussed on the confining effect of the potential and represented it as a colour dia-electric vacuum. This developed into a series of “bag” models of the hadron, which were pioneered by Bogoliubov in the 1960’s [48]. In the model, the quarks are seen as massless and effectively free inside the bag, while infinitely massive outside it, confined in a deep potential well. Although the model provided an excellent prediction of the Roper resonance state (with mass 1440 MeV, which is of particular interest as its mass appears to be lower than the total masses of its constituent quarks), it was far too simplistic. The MIT Bag model [49] went beyond this and incorporated asymptotic freedom and relativistic interactions into the picture. The quarks were seen as having small masses, bound by weak forces in a perturbative vacuum inside the bag (whose radius was now dynamically determined), while its exterior was kept at a lower, non-perturbative vacuum energy into which the quarks were not allowed to propagate.

The bag models discussed above suffered from a violation of chiral symmetry at the surface of the bag. To address this, a pion field was introduced into a bag to model the Goldstone boson and conserve axial current under chiral transformations of the new Lagrangian density. One such successful model, the Cloudy Bag Model [50], "dresses" the valence quarks of the MIT bag model in a pion cloud. The chiral bag model was also extended to chiral solitons, such as for example the Skyrmion model [51].

1.2.2.3 QCD exotica

Exotic states, having more than three quarks, have also been predicted from symmetry considerations and are, for example, allowed in the chiral solition models [52]. These postulate the existence of an anti-decuplet of excited baryon states, in which the three states representing the vertices of the decuplet triangle are required, by implication from their quantum numbers, to have a five-valence-quark composition [53], [54]. The remaining partners of the anti-decuplet are not exotic, but are predicted to have very narrow widths. Experimental searches for the pentaquark states have not been conclusive [55], however some evidence has emerged from η-production off the neutron which may be suggestive of the signal of a non-strange member of the anti-decuplet in the region of 1680 MeV [56]. This is currently strongly debated.

1.3 Experimental study of hadronic structure

The rest of this chapter gives the experimental context to measurements of observables which inform us of nucleon structure, with particular emphasis on those relating to the topic of this thesis. It introduces the picture of the hadron emerging from experiments as well as the importance, methods and challenges involved in data interpretation.

1.3.1 Emergence of the parton model

The dawn of experimental study into the structure of the nucleon dates back to the early 1950's, when the first experimental indications of its non point-like structure became apparent. The first glimpses inside came from measurements of cross-sections

in elastic e-p scattering, which provided information on the charge and magnetic moment distribution of the proton. The scattering cross-section can be expanded in terms of the electric and magnetic form-factors (G_E and G_M respectively), which relate, via a Fourier-transform, the spatial charge and magnetic moment distributions of the probed particle to the momentum transfer, Q^2, during the scattering. In the low Q^2 ($\leq$ 20 MeV^2/c^2) regime, the differential cross-section is dominated by G_E and gives convenient access to the root mean square charge radius of the proton, which has been measured at 0.86 $\pm$ 0.01 fm [57]. In the intermediate energy regime (0.02 GeV^2/c^2 $\leq$ Q^2 $\leq$ 3 GeV^2/c^2), the G_E and G_M contributions can be separated by exploring the different Q^2 and scattering angle dependence of the two terms. The results in recent decades have led to the concept that there could be a simple "dipole" description of the nucleon form factors:

$$G_E(Q^2) \approx G_M(Q^2)/\mu_p \tag{1.1}$$

where μ_p is the proton magnetic moment [58]. However, a rapid decrease of the ratio of electric to magnetic form-factors with increasing Q^2 has been recently observed in the higher Q^2 regime. The interpretation of the results is currently debated but may suggest differences between the spatial distributions of charge and magnetisation in the nucleon.

Further evidence of what experimentally became known as the parton distribution, came in the sixties from inelastic lepton scattering at SLAC [59]. Although the "partons" were identified with quarks by advocates of the quark model, it was not widely accepted for a number of years and, for historical reasons, the name has stuck. Inelastic lepton scattering from a nucleon can be viewed in terms of elastic scattering from an individual quark, followed by the recoiling quark and the rest of the target particles combining into other hadrons. The differential cross-section can be parametrised in terms of two structure functions, $F_1(x, Q^2)$ and $F_2(x, Q^2)$, where x is known as the scaling variable and represents, at $Q^2 \gg M^2$ (M being the mass of the target proton), the fraction of longitudinal proton momentum carried by the struck quark. The structure functions at fixed x were shown to be approximately independent of Q^2 [60] (a feature known as the Bjorken scaling or scale invariance), which suggests that the scattering takes place from point-like partons inside the proton. The Callan-Gross relation of the structure functions ($F_1 = F_2/2x$) suggests that the partons are spin-$\frac{1}{2}$ particles, supported by the observed data and in agreement with the quark model. Observation

of a slight break of the scaling invariance is made in deep inelastic scattering (DIS), where the momentum transfer is high enough for scattering to take place also from the "sea" quarks, introducing a weak dependence of the structure functions on Q^2 [61]. Information of the transverse momenta of the quarks can be gleaned from transversity distributions, also in DIS. The combined data leads to Generalised Parton Distributions (GPDs), where the momenta, charge and magnetic moments of the partons are incorporated into a single picture of the particle [62].

The parton model continues to function as a good first approximation when terms relating to anti-quarks are introduced, however experimental separation of quark and anti-quark contributions, as well as measurements of parton charges, rely on neutrino scattering which became possible with the creation of neutrino beams at CERN in the early '70s [63]. A break of scaling invariance is observed again at large Q^2, where the struck quark emits a gluon which carries off some of the momentum. As Q^2 increases, gluon-emission corrections become more significant. Measurements of the scaling deviation, which are induced by the sea, thus provide information on the strong coupling constant and are consistent with predictions from QCD.

1.3.2 Hadron spectroscopy

1.3.2.1 The importance of nucleon resonances

The ground state properties of the nucleon as explored in elastic and deep inelastic scattering provide valuable information on its structure. However, as is the case for many composite systems in nature, the detailed character of how the object can be excited gives additional crucial information on the dynamics of its constituents. The bound quark state of the baryon is of particular interest, not just because baryons are the building blocks of known matter, but also because it is one of the simplest systems in which QCD is manifest. Baryon resonances are states of the baryon with the same valence quark composition but differences in quantum numbers — for example isospin, orbital angular momentum and spin — and, because of the large excitation energies can poses very different invariant mass to the ground state. The resonance spectrum is therefore characterised by a classification in terms of quantum numbers. Thus an excited state would be given, in full, as $X(m)L_{2I,2J}$ where X describes the type of baryon, m its rest mass (in MeV/c^2), L is the lowest orbital angular momentum the

excited baryon must have to decay into its ground state with the emission of a pseudoscalar meson and I and J are the isospin and total angular momentum respectively. The naming convention reflects both the quark composition and the isospin, such that u, d quark baryons are called N if they have isospin $\frac{1}{2}$, Δ if it's isospin $\frac{3}{2}$. If one of the quarks is replaced by a strange, the excited state is called Λ with isospin 0 and Σ with isospin 1, and so on. The spectroscopic notation is used for the label L: S, P, D, F, G, H, etc, for the corresponding $L = 0, 1, 2, 3, 4, 5$ [64]. For example the $\Delta(1232)P_{33}$ resonance has an invariant mass of 1232 MeV/c^2, isospin $\frac{3}{2}$, total angular momentum $\frac{3}{2}$ and must have an orbital angular momentum of at least 1 to decay to a ground state nucleon. The importance of determining the resonance spectrum of the hadron rests on the direct correlation between the number of excited states and their quantum numbers with the effective degrees of freedom of the system. As such, this is a direct test of hadron models.

All known nucleon resonances have excitation energies above that of the lightest mesons (pions) and so decay predominantly via the strong interaction with the emission of a meson. Due to the associated time-scale for strong processes, they are incredibly short-lived (typically $\approx 10^{-24}$ s), which results in large energy widths, on the order of 100 MeV. This is wide compared to the typical spacing of different resonances, therefore most of them have considerable overlap, making their identification experimentally difficult. This is illustrated in the cross-section data (Fig. 1.8) for various meson decay channels in proton photoabsorbtion, in which, apart from the large peak at the Δ corresponding to a photon energy (E_γ) of $\sim$ 350 MeV, only small features from groups at higher resonances are visible.

1.3.2.2 Experimental challenges

Of the plethora of models developed over the years some are seen to give broad agreement with the currently experimentally established resonance spectrum, others predict only certain states — all of those still realistically considered having some significant experimental support. A crucial issue of every model, however, is the determination of the number of degrees of freedom of the system, which broadly determines the possible resonant states of the hadron. This has long been an issue of contention, as some of the resonances predicted vary from model to model and a great number of them have still not been experimentally observed (Table 1). The question arises — is this due to

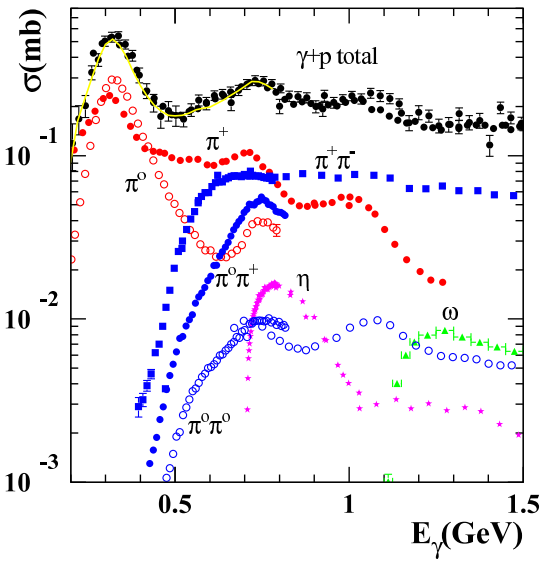

Figure 1.8: The total cross-sections for free proton photoabsorbtion (black data points), showing the three resonance regions. A number of meson channels contributing to the total cross-sections are shown in colour [65].

limited experimental capabilities, or to the fact that those resonances are simply not there, predicted by models which do not correspond to nature. The issue of "missing" resonances has driven the experimental quest over a number of decades.

The large experimental uncertainties on a significant number of partial decay widths for the observed resonances [21] is another long-standing problem in the study of the hadron. Discrepancies in the interpretation of the data from applying different reaction models complicate the matter further. These can only be resolved with a large dataset of precise measurements, which will both constrain the models more stringently and reduce model-dependence in the interpretation of the data overall. This world effort has developed real pace in the past five years and the data presented in this thesis will be a crucial component of this programme.

1.3.2.3 Electromagnetic and hadronic probes of the nucleon

Most experiments aimed at the study of the resonance spectrum use either hadronic or electromagnetic probes. Beams of baryons, notably protons, deuterons and alpha particles, require very high energies to reach a resonance invariant mass and the interaction

Resonance	KH	CM	Kent	GWU	BnGa
$N_{1/2^+}(1440)$	1410±12; 135±10	1440±30; 340±70	1462±10; 391±34	1485± 1; 284±18	1436±15; 335±40
$N_{3/2^-}(1520)$	1519± 4; 114± 7	1525±10; 120±15	1524± 4; 124± 8	1516± 1; 99± 3	1524± 5; 112±10
$N_{1/2^-}(1535)$	1526± 7; 120±20	1550±40; 240±80	1534± 7; 151±27	1547± 1; 188± 4	1530±30; 210±30
$N_{1/2^-}(1650)$	1670± 8; 180±20	1650±30; 150±40	1659± 9; 170±12	1635± 1; 115± 3	1705±30; 220±30
$N_{5/2^-}(1675)$	1679± 8; 120±15	1675±10; 160±20	1676± 2; 159± 7	1674± 1; 147± 1	1670±20; 140±40
$N_{5/2^+}(1680)$	1684± 3; 128± 8	1680±10; 120±10	1684± 4; 139± 8	1680± 1; 128± 1	1667± 6; 102±15
$N_{3/2^-}(1700)$	1731±15; 110±30	1675±25; 90±40	1737±44; 250±230	-	1740±20; 180±30
$N_{1/2^+}(1710)$	1723± 9; 120±15	1700±50; 90±30	1717±28; 480±330	-	-
$N_{3/2^+}(1720)$	1710±20; 190±30	1700±50; 125±70	1717±31; 380±180	1750± 5; 256±22	1720±30; 330±60
$N_{3/2^-}(1860)$	-	1880±100; 180±60	1804±55; 450±185	-	1875±25;105±25
$N_{1/2^+}(1880)$	-	-	1885±30; 113±44	-	1880±40; 220±60
$N_{5/2^+}(1890)$	1882±10; 95±20	-	1903±87; 490±310	-	1880±30; 250±50
$N_{3/2^+}(1900)$	-	-	1879±17; 498±78	-	1915±50; 220±65
$N_{1/2^-}(1905)$	1880±20; 95±30	-	1928±59; 414±157	-	-
$N_{7/2^+}(1990)$	2005±150; 350±100	1970±50; 350±120	2086±28; 535±120	-	-
$N_{3/2^-}(2080)$	2080±20; 265±40	2060±80; 300±100	-	-	2160±40; 340±65
$N_{1/2^-}(2090)$		2180±80; 350±100	-	-	-
$N_{1/2^+}(2100)$	2050±20; 200±30	2125±75; 260±100	-	-	-
$N_{5\ 2f}(2200)$	2228±30; 310±50	2180±80; 400±100	-	-	2060±30; 340±50
	KH	CM	Kent	GWU	Hendry
$N_{7/2^-}(2190)$	2140±12; 390±30	2200±70; 500±150	2127± 9; 550±50	2152±2; 484±13	2140±40; 270±50
$N_{9/2^+}(2220)$	2205±10; 365±30	2230±80; 500±150	-	2316±3; 633±17	2300±100; 450±150
$N_{9/2^-}(2250)$	2268±15; 300±40	2250±80; 400±120	-	2302±6; 628±28	2200±100; 350±100
$N_{11/2^-}(2600)$	2577±50; 400±100	-	-	-	2700±100; 900±100
$N_{13\ 2f}(2700)$	2612±45; 350±50	-	-	-	3000±100; 900±150
	KH	CM	Kent	GWU	BnGa
$\Delta_{3/2^+}(1232)$	1232± 3; 116± 5	1232± 2; 120± 5	1231± 1; 118± 4	1233± 1; 119± 1	1231± 4; 114± 5
$\Delta_{3/2^+}(1600)$	1522±15; 220±40	1600±50; 300±100	1706±10; 430±73	-	1620±80; 350±100
$\Delta_{1/2^-}(1620)$	1610± 7; 139±18	1620±20; 140±20	1672± 7; 154±37	1614±1; 71±3	1650±25; 250±60
$\Delta_{3/2^-}(1700)$	1680±70; 230±80	1710±30; 280±80	1762±44; 600±250	1688±3; 182±8	1640±40; 270±60
$\Delta_{1/2^+}(1750)$	-	-	1744±36; 300±120	-	-
$\Delta_{1/2^-}(1900)$	1908±30; 140±40	1890±50; 170±50	1920±24; 263±39	-	-
$\Delta_{5/2^+}(1905)$	1905±20; 260±20	1910±30; 400±100	1881±18; 327±51	1856± 2; 321± 9	1800±50; 370±110
$\Delta_{1/2^+}(1910)$	1888±20; 280±50	1910±40; 225±50	1882±10; 229±25	2068±2; 543±10	-
$\Delta_{3/2^+}(1920)$	1868±10; 220±80	1920±80; 300±100	2014±16; 152±55	-	1990±35; 330±60
$\Delta_{5/2^-}(1930)$	1901±15; 195±60	1940±30; 320±60	1956±22; 530±140	-	-
$\Delta_{3/2^-}(1940)$	-	1940±100; 200±100	2057±110; 460±320	-	1990±40; 410±70
$\Delta_{7/2^+}(1950)$	1913± 8;224±10	1950±15; 340±50	1945± 2; 300± 7	1921± 1; 271± 1	1895±20; 260±40
$\Delta_{5/2^+}(2000)$	2200±125; 400±125	-	1752±32; 251±93	-	-
$\Delta_{1\ 2f}(2150)$	-	2200±100; 200±100	-	-	-
	KH	CM	Kent	GWU	Hendry
$\Delta_{7/2^-}(2200)$	2215±10; 400±100	2200±80; 450±100	-	-	2280±80; 400±150
$\Delta_{9/2^+}(2300)$	2217±80; 300±100	2400±125; 425±150	-	-	2450±100; 500±200
$\Delta_{3/2^-}(2350)$	2305±26; 300±70	2400±125; 400±150	-	2233±53; 773±187	-
$\Delta_{7/2^+}(2390)$	2425±60; 300±80	2350±100; 300±100	-	-	-
$\Delta_{9/2^-}(2400)$	2468±50;480±100	2300±100; 330±100	-	2643±141; 895±432	2200±100; 450±200
$\Delta_{11/2^+}(2420)$	2416±17; 340±28	2400±125; 450±150	-	2633±29; 692±47	2400±60; 460±100
$\Delta_{13/2^-}(2750)$	2794±80; 350±100	-	-	-	2650±100; 500±100
$\Delta_{15\ 2f}(2950)$	2990±100; 330±100	-	-	-	2850±100; 700±200

Table 1. Breit-Wigner masses and widths (in MeV) of N and Δ resonances as extracted using five different partial wave analyses [64].

kinematics is complicated by significant final state interactions (FSI) between the three or more hadrons in the final state. Meson beams, on the other hand, have smaller FSI contributions as there are fewer baryons in the final state, and pion beams have been used very successfully to probe isospin degrees of freedom and determine significant parts of the resonance spectrum [66]. However, the data is coarse in invariant mass resolution and, since the pion has spin zero, carries limited polarisation information. A number of resonances are, moreover, predicted to couple only weakly to the pion channel, with a large branching ratio into other meson channels such as $\pi N \rightarrow \eta N$ for example, and the quality of pion scattering data is not sufficient to give sensitivity to their existence.

Electromagnetic production of mesons is generally accepted as the way forward to better establish the resonance spectrum and its properties as well as providing a means to excite and study the nucleon [67]. This process gives access to electromagnetic transition amplitudes of the photon which yields information on the spin-flavour correlations of quarks. The cross-sections are, however, a lot smaller than for hadronic probes and there are background contributions from non-resonant terms. Reaction models therefore have to be applied in the interpretation of the data.

The nucleon can be probed electromagnetically either with the use of virtual photons in the interaction of high energy beam electrons with the nucleon, a process known as electroproduction, or by using a beam of high energy real photons in photoproduction.

The possibility to vary momentum transfer, Q^2, for a fixed energy transfer in electroproduction allows the transition form factors of resonances to be extracted. This is active current work for the well-established $\Delta(1232)$ and $S_{11}(1535)$ states [68]. However, the variation of the EM coupling with Q^2 is not established for the vast majority of resonances and complicates the use of this reaction to disentangle other excited states. Therefore, real photons with $Q^2 = 0$ are the electromagnetic probe of choice to study the complete spectrum.

1.3.2.4 Polarisation in meson photoproduction

The power of photoproduction in the study of the nucleon resonances is greatly enhanced when polarisation information is also available. Specifically, meson photoproduction experiments using (any or all of) a polarised beam, polarised target and

having the capability of measuring the polarisation of the recoil nucleon can be carried out. In the case of pseudoscalar meson photoproduction, a total of 16 polarisation observables stem from different combinations of beam, target and recoil nucleon polarisations. Combinations of these observables can be related to different amplitudes in a partial wave expansion of the transition matrix describing the excitation of a nucleon from its ground to an excited state. These partial wave analyses (PWA) typically apply reaction models to separate the resonant and background terms but it has been shown [69] that a measurement of a carefully chosen set of eight polarisation observables is sufficient to determine the PWA amplitudes unambiguously. Crucial members of this set are the differential cross-section and the three single polarisation observables (measured in experiments where just the polarisation of the beam, target or recoil nucleon is known). Moreover, as a consequence of the isoscalar (isospin 0) and isovector (isospin 1) nature of the electromagnetic interaction, measurements of polarisation observables from both isospin partners, the proton and the nucleon, are required.

It is an enormous experimental challenge to obtain a "complete" set of observables due to the technological difficulties in the construction of polarised targets and measurement of the recoil polarisation, although recently great progress has been made in the area and a number of experiments into just those double-polarisation observables are currently under way [68].

1.4 Measurement of Beam Asymmetry

The measurement presented in this thesis is of the polarisation observable beam asymmetry, Σ, in charged pion photoproduction from the neutron:

$$\gamma + n \rightarrow p + \pi^-$$

The experiment was carried out as part of a large experimental programme in the study of the hadron spectrum, aiming to make the crucial step of providing new, precise measurements on both the proton and the neutron, of a wide range of single and double polarisation observables with good invariant mass and meson production angle resolution. Achieving this will allow long outstanding issues in our understanding of the nucleon spectrum to be addressed, such as the case of the "missing" resonances,

the large uncertainties on the decay widths and the discrepancies in the interpretation of the data using different analysis models.

Chapter 2

Pion Photoproduction

2.1 Introducing the pion

The pion is the lightest known meson and has an up-down valence quark composition. Its root mean square charge radius has been measured at 0.66 ± 0.01 fm [70]. Having an isospin $I = 1$, it is an isospin triplet and therefore comes in three charge states: π^+ ($I_3 = 1$), π^- ($I_3 = -1$) and π^0 ($I_3 = 0$). Their respective valence quark combinations are: $u\bar{d}$, $d\bar{u}$ and $(u\bar{u} - d\bar{d})/\sqrt{2}$. The mass[1] of the charged pions is 139.57018(35) MeV/c^2 and that of π^0 is 134.9766(6) MeV/c^2. The pion is an pseudoscalar particle, meaning it has negative parity and zero spin ($J^P = 0^-$). The neutral pion has a very short lifetime of 8.4(6)×10^{-17} s, corresponding to a maximum path length $c\tau$ of 25.1 nm, and decays mainly electromagnetically into

$$\pi^0 \rightarrow \gamma + \gamma$$

with a 98.8% branching ratio. The charged pions have a much longer lifetime, τ, of 2.6033(5)×10^{-8} s, corresponding to a path length of $c\tau = 7.8045$ m. Their decay channels are almost exclusively (99.988% branching ratio):

$$\pi^+ \rightarrow \mu^+ + \nu_\mu$$
$$\pi^- \rightarrow \mu^- + \nu_\mu$$

The comparatively long lifetime of charged pions makes it possible to detect them directly in experiments. This cannot usefully be done in the case of π^0, whose existence

[1] All numbers quoted in this section are from the Particle Data Group (PDG) [21].

is characterised by the detection, in electromagnetic calorimeters, of the two decay photons from the dominant $\pi^0 \rightarrow 2\gamma$ channel.

2.2 Pion photoproduction

This section outlines the most commonly employed theoretical formulation of pion photoproduction from the nucleon and its relation to experimentally measurable quantities.

2.2.1 Formalism

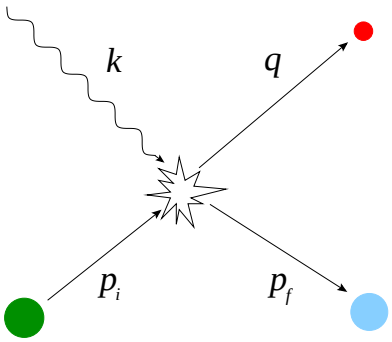

Figure 2.1: Diagram illustrating the kinematics of a reaction with two particles in the initial state (four-momenta k and p_i) and two in the final state (four-momenta q and p_f).

A process in which two initial particles, such as a real photon and a nucleon (with four-momenta k and p_i respectively) scatter into two particles in the final state, for example a pion and another nucleon (four-momenta q and p_f respectively as illustrated in Fig. 2.1), can be described in terms of the three Lorentz-invariant Mandelstam variables [71], s, t and u, where

$$\begin{aligned} s &= (q + p_f)^2 \\ t &= (p_i - p_f)^2 \\ u &= (p_i - q)^2 \end{aligned} \tag{2.1}$$

and the four-momentum, p, is defined in terms of particle energy, E, and its three-momentum $\boldsymbol{p}$, as usual:

$$p = [E, \boldsymbol{p}] \tag{2.2}$$

Using momentum-energy conservation

$$k + p_i = q + p_f \tag{2.3}$$

and the definition of Lorentz-invariant mass

$$p_i \cdot p_i = E_i^2 - \boldsymbol{p_i} \cdot \boldsymbol{p_i} = m_i^2 \tag{2.4}$$

the Mandelstam variables can be linearly combined to give the sum of masses of the four particles involved:

$$s + t + u = \sum_{i=1}^{4} m_i^2 \tag{2.5}$$

It is evident from momentum-energy conservation that only three of the four-momenta are independent and convention dictates [72] the use of k, q and a combined four-momentum for the nuclei

$$p = \frac{1}{2}(p_i + p_f) \tag{2.6}$$

as the independent kinematic variables. A similar argument is applied to the Lorentz invariants: since any of the three Mandelstam variables can be expressed in terms of the other two, the scattering process is described by functions of only two of the variables. These are usually s and t, which in the centre of mass of the initial (and final) state equal the invariant mass squared of the system (W^2) and the momentum transfer in the scattering process, respectively [72]. Moreover, for a fixed-s scenario, t is a linear function of $\cos\theta$, where θ is the scattering angle in the centre of mass frame. It is therefore usual to consider scattering functions simply in terms of s and cosine θ.

2.2.2 Photoproduction amplitudes

2.2.2.1 Momentum representation

The differential cross-section describes the distribution of scattered particles in a solid angle $d\Omega$ surrounding the scattering centre, and can be written in terms of the scattering

amplitude, A_s, which is a function of the momenta of the particles involved and the scattering angle θ [73]:

$$\frac{d\sigma}{d\Omega} = |A_s(s, \cos\theta)|^2 \tag{2.7}$$

From a quantum-mechanical point of view, the process is described in terms of a scattering matrix, S, which relates the initial and final states of the system such that

$$\Pi_{fi} = |\langle f|S|i\rangle|^2 \tag{2.8}$$

where Π_{fi} is the probability of a state $|i\rangle$ scattering into state $|f\rangle$. The elements of the scattering matrix can be expressed, in the Bjorken and Drell convention [74] and for the case of pion photoproduction, as:

$$\langle f|S|i\rangle = \delta_{fi} - \frac{i}{(2\pi)^2}\,\delta^4(P_f - P_i)\left(\frac{M^2}{4E_\gamma E_i E_\pi E_f}\right)^{1/2}\langle f|T|i\rangle \tag{2.9}$$

where P_i and P_f are the total initial and final four-momenta respectively, M is the nucleon mass and T is the transition matrix for the process [75]. The transition matrix determines the photoproduction amplitude in the relation

$$\frac{d\sigma}{d\Omega} = \frac{q}{k}\sum\left|\frac{M}{4\pi W}\langle f|T|i\rangle\right|^2 \tag{2.10}$$

where the sum runs across all photon polarisations and magnetic quantum numbers of the nucleon states.

Most generally, the matrix T is given in terms of the nucleon electromagnetic current, J_μ, and the photon polarisation vector, ϵ_μ:

$$T = \epsilon_\mu J_\mu \tag{2.11}$$

Following the formalism developed by Chew, Goldberger, Low and Nambu [76], the transition current **J** for photoproduction can be expressed, in the centre of mass frame of the final state, in terms of the spin operator $\boldsymbol{\sigma}$ and the unit vectors of the photon and pion momenta, $\hat{\mathbf{k}}$ and $\hat{\mathbf{q}}$, as:

$$\mathbf{J} = \frac{4\pi W}{M}\left(i\tilde{\sigma}\mathcal{F}_1 + (\boldsymbol{\sigma}\cdot\hat{\boldsymbol{k}})(\boldsymbol{\sigma}\times\hat{\boldsymbol{q}})\,\mathcal{F}_2 + i\tilde{\boldsymbol{k}}\,(\boldsymbol{\sigma}\cdot\hat{\boldsymbol{q}})\,\mathcal{F}_3 + i\tilde{\boldsymbol{k}}\,(\boldsymbol{\sigma}\cdot\hat{\boldsymbol{k}})\,\mathcal{F}_4\right) \tag{2.12}$$

where

$$\begin{aligned}\tilde{\boldsymbol{\sigma}} &= \boldsymbol{\sigma} - (\boldsymbol{\sigma}\cdot\hat{\boldsymbol{q}})\,\hat{\boldsymbol{q}} \\ \tilde{\boldsymbol{k}} &= \hat{\boldsymbol{k}} - (\hat{\boldsymbol{k}}\cdot\hat{\boldsymbol{q}})\,\hat{\boldsymbol{q}}\end{aligned}$$

and $\mathcal{F}_i(s,t)$ are four structure functions, alternatively known as CGLN amplitudes. These amplitudes describe photoproduction as a function of s and t, and therefore in terms of momentum transfer, however it is also possible to represent the process in terms of angular momentum transitions by an expansion of the structure functions as partial waves in derivatives of Legendre polynomials, $P'_l(\cos\theta)$. This results in the following four multipole series [77]:

$$\begin{aligned}\mathcal{F}_1 &= \sum_{l=0}^{\infty} \Big(lM_{l+} + E_{l+}\Big) P'_{l+1}(\cos\theta) + \Big((l+1)M_{l-} + E_{l-}\Big) P'_{l-1}(\cos\theta) \\ \mathcal{F}_2 &= \sum_{l=1}^{\infty} \Big((l+1)M_{l+} + lM_{l-}\Big) P'_l(\cos\theta) \\ \mathcal{F}_3 &= \sum_{l=1}^{\infty} \Big(E_{l+} - M_{l+}\Big) P''_{l+1}(\cos\theta) + \Big(E_{l-} + M_{l-}\Big) P''_{l-1}(\cos\theta) \\ \mathcal{F}_4 &= \sum_{l=2}^{\infty} \Big(M_{l+} - E_{l+} - M_{l-} - E_{l-}\Big) P''_l(\cos\theta)\end{aligned} \tag{2.13}$$

where the multipole amplitudes are labelled M for magnetic and E for electric transition, the subscript refering to the orbital angular momentum, l, of the final state and its total angular momentum, $j = l \pm \frac{1}{2}$. Since the ground state nucleon in the initial state has a definite spin and parity, the excited nucleon resonances will show up in specific partial waves depending on their quantum numbers. Thus M_{1+}, for example, represents a transition into a final $l = 1$ state with total angular momentum $l + \frac{1}{2} = \frac{3}{2}$. The multipole additionally depends on the isospin-transition component of the photoproduction process, the details of which are described in the following section.

2.2.2.2 Isospin representation

In the case of pion photoproduction, the isospin of the initial state is entirely due to the nucleon, $I_i = \frac{1}{2}$, while in the final state it is the combination of the nucleon and pion isospin ($I_\pi = 1$) and can therefore be either $\frac{1}{2}$ or $\frac{3}{2}$. The isospin transition can be understood in terms of the electromagnetic Hamiltonian, which has both an isoscalar and an

isovector part. The former always results in a net isospin transition of 0, resulting in a final state with total isospin $I = \frac{1}{2}$. The multipoles parametrising this transition component are labelled $M_{l\pm}^{(0)}$ and $E_{l\pm}^{(0)}$. The isovector part, however, enables an isospin change of either 0 or ±1, resulting in a total final isospin of either $\frac{1}{2}$ or $\frac{3}{2}$. These transition components have associated multipoles labelled $M_{l\pm}^{(2I)}$ and $E_{l\pm}^{(2I)}$.

In order to arrive at the separation of the different isospin-transition multipoles in the photoproduction process, an alternative expression of the transition matrix, T, is required. The matrix can be expanded, in the Born approximation, as a sum of Lorentz invariant operators M_i with their corresponding amplitudes $A_i(s,t)$:

$$T = \sum_{i=1}^{N} A_i(s,t)\, M_i \tag{2.14}$$

The M_i operators themselves are functions of the photon polarisation vector, particle momenta and Dirac matrices, while the invariant amplitudes A_i can be expressed as combinations of nucleon isospin transition operators τ_α, where the sign of α indicates, as dictated by convention [71] [75], the opposite sign of the pion isospin:

$$A_i = A_i^{(-)} \frac{[\tau_\alpha, \tau_0]}{2} + A_i^{(+)} \delta_{\alpha 0} + A_i^{(0)} \tau_\alpha \tag{2.15}$$

The amplitudes $A_i^{(\pm)}$ are related to the isospin amplitudes $A_i^{(2I)}$ (determining the particular isospin-transition components of the photoproduction process) via:

$$A_i^{(-)} = \frac{A_i^{(1)} - A_i^{(3)}}{3}, \qquad A_i^{(+)} = \frac{A_i^{(1)} + 2A_i^{(3)}}{3} \tag{2.16}$$

while $A_i^{(0)}$ corresponds, as in the nomenclature for the multipoles, to a zero net isospin transition resulting from the isoscalar component of the electromagnetic field.

The physical amplitudes for the four possible pion - nucleon combinations of the initial and final state particles in the pion photoproduction process are therefore expressed in terms of the isospin amplitudes as [75]:

$$\begin{aligned}
A_i(\gamma p \to n\pi^+) &= \sqrt{2}A^{(0)} + \frac{\sqrt{2}A^{(1)}}{3} - \frac{\sqrt{2}A^{(3)}}{3} \\
A_i(\gamma p \to p\pi^0) &= A^{(0)} + \frac{A^{(1)}}{3} + \frac{2A^{(3)}}{3} \\
A_i(\gamma n \to p\pi^-) &= \sqrt{2}A^{(0)} - \frac{\sqrt{2}A^{(1)}}{3} + \frac{\sqrt{2}A^{(3)}}{3} \\
A_i(\gamma n \to n\pi^0) &= -A^{(0)} + \frac{A^{(1)}}{3} + \frac{2A^{(3)}}{3}
\end{aligned} \tag{2.17}$$

It is evident from Eq. 2.17 that a separation of the isospin transition amplitudes requires measurements of photoproduction from both the proton and the neutron channels.

The invariant amplitudes $A_i(s,t)$ can be related to the CGLN structure functions $\mathcal{F}_i(s,t)$ via the following expressions [75]:

$$\begin{aligned}
\mathcal{F}_1 &= \frac{W-M}{4\pi}\,\frac{\sqrt{e_i e_f}}{2\,W}\,\Big(A_1 - \frac{k\cdot q}{W-M}(A_3-A_4) + (W-M)A_4\Big)\\
\mathcal{F}_2 &= \frac{W+M}{4\pi}\,\frac{qk}{2\,W\,\sqrt{e_i e_f}}\,\Big(-A_1 - \frac{k\cdot q}{W+M}(A_3-A_4) + (W+M)A_4\Big)\\
\mathcal{F}_3 &= \frac{W+M}{4\pi}\,\frac{qk}{2\,W}\,\sqrt{\frac{e_f}{e_i}}\,\Big((W-M)A_2 + A_3 - A_4\Big)\\
\mathcal{F}_4 &= \frac{W-M}{4\pi}\,\frac{q^2}{2\,W}\,\sqrt{\frac{e_i}{e_f}}\,\Big(-(W+M)A_2 + A_3 - A_4\Big)
\end{aligned} \tag{2.18}$$

where

$$\begin{aligned}
e_i &= E_i + M\\
e_f &= E_f + M
\end{aligned}$$

and E_i (E_f) is the energy of the initial (final) nucleon. M, W, k and q are as previously defined. A separation of individual isospin amplitudes achieved through a full set of measurements on both the proton and the neutron can then be applied in Eqs. 2.18 and 2.13 to identify the different isospin-transition multipoles which contribute to the photo-reaction and thus determine the quantum numbers of the resonant states encountered.

2.2.3 Polarisation observables

The four CGLN structure functions, $\mathcal{F}_i(s,t)$, arise from the four possible combinations of photon helicity (two transverse states for real photons) and nucleon spin. A full determination of the structure functions therefore requires experiments involving measurements of polarisation. For comparison with results from polarisation experiments, however, a more enlightening expression of the structure functions is in terms of helicity (or transversity) amplitudes.

Using the notation of [69], one can define four independent helicity amplitudes N, S_1, S_2 and D, which represent helicity transitions (flips) from the initial into the final

state. The pion has zero helicity, the photon ±1, therefore a net single helicity flip, for example, involves no effective change in helicity of the nucleon. These transitions are represented by the amplitudes S_1 and S_2. A double-flip is represented by D, while N is the no-flip amplitude. Due to parity symmetry, photon helicity does not affect the differential cross-section [78], therefore only nucleon helicity transitions are considered. These can be related to the invariant amplitudes A_i (to leading order in s) in the following way [72]:

$$\begin{pmatrix} A_1 - 2mA_4 \\ A_1 + tA_2 \\ 2mA_1 - tA_4 \\ A_3 \end{pmatrix} \sim \begin{pmatrix} 2m & \sqrt{-t} & -\sqrt{-t} & 2m \\ 0 & \sqrt{-t} & \sqrt{-t} & 0 \\ t & 2m\sqrt{-t} & -2m\sqrt{-t} & t \\ 1 & 0 & 0 & -1 \end{pmatrix} \begin{pmatrix} S_2 \\ D \\ N \\ S_1 \end{pmatrix} \tag{2.19}$$

where m is the nucleon mass and t is the momentum-transfer Mandelstam variable.

The four complex helicity amplitudes can be combined to yield a total of sixteen experimentally measurable quantities, which are called polarisation observables [71]. These arise as eight complex amplitudes combining the two helicity states of the photon, two of the target nucleon and two of the recoiling nucleon ($2 \times 2 \times 2$). Since physical observables must be real quantities, the complex amplitudes can be separated into a real part and a phase, resulting in sixteen observables in total: the differential cross-section, a set of three single-polarisation observables where either the beam or the target is polarised or recoil nucleon polarisation is measured (Σ, T and P respectively), and twelve double-polarisation observables, where a total of two polarisation measurements is made. The set of double-polarisation observables arises from four combinations each of beam-target (G, H, E and F), beam-recoil (O_x, O_z, C_x and C_z) and target-recoil (T_x, T_z, L_x and L_z) polarisations [69].

The expressions of the polarisation observables in terms of helicity amplitudes are given in Table 2, where the more instructive transversity representation is also shown. The four complex transversity amplitudes, b_i, are defined as linear combinations of

helicity amplitudes thus [69]:

$$\begin{aligned} b_1 &= \frac{1}{2}\Big((S_1 + S_2) + i(N - D) \Big) \\ b_2 &= \frac{1}{2}\Big((S_1 + S_2) - i(N - D) \Big) \\ b_3 &= \frac{1}{2}\Big((S_1 - S_2) - i(N + D) \Big) \\ b_4 &= \frac{1}{2}\Big((S_1 - S_2) + i(N + D) \Big) \end{aligned} \tag{2.20}$$

In this representation, the three single polarisation observables and the differential cross-section are expressed only in terms of magnitudes of the amplitudes. Their phases can be determined from the remaining double-polarisation observables.

The differential cross-sections, which enable the experimental extraction of polarisation observables from the above groups of experiments, have the following expressions (in the centre of mass frame of the final state) for the three groups of double polarisation experiments [69]:

- Beam - target:

$$\begin{aligned} \frac{d\sigma}{d\Omega} = \left.\frac{d\sigma}{d\Omega}\right|_0 \Big(& 1 - P_L\Sigma\, \cos(2\phi) - P_x\,(\,P_L H\, sin(2\phi) - P_\odot F\,) \\ & + P_y\,(\,T - P_L P\, \cos(2\phi)\,) + P_z\,(\,P_L G\, sin(2\phi) - P_\odot E\,)\Big) \end{aligned} \tag{2.21}$$

- Beam - recoil:

$$\begin{aligned} \rho_f \frac{d\sigma}{d\Omega} = \left.\frac{d\sigma}{d\Omega}\right|_0 \Big(& 1 + \sigma_y P - P_L\, \cos(2\phi)\,(\Sigma + \sigma_y T) \\ & - P_L\, sin(2\phi)\,(O_x\sigma_x + O_z\sigma_z) - P_\odot\,(C_x\sigma_x + C_z\sigma_z)\Big) \end{aligned} \tag{2.22}$$

- Target - recoil:

$$\begin{aligned} \rho_f \frac{d\sigma}{d\Omega} = \left.\frac{d\sigma}{d\Omega}\right|_0 \Big(& 1 + \sigma_y P + P_x\,(T_x\sigma_x + T_z\sigma_z) + P_y\,(T + \Sigma\sigma_y) \\ & - P_z\,(L_x\sigma_x - L_z\sigma_z)\Big) \end{aligned} \tag{2.23}$$

where (P_x, P_y, P_z) is the polarisation vector of the target, P_L and $P_\odot$ are the degrees of linear and circular photon polarisation respectively, ϕ is the angle the transverse linear

Usual symbols	Helicity representation	Transversity representation	Experiment required[a]
$\mathrm{d}\sigma/\mathrm{d}t$	$\lvert N\rvert^2+\lvert S_1\rvert^2+\lvert S_2\rvert^2+\lvert D\rvert^2$	$\lvert b_1\rvert^2+\lvert b_2\rvert^2+\lvert b_3\rvert^2+\lvert b_4\rvert^2$	$\{-;-;-\}$
Σ	$2\Re(S_1^*S_2-ND^*)$	$\lvert b_1\rvert^2+\lvert b_2\rvert^2-\lvert b_3\rvert^2-\lvert b_4\rvert^2$	$\{L(\frac{\pi}{2},0);-;-\}$
			$\{-;y;y\}$
T	$2\Im(S_1N^*-S_2D^*)$	$\lvert b_1\rvert^2-\lvert b_2\rvert^2-\lvert b_3\rvert^2+\lvert b_4\rvert^2$	$\{-;y;-\}$
			$\{L(\frac{\pi}{2},0);0;y\}$
P	$2\Im(S_2N^*-S_1D^*)$	$\lvert b_1\rvert^2-\lvert b_2\rvert^2+\lvert b_3\rvert^2-\lvert b_4\rvert^2$	$\{-;-;y\}$
			$\{L(\frac{\pi}{2},0);y;-\}$
G	$-2\Im(S_1S_2^*+ND^*)$	$2\Im(b_1b_3^*+b_2b_4^*)$	$\{L(\pm\frac{\pi}{4});z;-\}$
H	$-2\Im(S_1D^*+S_2N^*)$	$-2\Re(b_1b_3^*-b_2b_4^*)$	$\{L(\pm\frac{\pi}{4});x;-\}$
E	$\lvert S_2\rvert^2-\lvert S_1\rvert^2-\lvert D\rvert^2+\lvert N\rvert^2$	$-2\Re(b_1b_3^*+b_2b_4^*)$	$\{c;z;-\}$
F	$2\Re(S_2D^*+S_1N^*)$	$2\Im(b_1b_3^*-b_2b_4^*)$	$\{c;x;-\}$
O_x	$-2\Im(S_2D_2^*+S_1N^*)$	$-2\Re(b_1b_4^*-b_2b_3^*)$	$\{L(\pm\frac{\pi}{4});-;x'\}$
O_z	$-2\Im(S_2S_1^*+ND^*)$	$-2\Im(b_1b_4^*+b_2b_3^*)$	$\{L(\pm\frac{\pi}{4});-;z'\}$
C_x	$-2\Re(S_2N^*+S_1D^*)$	$2\Im(b_1b_4^*-b_2b_3^*)$	$\{c;-;x'\}$
C_z	$\lvert S_2\rvert^2-\lvert S_1\rvert^2-\lvert N\rvert^2+\lvert D\rvert^2$	$-2\Re(b_1b_4^*+b_2b_3^*)$	$\{c;-;z'\}$
T_x	$2\Re(S_1S_2^*+ND^*)$	$2\Re(b_1b_2^*-b_3b_4^*)$	$\{-;x;x'\}$
T_z	$2\Re(S_1N^*+S_2D^*)$	$2\Im(b_1b_2^*-b_3b_4^*)$	$\{-;x;z'\}$
L_x	$2\Re(S_2N^*-S_1D^*)$	$2\Im(b_1b_2^*+b_3b_4^*)$	$\{-;z;x'\}$
L_z	$\lvert S_1\rvert^2+\lvert S_2\rvert^2-\lvert N\rvert^2-\lvert D\rvert^2$	$2\Re(b_1b_2^*-b_3b_4^*)$	$\{-;z;z'\}$

[a] Notation is $\{P_\gamma;P_T;P_R\}$ where:

P_γ = polarisation of beam, $L(\theta)$ = beam linearly polarised at angle θ to scattering plane,
C = circularly polarised beam;
P_T = direction of target polarisation;
P_R = component of recoil polarisation measured.

In the case of the single polarisation measurements we also give the equivalent double polarisation measurement.

Table 2. Helicity and transversity representations of the polarisation observables [69].

polarisation vector makes to the reaction plane and ρ_f is the density matrix of the recoil nucleon. The axes of measurement, in accordance with the Basel convention [79], are defined in Appendix A.

Experiments where measurement of the polarisation of only one of photon, target nucleon or recoil nucleon is possible give access to Σ, P and T observables respectively. These, however, are not enough to determine amplitudes unambiguously. Double-polarisation experiments, where both of photon - target nucleon (BT), target - recoil nucleon (TR) or photon - recoil nucleon (BR) polarisations are measured are therefore required to access the remaining observables.

Experimentally, some of these measurements are extremely challenging to perform, and not all are required for a determination of the amplitudes. The question of which ones are crucial, and how best to choose the rest has been hotly debated over a number of decades. It has been shown that a measurement of all single polarisation observables is always required [69], however there is a choice regarding the double-polarisation measurements which will complete the set to enable unambiguous determination of the amplitudes. Disagreement in the literature [80], [81], [82] was initially settled by Barker, Donnachie and Storrow who showed in 1975 that a "necessary and sufficient" condition for determining the amplitudes to an overall phase and discrete ambiguities is that they do not all belong to the same set of BT, BR or TR [69]. A further two measurements, again taken such that of the five double-polarisation observables, no more than three come from the same set, eliminates discrete ambiguities. Although these selection criteria were examined again by Keaton and Workman in [83] and were found to be more complicated, Chiang and Tabakin showed soon after that only four appropriately-chosen double-polarisation observables are sufficient to achieve the same goal, although with more restrictions in their choice. Their paper [84] details the method of selection.

2.3 Partial Wave Analyses

Interpretation of the data in terms of the resonant behaviour of the nucleon relies on theoretical models. Most approaches start by a parametrisation of the invariant transition matrix T in terms of a resonant and a background term. The differences in

treatment arise from the amplitude decomposition of these terms and the subsequent fits to the experimental data.

In the Hamiltonian formulation, the reaction can be described in terms of a free term, H_0, pertaining to kinetic energy operators of the particles involved and an interaction term V which is composed of a background and a resonant contribution.

$$H = H_0 + V = H_0 + v^B + v^R \tag{2.24}$$

The background is due to processes resulting in a nucleon-meson final state without a resonance being created in the transition.

The T-matrix for an interaction taking state a into state b is generally expressed as:

$$T_{ab}(W) = V_{ab} + \sum_c V_{ac}\, g_c(W)\, T_{cb}(W) \tag{2.25}$$

where the sum is over all possible paths via states c that result in the final state b, their contribution being determined by the propagator $g_c(W)$, defined as

$$g_c(W) = \langle\, c|g(W)|c\,\rangle \tag{2.26}$$

The propagator, in momentum space, typically takes the following form:

$$g(p) = \frac{1}{p^2 - m^2 + i\xi} \tag{2.27}$$

where p and m are the four-momentum and mass of the intermediate state respectively. An expansion of the expression into the real and imaginary parts shows that for the on-mass-shell case of a physically observed resonance, where $p^2 = m^2$, the real part of the expression reduces to zero and the propagator takes the form of

$$g(p) = \frac{-i\xi}{(p^2 - m^2)^2 + \xi^2} \tag{2.28}$$

showing an imaginary peak in the on-mass-shell case. One signature of a resonance therefore, and an indication that a particular resonant state has been observed, is the combination of a zero in the real part and a maximum in the imaginary part of the transition amplitude via that intermediate state.

The T-matrix of the interaction can itself be split into a resonant and background contribution through

$$T_{ab} = T^B_{ab} + T^R_{ab} \tag{2.29}$$

allowing a separate treatment of both, the details of which vary from model to model.

A number of partial wave analyses (PWA) have been developed to extract resonance parameters from the data, variably applicable to the different electromagnetic meson-production channels [67]. Two models are most relevant to pion photoproduction, MAID and SAID, developed by the Mainz and the George Washington University groups respectively, and the approaches of both are discussed in more details below.

An issue which complicates the relation of determined multipoles to quark models is the fact that reaction models, although designed to extract multipoles from experimental observables, cannot differentiate between properties of the "bare" reaction vertex and a dressed one, where rescattering effects play a role. An off-shell pion, for instance, may be produced in a non-resonant process which then couples to the nucleon and leaves it in an excited state. To separate out the bare vertex, dynamical reaction models have been developed, which strive to separate hadron structure from reaction mechanisms governing the interactions in the various decay channels. Much progress has been achieved for the $\Delta(1232)$ resonance [85], but work is ongoing to describe the higher energy N^* states. It has been claimed that a number of established "resonances" may in fact be dynamically generated by resonance mechanisms [86].

Coupled channel analyses attempt to look at the resonance with all of its final states and their potential coupling by final state rescattering. Dispersion relation approaches use the partial wave decomposition of the T-matrix in terms of the CGLN and isospin amplitudes to extract resonance parameters from fits of the multipole amplitudes [87]. As with dynamical models, the data is best described at lower energies, in the Δ resonance region.

2.3.1 MAID

The unitary isobar MAID model, developed by the Mainz group [88], employs the Effective Lagrangian Approach (ELA) in an attempt to link photoproduction observables directly to the degrees of freedom from various quark models, with the advantage of a smaller resulting number of parameters in the model [89]. MAID is based on a single-pion channel, πN, reducing the sum over possible channels in Eq. 2.25 to the single $T_{\pi N}$ contribution with its corresponding $g_{\pi N}$ propagator. It is separated into resonant

and background terms as in Eq. 2.29:

$$T^R_{\gamma\pi}(W) \;=\; v^R_{\gamma\pi}(W) + V^R_{\gamma\pi}(W)\; g_{\pi N}(W)\; T_{\pi N}(W) \tag{2.30}$$

and the corresponding term for the background part [90]. Both parts are decomposed into partial waves with associated amplitudes characterised by the four quantum numbers of the transition: its orbital and total angular momenta (j, l), isospin (I) and the type of electromagnetic coupling in the transition (magnetic, M, or electric, E). The background part of the physical amplitudes, provided by the decomposition of $T^B_{\gamma\pi}(W)$, is modelled with the Born approximation, in which a single-particle intermediate state is assumed, requiring no quantum corrections (such as due to loops in the Feynman diagrams of the process). It relies on eight parameters to determine the partial wave contributions, which are extracted from a fit to experimental data.

The partial wave expansion of the resonant T-matrix term assumes a Breit-Wigner form and includes a selection of the best-verified resonances. In the current MAID-2007 version included are 13 resonances below 2 GeV having four-star rating in the PDG. This results in a total of 52 coupling parameters which can be expressed in terms of helicity and isospin amplitudes and determined from a fit to the available data. The ability to modify the fit by "switching on" or "off" certain resonances in the partial waves allows an investigation of the contributing resonant states by a comparison with the data.

A similar model applicable to η-production has also been developed (η-MAID).

2.3.2 SAID

The multi-channel SAID model, developed by the Centre for Nuclear Studies at George Washington University, does not *a priori* assume certain resonances, nor is it necessarily limited to the πN channel. Rather, resonance couplings, in terms of angular momentum and isospin quantum numbers, are extracted from a fit-based determination of multipoles using both an energy-dependent and an energy-independent parametrisation. Its T-matrix photoproduction amplitude is again assumed to be a sum of a Breit-Wigner and a background term [91]:

$$T_{\gamma\pi} \;=\; A_I(1 + iT_{\pi N}) + A_R\Big(\frac{k_0 q_0}{kq}\Big)^{1/2} \frac{W_0\,\sqrt{\Gamma\Gamma_\gamma}}{W_0^2 - W^2 - iW_0\Gamma} \tag{2.31}$$

in which A_I and A_R are background and resonant parameters respectively, with

$$A_R \equiv \frac{\mu}{q}\left[\frac{k}{q}\right]^l \sum_{n=0}^{N} p_n \left[\frac{E_\pi}{\mu}\right]^n \tag{2.32}$$

where k_0 and q_0 are the pion and photon momenta at the resonance energy; W_0, Γ and Γ_γ are functions of the full width Γ_0; μ is the pion mass; E_π is the pion laboratory kinetic energy for the interaction $\pi + N \rightarrow \gamma + N$; and p_n is a free parameter. The background term is expanded as a sum of a pseudoscalar Born partial wave and a set of Legendre polynomial terms with associated free parameters, which are determined by fitting the data. Multipoles can then be extracted by a fit of $T_{\gamma\pi}$ close to the resonance position.

2.4 Summary

Experimental measurements of yields and angular distributions give access to differential cross-sections and polarisation observables, a full set of which is required for the unambiguous determination of helicity amplitudes. These can be related to the invariant amplitudes, functions of W and cosine θ, for the separation of the isospin contributions of which data on both isospin partners, the proton and the neutron, are required. An understanding of the invariant amplitudes, and their expression in terms of the CGLN structure functions, can give information on the multipole transitions taking place. These provide direct information on the quantum numbers of the resonant states encountered.

Multipoles cannot be extracted directly from the data, however, as the expressions carry no sensitivity to separate background and resonant contributions in interaction. This can be done by applying various reaction models to the data, typically in the form of partial wave analyses. Different approaches yield sometimes drastically different results, with the same data being interpreted as showing certain resonances by some partial wave analyses but not others (see Table 1 in the Introduction). No fully constrained analysis has yet been possible and interpretation of the data is still model-dependent to various degrees. As a result, the nucleon resonance spectrum is only reliably determined in the first resonance region, leaving open questions both on whether many resonant states have indeed been observed and whether the “missing” resonances feature in the spectrum at all.

The work of this thesis is therefore set in the context of expanding the measurements of polarisation observables in a wide kinematic range of invariant mass and meson production angle, and obtaining data on the experimentally more challenging neutron channel. This is particularly topical as the world dataset on the neutron is currently pitifully sparse. The details thereof are discussed in the following chapter.

Chapter 3

Past Measurements

There have been, to date, eight previous experiments where information on the photon beam asymmetry from the neutron in the channel

$$\gamma + n \rightarrow p + \pi^-$$

has been obtained. Five of them fall in the first resonance region and as such are at photon energies below those of the present work, which covers the third resonance region and above for photon energy $E_\gamma > 1600$ MeV. These earlier measurements were conducted at Stanford in 1964 and 1974 [92], [93], Kharkov accelerator in 1976 [94], and the Tokyo tandem accelerator in 1970 and 1974 [95], [96]. Their measurements collectively cover the photon energy range 225 – 770 MeV.

There are three experiments whose data, a total of 68 points, overlap the kinematic range of the current measurement, which are summarised in Fig. 3.1. The earliest of these was conducted in 1972 by J. Alspector *et al.* at the Cambridge Electron Accelerator [97], using an electron beam of 5.5 GeV to produce, via the process of coherent bremsstrahlung, linearly polarised photons ranging from 0.8 to 2.2 GeV[1]. They used a liquid deuterium target and the Moby Dick spectrometer in combination with a second detector to detect the proton and π^- in the final state, but only measured the asymmetry at one centre-of-momentum pion production angle, 90°. The experiment was aimed at exploring the third resonance region containing the $F_{15}(1688)$, $D_{15}(1670)$

[1] Coherent bremsstrahlung as a source of linearly polarised photons is discussed in detail in Chapter 4, Section 3.

and $F_{37}(1950)$ resonances, while also conducting measurements of differential cross-sections in the channels $\gamma+p \rightarrow p+\pi^0$ and $\gamma+p \rightarrow n+\pi^+$. They observed no indication of the F_{15} or D_{15} state in the cross-section and asymmetry data from the neutron, but did see an indication of the F_{37} state. Both results were in agreement with the quark models as the F_{15} and D_{15} are predicted not to couple to the neutron. The F_{15}, D_{15} and F_{37} have since been well-established in other measurements and carry a four-star rating in the PDG [21].

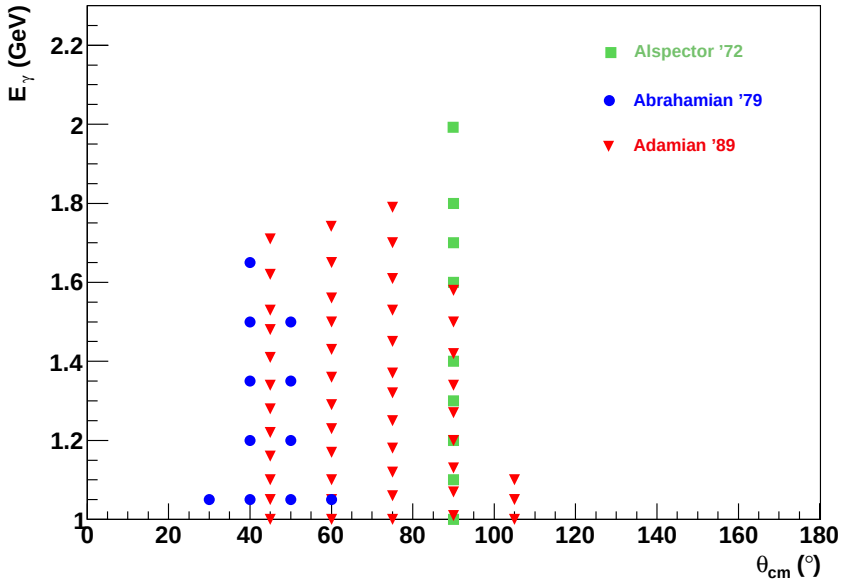

Figure 3.1: Previous Σ measurement points in the E_γ range 1.0 – 2.3 GeV.

The two experiments in the third resonance region which followed were conducted by L. Abrahamian *et al.* in 1979 [98] and F. Adamian *et al.* in '89 [99] using the Yerevan electron synchrotron. Both experiments used the same detectors, and were performed with linearly polarised photons in the energy range 0.90 to 1.65 GeV in '79 and a slightly extended range of 0.80 to 1.75 GeV ten years later. The polarised photons were produced by coherent bremsstrahlung using 4.6 GeV and 3.0 – 4.5 GeV electron beams respectively, and were incident upon a 10 cm long liquid deuterium target. The pions were detected by a magnetic spectrometer with a momentum acceptance

of $\Delta p/p \sim 5\%$ and a solid angle of $\Omega = 1.2 \times 10^{-3}$ sr. A time-of-flight spectrometer was used to detect the corresponding recoil nucleon in the final state of the interaction.

The first experiment obtained 12 measurements of beam asymmetry at four centre-of-momentum angles 30°, 40°, 50° and 60°, with statistical errors of 3 – 5% and systematic uncertainties, mainly due to determining the degree of linear polarisation of the photon beam, of the order of 10%. Their results were compared to previous partial wave analyses featuring the inclusion of ten resonances in the third resonance region. Although they observed a qualitative correspondence with one of the analyses (Metcalf and Walker [100]), they could not comment conclusively on the correspondence. Based on a comparison of earlier results measuring the beam asymmetry in the $\gamma + p \rightarrow \pi^+ + n$, however, they conclude that the non-zero difference in asymmetries from the two channels indicates the presence of both isoscalar and isovector amplitudes in the energy range tested, and suggests dominance of the $F_{37}(1950)$ resonance. However, since both asymmetry values disagree with those predicted for the $F_{37}(1950)$ by quark models, the suggestion was made that contributions from other $I = \frac{3}{2}$ resonances are significant in that energy range.

The second experiment took measurements at 45°, 60°, 75° and 90°. A comparison to the previous Cambridge data showed good agreement, however discrepancies were observed with phenomenological analyses. An investigation of the angular dependence in the energy region of the $P_{11}(1710)$ resonance, which is still only assigned a three-star rating in the PDG, showed particular disagreement between data and partial wave analyses at large meson production angles. The need was stressed for much more data to be able to constrain the partial wave analyses and make an effective comparison to quark model predictions.

The conclusions of these experiments, therefore, all point to the pressing need for a large dataset covering the full extent of pion production angle and a large range of energies to better constrain PWA. Moreover, high statistics are required to scan both energy and meson production angle at a high resolution, which is particularly important if any sensitivity to long-lived states is to be obtained. The experiment presented in this thesis provides 1176 new data points, spanning the meson production angle range from -0.8 to 1.0 in 18 $\cos\theta$ centre-of-momentum bins and the invariant mass range from 1610 MeV to 2320 MeV with a bin size of 10 MeV.

Chapter 4

Experimental Facility - Jefferson Lab

The experiment presented in this thesis was carried out at the Thomas Jefferson National Accelerator Facility (JLab) in Newport News, Virginia, USA. JLab is a laboratory dedicated to the study of hadronic and nuclear physics staging experiments on a variety of targets and using both electron- and photon-beams at energies up to 6 GeV. An upgrade of the facility to 12 GeV is expected to complete in 2012. This chapter focuses on a discussion of the facility and experimental techniques employed, specifically the production, monitoring and measurement of the beam, a description of the target and detectors used to identify the outflying products of the reactions and an outline of the data acquisition process. The details of the experiment are presented in the last section of the chapter.

4.1 CEBAF

The Continuous Electron Beam Accelerator Facility (CEBAF) (Fig. 4.1) is a racetrack accelerator consisting of two superconducting radio-frequency (RF) linacs 1.4 km in length, connected at each end with recirculation arcs along which the electron beam is directed by two fixed steering magnets. The accelerator operates at close to 100% duty cycle, delivering a bunched beam of picosecond - wide pulses at a frequency of 499 Hz[1] [101]. The beam can be circulated around the racetrack up to five times, gaining just under 600 MeV in energy with each pass through a linac. Different numbers

[1]The beam is termed “continuous” due to its short and frequent pulses and in contrast to the typical pulse duration of a “pulsed” accelerator, which is on the order of nanoseconds.

of recirculations (passes) allow energies from ~ 1.2 GeV to just below 6 GeV to be reached. On each pass, the beam can be split by a transverse RF separator and delivered simultaneously to three experimental halls — A, B and C.

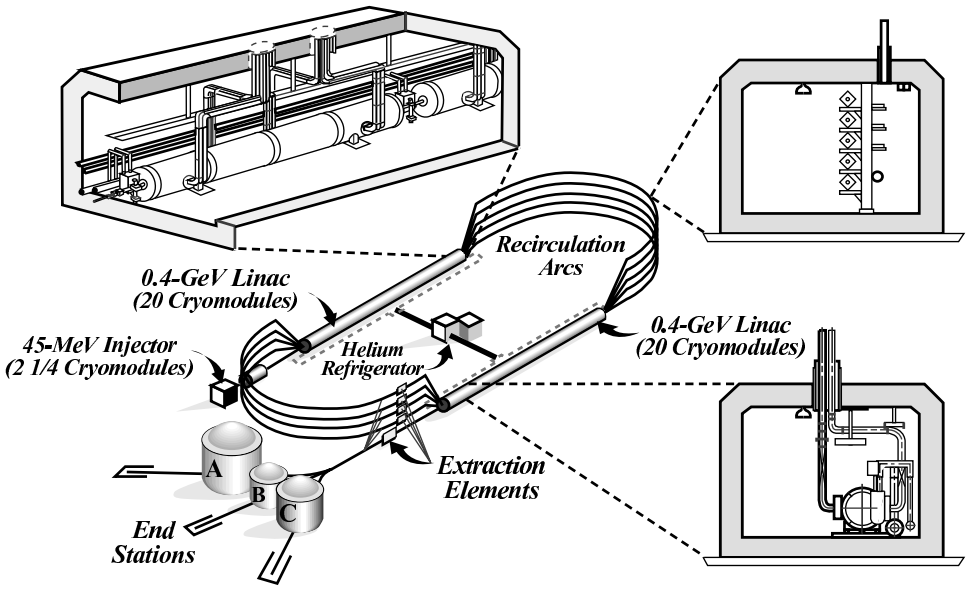

Figure 4.1: Cartoon showing CEBAF and the three experimental halls. The enlargements are, clockwise from the top: a module in the linac, a steering magnet and a part of the RF separator [101].

Halls A and C operate at high electron-beam luminosities (up to 10^{38} cm^{-2}s^{-1} at the target) and are exploited in high precision electron scattering experiments. The scattered electron and reaction products are detected in high-resolution magnetic focussing spectrometers. The high precision in the determination of the resolution comes at the price of having a small acceptance for particles (less than 1 sr in each spectrometer). In Hall A, the spectrometers are an identical pair [102] while those in Hall C are symmetrically positioned, offering a larger acceptance for high momentum particles on the one side and good detection of short-lived particles on the other [103]. Hall B houses CLAS, the CEBAF Large Acceptance Spectrometer which was used in this experiment and will be discussed in detail in this chapter.

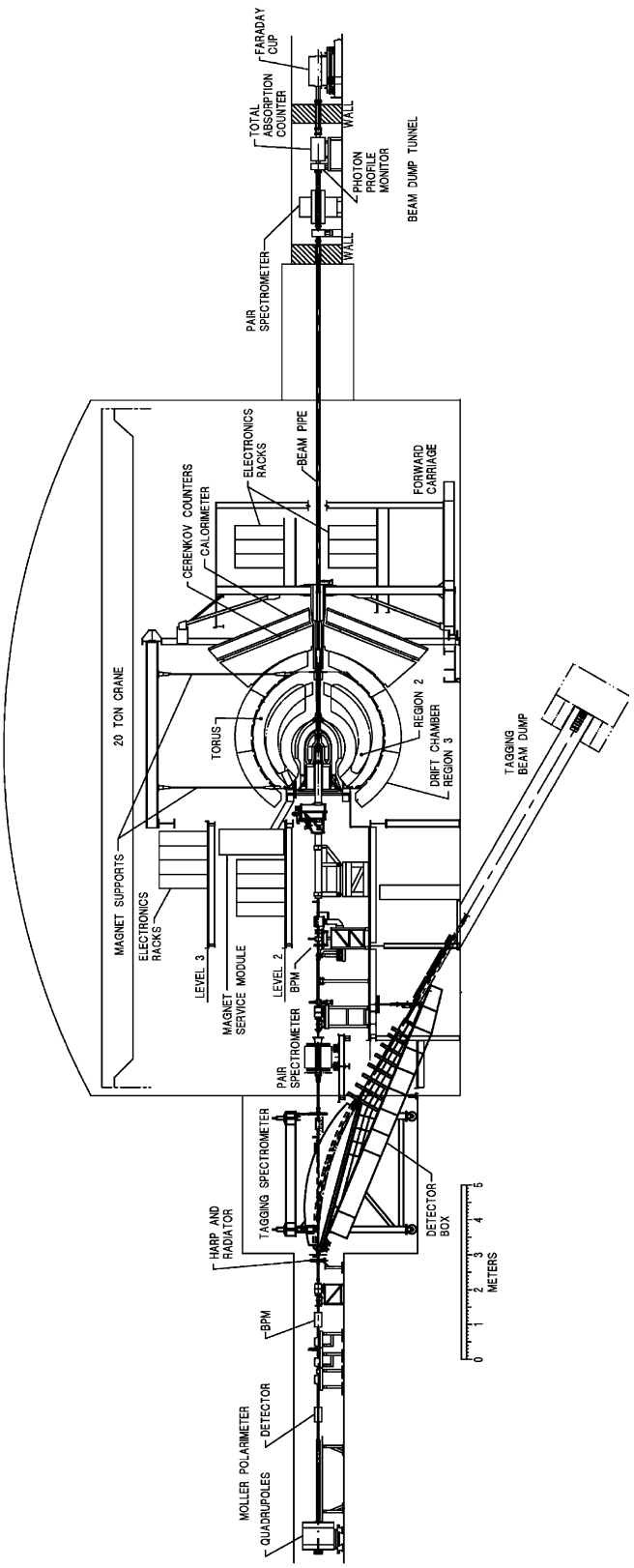

Figure 4.2: Beam-line components in Hall B [104].

4.2 Electron beam

The electron beam passes through a series of monitoring devices placed in the approach tunnel and the beam dump tunnel. These measure the position and intensity of the electron beam and the intensity of the photon beam. The layout of these devices is shown schematically in Fig. 4.2 and each device is discussed in turn in the following sections.

4.2.1 Position and intensity

To monitor the position and intensity of the electron beam, three sets of three resonant (RF) cavities are positioned along the beam-line at various distances upstream from the target. These are essentially non-destructive to the beam and are used to continuously monitor and maintain the position of the beam on approach to the hall. The beam position is adjusted through a feedback loop during data-taking.

The electron beam current, which is dumped after passing through the tagger and detector apparatus, is measured in the Faraday cup, which comprises a 4000 kg block of lead placed, on ceramic supports inside a vacuum, at the end of the beam line [104]. This operates by effectively stopping the beam and accumulating its charge, which is drawn off and measured continuously during operation.

4.2.2 Beam profile

Monitoring the electron beam profile is a destructive technique and data taking has to be stopped for the duration of the measurement process. The beam profile is determined whenever any significant changes are made to the beam, such as in the beam current for example. There are a total of three profilers, called harps, along the beam line in the hall. Each one is a set of wires (20 and 50 μm tungsten and 100 μm iron) orientated along the two orthogonal directions perpendicular to the beam. During monitoring, the harps are slid into the beamline and moved at 45° through the beam using a computer-controlled stepping motor to allow a measurement to be taken at regular intervals across the beam. A small fraction of the electrons is scattered by the wire and the signal from the resulting Čerenkov light produced in the glass windows of the

photomultiplier tubes (PMTs), which are positioned forwards from the harps, is used to map out the profile of the beam (Fig. 4.3).

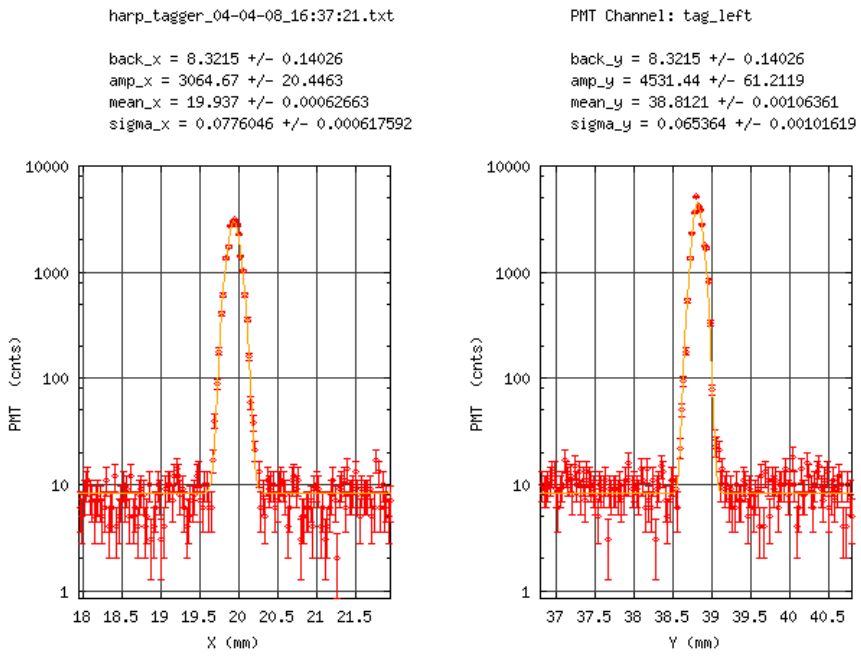

Figure 4.3: Example of a beam profile scanned along two perpendicular axes by the harps. The profile indicates a good quality, narrow, circular beam of width $\sim 70\ \mu$m.

4.2.3 Polarisation of the electron beam

Measuring the degree of longitudinal polarisation of the electron beam every few days is of crucial importance to the physics programme which exploits this information in electron scattering or for the production of circularly polarised photons[1]. Measurements are carried out with the Möller polarimeter, which is moved into the beam line for the duration of the calibration measurement. The polarimeter consists of a 25 μm thick Permendur[2] foil magnetised to produce a polarisation of surface electrons $\sim 8\%$ along the plane of the foil, a set of quadrupole magnets downstream of the foil and

[1] This information is not necessary for the linearly polarised photons used in the current experiment.
[2] A cobalt-iron alloy.

two detectors. Beam polarisation is obtained by measuring, with different target polarisation directions, the asymmetry of the scattered electrons resulting from elastic Möller electron-electron scattering taking place in the foil. The magnets separate out the scattered Möller electrons from the unscattered beam and direct them to a pair of lead/scintillator-fibre composite detectors positioned either side of the beam line. The measurement of the degree of longitudinal polarisation of the beam can be achieved with a typical accuracy of $< 2\%$ [105].

4.3 Techniques for producing photon beams

There are two main mechanisms of producing beams of real photons for photoproduction experiments, Compton back-scattering and bremsstrahlung, and both are used at laboratories world-wide. The Compton back-scattering technique involves firing a laser beam (typically UV or infrared) of photons at a circulating beam of electrons of a known energy (for example in a synchrotron). The photons then scatter with an appreciable fraction of the electron beam energy. This method is used at BNL (LEGS) and SPring8 (LEPS) and was also employed at ESRF (GRAAL).

The bremsstrahlung technique involves firing a relativistic electron beam though a thin radiator. The electrons undergo bremsstrahlung from the nuclei in the material structure, emitting photons with a range of energies which can be calculated by measuring the deflected electron's energy and time of radiation in a tagging spectrometer. Using a linearly polarised electron beam results in the transfer of circular polarisation to the photons, while linearly polarised photons can be produced by using a highly ordered, high purity crystal as a radiator. This technique is used in the US at Jefferson Lab (CLAS) and in Germany at ELSA and MAMI. The following sections describe the bremsstrahlung process in more detail.

4.3.1 Circularly polarised photons

If the electron beam incident on the radiator is itself longitudinally polarised, the resulting bremsstrahlung photons will posses circular polarisation. The longitudinal polarisation of the incoming electron beam is measured periodically using the Möller polarimeter described in Section 4.2.3. The degree of polarisation transfer to the photon

in the bremsstrahlung process is almost 100% when the photons carry off the maximum available energy, but decreases as the fraction of available energy given to the photon reduces. This transfer can be calculated with QED and is illustrated in Fig. 4.4, where it can be seen that for photon energies 50% of the beam energy, the polarisation transfer is around 60%.

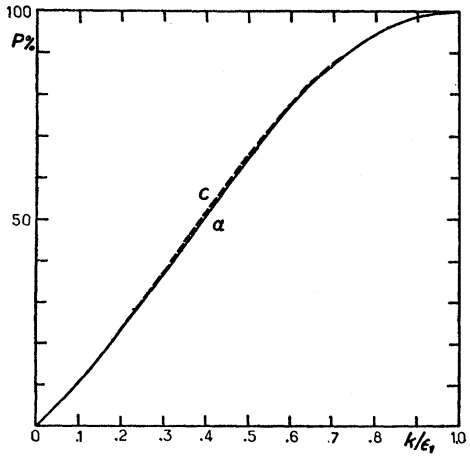

Figure 4.4: Graph showing degree of circular polarisation as a function of momentum transfer to the bremsstrahlung photon. The two curves are an exact calculation (a) and an approximation (c). The figure was taken from the theoretical treatment by Olsen [106].

4.3.2 Linearly polarised photons

Linear polarisation of photons produced in the bremsstrahlung process can be achieved using a crystalline radiator. Typically a 20 – 50 μm thick diamond crystal of the highest purity is aligned and held at the desired angle to the beam line with a goniometer [107]. For a particular orientation of the crystal, an electron scattering along a reciprocal lattice vector will have a restricted momentum transfer that can be absorbed by the crystal. This gives rise to sharp structures in the photon energy spectrum as can be seen in Fig. 4.5. Since these coherent photons were produced by momentum transfer along the fixed directions of the reciprocal lattice vector, the photon polarisation vector will lie predominantly in a single plane, resulting in linearly polarised photons at that energy. It is found that the highest photon polarisation is achieved by scattering from the planes described by the [022] and [02$\bar{2}$] reciprocal lattice vectors

[108]. An enhancement in the scattering, however, occurs not only from the primary reciprocal lattice vector, in this example [02$\bar{2}$], but to a gradually decreasing extent also from higher order planes, such as [04$\bar{4}$], [06$\bar{6}$], etc. This is seen as a series of peaks in Fig. 4.5, where the total photon spectrum has been divided by that obtained using an amorphous radiator to remove the characteristic bremsstrahlung $\frac{1}{E_\gamma}$ intensity dependence.

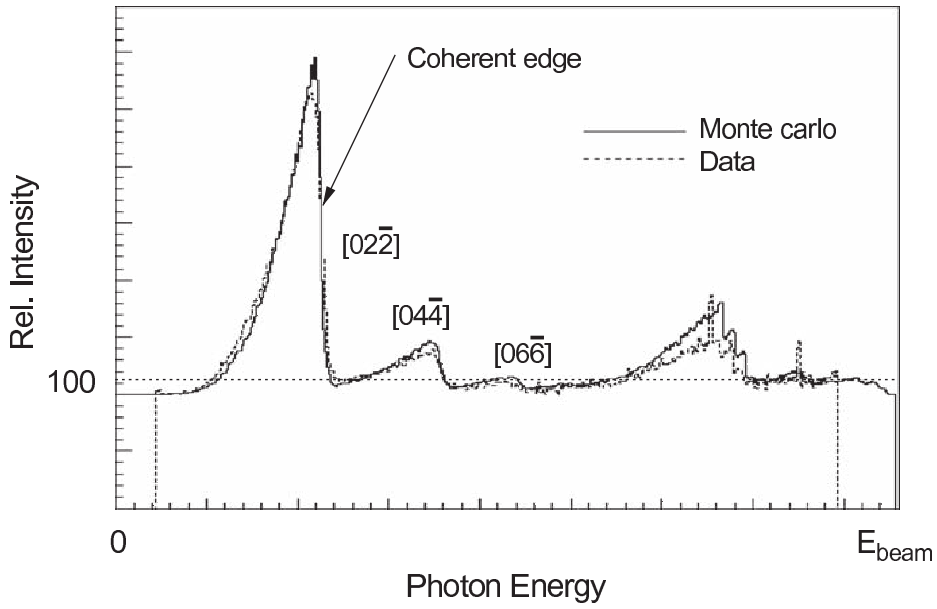

Figure 4.5: Data and Monte Carlo simulation of the photon intensity spectrum produced by the process of coherent bremsstrahlung [107].

The degree of linear polarisation of the photons depends on the position of the coherent peak relative to the energy of the electron beam. For the typical set-up at JLab the coherent peak is at an energy ~ 30% of the full beam energy and the degree of polarisation can reach up to ~ 80%. As a result of the angular dependence of the coherent bremsstrahlung process, the degree of polarisation depends strongly on the degree of collimation (see Section 4.3.3).

The degree of polarisation is calculated analytically [109] using the initial energy of the scattered electron and the alignment of the crystal relative to the electron beam. The calculation also includes realistic parameters for multiple scattering in the crystal, collimation, electron beam spot size and divergences.

4.3.3 Beam collimation and monitoring

The bremsstrahlung photons are radiated in a cone along the axis of the electron beam, where the highest degree of polarisation is along the axis, closest to the original direction of the electron. To select photons with the greatest degree of polarisation, therefore, the photon beam is collimated before reaching the target. This is achieved by passing it through an aperture, the diameter of which is chosen to optimise the required polarisation of the beam while still maintaining a high photon flux. Experiments with unpolarised or circularly polarised beam use a large, 0.861 cm diameter nickel block (25 cm long), which constricts the beam spot at the target to a diameter less than 3 cm. A smaller, 2 mm bore nickel/tungsten collimator is used for linearly polarised beam, reducing the beam spot to < 5 mm in diameter at the target. Any showers of secondary electrons produced by the photon beam hitting the collimator material are removed with a small sweeping magnet downstream [104].

The position and size of the beam spot is monitored via an array of scintillator fibres placed behind the target, which map the beam from the reconstructed vertex positions of electron-positron pairs produced along the beam path.

Although not necessary for the experiment presented in this thesis, a determination of the beam flux is crucial if a photoproduction cross-section is to be measured. To this end, a pair spectrometer is positioned upstream from the target, which consists of a thin foil for electron-positron pair production. It removes approximately 1% of the photons from the beam but produces a continuous indication of the flux during data-taking.

4.4 The Photon Tagging Spectrometer

The photon tagging spectrometer (tagger), positioned immediately downstream of the radiator, momentum analyses the recoiling electrons following bremsstrahlung. Since the incident electron beam energy is well known, this allows the energy of the bremsstrahlung photons to be determined event by event. The tagger is a C-shaped dipole electromagnet in which the field is set up such that electrons which do not produce bremsstrahlung in the radiator are directed into a beam dump in the floor of the experimental hall. The electrons producing bremsstrahlung photons are dispersed in the magnet according to their momentum (Fig. 4.6).

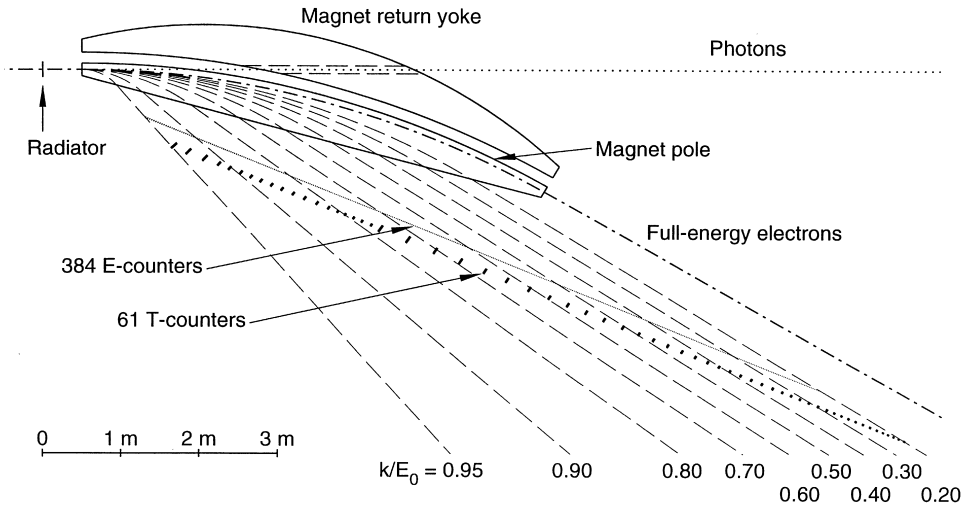

Figure 4.6: The tagging spectrometer in cross-section, showing the photon beam, the paths of scattered electrons deflected in the tagger magnetic field and the two planes of the scintillator hodoscope [110].

Timing and energy measurements for the scattered electrons are made by two planes of plastic scintillators positioned along the focal plane in the magnet. The first plane (E-plane) is used to determine energy information on the scattered electrons by "tagging" the electron exit position from the spectrometer. It comprises 384 plastic scintillator strips which are 20 cm long, 4 mm thick and range from 6 to 18 mm in width. The variable widths ensure each covers the same momentum range (0.003 times the original energy of the electron beam, E_0). Since the counters overlap each other by a third of their width on each side, there is a total of 767 different tagger channels resulting in a resolution of $0.001 \times E_0$. The geometry of the magnet and positioning of the hodoscope limits the tagger range to energies from 25% to 95% of E_0 [110].

The second plane (T-plane) is used to obtain timing information about each recorded electron. It is shifted by 20 cm downstream of the E-plane and comprises 61×2 cm thick scintillators, the scintillation light from which is recorded in two PMTs, attached one to each end. The attainable root-mean-square (rms) timing resolution from the modules is 110 ps. The time difference between the hit in the T-plane and a resulting hit in the CLAS detector can be used to identify the electron associated with the bremsstrahlung photon which produced the reaction in the target.

The time of creation of each photon, however, can be determined to much greater accuracy than the intrinsic timing resolution of the T-counters, since the tagger allows separation of the electron beam bunches. These are delivered at 2.004 ns intervals and the timing is determined accurately from the RF signals driving the linacs in the accelerator. The beam bunches themselves are only a few ps wide and identifying the closest RF pulse to the measured time from the tagger T-counters can improve the resolution significantly.

4.5 CLAS

The CEBAF Large Angle Spectrometer, CLAS, provides particle identification and momentum determination for particles produced following reactions of the photon beam with the target. CLAS is a formidable structure of layered detectors (Fig. 4.7). The skeleton of CLAS comprises six superconducting coils located radially around the beamline, which produce a toroidal magnetic field. Measurement of the momentum of reaction products is provided by tracking particles through the three layers of drift chambers, located within the areas of highest magnetic field. Time of flight measurements and fast information for event triggering is provided by the barrel-shaped start counter inside and the shell of scintillation counters outside the drift chambers. The Čerenkov counters are used to distinguish between pions and electrons while neutral particle identification as well as energy measurements are provided by the two types of calorimeters at the outside of CLAS [104]. The rest of this section describes each detector system in more detail.

4.5.1 Torus Magnet

Each of the six coils of the torus magnet is wound into a kidney shape from 216 layers of aluminium-stabilised NbTi/Cu wire and fixed to a 4.5 K super-critical He cooling cryostat (Fig. 4.8 and 4.9). For fixed target experiments the highest momentum particles are generally emitted at forward angles. Correspondingly, to provide optimum degrees of curvature in the tracks of charged particles, the coils were designed to have a high magnetic field at forward angles and a lower field at larger angles, where particle momenta are typically smaller. At the maximum design current of 3860 A, the

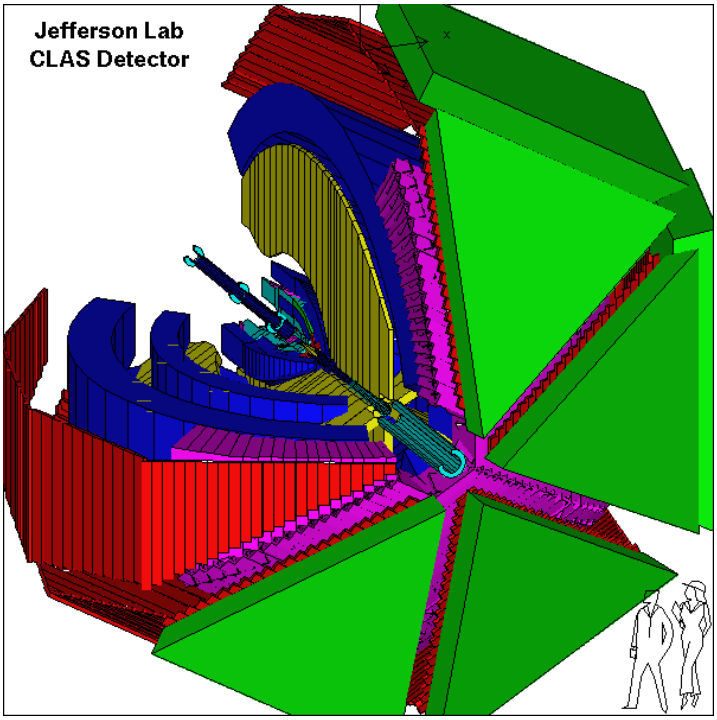

Figure 4.7: Geant 3 visualisation of CLAS showing, symmetrically arranged around the beam axis, the superconducting coils (yellow), three regions of drift chambers (blue), the Čerenkov counters (pink), the shell of time-of-flight scintillation counters (red) and the electromagnetic calorimeters covering the forward angles (green) [104].

field reaches 2.5 Tm in the very forward region and falls to 0.6 Tm perpendicular to the beamline [104]. The centre of CLAS remains close to field-free allowing the use of a polarised target and causing negligible deflections to a charged beam.

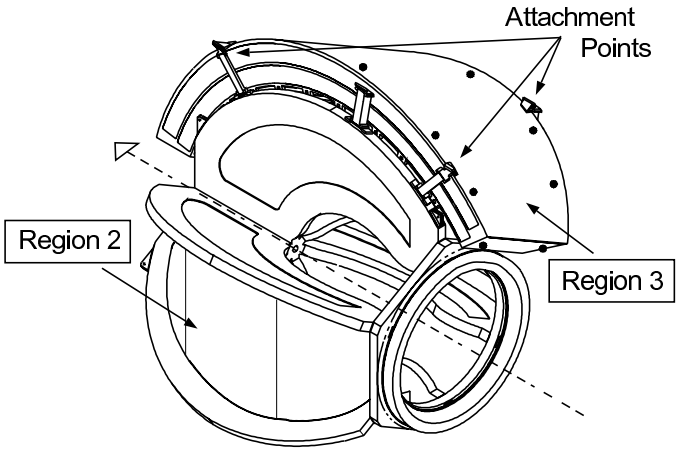

Figure 4.8: Schematic showing the torus magnet cryostats radially positioned around the beam axis (dashed line) and two regions of the drift chambers. [104].

Figure 4.9: Photograph of the torus magnet cryostats, showing one of the two support rings on which they are mounted and the carbon-fibre support rods between neighbouring cryostats (Jefferson Lab Hall B archive).

4.5.2 Start Counter

The start counter, ST, is the first detector encountered on the path into CLAS by a particle produced in a photoreaction in the target and provides the crucial, most accurate timing information for the event, which is used in the trigger decisions for data acquisition and event reconstruction. It comprises 24 EJ-200 organic plastic scintillator paddles arranged azimuthally in six sectors around the target (Fig. 4.10 and 4.11). They form a barrel 619.5 mm long, designed to provide full coverage of the acceptance for a 40 cm long liquid hydrogen target. Each paddle has a straight rectangular section 502 mm long (the "leg") and either a triangular or a trapezoid "nose" tapered inwards to increase the coverage of the detector at forward angles. To provide light isolation, the paddles are wrapped each in radiant mirror film (VM-2000), with alternate ones being additionally covered in black Tedlar film. The paddles are assembled into sectors and mounted onto a 5.3 mm thick Rohacell PMI foam support structure, shielded on top with a further 9.8 mm foam layer. At the upstream end of each paddle, a 127 mm long acrylic light guide couples the scintillator to a Hamamatsu 10-stage R4125HA photomultiplier tube 15 mm in diameter, both positioned out of the acceptance window of CLAS. The PMT signals are digitised in LeCroy FASTBUS time-to-digital converters (TDCs) and analogue-to-digital converters (ADCs) before being read out into the data stream [111].

The timing resolution of each start counter paddle varies from 292 ± 1 ps in the "leg" region to 324 ± 2 ps in the "nose", with $< 0.5\%$ of the hits lying outside ± 1 ns of the mean, which is the range required to differentiate in time between neighbouring electron beam bunches. The lower timing resolution in the "nose" of each paddle is due to an inevitable degradation in the light response of the scintillator as a result of mechanical bending of each paddle, which was performed to allow better coverage of the forward angles.

4.5.3 Drift Chambers

The trajectories of charged particles produced in the reactions with a momentum higher than the threshold 100 MeV/c are mapped through 18 separate drift chambers arranged concentrically in three layers (regions) around the target [112]. Each region consists of six drift chambers positioned at the same radius in the six sectors of CLAS (as

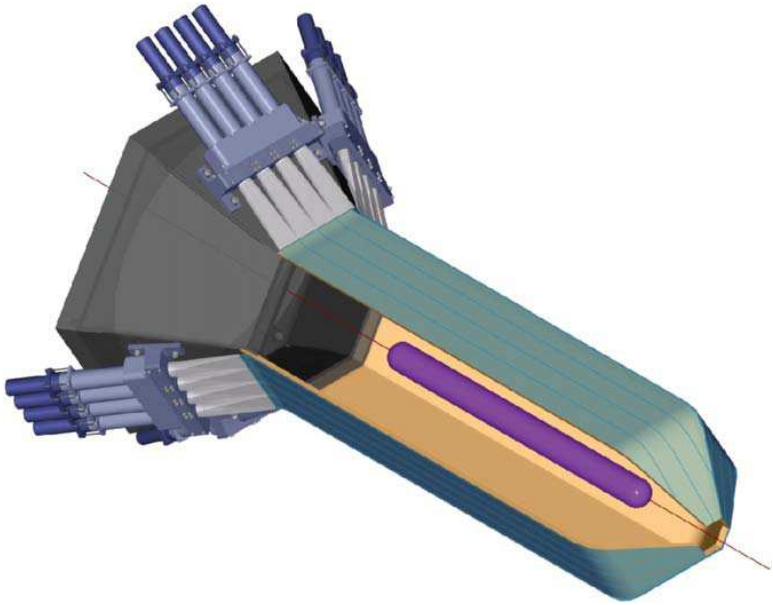

Figure 4.10: Start counter with one of the six paddle sectors removed to show the target cell inside [111].

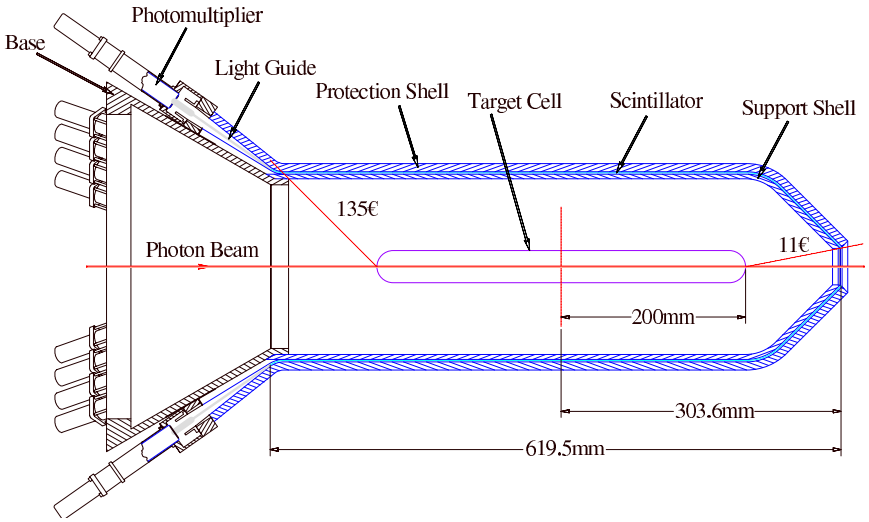

Figure 4.11: Cross-section through the start counter, showing the target surrounded by scintillator paddles [111].

delineated by the coils of the torus magnet) — Region One is in the low magnetic field just outside the start counter, Region Two fills the area of highest magnetic field between the coil cryostats, while Region Three covers the farther reaches just above the coils (Fig. 4.12 and 4.13).

Figure 4.12: Photograph of CLAS opened up, showing, from the upstream end, the sphere formed by the six sectors of the drift chambers. At the left edge of the photograph and in the bottom right corner (behind the drift chambers), the wrapped scintillator paddles of the time-of-flight system can be seen (Jefferson Lab Hall B archive).

Each drift chamber was designed to fill maximally the sector volume available and to this effect has a trapezoidal cross-section, where the wires are stretched between two endplates tilted out at 60° to each other (top of Fig. 4.13). When *in situ*, the two endplates of each region sector are positioned parallel to the planes of adjacent torus coils, thus ensuring maximum coverage (~ 80%) in the azimuthal angle. The entire drift chamber system covers from 8° to 142° in the polar angle.

The arrangement of the wires in each chamber (Fig. 4.14) is reminiscent of close-packing, where a layer of sense wires (at a high positive potential) is followed by two layers of field wires (at a high negative potential of half the strength), forming cells hexagonal in cross-section and gradually increasing in size with radial distance from the target. Six layers of these cells are grouped into a superlayer, which is surrounded by guard wires to simulate, at the edges, the electric field of an infinite grid. Each

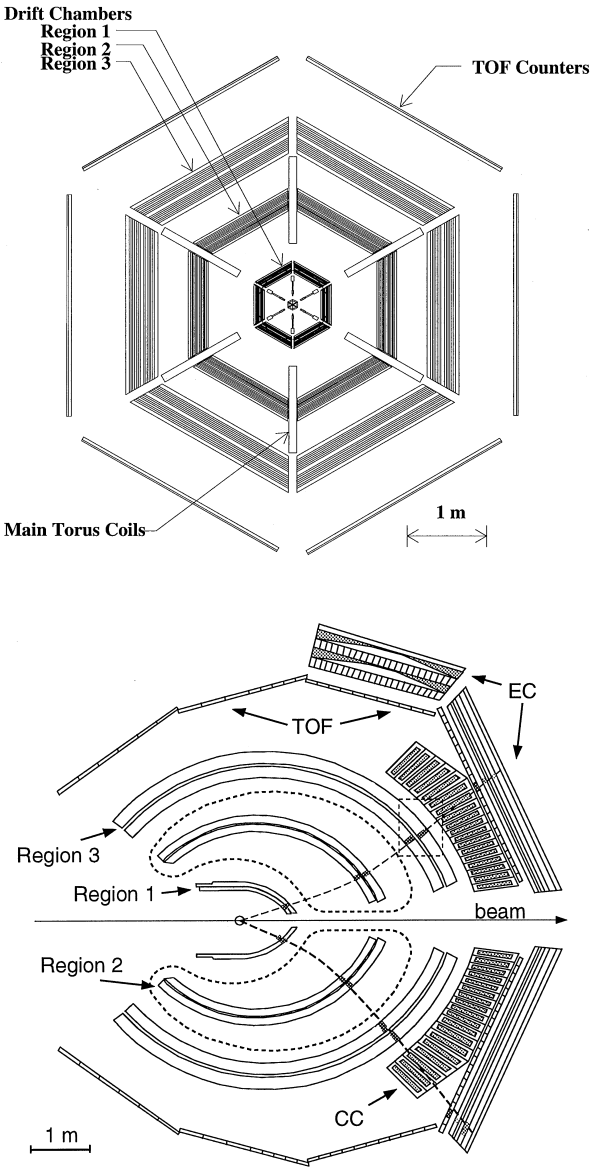

Figure 4.13: Schematic showing a cross-section through CLAS perpendicular to the beam axis (top) and parallel to it (bottom) [113].

chamber consists of two superlayers, one aligned along the direction of the magnetic field of the torus, the other tilted at 6° stereo to it, providing azimuthal information. The chambers are filled with a mixture of 88% argon and 12% carbon dioxide.

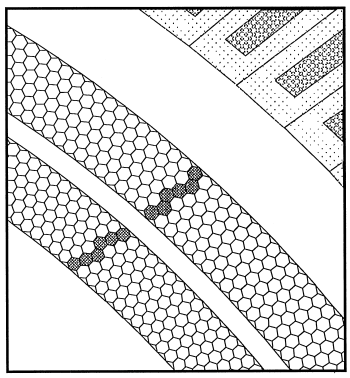

Figure 4.14: A section through Region 3 of the drift chamber, showing the two superlayers and the hexagonal array of cells formed by the arrangement of field wires. A possible particle track through the regions is shown as shaded cells where a hit is registered in the sense wire at the centre of each cell [113].

The sense wires, 20 μm diameter, were constructed from gold-plated tungsten. The composition of the wire provides durability, chemical inertness and a smooth surface. Typical operation results in an electric field of $\sim$ 280 kV/cm at the surface. The field wires are 140 μm diameter gold-plated aluminium alloy, chosen for its long radiation length and low density. The surface electric field is kept below 20 kV/cm to minimise cathode deposition.

Electrical signals from each sense wire are output to a single channel differential pre-amplifier board attached to each endplate. The signal from the amplifier is fed via 20 m twisted-pair cables to the front-end electronics in CLAS, which comprise a post-amplifier and discriminator board. The resulting digital output pulses are multiplexed and passed to TDCs operating in common stop mode, the stop signal originating from the (delayed) CLAS trigger. The timing of the output signals referenced to the CLAS trigger are then recorded by Data Acquisition (DAQ) if they fall within a preset time window of 20 ns from the trigger. The timing signals are subsequently used in calculations of drift time and velocity to determine the distance of closest approach (DOCA) to each triggered wire and improve accuracy in the determination of the particle track.

The performance of the drift chambers can be characterised in two ways, by how efficiently the chamber registers tracks and how accurately the tracks are determined. Regarding the first, the discriminator thresholds and high voltage settings for each layer are set to keep electronic noise below 2% and wire hit efficiencies above 98%. The tracking efficiency — that of reconstructing an expected track — is above 95% for low hit occupancies. Typical accidental occupancies are well under 5% at full design luminosity, and significantly lower for photon beam experiments.

Regarding the accuracy of tracking, track resolution varies from region to region. The single wire resolution is $\sim 200 - 250$ μm in the centre of each cell and averages to 330 μm over the entirety of the drift chamber system. However this is degraded by multiple scattering in the chambers, uncertainties in the magnetic field and mechanical misalignments of the system, resulting in track resolution which ranges from 300 to 450 μm from Region One to Three. This results in a momentum uncertainty of $< 0.5\%$ for 1 GeV/c particles and an angular resolution of < 2 mrad for the reconstructed tracks.

4.5.4 Čerenkov Counters

It is notoriously difficult to separate high energy electrons and pions using track curvature or ΔE - E techniques. To this end an array of Čerenkov counters is positioned outside the drift chambers at forward angles up to $\theta = 45^\circ$. Each sector of CLAS is split into 18 regions of θ, each with its own Čerenkov counter. The Čerenkov counters consist of two modules symmetrical about the central plane of constant ϕ in each sector. They are filled with perfluorobutane (C_4F_{10}), which emits Čerenkov radiation, mainly in the UV region, when a charged particle passes through it. Additionally, this high refractive index gas (n = 1.00153) has a high threshold[1] for pions (2.5 GeV/c), which aids in discriminating pions in this momentum range from electrons. An elliptical and a hyperbolic aluminium mirror focus the emitted photons through a Winston light collection cone onto a 5 inch Phillips XP4500B PMT. These PMTs are highly sensitive and capable of triggering on a single photoelectron. The imperfections in the light focussing are corrected with a cylindrical mirror at the side (Fig. 4.15). The

[1]The Čerenkov threshold is the minimum particle velocity required to produce Čerenkov light in the medium.

PMT and light collection cone are surrounded in magnetic shielding and placed in the shadow of the torus magnet coils.

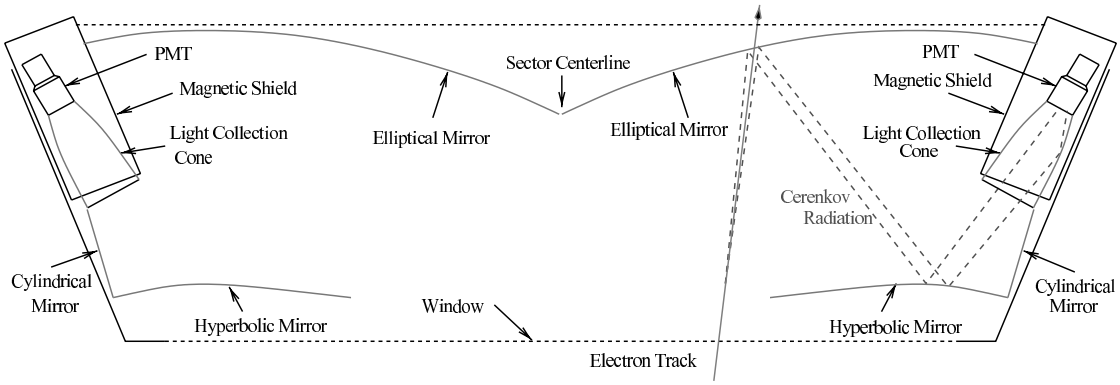

Figure 4.15: Schematic showing a segment of a Čerenkov counter and an electron track through it [104].

The signals from the PMTs are amplified and passed to a discriminator module. The logic output signals of the discriminator are sent to TDCs and may be also used in the experimental trigger where they allow event triggering on a single electron. The TDC signals are additionally sent to ADCs, allowing the amplitude information to be used in off-line analysis. The overall efficiency of the Čerenkov counters is above 99.5% over most of the acceptance, its greatest limiting factor being the imperfect reflectivity of the mirrors [114].

4.5.5 Time of Flight system

The timing of the particle crossing CLAS is measured by the time-of-flight (ToF) scintillation paddles which slot together to form a shell outside the drift chambers and Čerenkov counters, covering $8^\circ - 142^\circ$ in polar angle and the full available range in ϕ. The paddles, cut from Bicron BC-408 organic plastic scintillator, are aligned perpendicular to the beam direction in a hexagonal geometry where one paddle subtends each sector of CLAS for a given interval of $\delta\theta$. The scintillation light produced when a particle interacts in the scintillator is read out by PMTs optically connected to each end of the paddle. The PMT's fit into the shadow region of the torus magnet coils to avoid further loss of detector acceptance. The PMT output signals are fed to ADCs

and via discriminator modules to TDCs which record the size and timing of the pulses. The scintillator paddles are uniformly 5.08 cm thick and vary in length from 32 cm to 445 cm depending on their location in the array. Their width is 15 cm in the forward region ($\theta < 45°$) and 22 cm at larger polar angles. The paddles are tilted so that the average particle trajectory at that location is normal to the paddle face (Fig. 4.16). The time resolution of the ToF counters was measured using cosmic ray events and ranges from $\sim$ 150 ps for the shortest to $\sim$ 250 ps for the longest paddles [115].

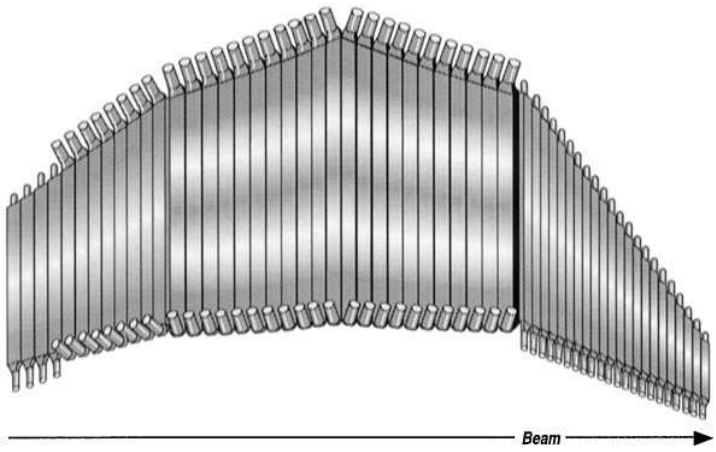

Figure 4.16: A diagram of a ToF sector, showing the scintillation counters arranged, in four panels, perpendicular to the beam line. At both ends of each paddle is a light guide and a PMT [115].

4.5.6 Forward Electromagnetic Calorimeter

The forward electromagnetic calorimeter (EC) in CLAS is a sampling calorimeter, comprising a sandwich of alternating passive sheets of lead, providing a high-Z material to produce electro-magnetic showers, and scintillator, to measure the location, energy and timing of the charged particles in the resulting showers. The EC is primarily responsible for the detection and event triggering on electrons above 0.5 GeV and neutral particles (specifically neutrons and photons above 0.2 GeV from the decay of π^0 and η mesons). The calorimeter covers the region 8° – 45° in the polar angle and

consists of six modules, one for each sector, with the cross-section of an equilateral triangle. Each module has a total of 39 lead-scintillator layers totalling approximately 16 radiation lengths. Each layer comprises a 2.2 mm thick lead sheet followed by a layer of 36 side-by-side BC412 scintillator strips 10 mm in thickness and approximately 10 cm wide (Fig. 4.17).

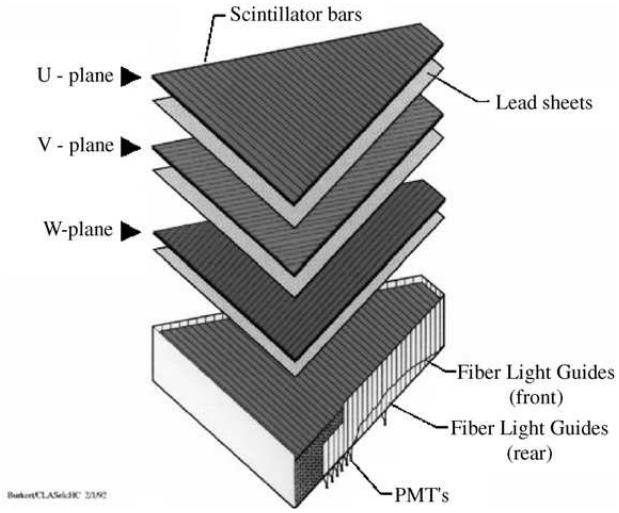

Figure 4.17: Diagram showing the layered structure of the electromagnetic calorimeter and the arrangement of scintillation bars inside. The bars are aligned parallel to one of the three long sides of the module. The alignment is rotated for each consecutive layer, forming a grid [116].

Each successive layer is rotated through 120°, effectively creating three orientations and splitting the EC module into an array of triangular cells used to locate the area of energy deposition. Every orientation is split into an inner stack, consisting of the bottom five layers, and an outer stack for the top eight. In each stack, all the scintillators on top of each other are coupled via fibre-optic light guides to the same PMT, thus giving 72 PMTs in total for each of the three orientations. The PMTs have been chosen to behave linearly over a very large dynamical range and for a typical signal from a 1 GeV electron have an amplitude resolution of $\sim$ 4% and time resolution of 100 – 150 ps. The PMT gain is monitored during data-taking by periodic illumination of the PMT using UV light from a nitrogen laser [116].

4.5.7 Large Angle Calorimeter

The Large Angle Calorimeter (LAC) is complementary to the EC and is used to detect scattered electrons and neutral particles at large polar angle ($45^\circ < \theta < 75^\circ$). There are only two units covering the two top sectors of CLAS (a total of 120° in ϕ). Similar in design to the EC, each unit is a sandwich of alternating square sheets of lead 2 mm thick and 1.5 cm thick NE110A scintillator bars (on average 10 cm wide, up to a maximum width of 11.15 cm), forming a total of 33 layers. Each layer of scintillator bars is rotated at 90° to the previous one, thus forming a grid of cells $\sim 10 \times 10$ cm^2 (Fig. 4.18) and each scintillator is connected at each end via a Lucite light guide to an EMI 9954A PMT. Similarly to the EC, each of the two units is divided into 17 inner layers and 16 outer ones to improve discrimination between pions and electrons, for which good energy resolution is essential. The energy resolution is $\sim 7.5\%$ for 1 GeV electrons and improves with increasing momentum. Timing information is required for calculations of the momentum of uncharged particles crucial to differentiate neutrons and photons. The timing resolution is 260 ps for neutron momenta > 0.5 GeV/c. The neutron detection efficiency of the calorimeters is measured to be $\sim 30\%$ [104].

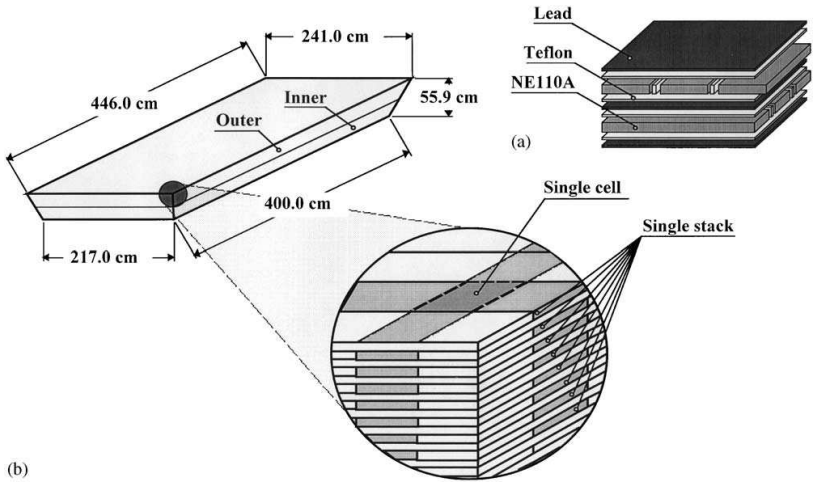

Figure 4.18: Schematic showing the arrangement of lead, Teflon and scintillator layers inside a LAC module [117].

4.6 Targets

A variety of cryogenic and solid targets have been developed for CLAS. The cryogenic targets are typically kapton cylinders with thin aluminium windows, ranging in length from a couple to a few dozen cm, and designed to hold liquid hydrogen, deuterium or helium. Solid aluminium, carbon, iron, lead and certain compounds have also been used.

Polarised targets have also been developed, most recently in a project entitled FROST, which used a butanol target (with polarised protons being the item of interest) cooled by a custom-built dilution refrigerator to below 40 mK to extend the polarisation relaxation time during operation. The level of polarisation was maintained by a 0.5 T solenoid kept around the target cell during the experiment with longitudinally polarised protons, and a specially constructed transverse holding coil for a transversely polarised target. In the early part of my PhD I constructed the prototype of the superconducting transverse holding coil.

The target used in the experiment presented in this thesis was a 40 cm long cylinder containing liquid deuterium. It was positioned 20 cm upstream from the centre of CLAS to increase coverage in forward angles.

4.7 Detector electronics and software

4.7.1 Trigger

The prompt analogue signals from the PMTs and drift chamber wires in CLAS are passed to a two level trigger system. The Level 1 trigger is used to set the timing of the integration gates for the ADCs and also as a start signal on TDCs. An optional Level 2 trigger can impose further conditions which need to be met for the signal to proceed to digitisation and readout, such as particular tracks in the drift chamber.

The Level 1 trigger consists of a three stage process taking on average 90.5 ns to complete. The first two stages combine prompt hits from different detectors and compare the emerging hit patterns to those stored in look-up tables in the memory. These are configured for every experiment using a graphical package called TIGRIS and list possible hits associated with chosen particles. The third stage correlates patterns in

each sector to identify likely events, for example a negative track in one sector accompanied by a positive one diametrically opposite. Additional information, such as the requirement of a timing coincidence with a hit in the tagger, is introduced at this stage and the signals are passed to the Trigger Supervisor.

To further refine event selection, a second stage of triggering may be added. The Level 2 trigger maps likely tracks through the drift chambers and sends a fail signal to the trigger supervisor if the tracks do not correspond to particle information from Level 1. Due to the drift time in the chambers, this takes a long time to process, approximately 4 μs, and, unlike Level 1, contributes to the deadtime of the system.

The Trigger Supervisor is the electronic control centre which processes all trigger output and sends common gate, start/stop and reset signals to detector electronics, initialising ADCs and TDCs and queues the event for readout. If it is configured to run with the two level trigger system, it will hold digitisation until a pass or a fail signal is received from Level 2 trigger. The event information is then digitised and written to readout.

4.7.2 Data acquisition

In the first stage of the data acquisition process, digitised ADC/TDC outputs from the detectors within the hall (in 24 FASTBUS and VME crates) are assembled into tables. Each element is indexed to the corresponding active detector component, then transferred to the main CLAS on-line acquisition computer (CLON) in the control room for event building and processing. The tables of event fragments are there elaborated into "banks" with the addition of headers and data labels, while some are grouped together into larger banks describing extended systems, such as the drift chambers, which require information from several crates [118]. The Event Builder (EB) then combines the corresponding banks into whole events and finally labels those with a run number, event number, event type, and other information in a header bank. By now the event is ready for off-line analysis and is written across the local array of RAID disks, from whence it is transferred along a fibre link for permanent storage on a tape silo 1 km from the experimental hall. Some events are also sent for on-line monitoring, reconstruction and analysis on other computers.

The CEBAF On-line Data Acquisition system (CODA) controls the DAQ process and all communication with detectors, starting and ending runs. The first stage is DAQ configuration, where detector parameters, such as trigger logic and TDC thresholds, are loaded from a prepared run configuration file, relevant software is downloaded to the detector readout controllers, and the correct EB processes are set up. Next, during "prestart", loaded run parameters are checked against the original configuration data and information about current run conditions is written to the database and parameter files. The run is then started, at which point the trigger is enabled and data begins to accumulate in 2 GB files (this limit is set by the maximum file size on the Linux machines). Each run takes typically 1 - 2 hours and contains ~ 40 files.

4.8 The g13 experiment

The experiment described in this thesis was carried out between March and June 2007 in Hall B of Jefferson Lab, using a linearly polarised photon beam incident on a liquid deuterium target. It was labelled g13b as it formed the second half of the g13 experiment, the first half of which ran in autumn 2006 on the same target but used a circularly polarised beam.

During the run period electron beam energy was varied from 3.3 to 5.2 GeV to produce photons at six equally-spaced energies in the 1.1 - 2.3 GeV range, with a degree of linear polarisation reaching above 80%.

The experiment was run with a single charge trigger to accept a wide range of events for the large number of reaction channels being analysed [119], triggering at a rate of 7 - 8 kHz. A total of 3×10^{10} events have been recorded in the g13 run period. Approximately 0.5% of these events were of the $n(\gamma, \pi^-)p$ reaction channel presented in this thesis.

Chapter 5

Detector Calibration

The detector calibration process enables the raw information from the individual detector elements to be converted into real physical observables. This chapter outlines the calibration procedures of the different systems which were relevant to the g13 experiment.

5.1 Overview of calibration process

The response of CLAS detectors can vary appreciably between different experiments. This can be due to changes in the experimental set-up, for instance torus magnetic field settings, or due to changes in component performance, such as drifts in photomultiplier tube (PMT) gain or dead drift chamber wires. Some of these are monitored and adjusted continuously during the run. For example, the energy response of the large angle calorimeter PMTs tended to drift and was corrected by an adjustment to the PMT gain [117]. However, corrections to the magnitude and time dependence of the calibration parameters were also required in off-line analysis to compensate for any changes in the running conditions or detector response.

At the end of the experiment the detector systems involved in the reconstruction of events were calibrated by a team of collaborators. Specifically, the tagger and time-of-flight calibrations were carried out by Russell Johnstone and Neil Hassall, from Glasgow University, respectively, the drift chambers were calibrated by Edwin Munevar from George Washington University while Paul Mattione (Rice University) calibrated

the electromagnetic calorimeter. The start counter calibrations were carried out by the author.

Each system has a certain number of calibration constants which were used in the calculation of physical quantities associated with it, most usually timings and energies deposited in the detector. The systems had to be calibrated in a certain order and the calibration cycle iterated a number of times as the measurements from the various systems were often inter-dependent. This was particularly true for timing calibrations where the optimisation of the relative timings of different detector systems was crucial.

The calibration of each detector was initially carried out on a selection of agreed runs, one from each set where the running conditions were approximately constant. The calibration parameters were then extended to the rest of the uncalibrated runs in that set. Once a satisfactory level of alignment was reached on each detector system for the selected runs, fine-tuning was performed by calibrating every fiftieth run. Final adjustments were made to those runs where alignment could still be optimised.

The requirements of detector calibration were dictated by the procedures of data analysis, the details of which, for the selection of the reaction channel $n(\gamma,\pi^-)p$, are expounded in Chapter 6 and mentioned, when relevant, in the following sections. In brief, selection of events consisted of the following steps:

- Initial identification of final state particles. In the case of charged particles, this was done based on their mass calculated using measured momenta and velocity. The determination of momentum relied on accurate tracking through the drift chambers. For the calculation of velocity, an additional accurate measurement of the time of flight, based on the hit times in the start counter and the scintillation counters, was required (Section 6.2).

- A reconstruction of the particle creation time, based on the particle's velocity, time of flight and vertex position (which is extrapolated from the tracking information). This was required to identify final state particles created in the same hadronic interaction in the target.

- Reconstruction of the full event, including the identification of the photon which caused the reaction based on its time of arrival at the reaction vertex. To this end, timing information from the tagger needed to be correlated to the start of the event as measured by the detectors of CLAS. An absolutely crucial aspect

of the calibration process was therefore to identify the timing offsets between the different detectors. It was then possible to align the time measured by each detector to a common "zero" start time for each event, as discussed in Section 5.2.3.

The sections below outline the calibration procedures for the individual detectors relevant to the $n(\gamma,\pi^-)p$ reaction channel.

5.2 Common features of timing calibration

This section introduces some aspects of the timing calibration process which are common to a range of systems in the CLAS and tagger apparatus. The details of the calibration process for each detector will be presented in later sections.

5.2.1 TDC timing calibration

The timing information of the tagger and all detectors in CLAS was read out from a collection of TDCs, each of which required calibration parameters to convert the TDC output (channels) into time (ns). To perform the calibration, pulsed logic signals were delivered simultaneously to every TDC, in sets of 50. The time interval between the pulses in each set was increased incrementally with a fixed period of 2.139 ns [120]. This enabled the response of the TDCs to be measured for a wide range of timings. The resulting data was then fitted, typically with a quadratic polynomial, to determine the individual constants for the TDC channel-to-time conversion, which were then entered into a common calibration database.

5.2.2 Time-walk corrections

The TDCs in most systems of CLAS are fed with the logic output signals from a leading edge discriminator, LED. In such devices, the output logic signal is timed to the point where the input analogue signal exceeds a certain pre-determined threshold voltage. A problem arises, however, when the input analogue signals can have a wide range of pulse heights. Since the rise-time to the peak height depends predominantly on the detector characteristics (such as scintillator material), it is approximately constant for

different pulse heights. However, the difference in pulse heights means the threshold level of the discriminator will be reached at different times (see Fig. 5.1), thus introducing a pulse-height dependent shift (called a time-walk) in the time measurement. The time-walk correction is carried out in slightly different ways for the different detector systems in Hall B and is discussed in the corresponding sections below.

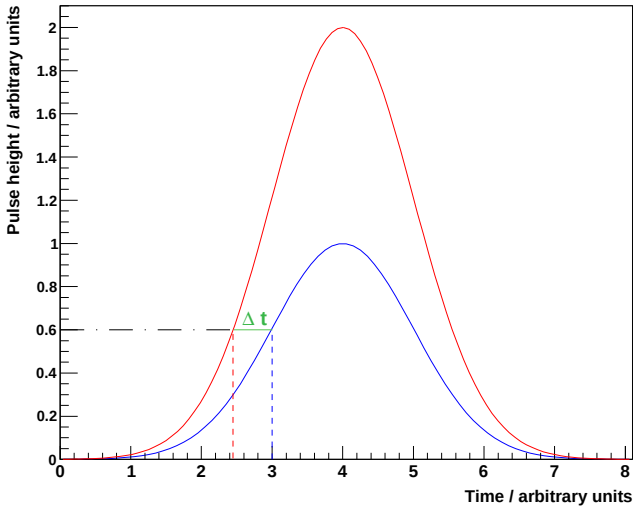

Figure 5.1: Graph showing two signals with identical rise time but different pulse heights. The larger signal will reach a threshold value, shown at a height of 0.6, earlier, by a value of Δt, than the smaller signal.

5.2.3 "Zero time" for the event

The common timing origin for each event was most accurately provided by the timing of the RF signal used to drive the accelerator linacs. As has been discussed in Section 4.1, the electron beam arrives in bunches at 2.004 ns intervals. The beam bunches can be well separated by the timings of the events in the tagger focal plane, as can be seen in Fig. 5.2, where the tagger timing resolution was measured to be $\sim$ 110 ps for 1 σ. Once the few-picosecond-wide beam bunch containing the photon associated with the event is identified, the most accurate event time can be derived from the RF timing of this beam bunch. This is discussed in more detail in Section 5.3 below.

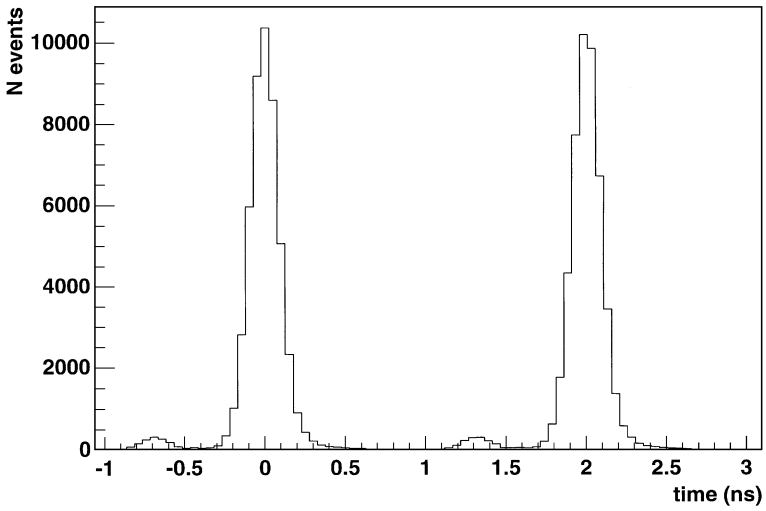

Figure 5.2: Neighbouring beam bunches arriving at ~2 ns intervals. The small secondary bumps are from the beam being delivered to one of the neighbouring experimental halls [110].

Once the tagger had been calibrated to the RF signal, subsequent detector systems were calibrated relative to the tagger, thus ensuring that timing was measured, by each system, from a common zero time: t_0.

5.3 Tagger calibration

As discussed in Section 4.4, the focal plane of the tagger includes 61 scintillator paddles (T-counters), which through their overlap provide 121 time channels yielding information on the scattered bremsstrahlung electrons. Each T-counter was equipped with two TDCs which received logic signal input from the discriminators connected to the PMTs on each end of the scintillator. The first stage of the calibration was to convert the raw output of the TDC (channels) into nanoseconds using the pulser signals (Section 5.2.1). Typical conversion factors were ~ 50 ps/channel, but varied by a few percent from counter to counter. A mean timing for each T-counter was obtained from the sum of the TDC timings at each end, to ensure that the single time measured by each T-counter, t_T, was independent of the hit position along the paddle.

An integral part of the Level 1 event trigger was the requirement of an electron hit in the tagger. When a hit was registered, all the T-counter TDCs in the tagger focal plane

were started simultaneously by the common start signal from the trigger. The counters were stopped either by a hit or by the same signal with a 20 ns delay. The TDCs were thus effectively "self-timed", each triggered counter's start and stop signals originating from the same electron hit. As a result, the timing spectrum of each TDC exhibited a sharp peak corresponding to the trigger start signal, t_{trig}. This value was subtracted from each TDC reading so that all T-counters were accurately timed relative to t_{trig}. The same procedure was also carried out for the TDCs of the E-counters to ensure correct identification, based on timing coincidence, of the associated E-counters for each reconstructed photon [121].

The final stage of tagger timing calibration was to adjust, independently, the timing of each tagger channel to the RF, thus setting each t_T to the common zero time t_0 (Fig. 5.3). A good calibration of the tagger is crucial for the reconstruction of the event. For example a misidentification of the correct beam bunch may result in errors of a few hundred MeV/c^2 in the calculated particle masses, from the resulting error in the time of flight [122].

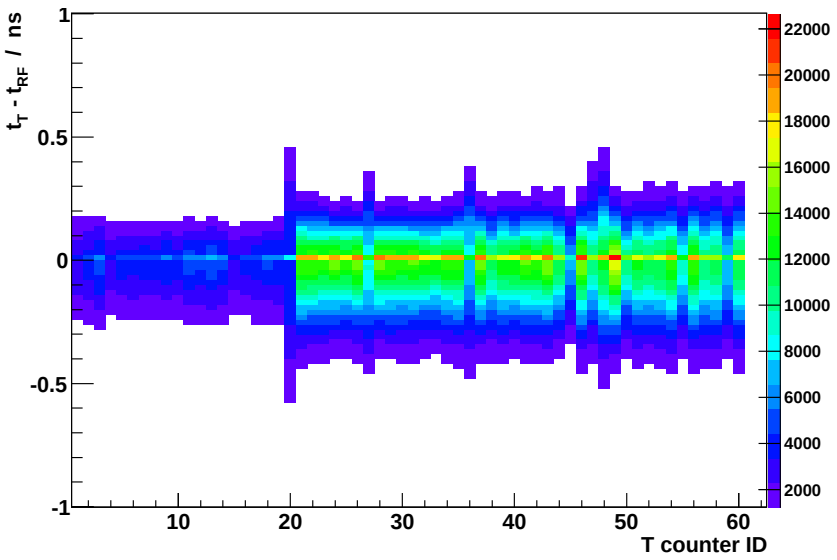

Figure 5.3: Histogram showing alignment of individual T-counters to the RF signal.

The RF time in relation to the trigger, t_{RF}, is given by the time of the photon being produced (relative to the trigger), t_{bunch}, plus a timing offset corresponding to an integer

number of beam bunches, k_e, which typically varied from event to event:

$$t_{RF} = t_{bunch} + k_e\, 2.004 \tag{5.1}$$

Calibration of the tagger channels to the RF signal involved a calculation of the tagger - RF offset parameters C_i, one for each of the 121 tagger channels, followed by the determination of k_e on an event-by-event basis.

The offset parameters C_i can be decomposed into an overall phase offset C_i^{RF} for each tagger channel i relative to the RF signal and an integer number of beam bunches, k_i, which depended on the channel in question:

$$\begin{aligned} t_i - t_{RF} &= t_i - t_{bunch} - k_e\, 2.004 \\ &= C_i - k_e\, 2.004 \\ &= C_i^{RF} + (k_i - k_e)\, 2.004 \end{aligned} \tag{5.2}$$

where t_i is the timing of tagger channel i. Since the total beam-bunch offset was not constant between events, the timing differences between the RF signal and the tagger channels could only be used to determine the phase offset parameters C_i^{RF}. These were calculated from a fit to the distributions of $(t_i - t_{RF})\, mod\, 2.004$.

To determine the constants k_i for each tagger channel a timing comparison was made with a reference detector, the start counter. First, the timing offset, C_i^{ST}, was determined between each tagger channel and the time of a hit in the start counter, t_{ST}:

$$C_i^{ST} = t_i - t_{ST} \tag{5.3}$$

This was done from a fit to a distribution of Eq. 5.3. Next, the difference between the offset constants C_i^{ST} and C_i^{RF} was used to determine k_i channel by channel:

$$\begin{aligned} C_i^{ST} - C_i^{RF} &= t_{bunch} - t_{ST} - k_i\, 2.004 \\ &= K_{det} - k_i\, 2.004 \end{aligned} \tag{5.4}$$

where K_{det} is a detector-specific offset between the two constants, which was first determined from a fit to the total distribution of $(C_i^{ST} - C_i^{RF})\, mod\, 2.004$, summed over all channels. Eq. 5.4 was then used to calculate k_i for each tagger channel and consequently determine the tagger - RF offset parameters C_i:

$$C_i = C_i^{RF} + k_i\, 2.004 \tag{5.5}$$

These constants were finally used in Eq. 5.2 to adjust the timing of each tagger channel to the RF time, thus setting the tagger time to the common zero, t_0, for each event [122].

5.4 Start Counter calibration

The start counter (ST) timing information was crucial in reconstructing the time of the event and thus correlating events in CLAS to the tagged photons in the beam. It was therefore essential to achieve a careful calibration of the TDC timings of each of the 24 paddles.

The calibration procedure was as follows. First, the timings of each of the paddles were aligned to each other. Next, the resultant time of the hit in the start counter with respect to the trigger, t_{ST}, was calibrated relative to the RF-adjusted tagger time, t_T, (which, after careful tagger calibration, should be equivalent to t_0) allowing an event time resolution of < 25 ps.

A good calibration of the start counter therefore relied on the correct determination of the beam bunch which contained the photon associated with the event. To this end, the resolution in $t_{ST} - t_T$ had to be no more than 388 ps, which would place 99% of the data within the confidence interval $\pm$ 1 ns, separating neighbouring beam bunches. Following the calibration procedure, a $\sigma \sim 300$ ps was achieved (see Fig. 5.6)

The timing calibration of the start counter TDCs proceeded in a calculation of t_{ST} for each paddle:

$$t_{ST} = t_{TDC} - t_p - t_w \tag{5.6}$$

where t_p is the propagation time for light along the paddle, t_w is a time-walk correction and t_{TDC} is the raw time of the TDC, calculated from a time-conversion constant C_T (ns/channel) and the TDC output (channels), T:

$$t_{TDC} = C_T T \tag{5.7}$$

The channel-to-time conversion C_T was determined from a pulser run as described in section 5.2.1 and was ~ 0.042 ns / channel for most TDCs.

Finally, t_{ST} was adjusted relative to the zero time for the event, t_0. This was done by first reconstructing the event time based on the start counter timing, $t_{e_{ST}}$, for a particular particle producing a hit in the paddle, and on tagger timing, t_{e_T}. The two timings for the event were calculated thus:

$$\begin{aligned} t_{e_{ST}} &= t_{ST} - \frac{l}{\beta c} \\ t_{e_T} &= t_0 + t_\gamma \end{aligned} \tag{5.8}$$

where l is the distance travelled by the particle from the event vertex to the paddle hit position, β is its velocity as a fraction of the velocity of light, c, and t_γ is the flight time for a photon from the tagger to the event vertex. Any differences between the reconstructed event time were corrected by a timing offset constant K_{RF}:

$$\Delta t = t_{e_{ST}} - t_{e_T} + K_{RF} \tag{5.9}$$

The procedures to establish the timing offsets t_p and t_w from Eq. 5.6 and K_{RF} from Eq. 5.9 is outlined in the following two sections.

5.4.1 Time for light propagation along the paddle

The non-linear geometry of each paddle, which consists of a straight rectangular "leg" followed by a tapered forward "nose" section (Fig. 5.4) results in a non-linear relation between the hit position in the scintillator and the light propagation time along it, t_p.

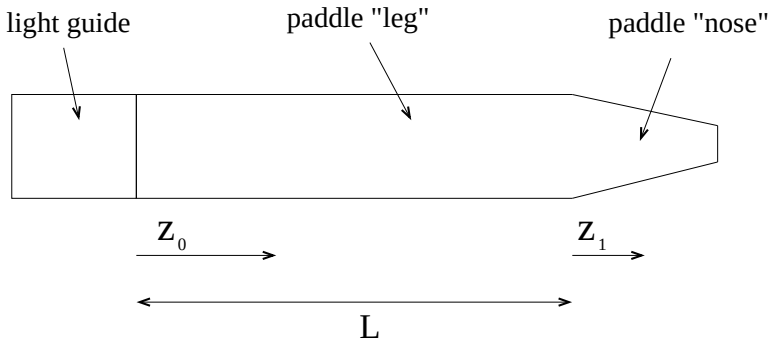

Figure 5.4: Diagram of a start counter paddle from the middle of a sector (not to scale), view from the top.

It was found that a suitable empirical function to fit this dependence was a combined polynomial of the form:

$$t_p = \frac{z_0}{V_{eff}} + k_0 z_1 + k_1 z_1^2 \tag{5.10}$$

where z_0 is the distance of the hit position from the light guide along the "leg" part of the paddle (length L) and z_1 is the distance from the "leg" - "nose" junction along the "nose". These variables are defined in Fig. 5.4. V_{eff} is the effective velocity for

light propagation through the "leg" and along with k_0 and k_1, which describe the z-dependence of the propagation time, was determined from the fit.

The fit procedure to extract these parameters was as follows. The event vertex time difference Δt was initially plotted in a 2-D histogram vs. the distance d along the start counter paddle, where:

$$\begin{aligned} d(z_0, z_1) &= z_0, \qquad z_0 \leq L \\ &= z_0 + z_1, \quad z_0 > L \end{aligned} \tag{5.11}$$

Next, the 2-D distribution was projected into slices in the d-axis and each projection was fitted with a Gaussian to determine the peak Δt for each bin in d. These peak positions were then fitted with the following polynomial, which is composed of Eq. 5.10 and the addition of the constant K_{RF}, which at this stage was left as a free parameter in the fit:

$$\Delta t = \frac{z_0}{V_{eff}} + k_0 z_1 + k_1 z_1^2 + K_{RF} \tag{5.12}$$

An example of the fit performed on the data from one paddle is shown in Fig. 5.5.

5.4.2 Alignment of the start counter to t_0

After an initial fit to determine v_{eff}, k_0 and k_1 was performed, the new constants were used to correct t_{ST} for the position of the hit along the paddle using Eq. 5.10 and 5.6, where t_w from the previous calibration was used. The propagation-time corrected Δt was then fitted for each paddle with a Gaussian to extract the constant K_{RF}. An example is shown in Fig. 5.6, where the estimated timing resolution is $\sim$ 300 ps. The Δt alignment, paddle by paddle, is shown in Fig. 5.7.

During the course of this experiment, we made significant improvements to the start counter calibration package, specifically in the fitting routines and to make the calibration procedure more automated and user-friendly. A GUI interface allowed interactive control of the fit parameters and limits, including new routines to more accurately determine the K_{RF} constant. Other improvements included a shell script to run the entire calibration process for selected runs in one go, and adjustments to the fitting functions and routines to improve the quality of the fit.

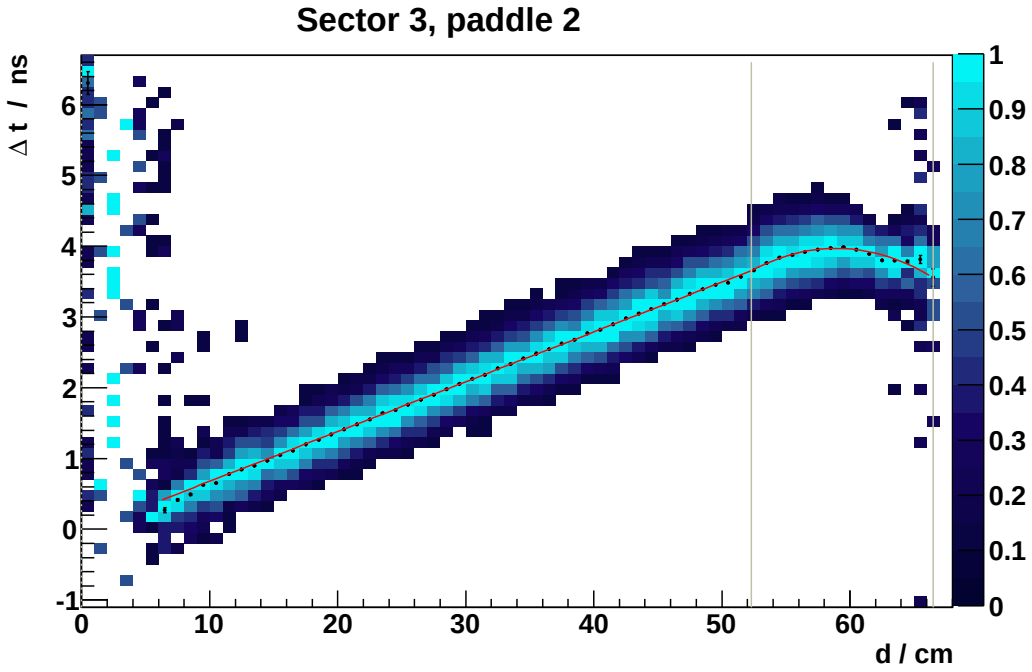

Figure 5.5: 2-D distribution of Δt vs distance d along the paddle. A plot of the peak positions in each d bin (black points) fitted with Eq. 5.12 (red line) is overlaid.

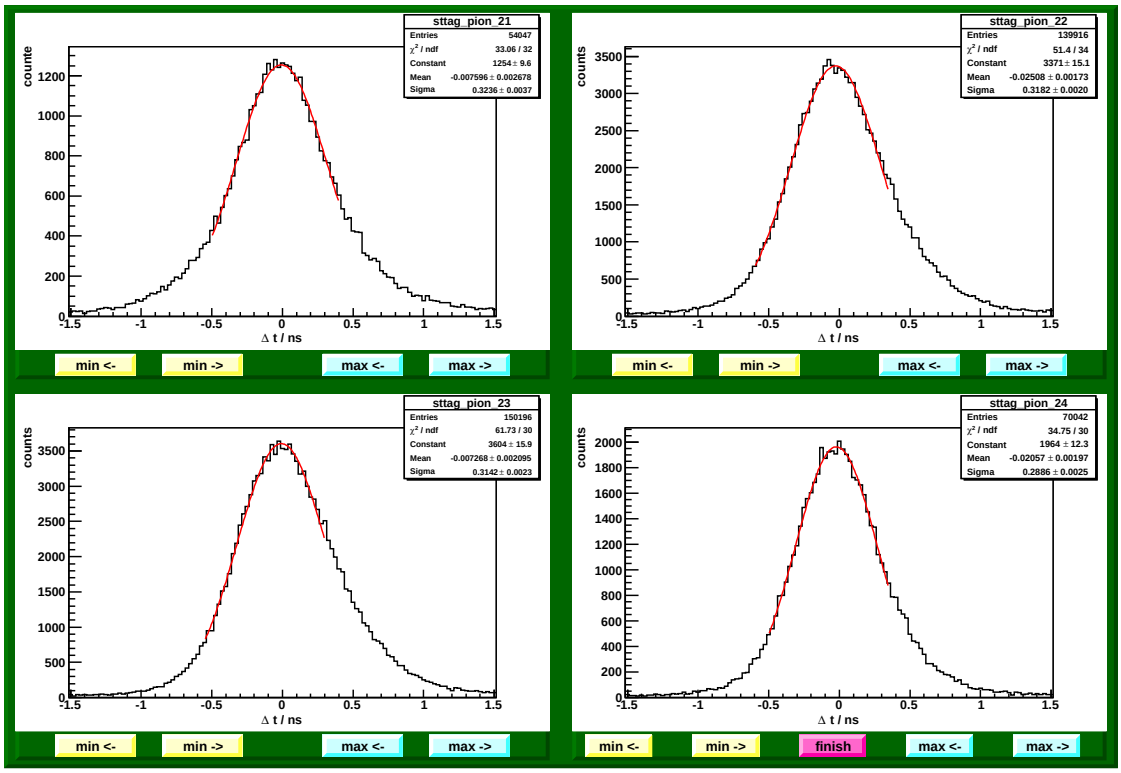

Figure 5.6: A GUI panel from the start counter timing calibration process, showing Δt for four paddles in sector 6 of the start counter. The timing of each paddle has been corrected for propagation time of the signal along the scintillators. Average resolution, based on the σ of the Gaussian fits (shown in red) is $\sim$ 300 ps. The buttons underneath each panel allow the individual fit range and limits to be changed for an improved fit.

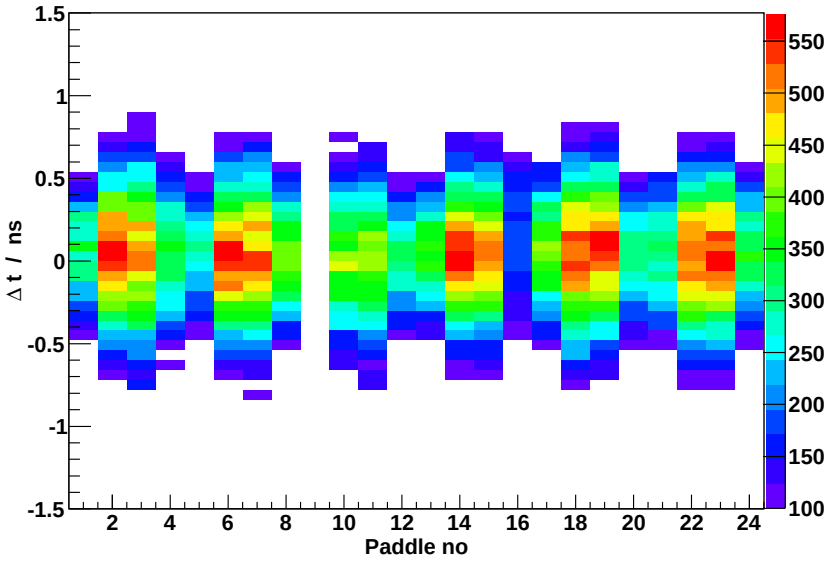

Figure 5.7: Paddle-by-paddle alignment of Δt. Paddle 9 was damaged during fabrication and typically yields too few data points.

5.4.3 Time-walk corrections

The next stage in the start counter calibration was to calculate the energy-deposit dependent time-walk corrections, t_w, described in section 5.2.2. This was done by plotting a distribution of Δt vs the ADC channel, A, which is a measure of the pulse height. To get data with a wide range of pulse heights, both pion and proton signals were used. This is because pions are minimally ionising, typically producing small pulse heights, while protons, with higher mass and lower momenta, deposited more energy, producing larger pulse heights. The 2-D distribution was projected in bins along the A-axis and fitted with a Gaussian to find the peak value of Δt for each bin in A. The scatter graph of peak Δt vs A was then fitted with the empirical function

$$t_w = W_0 + \frac{W_1}{A - W_2} \tag{5.13}$$

The three constants W_0, W_1 and W_2 were determined from the fit. An example of this is shown in Fig. 5.8, where the fit was performed on the summed distributions of signals from protons and pions. For illustration, the distribution of Δt vs A from just proton and just pion signals is shown for a paddle in the top left and top right plots respectively.

As expected, the proton signals are mostly observed at higher pulse heights, while the pion signals are predominantly at the low pulse height values. The two plots at the bottom show the summed distributions of proton and pion signals, covering a wide range of pulse heights, to which the fits were performed.

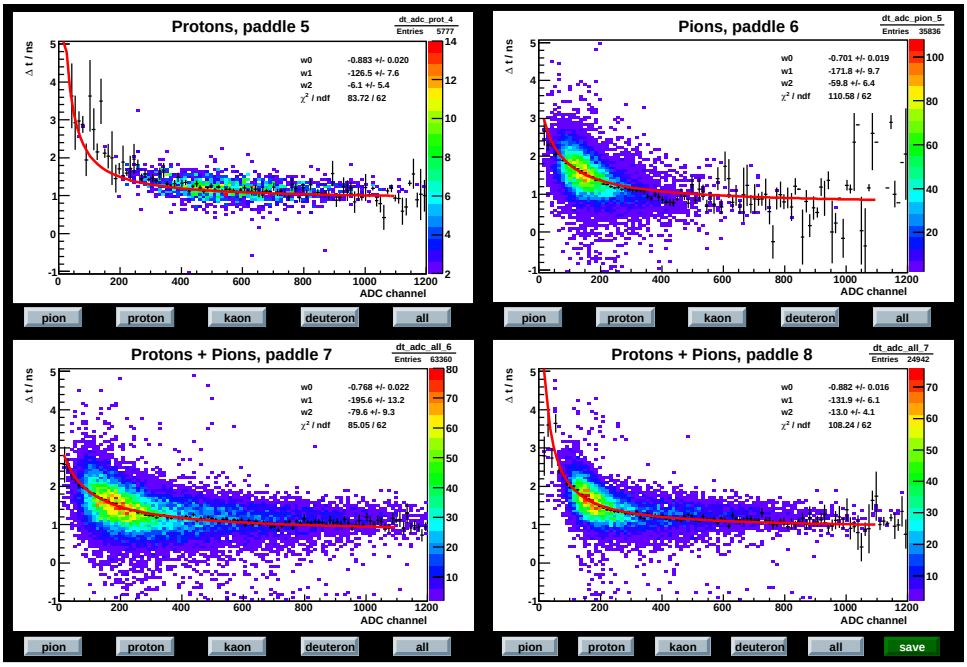

Figure 5.8: A GUI panel for the time-walk calibration, showing Δt vs ADC channel number histograms for four paddles in a single sector of the start counter. Overlaid is a graph of the Gaussian peak positions for each bin on the ADC axis (black points) and its fit with Eq. 5.13. The fit was performed based on the summed distributions of protons and pions, examples of which from two paddles are shown in the bottom panels. The top panels illustrate the contributions from protons (left) and pions (right) to the hits in the remaining two paddles of the sector.

5.5 Time of Flight system calibration

The time of flight (TOF) detector array had to be calibrated both for the timing of particle arrival at a particular paddle and the energy deposited therein. These calibrations are discussed below.

5.5.1 Energy corrections

The first stage of calibration determined the "pedestals" for each ADC, which were the ADC channel values, A_p, in the absence of a real PMT signal and reflected the residual current present in the ADCs. This was obtained using data from a separate pulser run taken at the beginning of the experiment and after any configuration changes.

Each paddle was equipped with a PMT, TDC and ADC at both ends. The pulse heights from the two ADCs, A_L and A_R, at either end of the paddle were used to find a geometric mean ADC pulse height for normally incident minimum ionising particles, A_{mip}, for that paddle:

$$A_{mip} = \sqrt{A_L \times A_R} \tag{5.14}$$

This provided a hit-position independent measurement of energy deposition in each counter and was used to convert the ADC channel, A, to energy deposited in MeV, E_{ADC}, thus:

$$E_{ADC} = \frac{C_{acd}(A - A_p)}{A_{mip}} \tag{5.15}$$

where C_{adc} is a conversion factor. The light attenuation length, λ, of each paddle was extracted from the data by a fit to the distribution of deposited energy ratio as measured at both ends of the scintillator vs hit position from the centre of the paddle, x:

$$\begin{aligned} \frac{ln(E_L)}{ln(E_R)} &= C_\lambda - \lambda\, x \\ &= C_\lambda - \lambda\, \frac{v_{eff}(T_L - T_R)}{2} \end{aligned} \tag{5.16}$$

where v_{eff} in the effective velocity of light propagation along the scintillator, T_L, T_R are the timings from the left and right TDCs of the paddle respectively and C_λ is an offset parameter. Adjustment of this parameter was important to ensure that consistent energy deposit measurements were obtained from both ends of the paddle. Attenuation length measurement was used to correctly determine the energy deposited in the paddle independent of the hit position along it [120].

A calculation of v_{eff} was obtained for each paddle from the slope of the linear distribution of hit distance from the edge of the counter, l, vs time as measured in the TDC at that end of the counter, t_{TDC}:

$$v_{eff} = \frac{l}{t_{TDC}} \tag{5.17}$$

Typical values of v_{eff} were $\sim$ 16 cm/ns, but varied within $\pm$ 3 cm/ns amongst the paddles.

5.5.2 Timing corrections

The timing correction of the scintillation counter TDCs required four main adjustments: the TDC channel to time conversion and time-walk correction discussed in sections 5.2.1 and 5.2.2, the left-right balance between the TDC times from each end of the paddle and the alignment of paddle hit times to the common zero time t_0.

The time-walk correction and the left-right balance relied on the use of an external laser light source which was pulsed, through a neutral density filter, at the central part of each scintillator paddle and at a diode simultaneously. The diode provided reference timing information to which the TDC time of the scintillator could be compared, while a measure of the corresponding pulse height, which was varied by the filter, was obtained from the ADC. A fit to the TDC time vs ADC value was used to determine the function parameters for the time-walk correction [123].

The same laser-triggered data was used to correct the left-right balance between the TDC times read out from each end of the scintillator paddle. The adjustment ensured that for light originating from the centre of the paddle the PMTs at either end gave the same timing.

The final timing calibrations concerned adjustments of any timing offsets between the paddles, due to different electronic delays, for example, followed by an overall offset to the common zero time t_0.

With calibrations in place, the typical time resolution of the scintillation counters ranged from 150 ns for the 100 cm long scintillators in the forward region to $\sim$ 250 ns for the longest counters at backward angles [115].

5.6 Drift Chamber calibration

The drift chamber (DC) calibration centred on reconstructing the particle tracks through the six superlayers in each sector. Initial reconstruction was done during the running of the experiment in a process known as “hit-based” tracking which first fitted individual tracks to the hit positions in the sense wires, linked them up across superlayers

and finally joined them across the three regions of the drift chambers. At that stage, reconstructed momenta were accurate to 5% [113] and particle identification was possible using information from the start counter, TOF systems, Čerenkov counters and calorimeters.

The next calibration stage, which was undertaken after the initial start time calibrations, is called "time-based" tracking and involved the following additional corrections to the drift chamber data used for the calculation:

- a correction to the drift time which was recalculated based on the start time of the event (reconstructed from tagger calibrated to the RF, the time-of-flight and start counter time measurements),
- a calculation of the time of flight of the particle to the hit position,
- the propagation time for the signal along the sense-wire corrected for the time-walk,
- a fixed time-delay constant for the individual wire (mainly due to electronic delays in the cables)
- and implementation of the channel-to-time calibration of the TDCs for the wire.

The drift time was then translated into the distance of closest approach (DOCA) to the sense wire via reference to a look-up table for the particular magnetic field and angle of approach, generated from a GEANT 3 simulation. Drift time alone, however, could not establish on which side of the sense wire the particle had passed, and this was determined by the minimum χ^2 from a fit to all permutations of tracks passing on either side of each sense wire.

The entire track was then fine-tuned by a fit to a residuals vs drift time plot for each superlayer [124]. The residuals, r, provided a measure of how well the fitted DOCA, D_f, agreed with that predicted for each hit based on its drift-time, D_p:

$$r = D_f - D_p \tag{5.18}$$

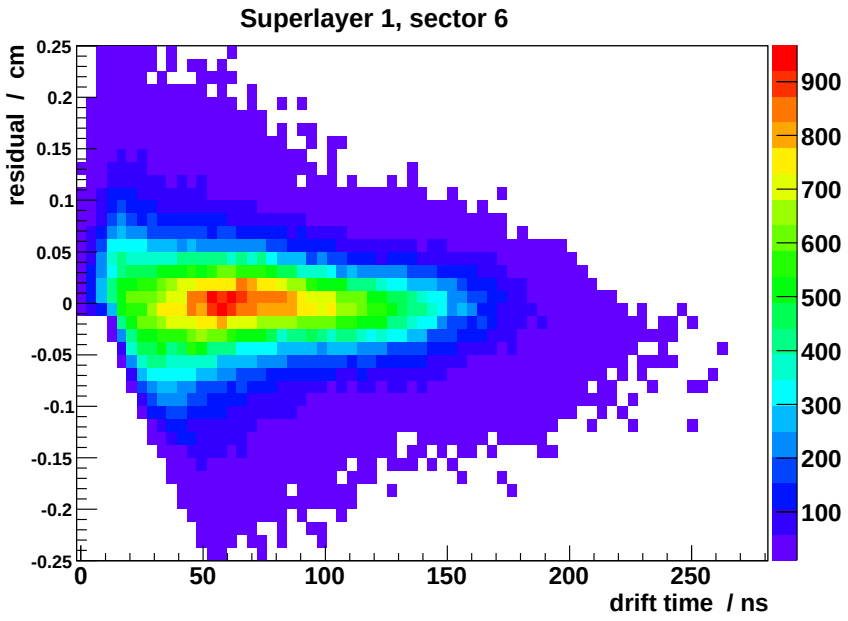

Figure 5.9: Drift chamber residuals vs drift time in time-based tracking for a single superlayer.

5.7 Calorimeter calibration

The final stage of detector calibrations dealt with the alignment of the Electromagnetic (EC) and Large Angle Calorimeters (LAC). These were not required for the reconstruction of either the π^- or a proton, which are the final state particles of the studied reaction, and are therefore mentioned only for completeness.

The electromagnetic calorimeter plays a major role in the identification of neutral particles, in particular the separation of neutrons and photons based on their time of flight information. As such, the main calibration required was of the EC TDC timing. This was performed on electrons and charged pions, for which the time of flight could be easily established. A five-parameter fit to the EC time distribution incorporated TDC channel-to-time conversion, time-walk correction, an overall detector offset relative to the common zero time, t_0, and parameters describing signal propagation through the scintillator counters.

An estimate of the hit position resolution was obtained from a fit to the DC - EC residuals, determined from the difference between the extrapolation of the DC track to

the EC counter and the calculated hit position therein [116].

A similar calibration procedure is employed for the LAC, the details of which are outlined in [117].

Chapter 6

Data Analysis I: Event Selection

6.1 Overview

Data acquired during the experiment, as discussed in Chapter 4, was written into BOS (Bank Object System) files which are kept on the JLab data storage silo. The "raw" data files written during the experiment contained only detector-specific information such as ADC and TDC channels and detector status flags. In the process of calibration the data was "cooked" (as it is refered to in the JLab terminology) where raw information was translated, using calibration parameters, into physical quantities. New banks containing physics observables were also added to the data-stream (and some raw detector banks dropped from the cooked files to save space). These contained information on the reconstructed events and served as the basis of subsequent physics analysis. During the cooking process, the BOS data files were converted into a more compact ROOT DST (Data Summary Tape) format.

The data contained in the cooked and calibrated DST files were analysed using a ROOT/C++ [125] analysis framework called "ROOTBEER" [126]. This allowed the data banks in DST and BOS files to be read directly into a ROOT framework, utilising libraries for data analysis procedures, fitting and histogramming of results.

This chapter discusses in detail the stages of analysis concerned with identifying and reconstructing the reaction

$$\gamma + d \quad \rightarrow \quad (p) + p + \pi^- \tag{6.1}$$

6.2 Event reconstruction

This section outlines the methods used for the initial event reconstruction which determine a basic set of physical quantities for each event, such as particle charges, momenta and velocities. More sophisticated event reconstruction in the physics analysis of the data will be discussed from Section 6.3 onwards.

6.2.1 Charge and momentum

The particle charge was determined from the direction of curvature of the particles' reconstructed tracks through the toroidal magnetic field within the drift chambers. The radius of curvature yielded information on their momenta via application of the Lorentz Law:

$$\boldsymbol{F} = q(\boldsymbol{v} \times \boldsymbol{B}) \tag{6.2}$$

where $\boldsymbol{F}$ is the force acting, due to magnetic field $\boldsymbol{B}$, on a particle moving with velocity $\boldsymbol{v}$. The momentum $\boldsymbol{p}$ of the particle is therefore given by

$$\boldsymbol{p} = q(\boldsymbol{r} \times \boldsymbol{B}) \tag{6.3}$$

where r is the curvature radius of the track. The toroidal magnetic field is always approximately perpendicular to the velocity of the particles traversing CLAS, which maximises the sensitivity of the track curvature to small differences in momentum.

6.2.2 Velocity

The time-of-flight of the particle between its hit in the start counter (ST) and the scintillation counter (SC), t_f, was calculated from the time difference between the hits in these two detectors. The associated path length, d, was determined from the reconstructed track through the drift chambers. This information was combined with the time-of-flight to calculate β, the particle's velocity as a fraction of c, the velocity of light:

$$\beta = \frac{d}{ct_f} \tag{6.4}$$

The two independent measurements of momentum and β allowed the invariant mass of the particles to be calculated, as will be discussed in Section 6.3.

6.2.3 Event vertex

An intersection point of the beam axis with the particle's extrapolated track gave an estimate of the track origin, which in the case of the $p\pi^-$ final state corresponds to the reaction vertex. Individual particles were initially associated with each other — and with the photon which caused the interaction — based on a coincidence of their vertex position and time.

6.3 Selecting the p π^- final state

The steps taken to reduce the data to the the $n(\gamma,\pi^-)p$ events of interest are outlined in this section.

The first step in identifying the reaction was to select all events with just two detected particles and an associated hit in the tagger. This was followed by a selection based on the charges of the detected particles. Only those events with one positive and one negative particle were retained for further analysis.

The next cut applied was to select events with a reconstructed vertex location which was consistent with particles being produced within the target. The event vertex was calculated during reconstruction from the kinematics of the particle trajectories by determining the closest approach of the particle tracks and setting the vertex as the mid-point between them. The distribution of reconstructed vertex positions from the event sample is shown in Fig. 6.1. A cut was applied on events having vertices in the range -39 cm < z < -1 cm (measured from the CLAS centre) which included the liquid deuterium target cell, centred at -20 cm, and excluded events originating from its windows.

At this stage the particle ID capabilities of CLAS are exploited to select the proton - π^- final state from other background final states containing two charged particles. Two independently measured quantities are used for mass identification: the particle momentum, p, and β, its velocity as a fraction of that of light. The particle's rest mass

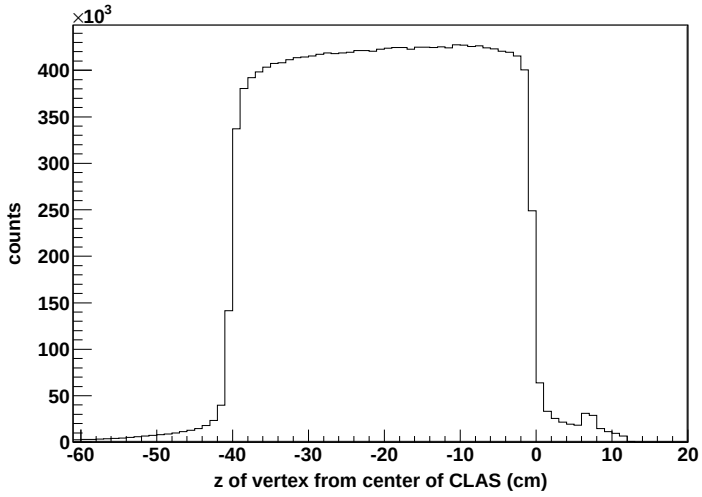

Figure 6.1: Z-position of the reconstructed event vertex showing the target cell and the aluminium exit window of the scattering chamber at $Z = 7$ cm.

can be calculated via:

$$m_c^2 = \frac{p^2(1-\beta^2)}{\beta^2} \tag{6.5}$$

The magnitude of momentum, determined from the curvature of the track in the magnetic field, was measured to an accuracy of $< 1\%$ in CLAS [104]. The recorded value of β has a larger uncertainty (up to $\sim 5\%$) as it incorporates the uncertainties in the time-of-flight and path length determination from tracking. The momentum - β distributions of all positive and negative particles are shown in Fig. 6.2. The plots highlight the excellent separation of the proton and pion events. The calculated loci for proton and pions are shown by the green and red lines overlaid on the plots. The fan-like shadows occuring above and below the main band are due to events where the time-of-flight was incorrectly calculated as a consequence of the reaction being attributed to the wrong beam bucket. This small fraction of events was rejected in the following cut.

An initial selection of protons and pions was performed using a momentum-dependent β cut. This was achieved by plotting the difference between the particle's measured, β_{meas}, and calculated, β_{calc}, velocity based on its measured momentum and an

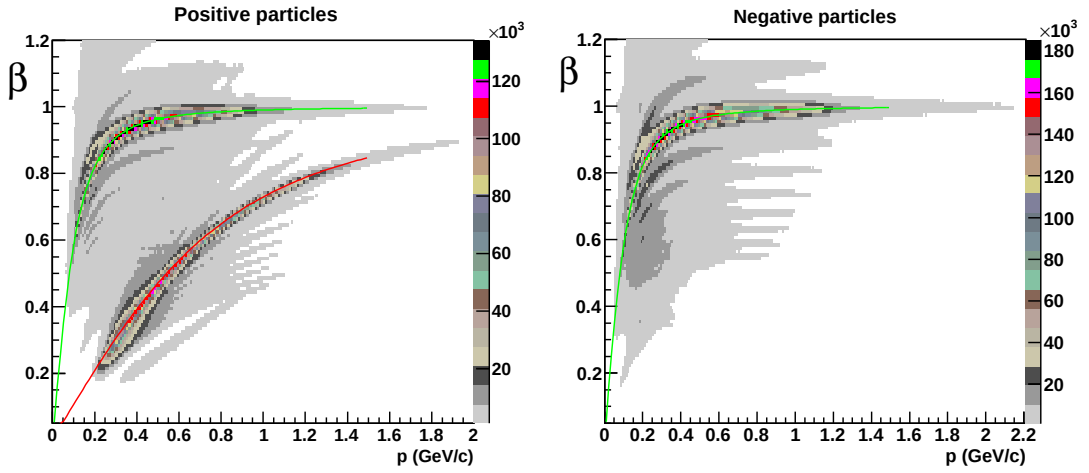

Figure 6.2: Measured β versus momentum for all positive (left) and negative (right) particles in two-particle events. The green line traces the kinematic relation for charged pions, red line that for protons.

assumption about its mass, m:

$$\Delta\beta = \beta_{meas} - \beta_{calc} = \beta_{meas} - \sqrt{\frac{p^2}{m^2 + p^2}} \tag{6.6}$$

The resulting distributions of $\Delta\beta$ versus momentum are presented in Fig. 6.3, where the left (right) plot shows the calculation of $\Delta\beta$ assuming a π^- (proton) mass in Eq. 6.6. The 2-D distributions were split into a series of 1-D projections along the momentum axis in bins of 50 MeV/c. The peaks around $\Delta\beta = 0$ correspond to the particles of interest and were fitted with a Gaussian function (Fig. 6.4). The parameters extracted from the fitted Gaussian were used to apply a cut, for each momentum bin, discarding all events outside 3σ from the mean $\Delta\beta$, where σ is the width of the fitted Gaussian.

For event-by-event data analysis, the momentum dependence of $\Delta\beta$ was parametrised by fitting an eighth-order polynomial to the extracted positions of the 3σ edges. An example for the case of pion selection is shown in Fig. 6.5.

Once the 3σ boundaries had been established, the $\Delta\beta$ cut was applied to the event sample. The effect of the cut can be observed in Fig. 6.6, where the invariant mass squared of the positively and negatively charged particles is compared with and without application of the $\Delta\beta$ cut. A comparison of the distributions of β_{meas} versus momentum

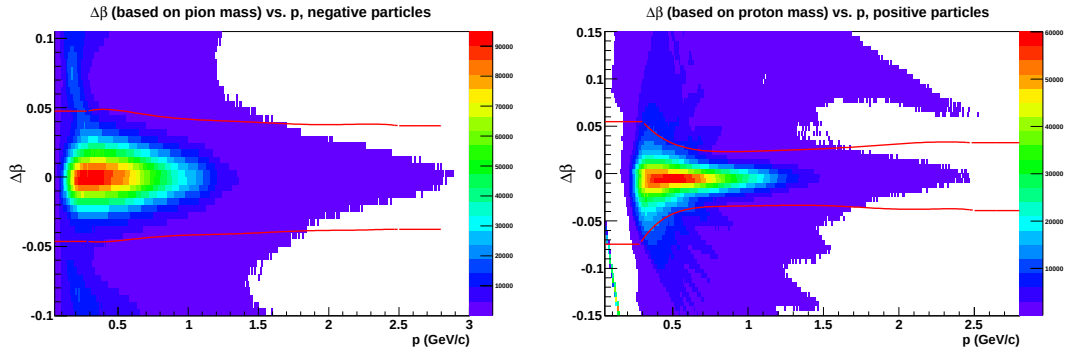

Figure 6.3: Distribution of $\beta_{meas} - \beta_{calc}$, where β_{calc} is calculated based on the particle's assumed mass (left: pion, right: proton). The eventual data cut is shown by red lines.

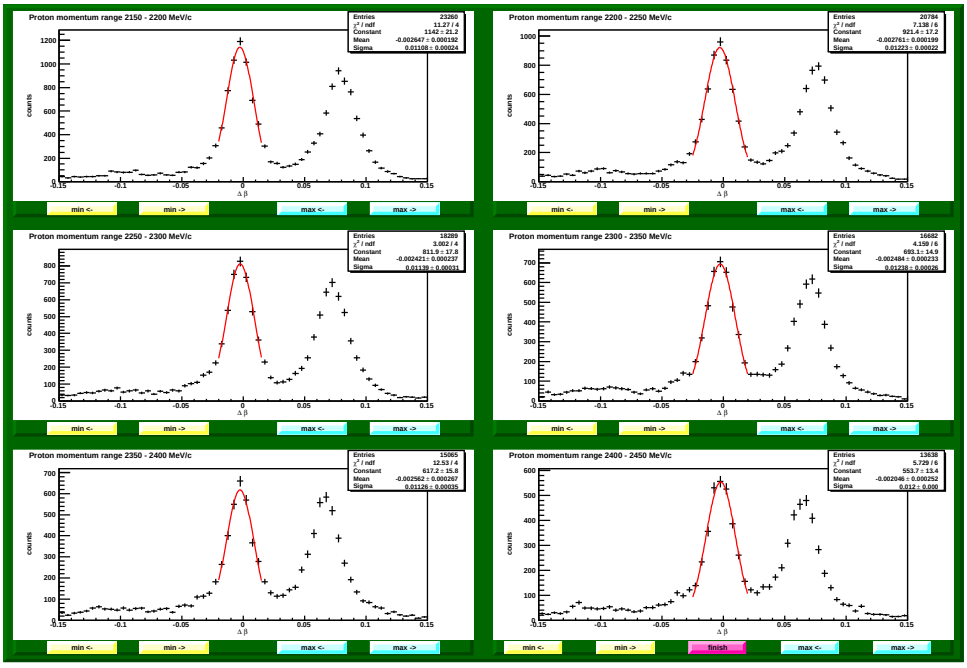

Figure 6.4: Projections of $\Delta\beta$ vs momentum, showing the $\Delta\beta$ peak for the proton in a range of momentum bins, as indicated in the histogram titles. A second peak on the right, due to π^+, can be observed.

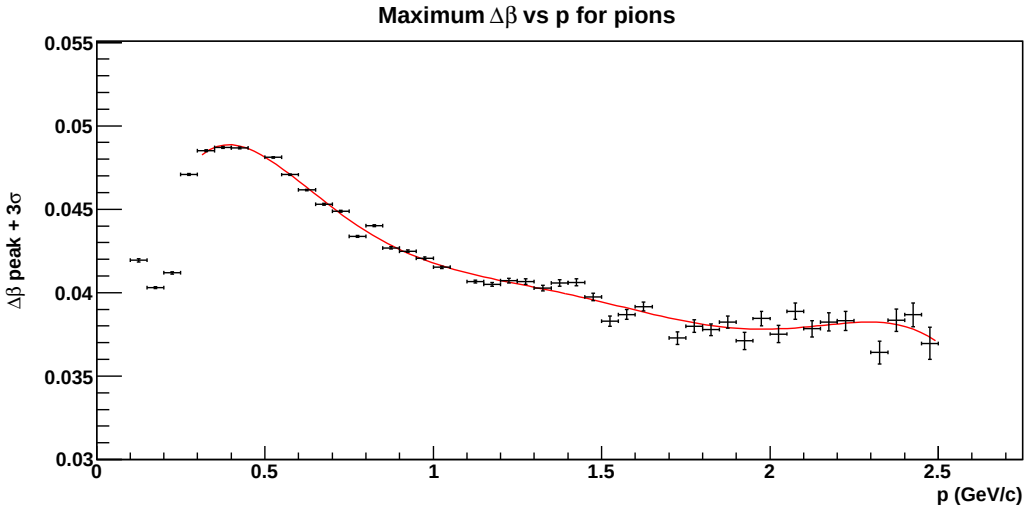

Figure 6.5: Edge of $\Delta\beta$ cut used to select π^- events, showing in red an eighth-order polynomial fit.

before and after the cut in Figs. 6.2 and 6.7 shows clean selection of the proton and π^- bands.

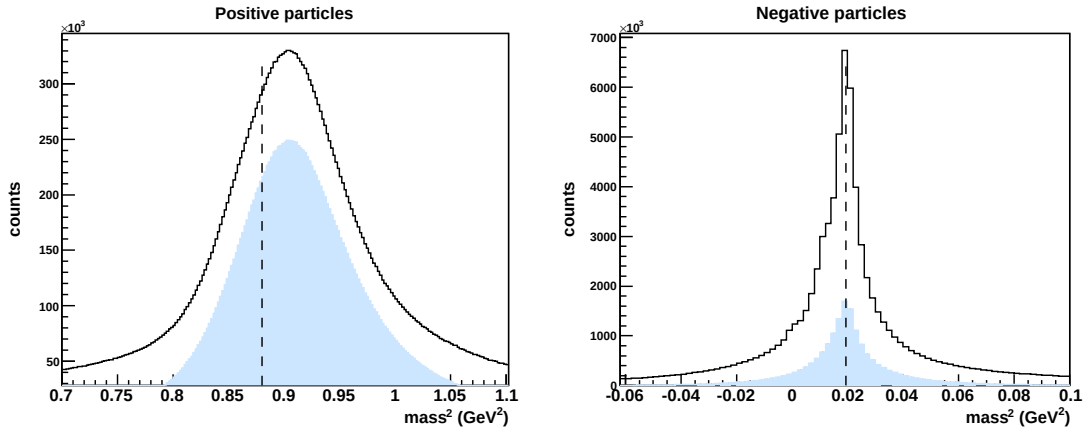

Figure 6.6: Mass squared as measured for positive and negative particles showing data remaining after the $\Delta\beta$ cuts shaded in blue. Dashed lines indicate the mass squared values for protons and pions respectively. The small offset of the invariant proton mass peak from its true position is due to larger momentum losses in the drift chambers for particles of higher invariant mass.

At the completion of initial particle identification, the four-momenta of the π^- and

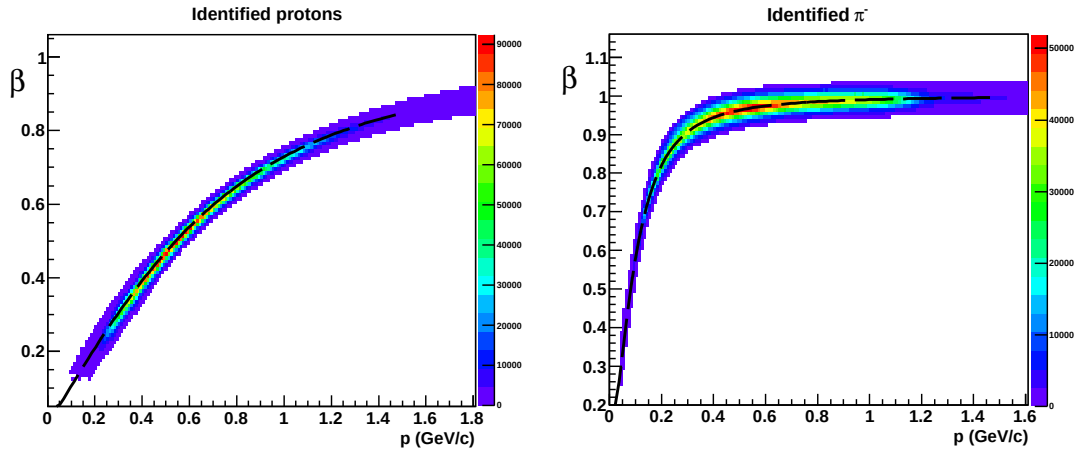

Figure 6.7: β (as measured) vs momentum plots for the identified protons and π^- after a $\Delta\beta$ cut. Dashed black lines trace the theoretical curve for both types of particle.

proton were constructed from a calculation of the particle's energy, E, based on its known invariant mass, m:

$$E^2 = m^2 + p^2 \tag{6.7}$$

6.4 Fiducial Cuts — excluding regions of limited acceptance

At this stage of analysis, the final state $p\pi^-$ events had been identified. To ensure accurate four-momentum determination, our sample of events was further refined by removing those in which either of the final state products were observed close to the inactive regions of CLAS — namely those surrounding the coils of the torus magnet. Although the coils themselves will block particles whose trajectories they intersect, the magnetic field in the regions immediately surrounding the coils changes rapidly with position and therefore cannot be mapped very accurately. Events in those regions have a larger systematic uncertainty in their trajectory, and therefore momentum, and it is common practice to discard them. The remaining regions of good acceptance are refered to as "fiducial regions".

Figs. 6.8 and 6.9 show the angular distributions of the yield of proton and pion hits for a selection of bins in particle momentum. The six active sectors of CLAS are clearly evident as regions with a high yield of particles, while the coils of the torus magnet result in the strips of low statistics centred at ϕ = 150°, 90°, 30°, −30°, −90° and −150°. The effects of the reaction kinematics are clearly evident in the event distributions, with high momentum particles observed predominantly at forward polar angles.

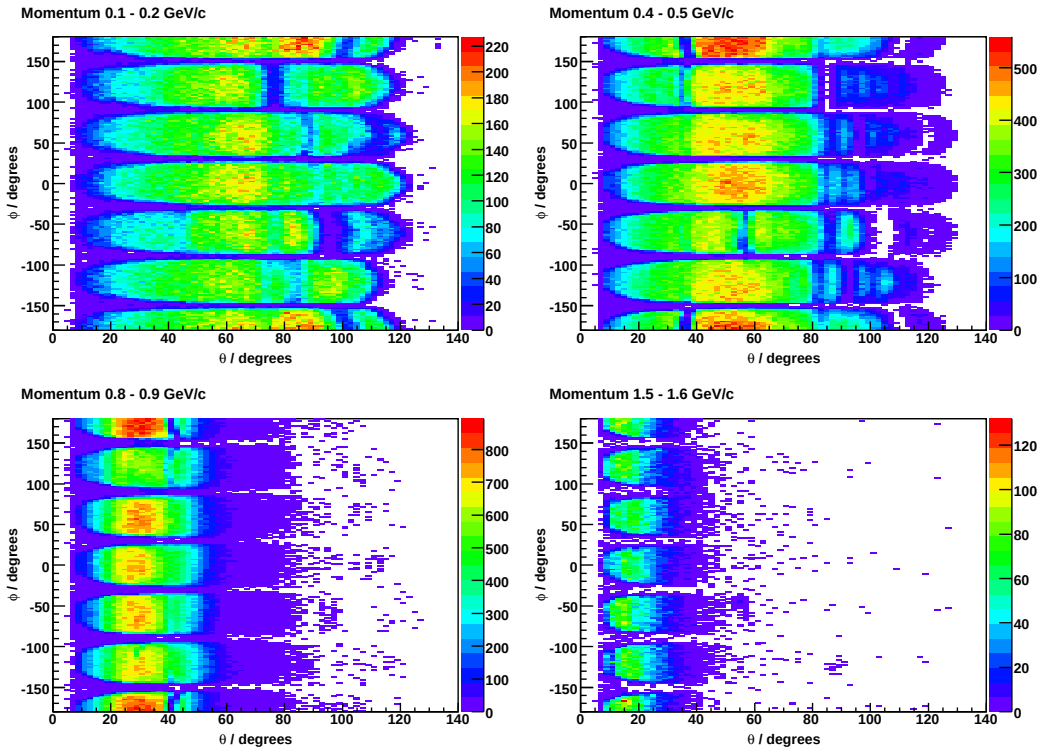

Figure 6.8: Angular distributions of π^- showing the sectors of CLAS and statistics depleted torus magnet regions, for a selection of four momentum regions 100 MeV wide.

To select the fiducial regions, the ϕ-distributions were summed over all detected particle momenta and split into 10° bins of θ in the range $7° < \theta < 130°$ for pions and $12° < \theta < 130°$ for protons. The difference in the lower θ limit was due to the fact that pions were observed at lower θ values than protons, as a consequence of typically having higher momenta. The resulting ϕ distributions (Fig. 6.10) clearly show a fall-off in the yield of events as the ϕ angles approach a torus coil. These edge regions are

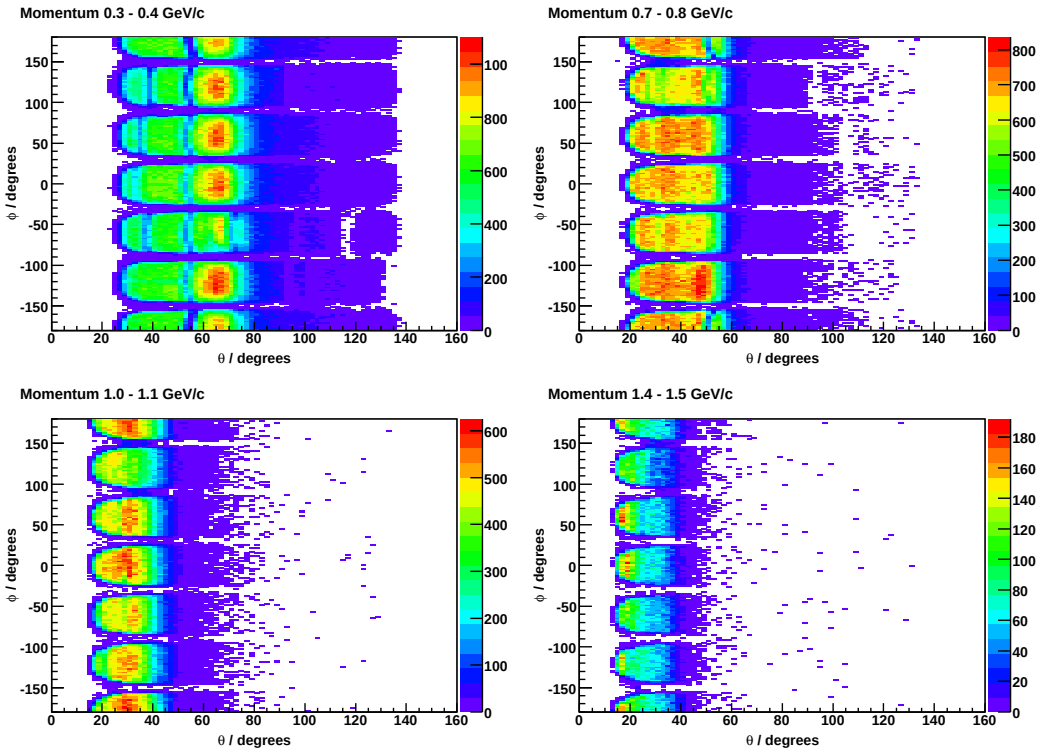

Figure 6.9: Angular distributions of protons showing the sectors of CLAS and statistics depleted torus magnet regions, for a selection of four momentum regions 100 MeV wide.

fitted with half-Gaussians and the extracted parameters of the Gaussian fit were used to define an angle dependent cut to select events from fiducial regions away from the coils. The θ dependence was fitted with a sixth degree polynomial, as illustrated in Fig. 6.11 where one edge of the fiducial region defined from the fitted half-Gaussian peak + 2σ is shown. The parameters of the fit defined the fiducial region for that edge of the sector. The procedure was repeated for the other edge of the sector and for the remaining sectors of CLAS. Separate parametrisations of the fiducial region for protons and pions were obtained because of the different behaviour of the particles near the coils.

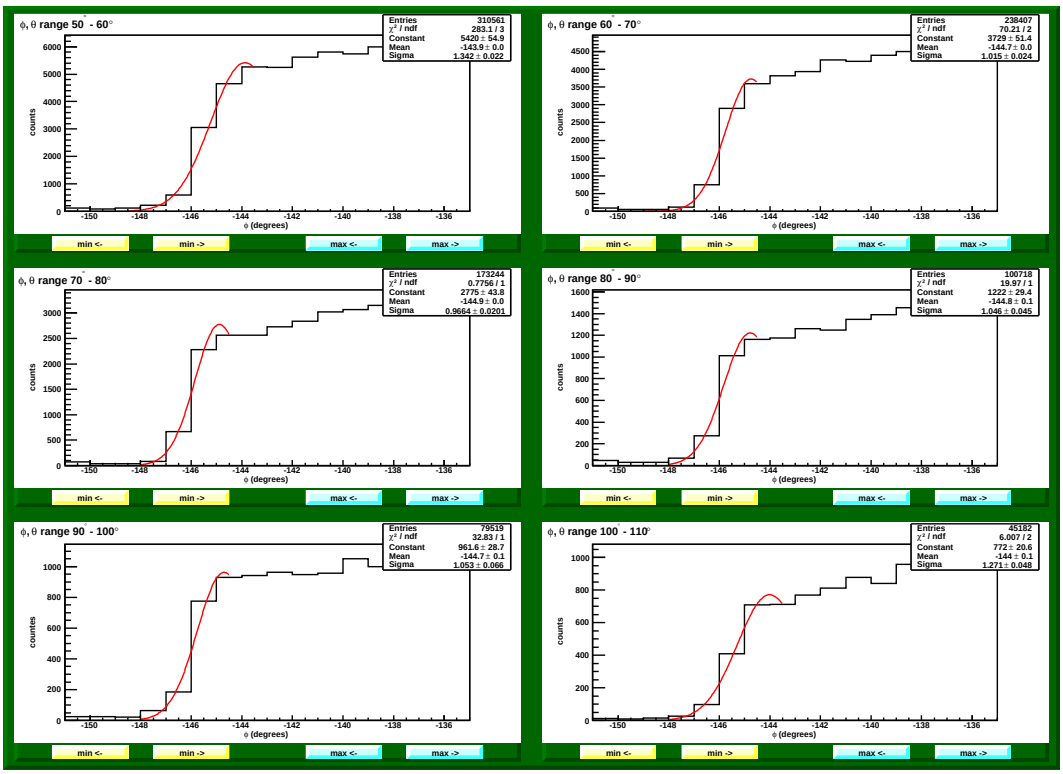

Figure 6.10: An example of half-Gaussian fits to the π^- ϕ-distributions at the edge of a sector, for a range of θ bins.

The fiducial regions may be expected to show some variation with the momentum of the detected particles. High-momentum particles, whose trajectory is less likely to be deviated by variations in the magnetic field near the coils, yield the narrowest fiducial regions — and a more geometrically accurate picture of the detector. The

effect was investigated in a comparison of the fits produced for pions of all momenta and those in a low- and a high-momentum sample (100 – 200 MeV/c and 1500 – 1600 MeV/c respectively). As can be seen in Fig. 6.11, the location of the fiducial region edges does not have a strong dependence on particle momentum and typically variations were on the order of one degree. Due to the lack of statistics to accurately define the edge of the fiducial regions for high momentum particles it was decided to base fiducial cuts on particle distributions of all momenta and widen the 2σ cut by 1° at each sector edge, which had a small effect on statistics while minimising possible systematic effects from the coils.

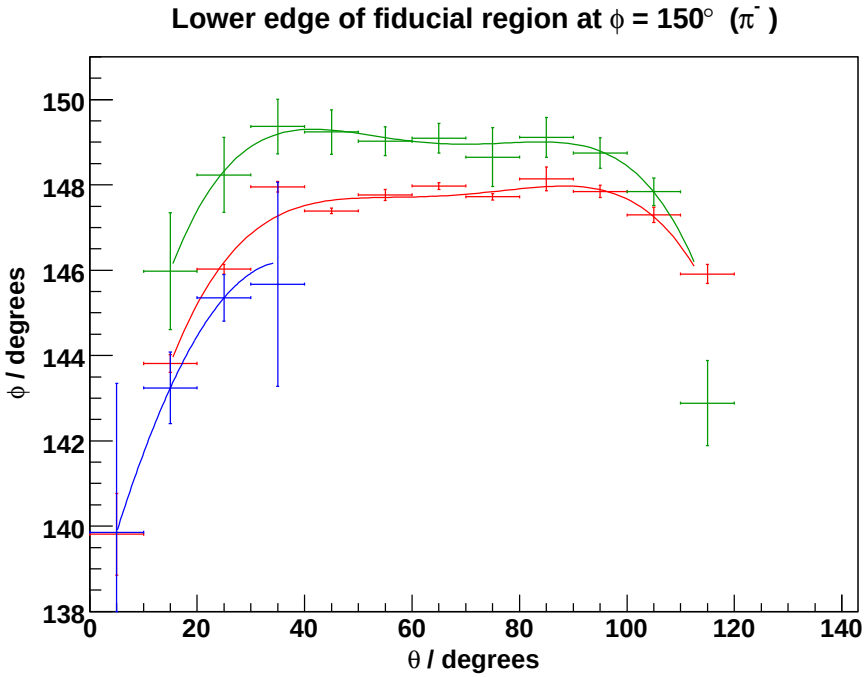

Figure 6.11: An example of fits to one sector edge (peak - 2σ) for π^- particles of low momentum (100 – 200 MeV, points and fit in green), high momentum (1500 – 1600 MeV, points and fit in blue) and all momenta (points and fit in red).

A cut on minimum and maximum θ was also applied, determined from half-Gaussian fits to the θ-distributions in each sector.

All events in which either of the two final state particles fell outside the fiducial regions were discarded (Fig. 6.12).

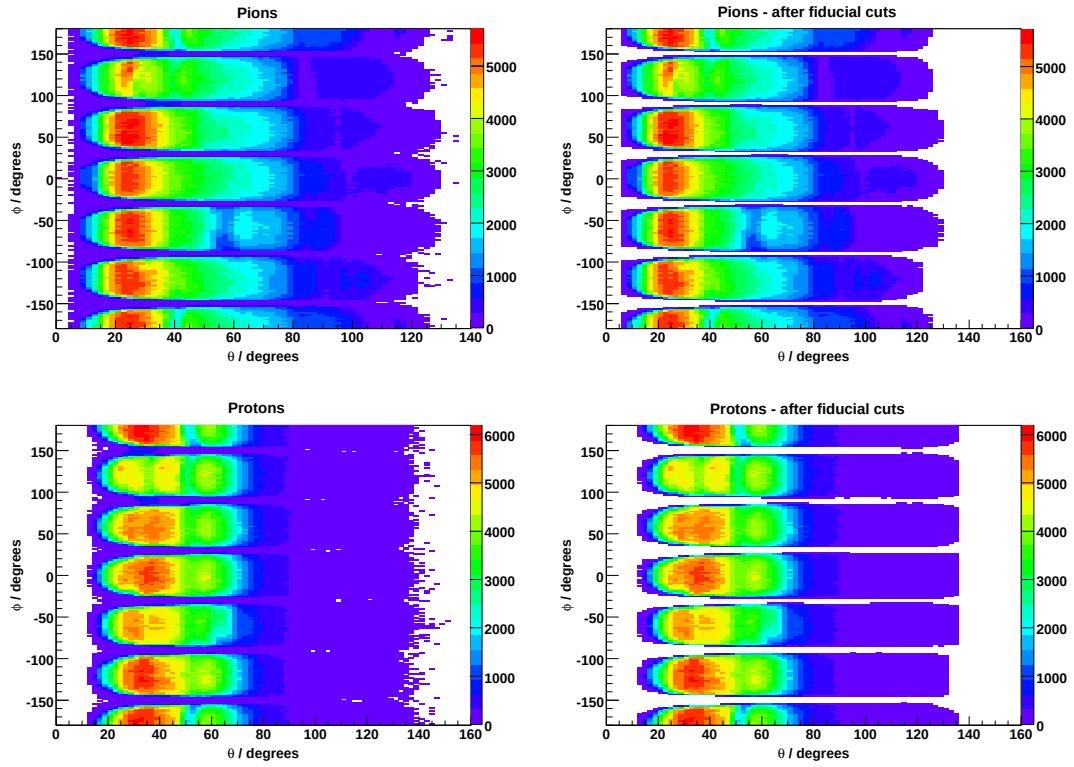

Figure 6.12: Angular distributions for π^- (top) and protons (bottom), summed over all momenta, before and after fiducial cuts have been applied.

6.5 Energy loss corrections

Between the event vertex and the drift chamber the particles passed through a significant amount of material such as the deuterium target, the target cell walls, the 1.5 mm thick carbon fibre beam pipe and the 2.15 mm thick start counter scintillator paddles. These materials resulted in significant energy loss for the particles, which was calculated on an event by event basis. The measured four-momenta of the particles at the inner surface of the drift chamber were used to track the particle back to the reaction vertex, calculating the energy loss in all of the materials on the particle trajectory. The four-momentum of the particle was then corrected by this energy loss and used in subsequent analysis.

Corrections typically resulted in a 2 – 3 MeV adjustment for pions, while protons typically required a greater correction, of around 6 MeV. The distribution of the

calculated energy loss for protons and pions in the event sample is shown in Fig. 6.13.

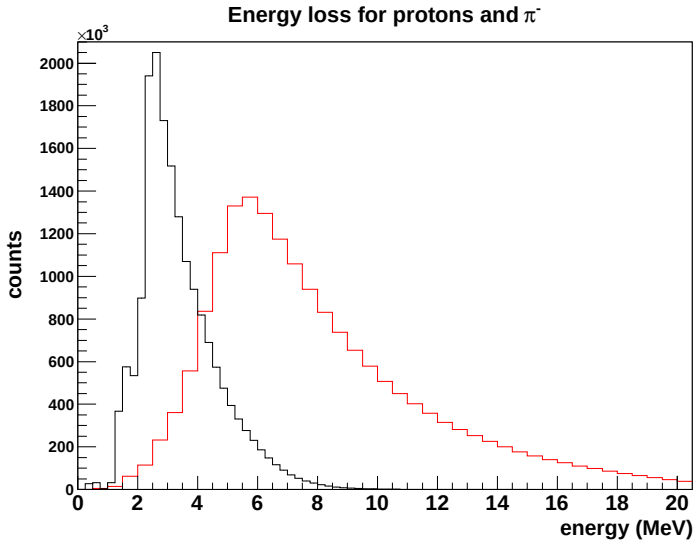

Figure 6.13: Energy loss undergone by protons (red) and π^- (black) on their trajectory through the target, start counter scintillators and beam pipe.

6.6 Identifying the incident photon

The photon tagger momentum analyses the recoiling electrons following bremsstrahlung of the electron beam incident on the diamond radiator. Therefore, in order to determine the photon which produced the photonuclear reaction observed in CLAS, the correct hit in the tagger focal plane had to be identified. For each trigger, typically around 13 associated electron hits in the tagger were recorded in the timing range 20 ns (Fig. 6.14).

Timing correlations between the calculated arrival time of the photon at the vertex, t_γ (from tagger timing and photon flight time to the vertex), and the vertex time of the reaction calculated using information from CLAS, t_v, was sufficient to identify the incident photon for each event. The CLAS event time was calculated from time-of-flight and tracking information and is given with respect to the common zero time for

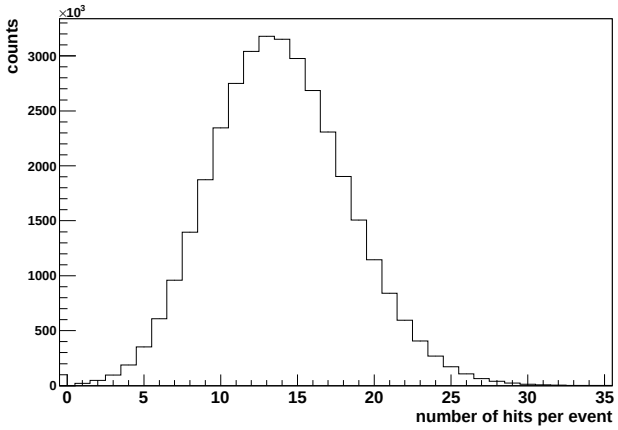

Figure 6.14: Multiplicity of bremsstrahlung-induced hits in the tagger.

the event (see Chapter 5, Section 2.3) as:

$$t_v = t_{sc} - \frac{d}{c\beta} \tag{6.8}$$

where t_{sc} is the time-of-flight, with respect to the global start time, as measured in the scintillation counters (SC), d is the length of track from the particle's vertex to the SC and β is, as usual, the particle's velocity as a fraction of c, the speed of light. To determine t_v we used the calculated value of β, based on the identified particle's known invariant mass and its measured momentum.

Typically, the pion event time is more accurate than that for protons, as the smaller momentum losses for pions throughout the detector result in a more accurate calculation of β and therefore time-of-flight.

The next step was to calculate the time of arrival at the event vertex of each "good" photon recorded for the event. A "good" photon is one whose associated T-counter hit has passed a set of consistency checks in the tagger, such as requirement of a coincident hit in the corresponding E-counters and depositing energy in a certain range, along with a PMT signal on both ends of the the E- and T-counters. This is designed to strongly reduce the background and random electron hits not associated with a bremsstrahlung event. The reconstructed time of photon arrival at the vertex, t_γ, for each hit in the tagger focal plane is then calculated from the timing of the hits in the T-counters. In

calculating the vertex time, account is taken of the (small) correction in the flight time due to variations in the position of the reaction vertex along the target cell:

$$t_\gamma \quad = \quad t_t + \frac{z + d_c}{c} \tag{6.9}$$

where t_t is the time of photon arrival at the centre of the target, z is the co-ordinate of the event vertex along the beam axis, measured from the usual origin of the centre of CLAS, and d_c is the offset, along the beam axis, of the target centre from the origin (-20 cm). The small (x, y) offsets of the event vertex due to the finite beam spot size ($\sim$ 2 cm) are neglected as they are comparable to the vertex resolution.

The coincidence time, Δt, between the reaction time calculated using information from CLAS and tagger information,

$$\Delta t \quad = \quad t_v - t_\gamma \tag{6.10}$$

is shown in Fig. 6.15, where the expected coincidence peak centred on $\Delta t = 0$ can be observed. The bunched nature of the beam is evident in the small neighbouring peaks at 2 ns intervals. These arise from photons originating from other beam bunches being recorded in the time-window opened by this event's trigger.

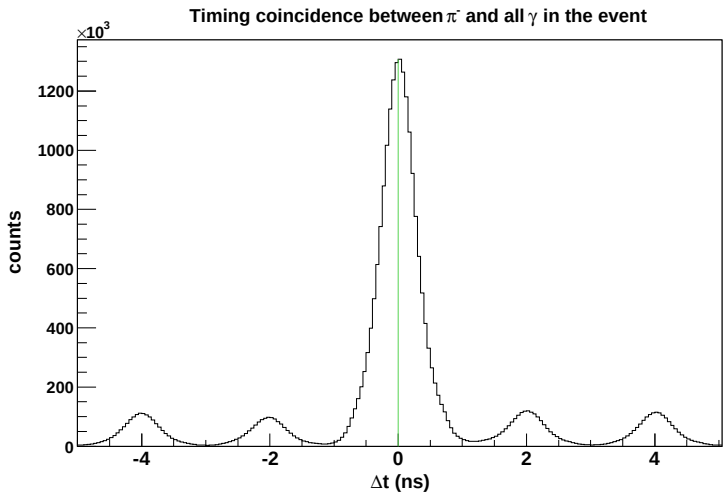

Figure 6.15: Timing coincidence between π^- and all the "good" γ in the event. Green line traces $\Delta t = 0$.

An initial selection is performed by choosing the photon with the smallest $|\Delta t|$, the result of which can be seen in Fig. 6.16 where no discernible contribution from nearby

buckets can be seen. This indicates a very high probability that one of the tagger hits was due to the photon which caused the reaction.

Application of an additional cut of $|\Delta t| < 1$ ns effectively eliminated most of the background. The background contribution under the peak was estimated from the distribution in Fig. 6.16 to be 0.08%.

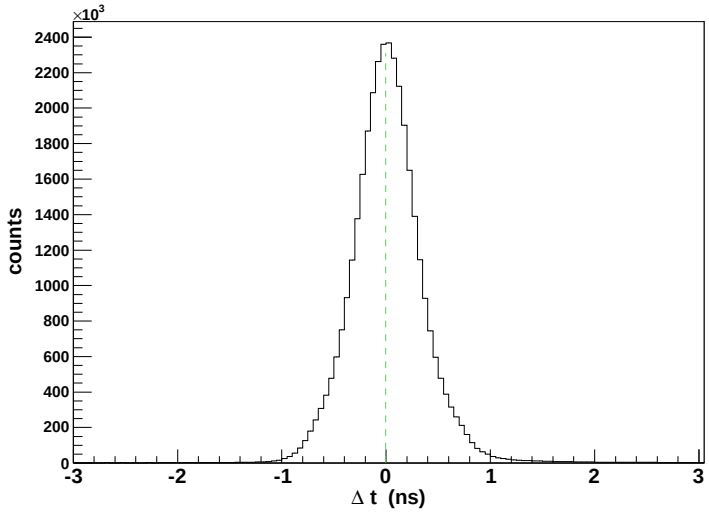

Figure 6.16: Timing coincidence between π^- and the γ in the event with the smallest $|\Delta t|$. Green line traces $\Delta t = 0$ for ease of comparison.

This background can be separated into two different contributions. The first of these is focal plane hits correlated with a photon which did not produce the reaction in CLAS but by chance arrived in the same narrow time window defined by the central beam bucket and with a smaller Δt than the real photon. Such events could be removed, by requiring only a single photon hit associated with the central beam bucket.

The second contribution to the background is due to accidental photons which were there when the real photon was not recorded. Although this contamination cannot be eliminated, an estimation of its degree can certainly be made, as outlined below.

Applying a cut on only one photon being registered per event in the central beam bucket, the distribution in it can be split up thus:

$$N_0 = \epsilon N + (1 - \epsilon)R \tag{6.11}$$

where N_0 is the total number of photons within ±1 ns in the beam bucket centred on $\Delta t = 0$, which incorporates all the "good" photons detected in that range (efficiency ϵ times the total number of events, N), plus the accidental photons, R, in events where no "good" photon was detected in the beam bucket, but a single accidental was. R can be estimated from a beam bucket with accidental photons where a cut on a single photon per bucket was imposed. The ratio $\frac{R}{N}$ was thus estimated to be 10% for all events in the tagger, however, after all data selection cuts have been applied in the reconstruction of the reaction, the ratio falls to 0.1%. Since the efficiency of the tagger is estimated to be very high [110] the background due to this contribution could be considered negligible. The photon responsible for the reaction could therefore be identified uniquely. The photon energy was then read from associated tagger information and stored with the event.

6.7 Identifying quasi-free events

Our interest is in photoproduction from a free neutron — it is only through the lack of a neutron target that we resort to the use of deuterium. We can, however, select kinematic regions to emphasize quasi-free reactions, where the proton in the deuterium nucleus, p_s, is a spectator to the reaction on the neutron. For such a process the spectator proton will simply recoil with the Fermi momentum it had in the initial state, i.e. momentum compatible with the deuteron wavefunction:

$$\gamma + d \quad \rightarrow \quad p_s + p + \pi^- \tag{6.12}$$

The tagger and CLAS enable the energies of the incoming photon and the final state proton and pion to be determined. This allows the entire final state, including the undetected proton, to be reconstructed. The reconstruction of the undetected proton is carried out on the basis of the "missing" four-momentum, which is constructed from the detected particles and the deuteron nucleus:

$$p_{missing} \quad = \quad p_\gamma + p_d - p_p - p_{\pi^-} \tag{6.13}$$

where $p = [E, p_x, p_y, p_z]$ according to convention.

Assuming that the trajectory of the photon is along the z-axis, Eq. 6.13 can be expanded as[1]:

$$[E,\vec{P}]_m \quad = \quad [E,0,0,E]_\gamma + [m,\vec{0}]_d - [E,\vec{P}]_p - [E,\vec{P}]_{\pi^-} \tag{6.14}$$

The invariant mass of the recoiling system was then calculated from the "missing" momentum and energy. As can be seen in Fig. 6.17, its distribution shows a peak at the mass of the proton, corresponding to the spectator reaction of interest. A shoulder is also observed in the distribution starting near the sum of the mass of a proton and a pion. These events are attributable to multi-meson production channels such as $\gamma + p \rightarrow p + \pi^- + \pi^0$. We applied a cut on the proton rest mass ± 0.1 GeV to select those events where the undetected state consisted only of the recoiling proton.

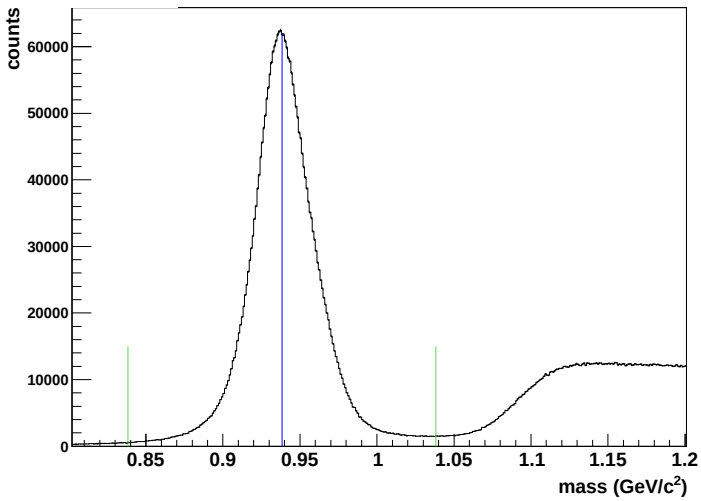

Figure 6.17: "Missing" mass distribution showing the cut position in green lines. Blue line indicates proton mass.

Fermi motion inside the deuteron nucleus results in most probable nucleon momenta of ~ 50 MeV/c, with a tail extending above 150 MeV/c [127]. These general features are what we observe for the momentum distribution of the recoil proton, consistent with what would be expected from the quasi-free spectator reaction (Fig. 6.18).

[1] It is assumed that the deuteron is, to all effects and purposes, stationary, as any momentum it may have due to thermal motion will be on a keV scale, orders of magnitude down from the energy scale of the reaction.

At high momentum, the relative contribution of final state interaction processes, which can result in more momentum being given to the recoiling nucleon, is expected to be bigger. We therefore remove events having a missing momentum above 120 MeV/c. The effects of final state interactions on the asymmetry are expected to be small for this low momentum as indicated by the close correspondence of the asymmetries for pion photoproduction off the free proton and a proton bound in deuterium [128].

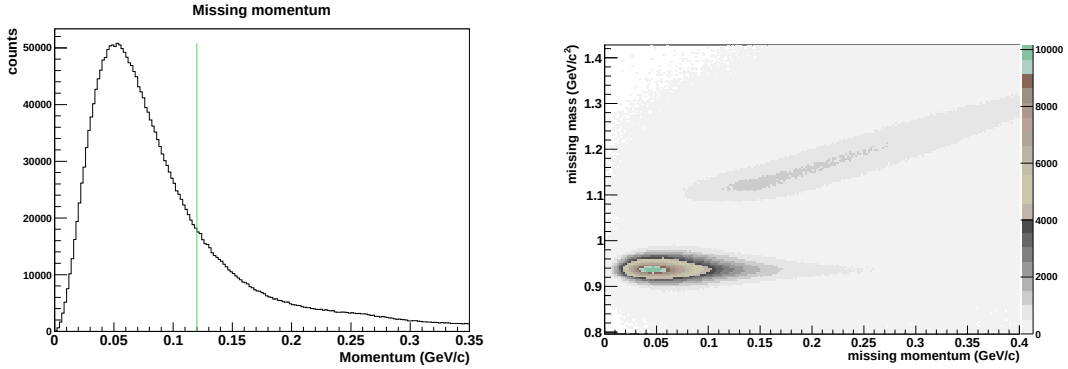

Figure 6.18: "Missing" momentum of the proton, showing, in green, the position of the cut at 120 MeV.

Fig. 6.19 shows "missing" momentum versus the polar angle, θ, of its direction. The distribution of "missing" momenta is similar below the cut at all angles. This is as expected from a true spectator process. Above $\sim$ 250 MeV/c, however, the distribution becomes clearly forward peaked.

An additional refinement of our event sample is based on a check of coplanarity of the proton and pion in the plane perpendicular to the beam. At very low spectator momenta their direction vectors should have a ϕ-difference of 180°, as would be expected from the reaction kinematics from a stationary neutron. As the spectator momentum increased, $\Delta\phi$ will become smeared in the laboratory frame. This is indeed what we observe, as can be seen in Fig. 6.20. The distribution was sliced into bins in spectator momentum, projected and fitted with half-Gaussians at each edge of the $\Delta\phi$ distribution. A cut was then applied at the peak + (-) 3σ at the high (low) edge of the $\Delta\phi$ distribution. This was done to eliminate some of the accidental background, where the proton and pion did not originate in the same event, and also remove any events where

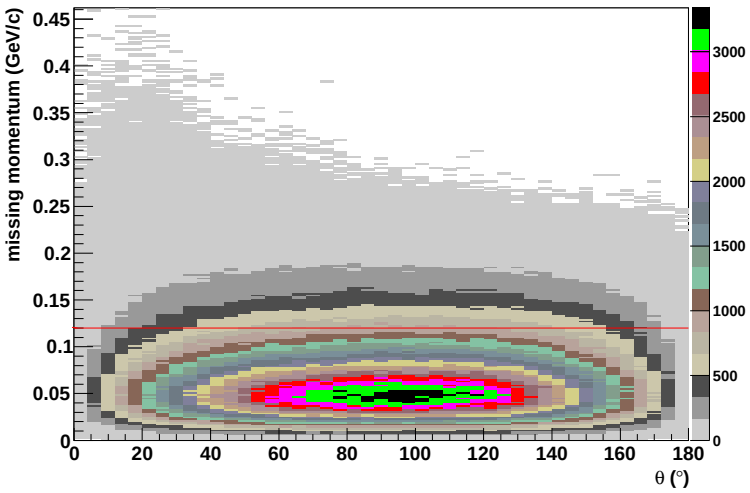

Figure 6.19: "Missing" momentum of the proton vs. polar angle θ in the laboratory frame. The red line indicated the position of the cut.

final state interactions led to a large angular deviation on the trajectory of one of the particles.

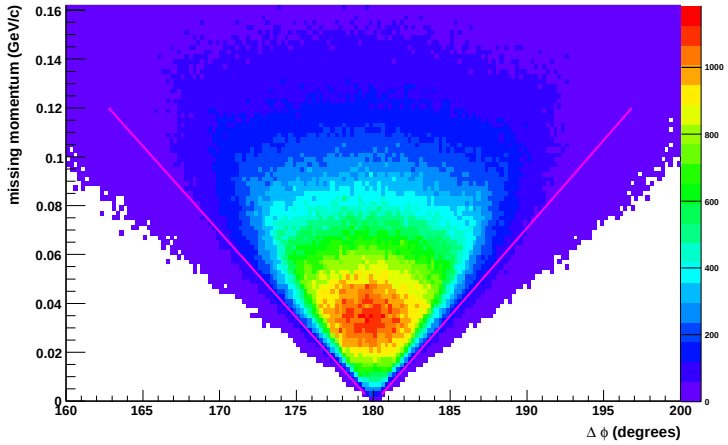

Figure 6.20: "Missing" momentum of the proton vs. $\Delta\phi$, the difference in azimuthal angles of the proton and π^- in the laboratory frame. A spectator momentum - dependent cut is shown with pink lines.

The next stage of analysis was to reconstruct the momentum of the neutron in the

initial state. This was done by assigning it a negative "missing" momentum. This follows from consideration of momentum conservation as the proton and neutron in the initial state deuteron will have equal and opposite momenta. The neutron's energy was calculated based on its momentum and known invariant mass using Eq. 6.7.

A check of any systematic errors in the reconstruction of our reaction was made by a comparison of the total energies from the initial and final states:

$$\Delta E \quad = \quad E_\gamma + E_n - E_p - E_{\pi^-} \tag{6.15}$$

which is shown, after all cuts, in Fig. 6.21. The peak is close to zero, showing that any systematic uncertainties in the reconstruction are very small.

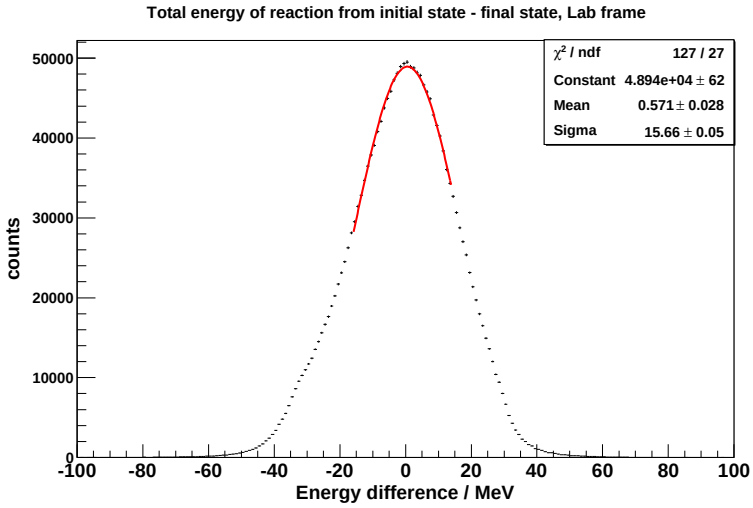

Figure 6.21: Difference between the total energy of the reaction calculated using the initial and final state.

The final cut to the data was a further refinement in the selection of the spectator proton based on its mass, which was possible once the initial state of the reaction, γn, was fully reconstructed. This was done by transforming both final state particles into the centre of momentum (CM) frame of the initial state, the photon and reconstructed neutron. The missing mass of the reconstructed proton was plotted against the 3-D opening angle, α, between the two final state particles in this frame, which should be back-to-back. The distribution of α is shown in Fig. 6.22, peaking, as expected, at 180°. The final cut on the event sample was to restrict this angle to $180 \pm 2°$.

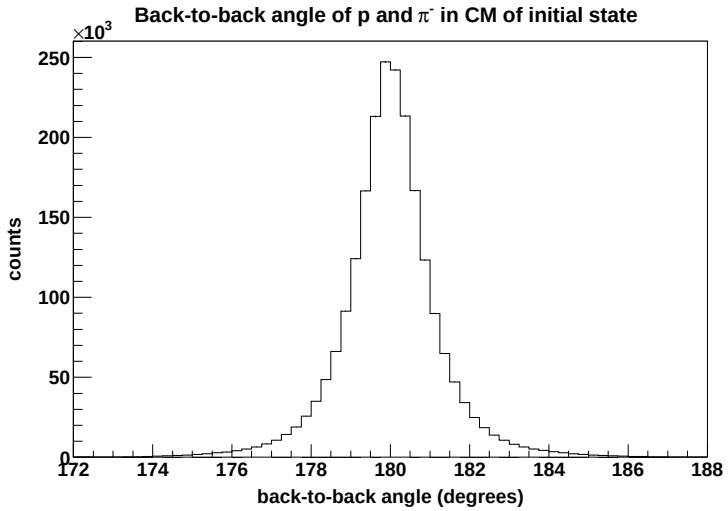

Figure 6.22: Back-to-back angle of proton and π^- direction vectors in CM frame of the initial state.

The final quality of the event sample can be assesed in Fig. 6.23, where the reconstructed invariant mass of the spectator proton is presented for different cuts. It is clear that there is negligible contribution from other background reactions, such as multiple meson production, in the final event sample.

6.8 Measurements for the extraction of Σ

The final stage of data treatment was to extract the quantities of importance for the measurement of beam asymmetry. These include photon energy, invariant mass of the reaction, π^- production angle θ, and the angle ϕ the polarisation vector makes to the reaction plane in the centre of mass frame.

The invariant mass of the system was calculated based on the final state, which removes any momentum smearing and allows a fine binning of the results in energy as it does not have the discreteness of the tagger energy channels. The pion four-momentum in this final-state CM frame, p', is then calculated via the standard Lorentz transformation:

$$p' = \Lambda p \tag{6.16}$$

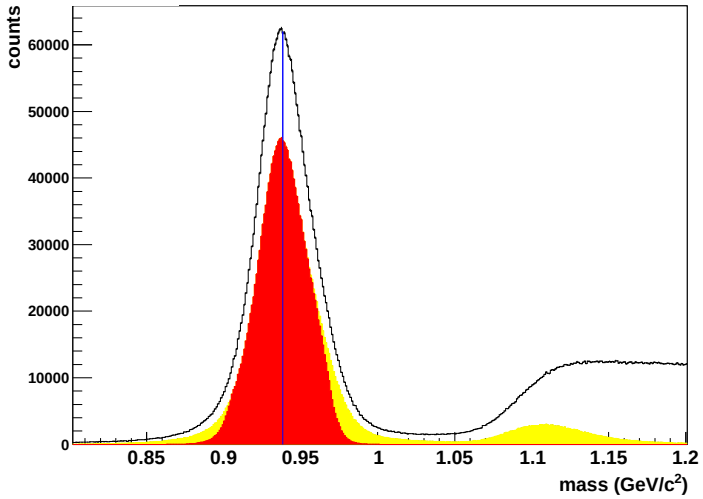

Figure 6.23: "Missing" mass distribution, showing the effect of the event selection cuts. The black outline is the distribution before any cuts were applied, yellow the distribution after the missing momentum and coplanarity cut, red the final distribution after an additional α cut.

where p is the original four-momentum in the lab frame and Λ is the general Lorentz transformation matrix:

$$\Lambda = \begin{pmatrix} -\beta_x\gamma & \frac{1+\gamma'\beta_x^2}{\beta^2} & \frac{\gamma'\beta_x\beta_y}{\beta^2} & \frac{\gamma'\beta_x\beta_z}{\beta^2} \\ -\beta_y\gamma & \frac{\gamma'\beta_y\beta_x}{\beta^2} & \frac{1+\gamma'\beta_y^2}{\beta^2} & \frac{\gamma'\beta_y\beta_z}{\beta^2} \\ -\beta_z\gamma & \frac{\gamma'\beta_z\beta_x}{\beta^2} & \frac{\gamma'\beta_z\beta_y}{\beta^2} & \frac{1+\gamma'\beta_z^2}{\beta^2} \\ \gamma & -\beta_x\gamma & -\beta_y\gamma & -\beta_z\gamma \end{pmatrix} \tag{6.17}$$

with

$$\vec{\beta} = \frac{\vec{p}\,c}{E}, \quad \beta = |\vec{\beta}|, \quad \gamma = \frac{1}{\sqrt{1-\beta^2}} \quad and \quad \gamma' = \gamma - 1 \tag{6.18}$$

The electric field vector (E-vector) of the photon in the CM frame can be determined by a Lorentz transformation of the photon's electromagnetic field tensor, $\mathcal{F}$:

$$\mathcal{F} = \begin{pmatrix} \frac{-E_x}{c} & 0 & B_z & -B_y \\ \frac{-E_y}{c} & -B_z & 0 & B_x \\ \frac{-E_z}{c} & B_y & -B_x & 0 \\ 0 & \frac{E_x}{c} & \frac{E_y}{c} & \frac{E_z}{c} \end{pmatrix} \tag{6.19}$$

(where E_x, E_y and E_z are the components of the electric field vector and B_x, B_y, B_z similarly of the magnetic field vector) as

$$\mathcal{F}' = \Lambda\mathcal{F}\tilde{\Lambda}. \tag{6.20}$$

Chapter 7

Data Analysis II: Beam Asymmetry Extraction

The beam asymmetry, Σ, was extracted from the differential cross-section of pion production with linearly polarised photons. In the single-polarisation case, where only the photon beam is polarised, Eq. (1.20) reduces to:

$$\frac{d\sigma}{d\Omega} = \left.\frac{d\sigma}{d\Omega}\right|_0 \left(1 - P\,\Sigma\, cos(2\phi)\right) \tag{7.1}$$

where P is the degree of linear photon polarisation and ϕ is the azimuthal angle between the photon polarisation E-vector and the reaction plane, in the centre of mass frame of the meson and nucleon (see Appendix A for details of the reaction axes). This chapter presents the methods used in the extraction of Σ from the experimental data.

7.1 Choice of bin size

The beam asymmetry is a function of both the invariant mass of the reaction, W, and the cosine of the scattering angle, θ. The data were therefore binned as finely as the resolution and statistics would allow in both variables. The bin width chosen for the invariant mass was 10 MeV, which is comparable to the attained resolution in the measurement of W.

The choice of bin width in $\cos\theta$ was motivated by the available statistics once the dataset had been divided into 10 MeV wide bins in W. It was found that 0.1

wide bins in $\cos\theta$ provided a good compromise between high enough statistics in the ϕ distribution to allow a high quality fit and a fine resolution sampling of the pion production angle.

7.2 Photon polarisation

During the experiment, the photon polarisation was rotated between two orthogonal orientations, parallel to the lab floor (refered to as PARA) and perpendicular to it (PERP). This was achieved by accurate changes in the orientation of the diamond radiator using a goniometer (see Chapter 4, Section 3.2). Additionally, one tenth of the data was taken using carbon as an "amorphous" radiator, which provided unpolarised photons. An example of the yield of photons as a function of photon energy in both unpolarised and polarised running conditions is shown in Figs. 7.1 and 7.2. The unpolarised distribution has the $\frac{1}{E_\gamma}$ energy dependence expected from the incoherent bremsstrahlung process. The spectrum from the crystalline radiator shows enhancements in the regions corresponding to coherent brehmsstrahlung.

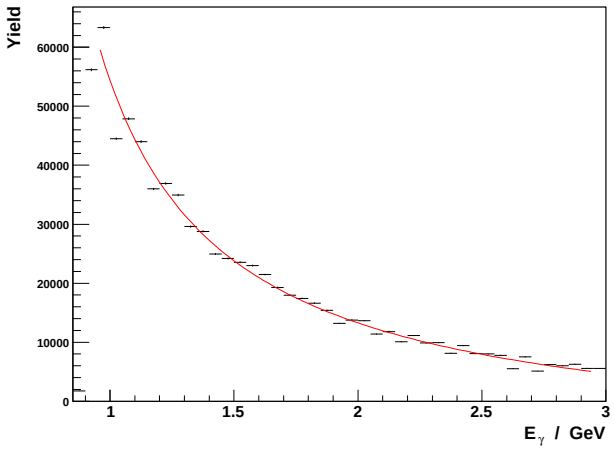

Figure 7.1: Energy distribution of photons which were produced in bremsstrahlung from an amorphous radiator, showing the expected $\frac{1}{E_\gamma}$ dependence (overlaid in red).

In order to extract the beam asymmetry from a fit to the ϕ distributions, a calculation of the degree of polarisation for all the photon energies near the coherent

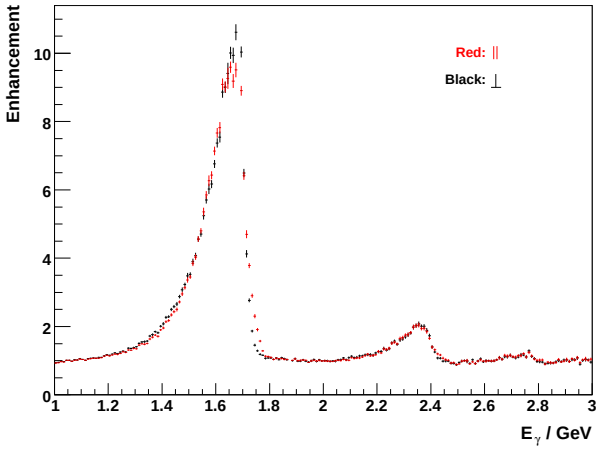

Figure 7.2: Enhancement plots showing the energy distribution from data using a diamond radiator oriented to produce a coherent peak at E_γ = 1.7 GeV, which was divided by the distribution of data obtained with an amorphous radiator to remove the unpolarised contribution. Secondary, smaller coherent peaks at higher energies are also evident from bremsstrahlung off other geometrically equivalent crystal planes in the radiator. The two photon polarisation orientations are shown in different colours and can be seen to agree well.

peak was required. The calculation was done by fitting the experimentally observed enhancement in the yield with the ANB (ANalytical coherent Bremsstrahlung) calculation [109], based upon the physics of the coherent scattering process but accounting also for the geometry of the radiator, collimator and electron beam parameters. The extracted parameters of the fit to the enhancement were used to calculate the corresponding degree of polarisation as a function of photon energy. The photon polarisation information was then written into reference tables. These polarisation tables are provided by collaborators [129] and at the time of writing the thesis have been obtained with a 10% systematic error[1] in the degree of polarisation.

The position of the coherent peak is very sensitive to small movements in the position of the electron beam during the run. The coherent peak position showed movement by up to 50 MeV, which of course affects the degree of polarisation for each of the photon energies. The edge position was monitored continuously at 2 s intervals during the run and the positions were read into the data stream. These shifts were accounted for

[1] In principle these systematics can be reduced to 5% at a later date.

in the calculation of the degree of polarisation for each bin in W and $\cos\theta$ as follows.

For each run period with a given electron beam energy a distribution of the measured coherent edge positions was extracted from the data. The data in the different polarisation tables for each coherent edge position were then weighted by the distribution of coherent edges, summed and their average found. This produced an average polarisation table associated with that run period. Next, the energy distribution of the photons which produced the events in each bin of W and $\cos\theta$ was determined. This was then used to calculate a weighted average degree of polarisation, P_{av}, for that bin:

$$P_{av} = \frac{1}{N_t} \sum_{i=Emin}^{Emax} N_i P_i \tag{7.2}$$

where $Emin$ and $Emax$ are the limits of the range of photon energies in the distribution in that bin, N_i are the number of events having a photon energy i, P_i is the degree of polarisation for a photon of energy i read from the appropriate table and $N_t = \sum_i N_i$ is the total number of events in that bin.

The distribution of photon energy for each bin in W is typically larger than the width of the bin in MeV. This is due to the Fermi motion of the target nucleon, which can be as large as 120 MeV/c with the applied cuts to the event sample. The corresponding variation in E_γ for $W = 1600$ GeV is 53 MeV. This rises to 138 MeV for $W = 2300$ MeV.

7.3 Removing acceptance effects

Fig. 7.3 shows the ϕ distribution of the yield for a single bin of $\cos\theta$. It is clear that acceptance issues dominate over any perceptible cosine modulation in these raw distributions, although clear differences are observed between the data with PARA and PERP polarisation. The six fiducial regions of CLAS are also clearly visible in the data.

Since acceptance effects are not polarisation-dependent, dividing the polarised PARA and PERP distributions by the amorphous data removes most of the acceptance effects. This is shown in Fig. 7.4, superimposed with an $a_0 + a_1 \cos\theta$ to highlight the cosine modulation. The expected $\pi/2$ shift of the distribution between PARA and PERP is clearly visible. This is by construction — the two polarisations, and therefore E-vector directions, were chosen to be perpendicular to each other.

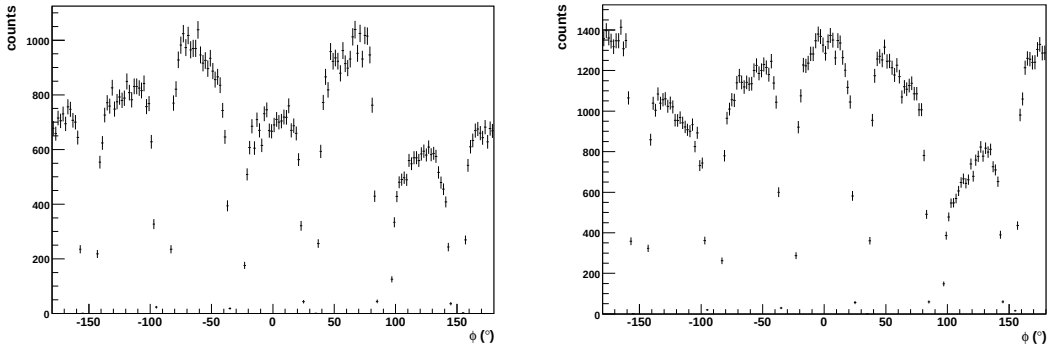

Figure 7.3: ϕ distributions in data taken with a parallel (left) and perpendicular (right) beam polarisation ($1735 < W < 1755$ MeV, $0.6 < \cos\theta < 0.8$), strongly dominated by the acceptance of CLAS. The non-fiducial regions due to the magnet coils are clearly seen as gaps in the distribution.

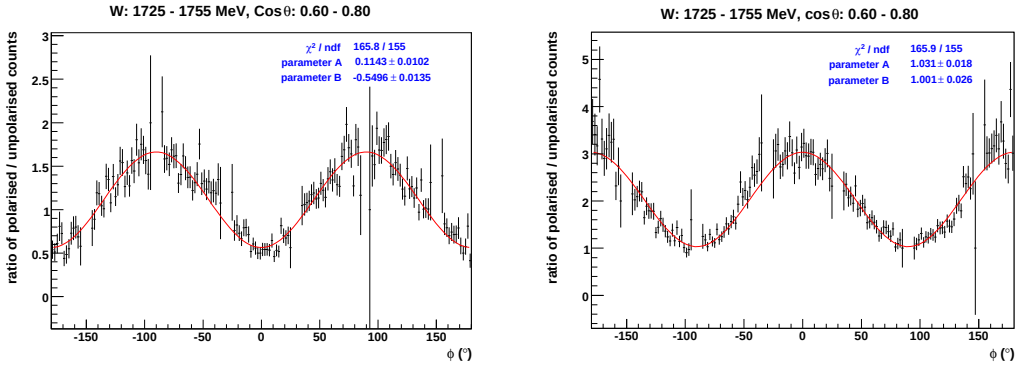

Figure 7.4: ϕ distributions in data taken with a parallel (left) and perpendicular (right) beam polarisation ($1735 < W < 1755$ MeV, $0.6 < \cos\theta < 0.8$), divided by the amorphous ϕ distribution and fitted with an $A + B\cos\theta$ function.

7.4 Σ extraction method

As can be seen from Fig. 7.4 it is in principle possible to extract the beam asymmetry from a fit to the ratio of polarised to unpolarised ϕ distributions. This method is not optimal, however, due to the poorer statistics of the amorphous dataset dominating the statistical uncertainty. A better method which makes use of only the polarised data to extract Σ from the cross-section ratios of PARA and PERP data is described below.

The separate normalised cross-sections for PARA and PERP are given by:

$$\begin{aligned} \sigma_\perp &= \sigma_0 \left(1 + P_\perp \Sigma \cos(2\phi)\right) \\ \sigma_\parallel &= \sigma_0 \left(1 + P_\parallel \Sigma \cos(2\phi + \pi)\right) \\ &= \sigma_0 \left(1 - P_\parallel \Sigma \cos(2\phi)\right). \end{aligned} \tag{7.3}$$

If the assumption is made that $P_\perp = P_\parallel$, the asymmetry of these cross-sections gives:

$$\frac{\sigma_\perp - \sigma_\parallel}{\sigma_\perp + \sigma_\parallel} = P \Sigma \cos(2\phi). \tag{7.4}$$

In the more general case, however, the polarisations $P_\perp$ and $P_\parallel$ are not necessarily equal. Further, the polarisation orientations may not be exactly parallel and perpendicular to the laboratory floor and could be rotated by an angle ϕ_0 with respect to the lab axes. This would introduce a phase shift into the cosine modulation of the cross-section.

Moreover, if the normalisation of the distributions has also not been perfectly performed before calculating the asymmetry then Eq. 7.4 would be generalised as:

$$\frac{\sigma_\perp - \sigma_\parallel}{\sigma_\perp + \sigma_\parallel} = \frac{(\frac{N_\perp}{N_\parallel} - 1) - (\frac{N_\perp}{N_\parallel} P_\perp + P_\parallel)\, \Sigma \cos\left(2(\phi - \phi_0)\right)}{(\frac{N_\perp}{N_\parallel} + 1) - (\frac{N_\perp}{N_\parallel} P_\perp - P_\parallel)\, \Sigma \cos\left(2(\phi - \phi_0)\right)} \tag{7.5}$$

where $N_\perp$ and $N_\parallel$ are the integrals of the polarised distributions. In the case of $N_\perp = N_\parallel$ and $P_\perp = P_\parallel$, Eq. 7.5 simplifies to Eq. 7.4.

Equation 7.5 can, for the purpose of applying it as a fit to extract Σ, be more usefully expressed in terms of polarisation ratios:

$$\frac{\sigma_\perp - \sigma_\parallel}{\sigma_\perp + \sigma_\parallel} = \frac{(N_R - 1) - \frac{N_R P_R + 1}{P_R + 1}\, 2\, \overline{P}\, \Sigma \cos\left(2(\phi + \phi_0)\right)}{(N_R + 1) - \frac{N_R P_R - 1}{P_R + 1}\, 2\, \overline{P}\, \Sigma \cos\left(2(\phi + \phi_0)\right)} \tag{7.6}$$

where

$$\begin{aligned} N_R &= \frac{N_\perp}{N_\parallel} \\ P_R &= \frac{P_\perp}{P_\parallel} \\ \bar{P} &= \frac{1}{2}(P_\perp + P_\parallel) \end{aligned} \tag{7.7}$$

The corresponding fit function is

$$y = \frac{(A-1) - \frac{AB+1}{B+1}\, 2\, C \cos\left(2(x+\phi_0)\right)}{(A+1) - \frac{AB-1}{B+1}\, 2\, C \cos\left(2(x+\phi_0)\right)} \tag{7.8}$$

where $A = N_R$, $B = P_R$ and $C = \bar{P}\Sigma$. The least constrained fit using Eq. 7.8 would have A, B, C and ϕ_0 as free parameters.

7.5 Optimisation of fit parameters

The ϕ_0 phase depends upon the accuracy of the alignment of the diamond radiator in the goniometer, which was aligned at the start of the experiment. As this value can be established with high accuracy and did not vary through the experiment this parameter was extracted in a separate analysis and its value fixed in the fit. The ϕ_0 determination was obtained from fits using Eq. 7.8 to high statistics ϕ distributions. An example can be seen in Fig. 7.5, where the distribution was integrated over all the $\cos\theta$ bins in the range 1.6 – 1.9 GeV having a positive asymmetry. The extracted value of ϕ_0 was $0.125^\circ \pm 0.172^\circ$.

The polarisation ratio $P_\perp/P_\parallel$ varied by no more than 3% from the peak ratio of 0.96. It was therefore decided to constrain the fit with the calculated ratio. This induces little systematic error in the extracted asymmetries as discussed later (Chapter 8, Section 2.1).

The constraints on ϕ_0 and $P_\perp/P_\parallel$ reduced the free parameters in the fit of Eq. 7.8 to two: N_R and $\bar{P}\Sigma$. Both of these parameters were extracted from the fit. The possibility of normalising the ϕ asymmetry-distributions in order to fix N_R was investigated and it was found that this could not be done to a high enough accuracy. Better fit results were obtained if the parameter was left free, however a starting value of N_R was determined

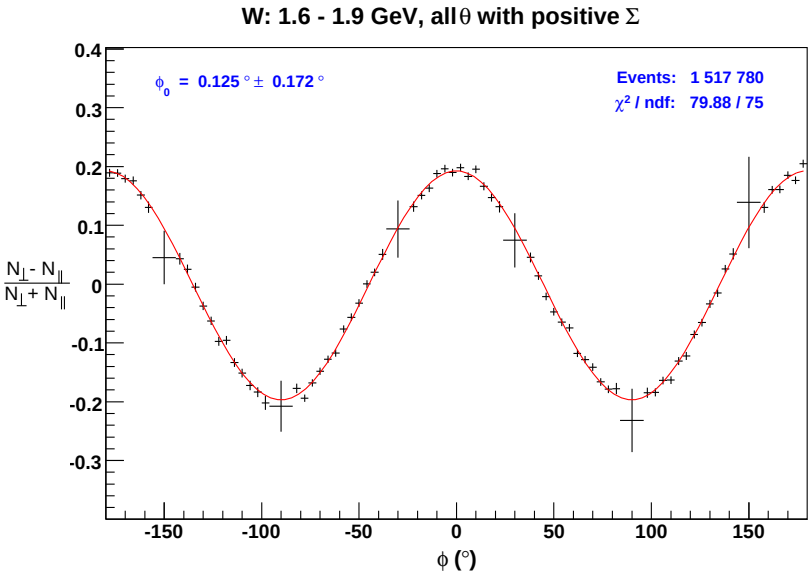

Figure 7.5: ϕ distribution for the W range 1.6 – 1.9 GeV and $\cos\theta$ in the range from -0.7 to -0.1 and 0.6 to 0.8, where Σ was always positive. The phase ϕ_0 was extracted from a fit with the function given in Eq. 7.5.

beforehand. The procedure used the ϕ distributions of PARA and PERP in narrow regions of ϕ centred on $\cos(2(\phi + \phi_0)) = 0$ and which lay well within the fiducial regions. The average ratio of perpendicular to parallel events in these regions for a given W, $\cos\theta$ bin gave the starting value for N_R.

The results of the fit using Eq. 7.8 with two free parameters, A and C, applied to the ϕ-asymmetry distributions in bins of 10 MeV in W and 0.1 in $\cos\theta$ are presented in the following chapter.

Chapter 8

Results and Discussion

8.1 Quality of fit

The quality of fit to the ϕ distribution in each W and $\cos\theta$ bin using the fit expression of Eq. 7.8 is shown in Fig. 8.1, where the distribution of χ^2 per degree of freedom for all the W and $\cos\theta$ bins in the analysis is presented. The distribution peaks close to χ^2 per degree of freedom of 1, which indicates a good overall fit to the data set.

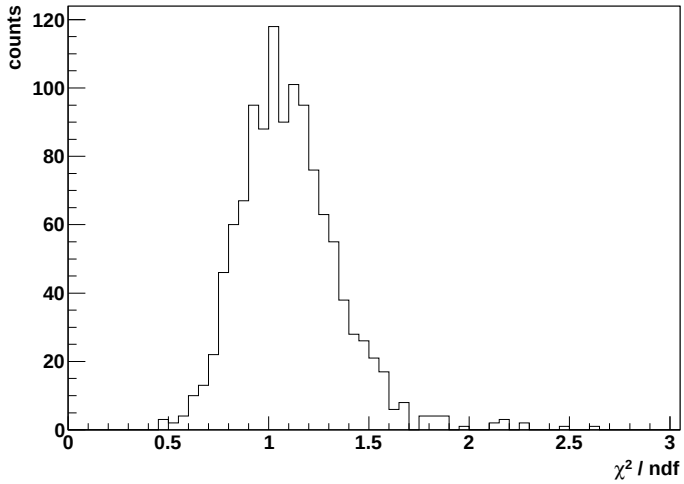

Figure 8.1: The χ^2 per degree of freedom distribution from fits to ϕ distributions in all W and $\cos\theta$ bins.

8.2 Systematic uncertainties in the extraction of Σ

8.2.1 Determination of degree of beam polarisation

The main systematic uncertainties in our extraction of the beam asymmetry arose from the calculation of the degree of polarisation of the photon beam, which was determined with an uncertainty of 10% [129]. The effect of this uncertainty on the extracted value of Σ is twofold.

Firstly, since the ratio of $\frac{P_\perp}{P_\parallel}$ is a fixed parameter in the fit, an uncertainty on that ratio will affect the fit quality and result in an error on the calculation of the free fit parameters, most importantly Σ. The greatest effect from the uncertainty will be when one of $P_\perp$ and $P_\parallel$ is lower by 10% while the other is higher by 10%. This effect was investigated by comparing Σ determined from the fit where the ratio was fixed at the maximum and the minimum values within the error. An illustration of the comparison is shown for one of the bins in W and $\cos\theta$ in Fig. 8.2. It is evident that agreement is good with maximum uncertainty in Σ estimated, from a difference in the Σ values obtained using the two fits, to be 4%.

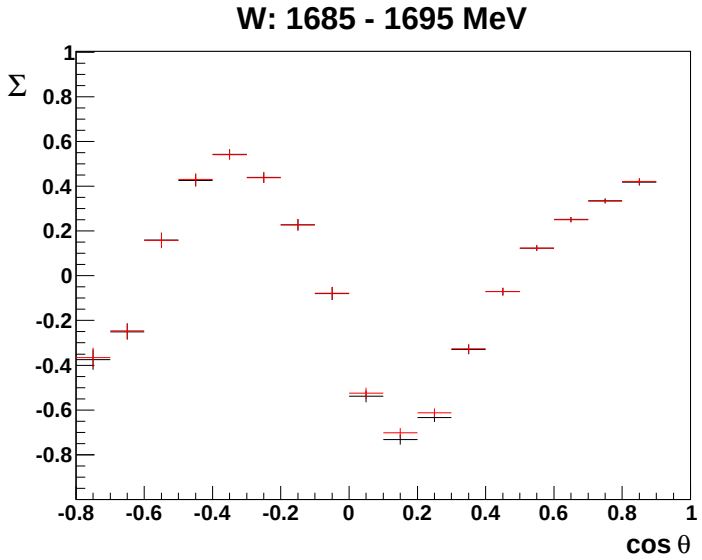

Figure 8.2: A comparison of the beam asymmetry extracted from events where the polarisation ratio was deliberately skewed to its maximum (red) and minimum (black). Any discrepancies in the value of Σ are within the statistical uncertainty.

A 10% systematic uncertainty in the calculation of both $P_\perp$ and $P_\parallel$ results, by the addition of errors in quadrature, in a 14% uncertainty in the calculation of the average polarisation, $\bar{P}$. Since Σ is obtained from the fit parameter $C = \bar{P}\Sigma$, which in itself has an estimated uncertainty less than 4%, the total systematic uncertainty on Σ due to the calculation of the degree of polarisation was estimated, by a combination of the errors, at 14.5%.

8.2.2 ϕ_0 offset

The fit used to extract Σ has only one other constrained parameter: ϕ_0. This was determined, from a fit to a very high statistics sample of the data, to be $0.125^\circ \pm 0.172^\circ$. Since the accuracy of this parameter again affects the quality of the fit, an estimate of the resulting change to the extracted value of Σ was obtained for the "worst" case scenarios by setting ϕ_0 to the maximum and minimum values of 0.297° and -0.047°. The Σ values obtained using both fits were then compared. A representative example of the comparison for a single W and $\cos\theta$ bin is shown in Fig. 8.3. The agreement in the results obtained using fits with both values of the fixed parameters is excellent. The uncertainty due to a determination of the parameter ϕ_0 was estimated to be < 0.2%, based on the maximum difference in the Σ values obtained with the two fits.

8.2.3 W and $\cos\theta$

The value of W, the invariant mass in the reaction, which is crucial for the relation of beam asymmetry to resonance parameters, was calculated from the final state of the reaction. Therefore W was entirely dependent on the correct identification of the final state particles and their momenta. As was illustrated in Chapter 6, the selection of $p\pi^-$ events was very clean, with negligible background. The reconstruction of particle momenta in CLAS has an uncertainty of 0.5 – 2.0%, depending on the polar angle. For the invariant masses on the order of 1.6 – 2.3 GeV, this is comparable to the width of the W bin chosen.

The absolute normalisation of W was investigated by comparison of the centre of mass energy calculated from the tagged incident photon and from the final state particles (Chapter 6, Section 7). The two methods were found to agree within 1 MeV/c^2.

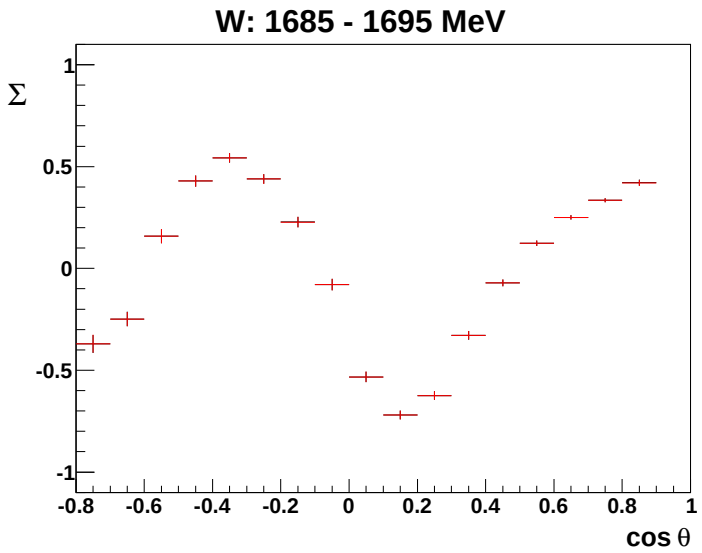

Figure 8.3: Σ extracted from a fit with $\phi_0 = -0.047°$ (red) and $\phi_0 = 0.297°$ (black). These values of ϕ_0 are the lower and upper limits of the parameter within its error, $\phi_0 = 0.125° \pm 0.172°$.

The same argument regarding detector resolution applies to the uncertainty in $\cos\theta$. A bin width of 0.1 in $\cos\theta$ corresponds to the smallest θ bin of 5.7° at $\theta = 90°$. The uncertainty on the reconstruction of θ is $< 0.1°$, which is well within the bin width.

8.3 Check of Final State Interaction effects

As has already been discussed, the effect of final state interactions (FSI), on the beam asymmetry is expected to be small because of the similarity of Σ for pion production on the free proton and the bound proton in deuterium [128] (Chapter 6, Section 7). However, internal checks of this hypothesis within the new data set were carried out by studying the dependence of the asymmetry on the momentum of the recoiling nucleon. As the FSI effects will tend to give more momentum to the recoiling proton, the comparison of the extracted asymmetries for low- and high-recoil proton momenta regions constrain the size of the the FSI effects. Fig. 8.4 shows the beam asymmetries obtained from events with the lowest recoil momentum in the sample, below 30 MeV, and the highest, 95 – 120 MeV, for one bin in $\cos\theta$. The asymmetries are in good agreement throughout the range of W supporting the previous indications [128] that the asymme-

try is not strongly affected by FSI for low values of recoil momenta. Similar agreement was observed at other angles.

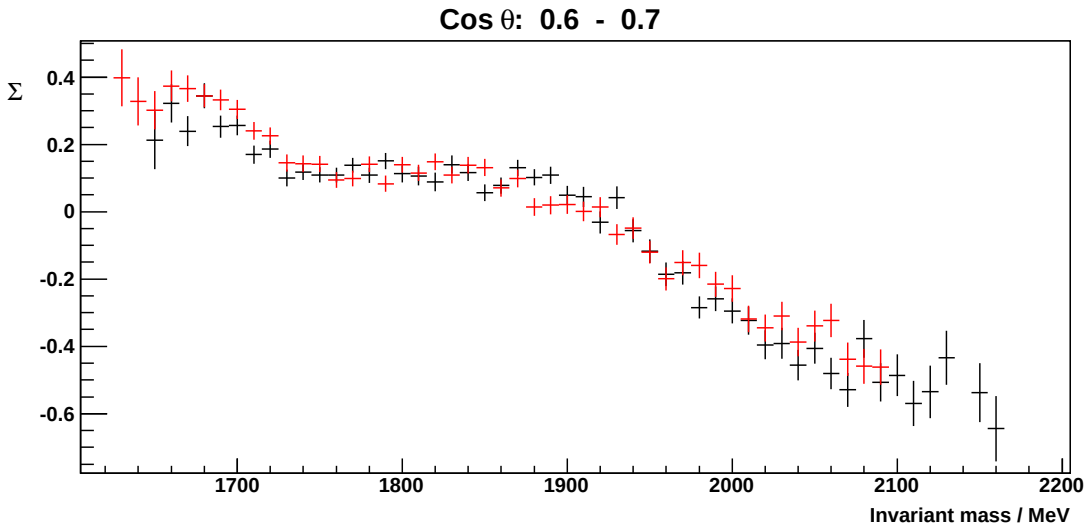

Figure 8.4: A comparison, for a single bin in $\cos\theta$, of the beam asymmetry extracted from events where the momentum of the recoiling proton in the deuteron nucleus is < 30 MeV (black) and 95 – 120 MeV (red).

8.4 Results

The extracted beam asymmetry for the $n(\gamma,\pi^-)p$ reaction is plotted as a function of the cosine of the pion production angle in the centre of mass ($\cos\theta$) for 72 W bins in the range 1605 – 2325 MeV in Figs. 8.11 – 8.28. The asymmetry is also presented as a function of W in Figs. 8.5 – 8.10. Only the statistical error bars are shown. The systematic uncertainties, as discussed in this Chapter, are estimated at ~ 14.5%. A good general agreement is observed throughout with the sparse data from the past experiments discussed in Chapter 3, which are shown with open circle [97], open square [98] and filled triangle [99] markers.

The graphs are overlaid, for comparison, with the calculation of the beam asymmetry from two partial wave analyses, SAID-09 (blue) and MAID-07 (green), based on fits to the world data set of meson photoproduction before the current measurement. The asymmetry measurements from the current experiment have also been used

in a new SAID PWA. The result of this SAID-09-NEW fit (executed by the SAID PWA group [130]) is shown in red. The χ^2 per degree of freedom from the fit was 2.6, which, in view of the incomplete information available for the full constraint of the PWA, indicates that the current data can be well-described by the parametrisation used. The result can also be observed in Fig. 8.29, showing a contour plot of the SAID-09-NEW asymmetry calculation overlaid on the set of experimental points. Fig. 8.30 additionally shows a 3D surface plot of the beam asymmetry calculation from SAID-09-NEW as a function of θ and photon beam energy in the range 1070 – 1470 MeV.

The SAID-09 solution does not give a good overall agreement with new data, in particular at backward angles ($\cos\theta < 0$) and at high values of invariant mass (above $\sim$ 2 GeV) where past data is particularly sparse. Departures from the MAID-07 calculations are also clear, particularly at backward angles and in the range 0.2 – 0.5 in $\cos\theta$. The SAID-09-NEW solution which uses our new asymmetry data can be seen to give, as would be expected, much better agreement with the data.

A better indication of the impact of the new data on the partial wave analysis can be obtained by studying the changes in the multipoles from the three partial wave solutions. A comparison of multipoles from the MAID-07, SAID-09 and SAID-09-NEW solutions are shown in Fig. 8.31 and the following pages by the green, blue and red lines respectively. The notation describing different multipoles follows the convention presented in Chapter 2, labelling multipoles $L_{2I,2J}$, where L is the orbital angular momentum of the transition, I is isospin and J is the total angular momentum. E and M refer to electric and magnetic multipoles respectively. The multipoles for proton or neutron transitions are indicated with p and n.

The importance of the multipoles lies in their relation to the particular resonant states observed in the transition. Significant changes in the multipoles as a result of the new data are therefore indicative of differences in the observed nucleon couplings to the different resonant states. Since the new data were taken in photoproduction from the neutron, the greatest impact will be on the determination of the neutron couplings which, due to the challenges of conducting experiments on the neutron, are currently particularly ill-established ([21]).

The new data clearly results in very major changes in the values of some multipoles. For example, the real parts of the G_{17} and P_{11} magnetic multipoles for the neutron even show a change of sign between the SAID-09 and SAID-09-NEW solutions. Clearly

our new data should also be used to generate a new MAID PWA solution, a task which will also be carried out in the near future. Significant discrepancies with the MAID multipoles can be observed throughout.

Investigations of the impact of our new data on the properties of the nucleon resonances is currently underway. Early indications from the SAID PWA group show that the results will produce very significant changes in the helicity amplitudes for a range of the resonances. This work is currently is progress, along with a theoretical investigation into possible FSI effects, a calculation of which for polarisation measurements has never previously been done [130]. Since this is being finalised for a future publication, it is not available for presentation in this thesis.

A possible indication of resonances may, however, be gleaned from those multipoles where a zero in the real part coincides with a peak in the imaginary. As was discussed in Chapter 2, transition amplitudes exhibit this behaviour when the transitional state corresponds to an on-mass-shell case, as for a resonance. This is not conclusive evidence of a resonance, however, and it should also be stressed that no definite conclusion regarding the resonance spectrum can be made on the basis of the multipoles presented in this thesis as the SAID-09-NEW partial wave analysis is preliminary and a full consideration of the current data with improved systematic uncertainties is pending. Moreover, all three partial wave analyses are based on an incomplete set of measured polarisation observables. As such, they are model-dependent (although the SAID analysis is the least so, being maximally reliant on the world dataset) and contain unresolved ambiguities.

Nevertheless, the existence of several better-established resonances is suggested in the corresponding multipoles which strongly exhibit the resonance characteristic. For example, all three S_{11} electric multipoles for the proton transition (MAID-07, SAID-09 and SAID-09-NEW) are in agreement with the $S_{11}(1650)$ resonance. Likewise, the three F_{15} electric multipoles for both the proton and the neutron transitions appear to strongly support the $F_{15}(1680)$ resonance, while the $F_{37}(1950)$ may be observed in the magnetic F_{37} multipoles for the proton. The SAID G_{17} magnetic multipoles for the proton are indicative of the $G_{17}(2190)$ resonance (which is outside the energy-range of the MAID partial wave analysis). The three D_{15} magnetic multipoles for the neutron suggest support of the $D_{15}(1675)$ resonance. All five of these resonances hold a four-star rating in the PDG [21]. Agreement of the SAID-09-NEW multipoles with those

determined using previous partial wave analyses in the invariant-mass regions of these better-established resonances is an indication of the reliability of our data.

There may be some very tentative suggestion of resonances newly-observed in the SAID partial wave analysis where significant differences between the previous SAID-09 and the new SAID-09-NEW solutions are evident. An example of this is the P_{11} magnetic multipole for the neutron, which exhibits a zero in the real part and a maximum in the imaginary part of the multipole around an invariant mass of 1700 MeV/c^2. This is not observed in the SAID-09 solution, nor in MAID-07. A possible corresponding resonance is the $P_{11}(1710)$ state, which has a three-star rating in the PDG. A similar case is seen in the D_{13} magnetic multipole for the neutron in the region of 1700 MeV/c^2, which may potentially correspond to the $D_{13}(1700)$ resonance, also with three-star rating in the PDG. However, previous experiments in η-photoproduction and Compton scattering on the neutron also suggest the possible existence of a narrow resonance having an invariant mass in the region of 1685 MeV and quantum numbers of either P_{11}, P_{13} or D_{13}, seen to couple strongly to the neutron, while having its proton coupling heavily suppressed [56]. There is a tentative suggestion in the literature that some of these observations may correspond to a member of the exotic anti-decuplet (see Chapter 1, Section 2.2.3) which is expected to be a narrow P_{11} resonance [131].

Some small local maxima are also observed in the imaginary part of the F_{15} electric multipole for the neutron in the SAID-09-NEW solution corresponding to zeros in the real part around invariant masses 1760 MeV/c^2 and 2000 MeV/c^2. Although there is no previously observed resonance corresponding to the former, the latter may indicate some tentative agreement with the badly-established resonance $F_{15}(2000)$, carrying a two-star rating in the PDG. The F_{17} magnetic multipole for the neutron appears, albeit on a very small scale, to have an imaginary maximum and a real zero around 2200 MeV/c^2. Nothing corresponding to these invariant mass and quantum numbers can be found in the PDG baryon resonance list [21].

Although SAID-09-NEW gives a much better agreement with our new data it is evident on closer inspection that in certain regions of W the PWA could not closely match the data, even though it is included in the PWA fit. In these regions improvements in the agreement of PWA solutions with the data by inclusion of additional resonances will be explored. It should be stressed, however, that these new data are part of a world programme of measurements and that the most accurate determination

of the resonance spectrum and its properties will come from a combined analysis of the present data with the new double polarisation measurements currently under analysis at MAMI, JLAB and ELSA.

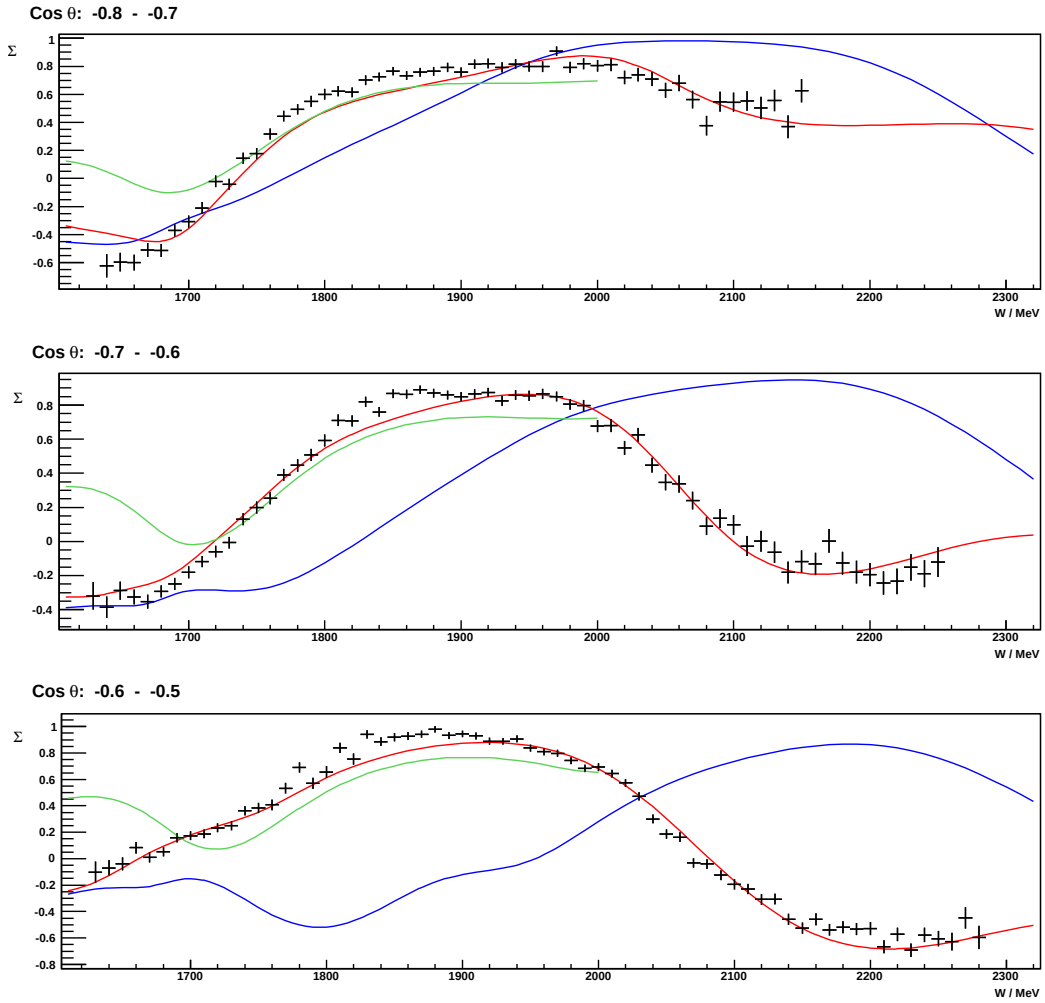

Figure 8.5: Beam asymmetry as a function of W, $\cos\theta$ from -0.8 to -0.5 in 0.1 wide bins, overlaid with SAID-09 (blue), MAID-07 (green) and SAID-09-NEW (red) partial wave analysis solutions.

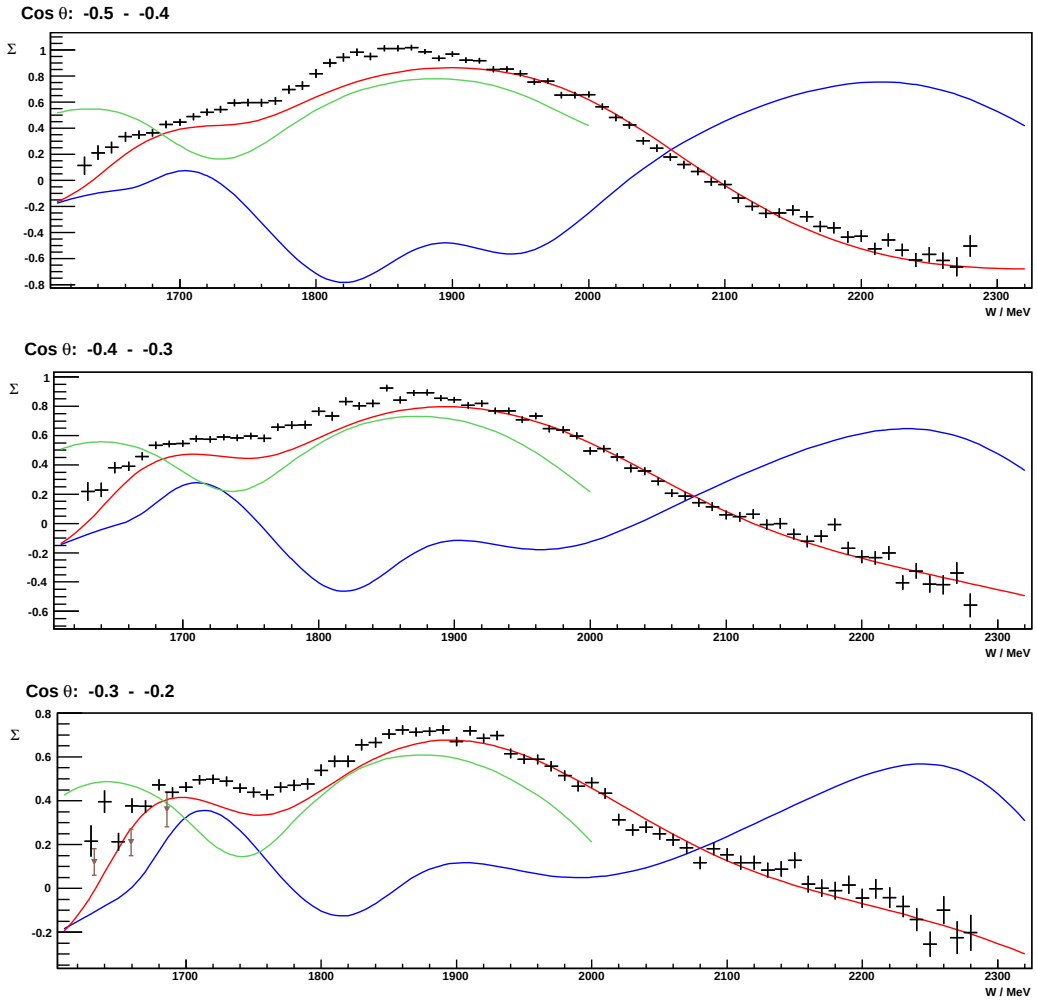

Figure 8.6: Beam asymmetry as a function of W, $\cos\theta$ from -0.5 to -0.2 in 0.1 wide bins, overlaid with SAID-09 (blue), MAID-07 (green) and SAID-09-NEW (red) partial wave analysis solutions. Previous data from [99] shown with filled triangles.

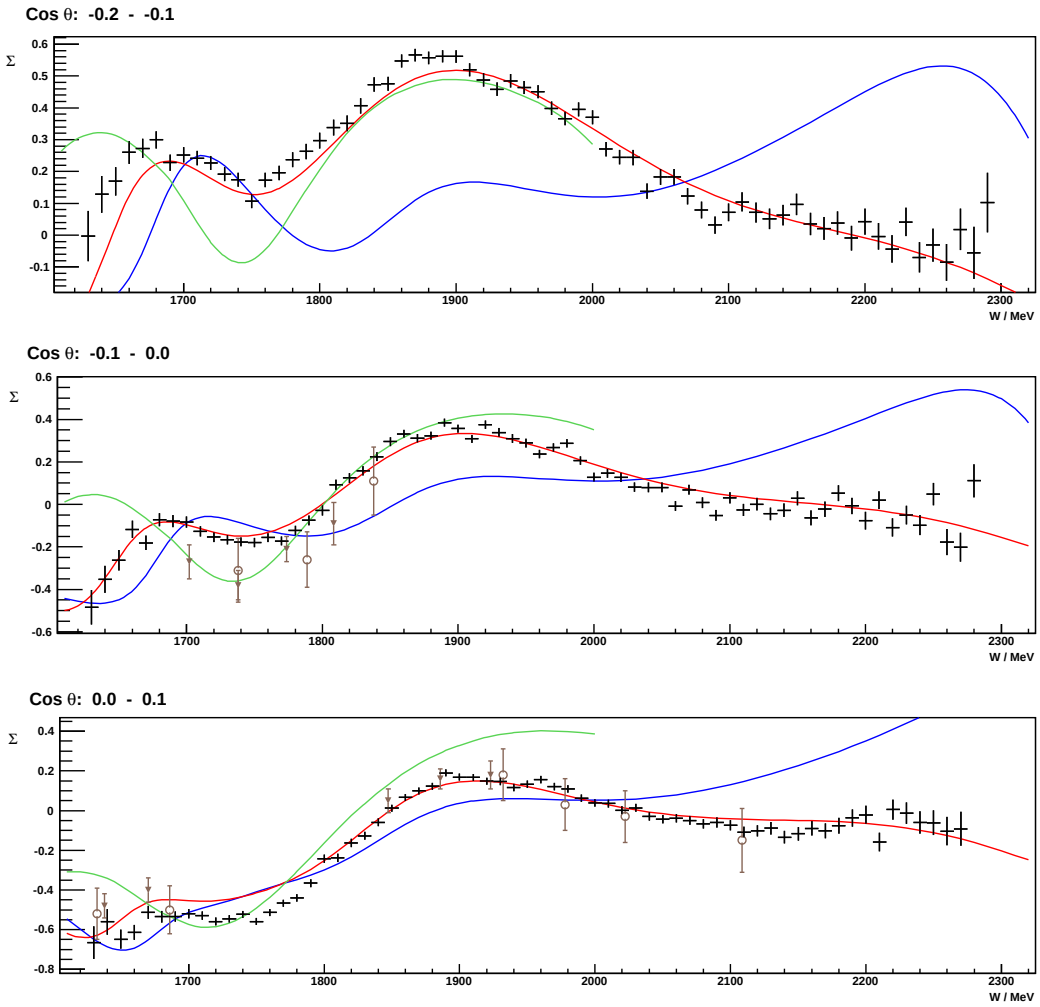

Figure 8.7: Beam asymmetry as a function of W, $\cos\theta$ from -0.2 to 0.1 in 0.1 wide bins, overlaid with SAID-09 (blue), MAID-07 (green) and SAID-09-NEW (red) partial wave analysis solutions. Previous data from [97] and [99] shown with open circles and filled triangles respectively.

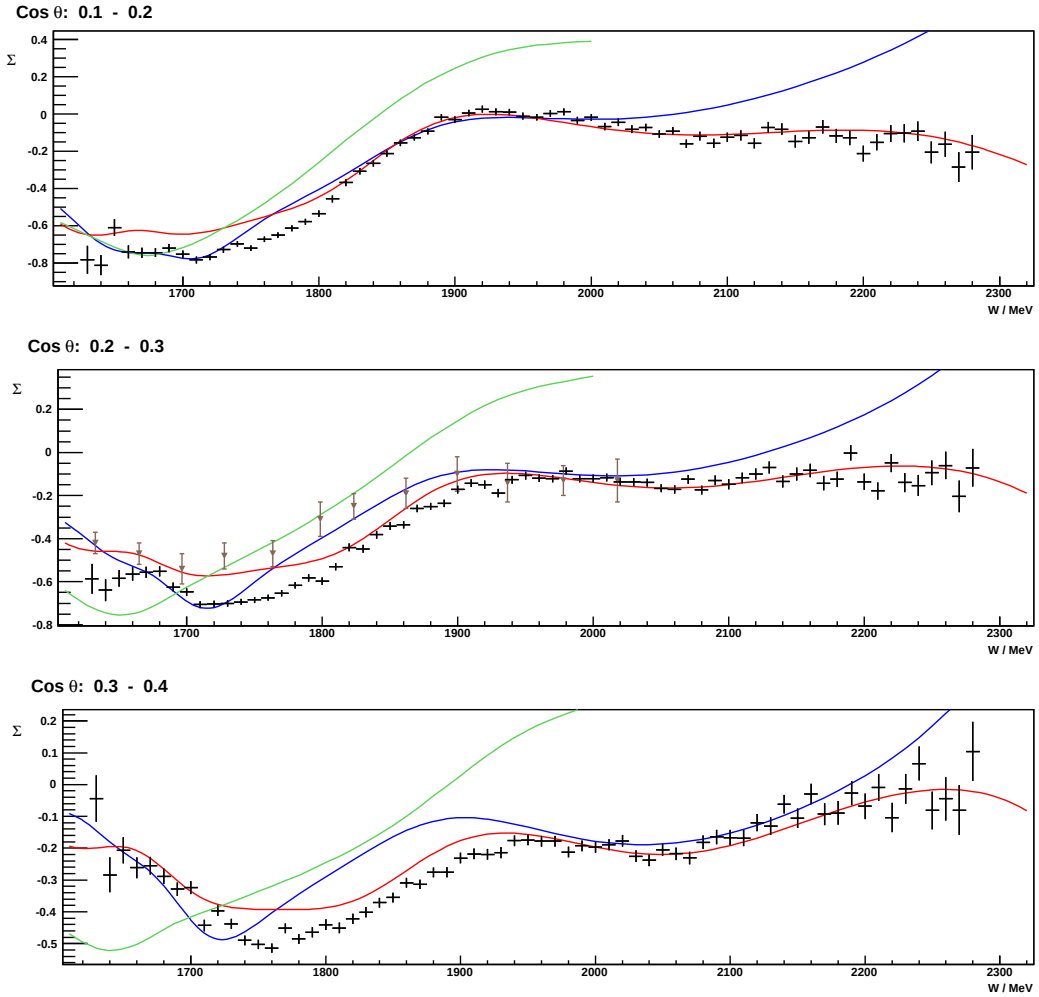

Figure 8.8: Beam asymmetry as a function of W, $\cos\theta$ from 0.1 to 0.4 in 0.1 wide bins, overlaid with SAID-09 (blue), MAID-07 (green) and SAID-09-NEW (red) partial wave analysis solutions. Previous data from [99] shown with filled triangles.

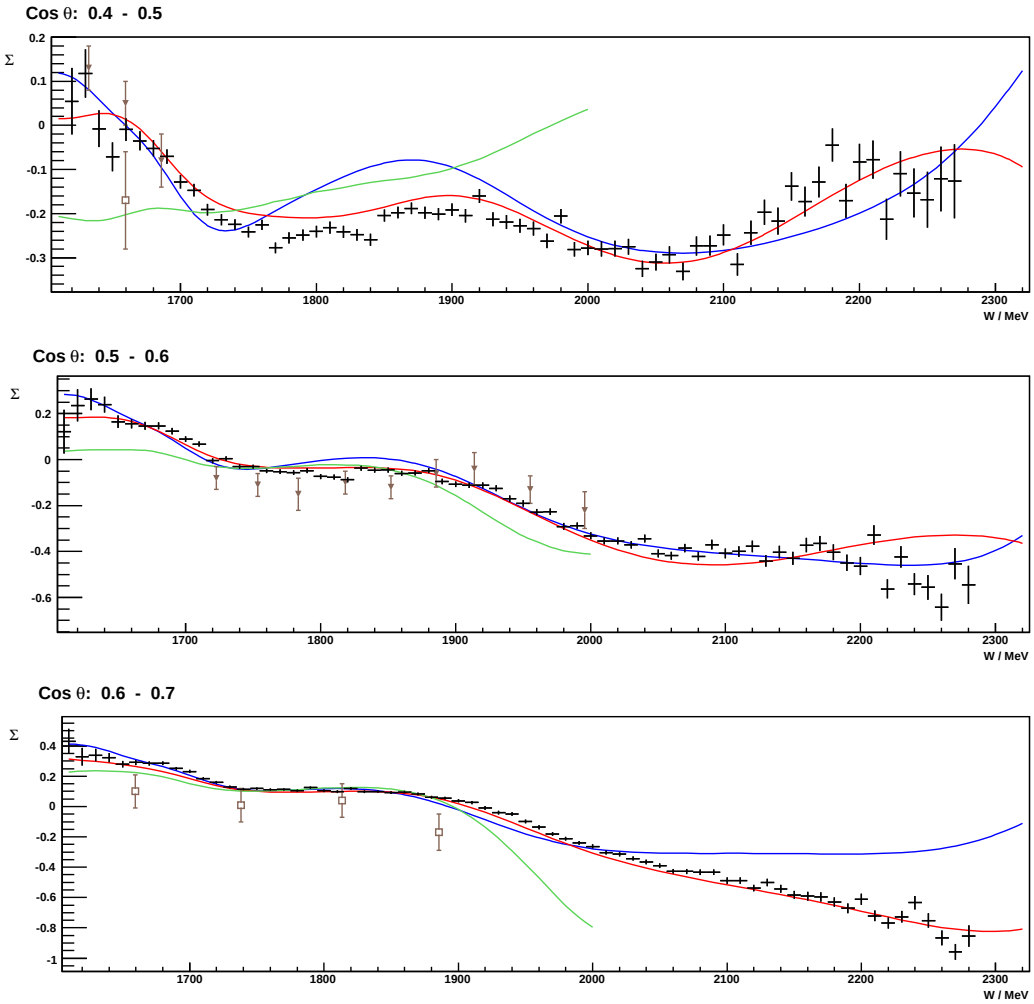

Figure 8.9: Beam asymmetry as a function of W, $\cos\theta$ from 0.4 to 0.7 in 0.1 wide bins, overlaid with SAID-09 (blue), MAID-07 (green) and SAID-09-NEW (red) partial wave analysis solutions. Previous data from [99] and [98] shown with filled triangles and open squares respectively.

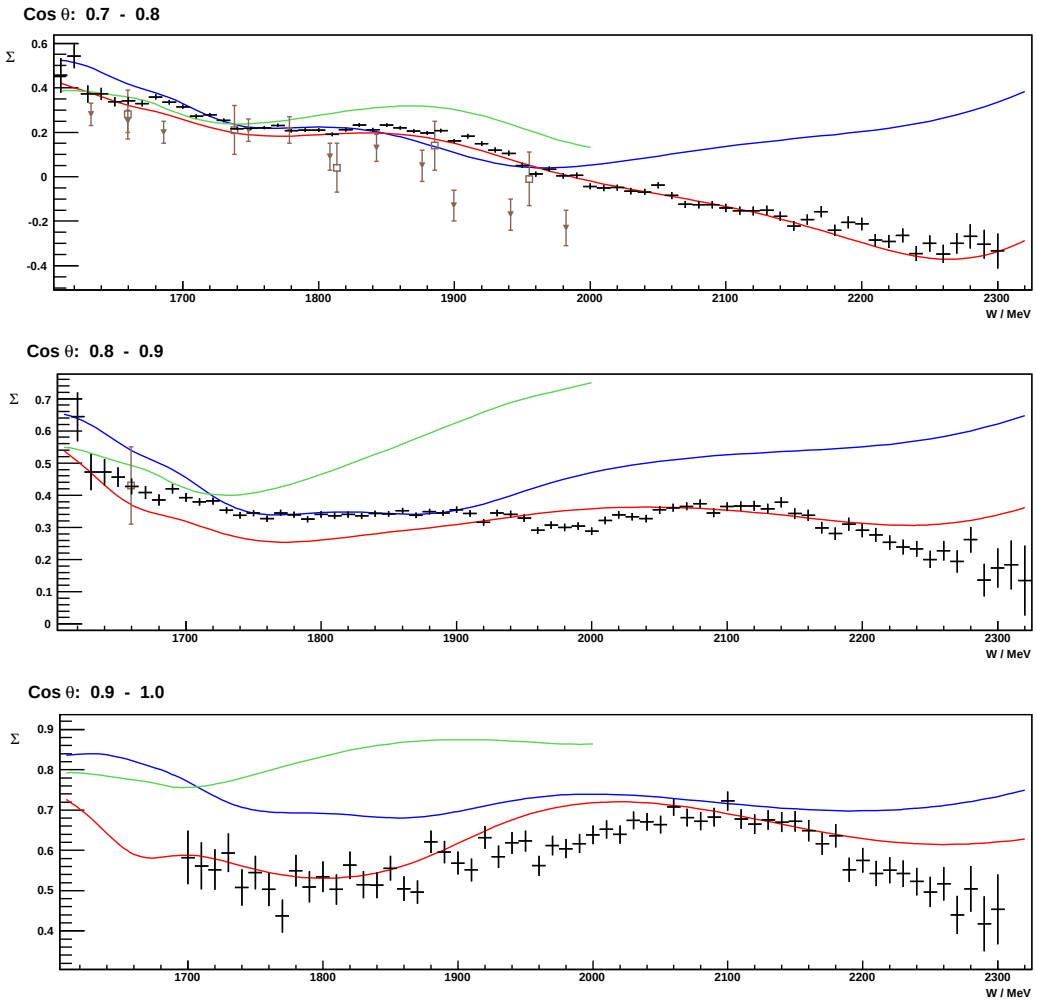

Figure 8.10: Beam asymmetry as a function of W, $\cos\theta$ from 0.7 to 1 in 0.1 wide bins, overlaid with SAID-09 (blue), MAID-07 (green) and SAID-09-NEW (red) partial wave analysis solutions. Previous data from [99] and [98] shown with filled triangles and open squares respectively.

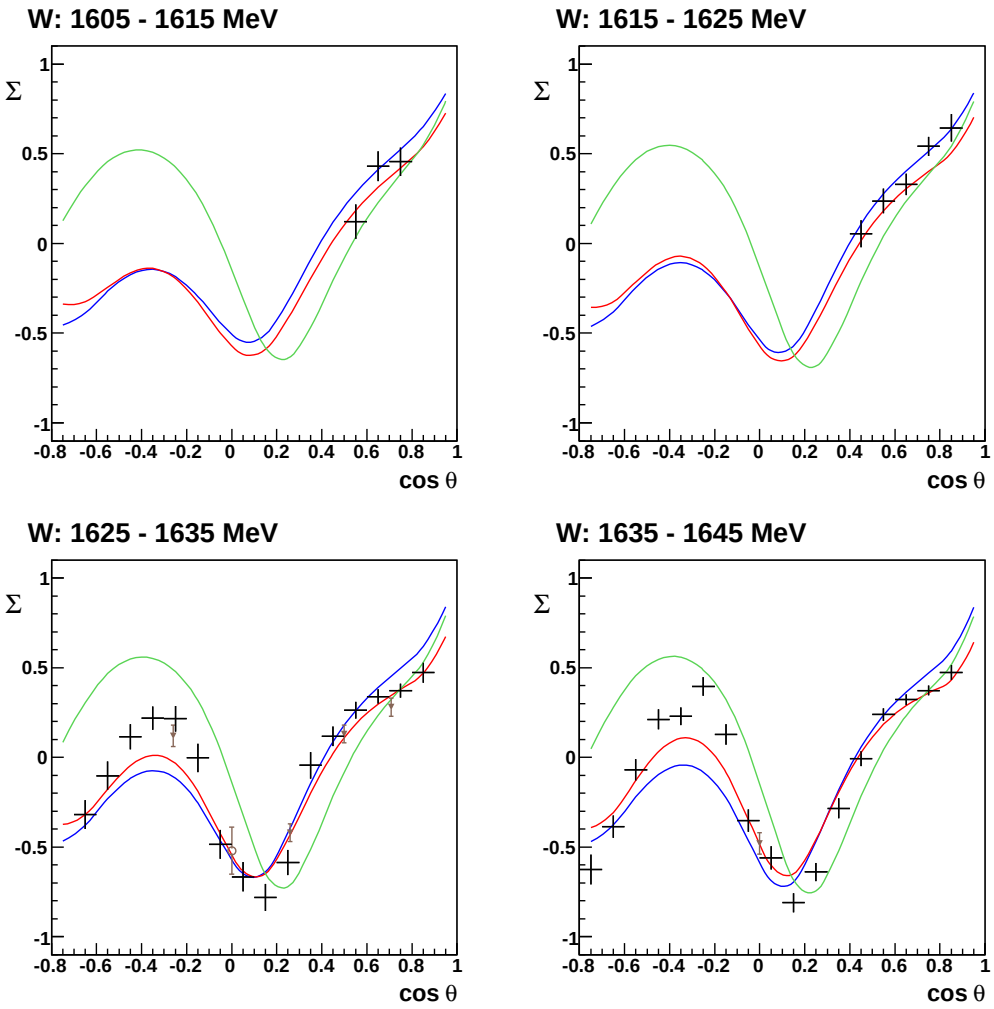

Figure 8.11: Beam asymmetry as a function of $\cos\theta$ for W 1605 – 1645 MeV, in 10 MeV wide bins, overlaid with SAID-09 (blue), MAID-07 (green) and SAID-09-NEW (red) partial wave analysis solutions. Data points not available in the entire range of W due to limited statistics in several bins. Previous data from [97] and [99] shown with open circles and filled triangles respectively.

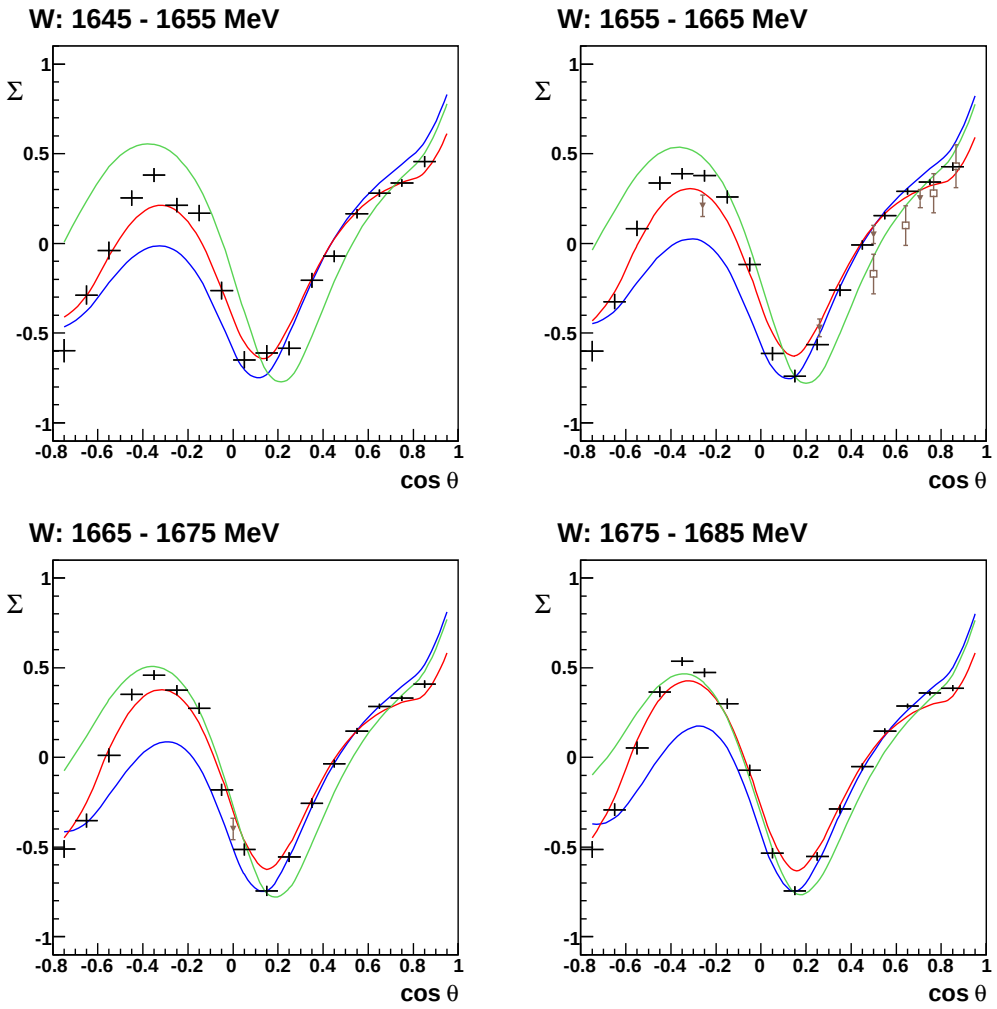

Figure 8.12: Beam asymmetry as a function of $\cos\theta$ for W 1645 – 1685 MeV, in 10 MeV wide bins, overlaid with SAID-09 (blue), MAID-07 (green) and SAID-09-NEW (red) partial wave analysis solutions. Previous data from [99] and [98] shown with filled triangles and open squares respectively.

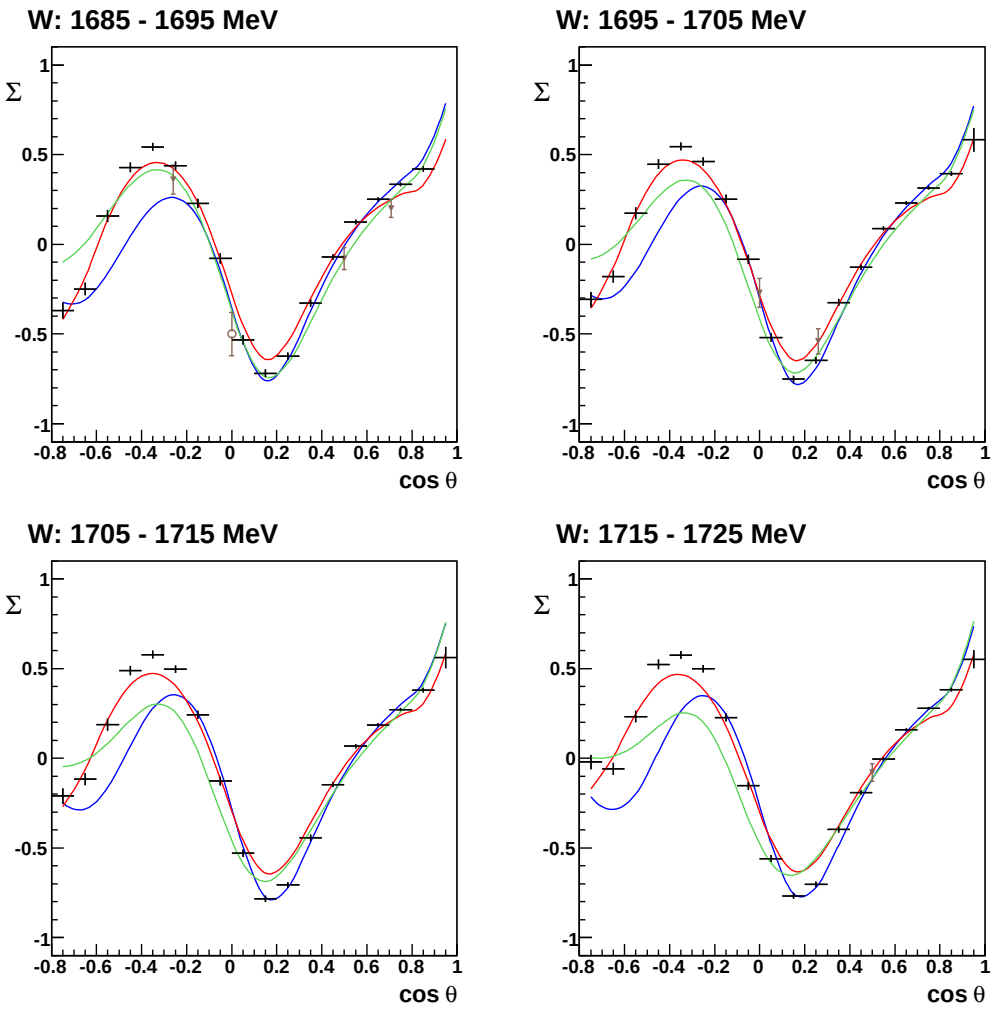

Figure 8.13: Beam asymmetry as a function of $\cos\theta$ for W 1685 – 1725 MeV, in 10 MeV wide bins, overlaid with SAID-09 (blue), MAID-07 (green) and SAID-09-NEW (red) partial wave analysis solutions. Previous data from [97] and [99] shown with open circles and filled triangles respectively.

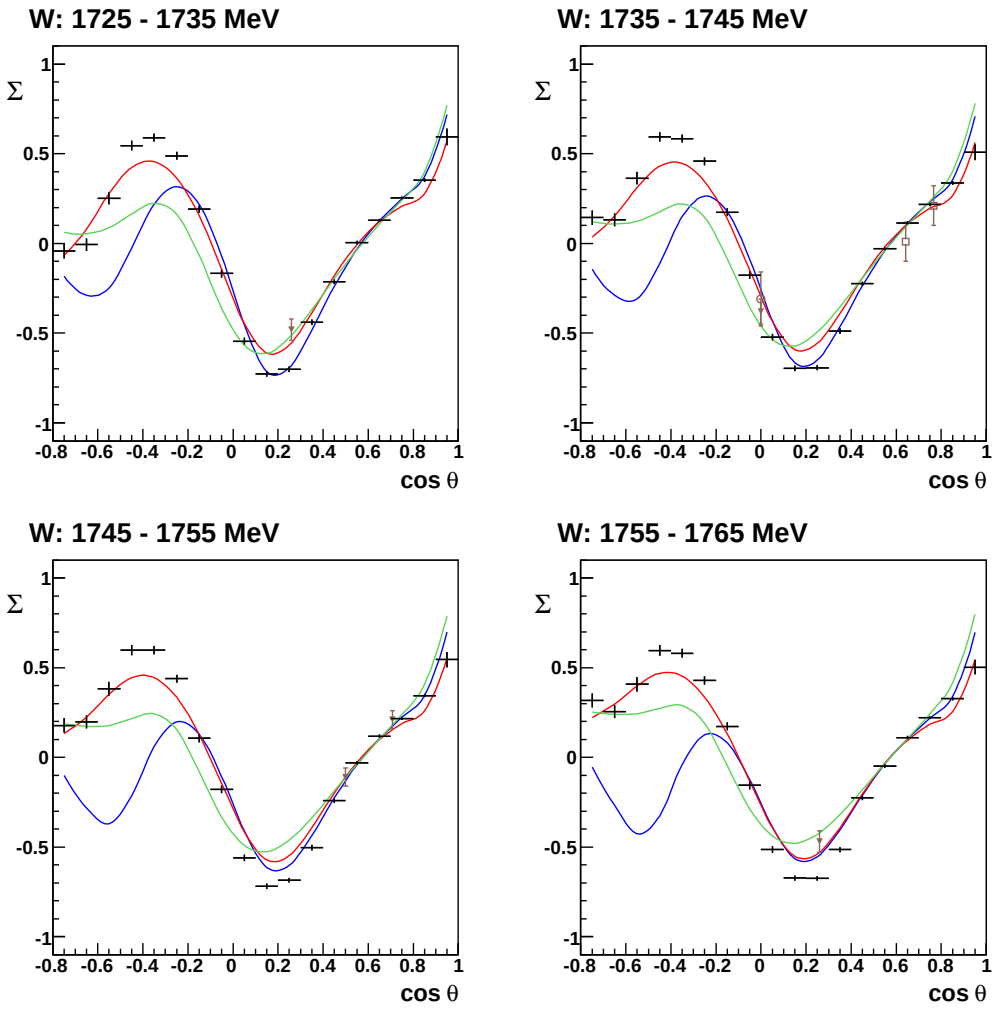

Figure 8.14: Beam asymmetry as a function of $\cos\theta$ for W 1725 – 1765 MeV, in 10 MeV wide bins, overlaid with SAID-09 (blue), MAID-07 (green) and SAID-09-NEW (red) partial wave analysis solutions. Previous data from [97], [98] and [99] shown with open circles, open squares and filled triangles respectively.

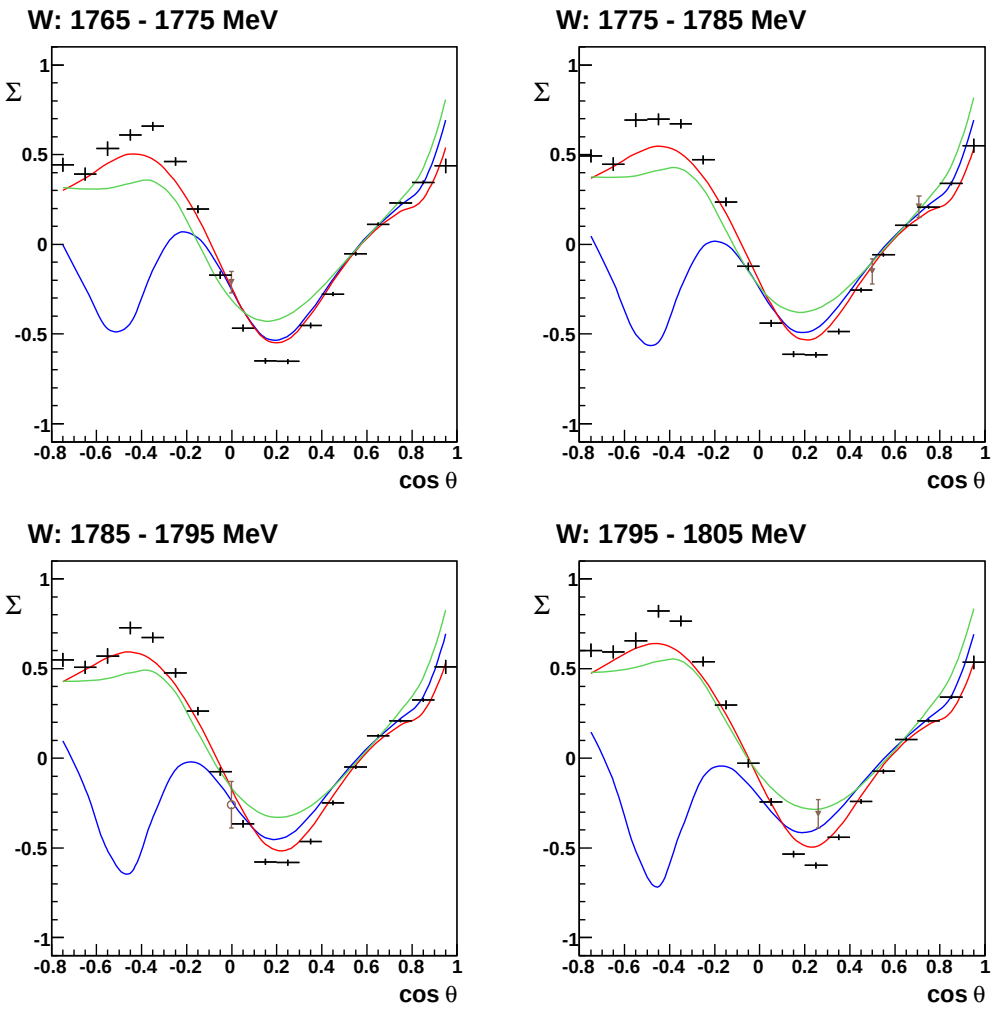

Figure 8.15: Beam asymmetry as a function of $\cos\theta$ for W 1765 – 1805 MeV, in 10 MeV wide bins, overlaid with SAID-09 (blue), MAID-07 (green) and SAID-09-NEW (red) partial wave analysis solutions. Previous data from [97] and [99] shown with open circles and filled triangles respectively.

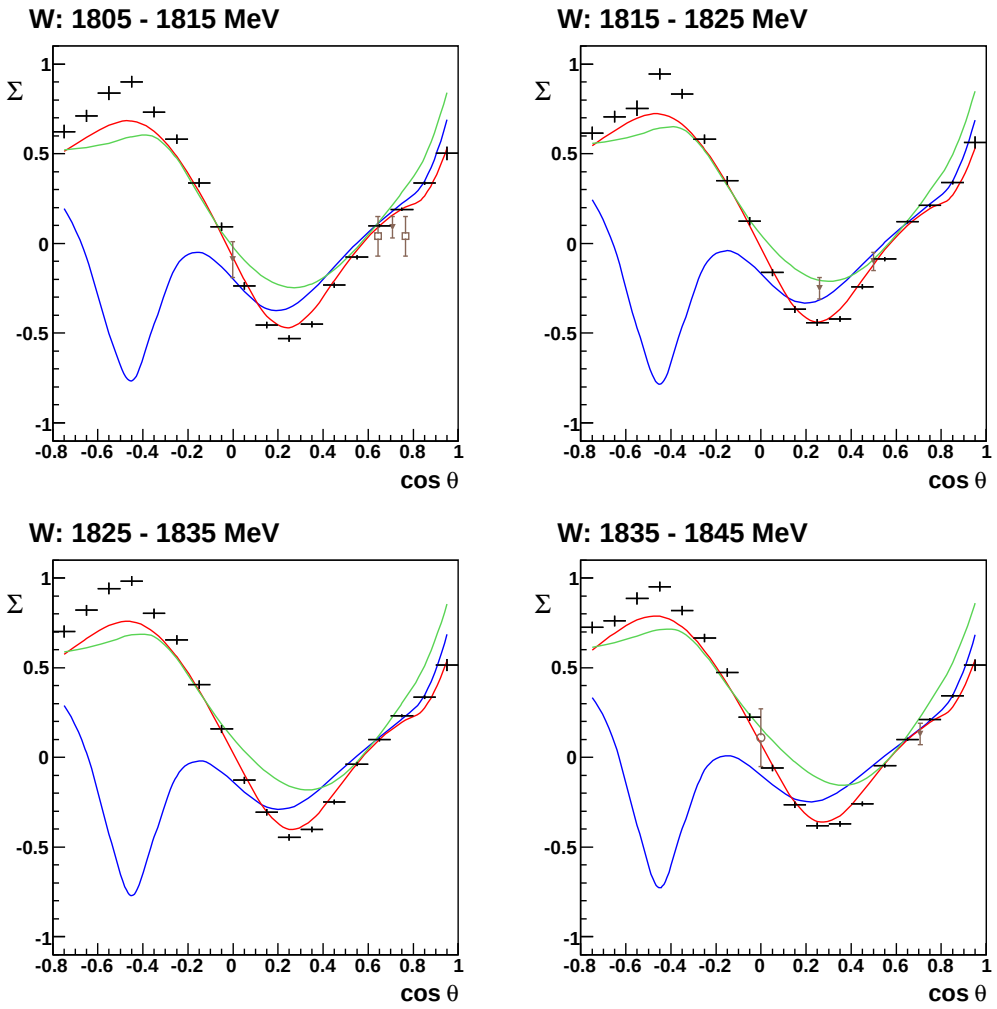

Figure 8.16: Beam asymmetry as a function of $\cos\theta$ for W 1805 – 1845 MeV, in 10 MeV wide bins, overlaid with SAID-09 (blue), MAID-07 (green) and SAID-09-NEW (red) partial wave analysis solutions. Previous data from [97], [98] and [99] shown with open circles, open squares and filled triangles respectively.

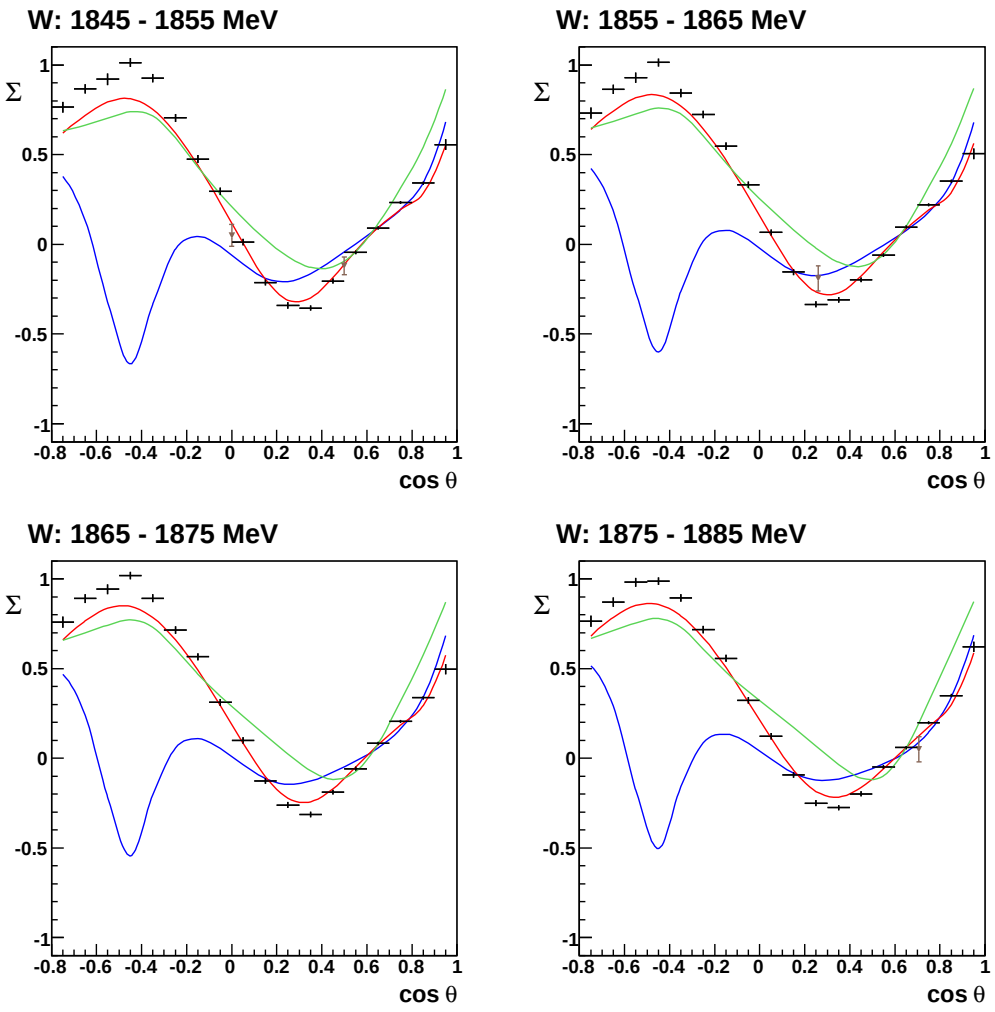

Figure 8.17: Beam asymmetry as a function of $\cos\theta$ for W 1845 – 1885 MeV, in 10 MeV wide bins, overlaid with SAID-09 (blue), MAID-07 (green) and SAID-09-NEW (red) partial wave analysis solutions. Previous data from [99] shown with filled triangles.

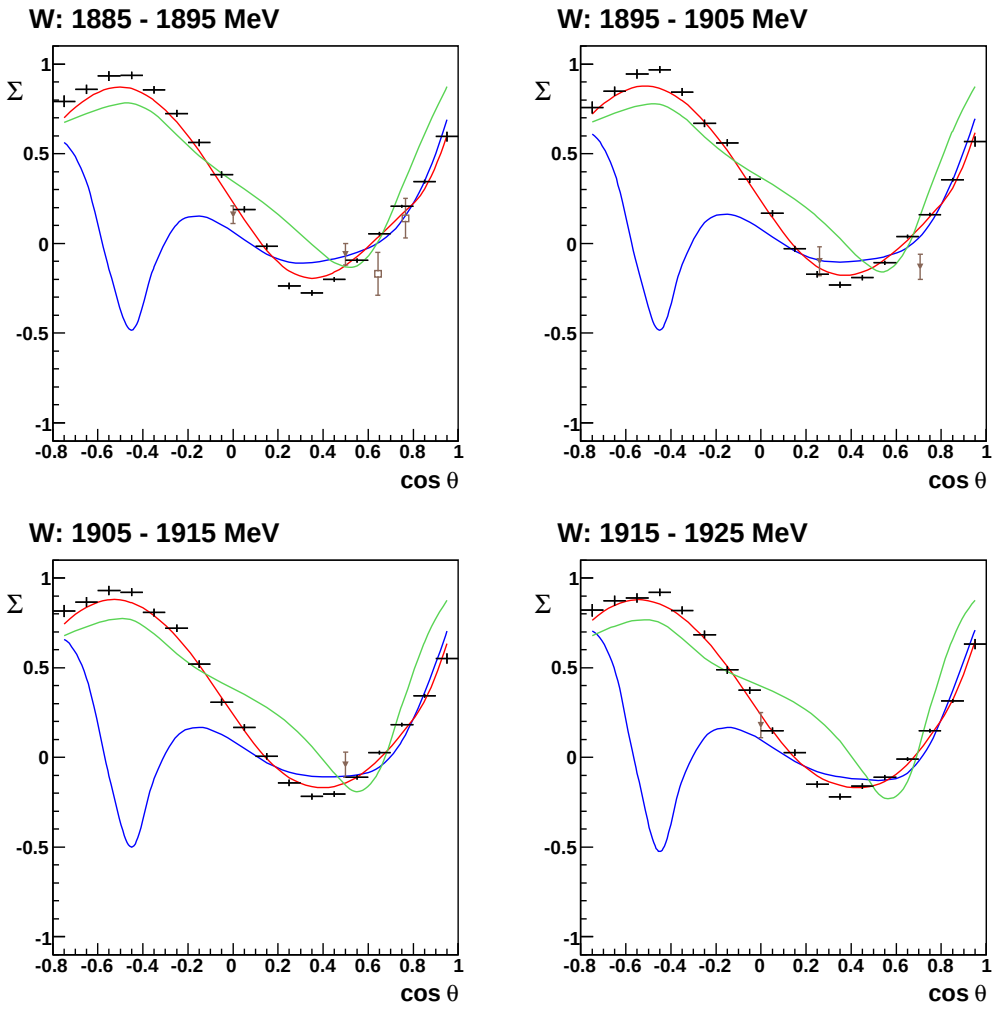

Figure 8.18: Beam asymmetry as a function of $\cos\theta$ for W 1885 – 1925 MeV, in 10 MeV wide bins, overlaid with SAID-09 (blue), MAID-07 (green) and SAID-09-NEW (red) partial wave analysis solutions. Previous data from [99] and [98] shown with filled triangles and open squares respectively.

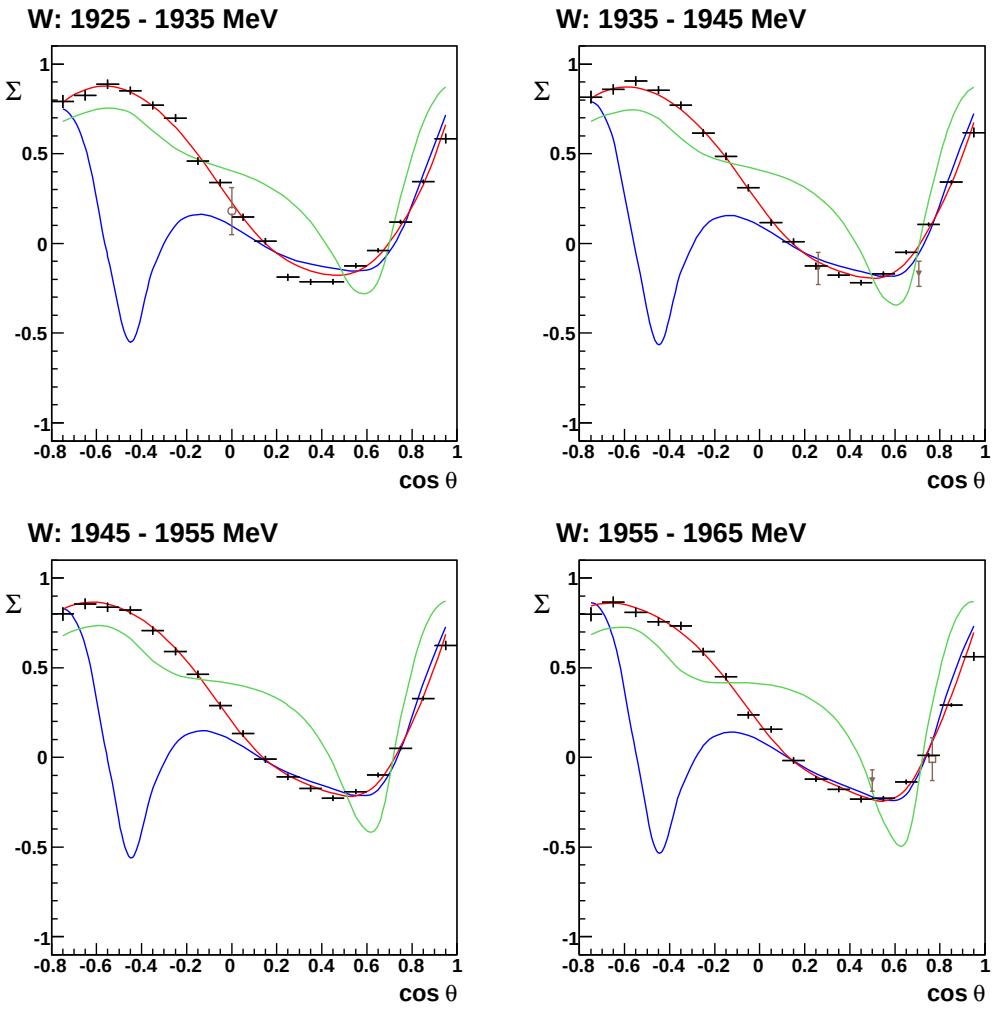

Figure 8.19: Beam asymmetry as a function of $\cos\theta$ for W 1925 – 1965 MeV, in 10 MeV wide bins, overlaid with SAID-09 (blue), MAID-07 (green) and SAID-09-NEW (red) partial wave analysis solutions. Previous data from [97], [98] and [99] shown with open circles, open squares and filled triangles respectively.

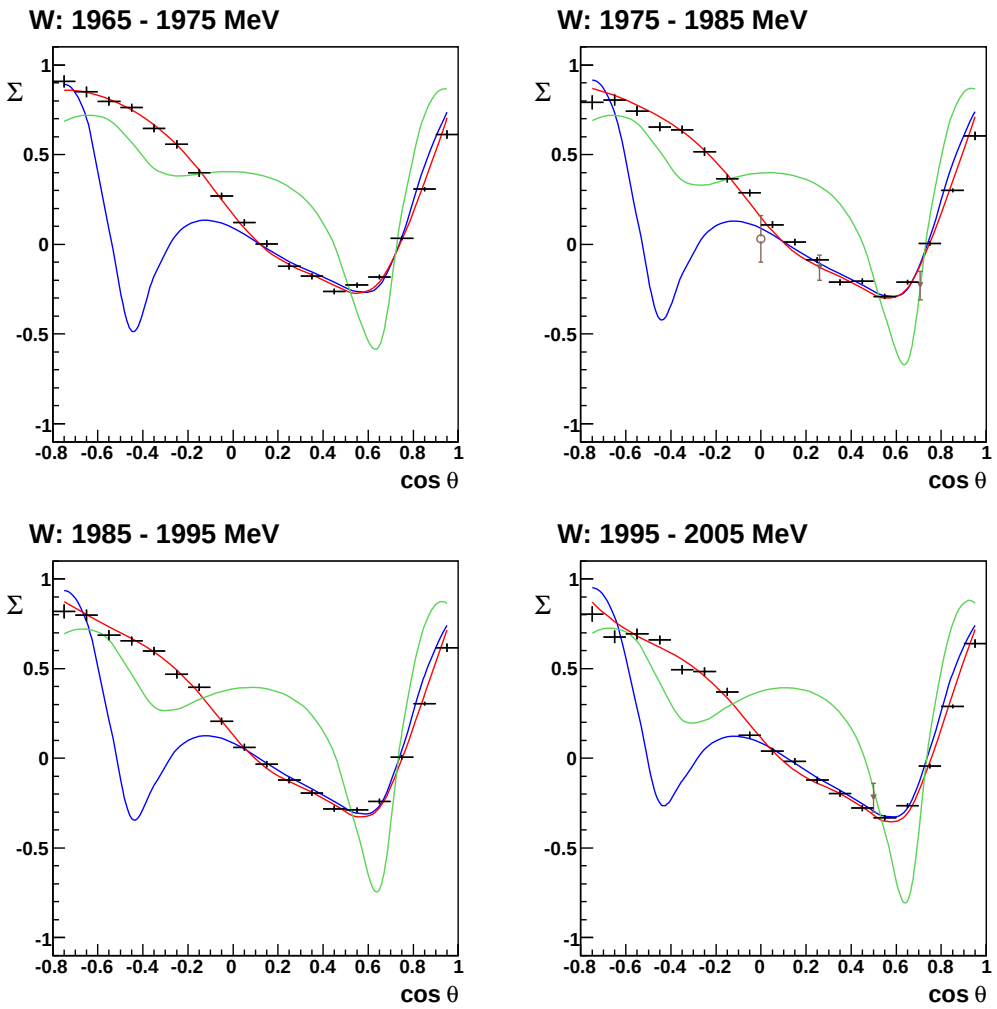

Figure 8.20: Beam asymmetry as a function of $\cos\theta$ for W 1965 – 2005 MeV, in 10 MeV wide bins, overlaid with SAID-09 (blue), MAID-07 (green) and SAID-09-NEW (red) partial wave analysis solutions. Previous data from [97] and [99] shown with open circles and filled triangles respectively.

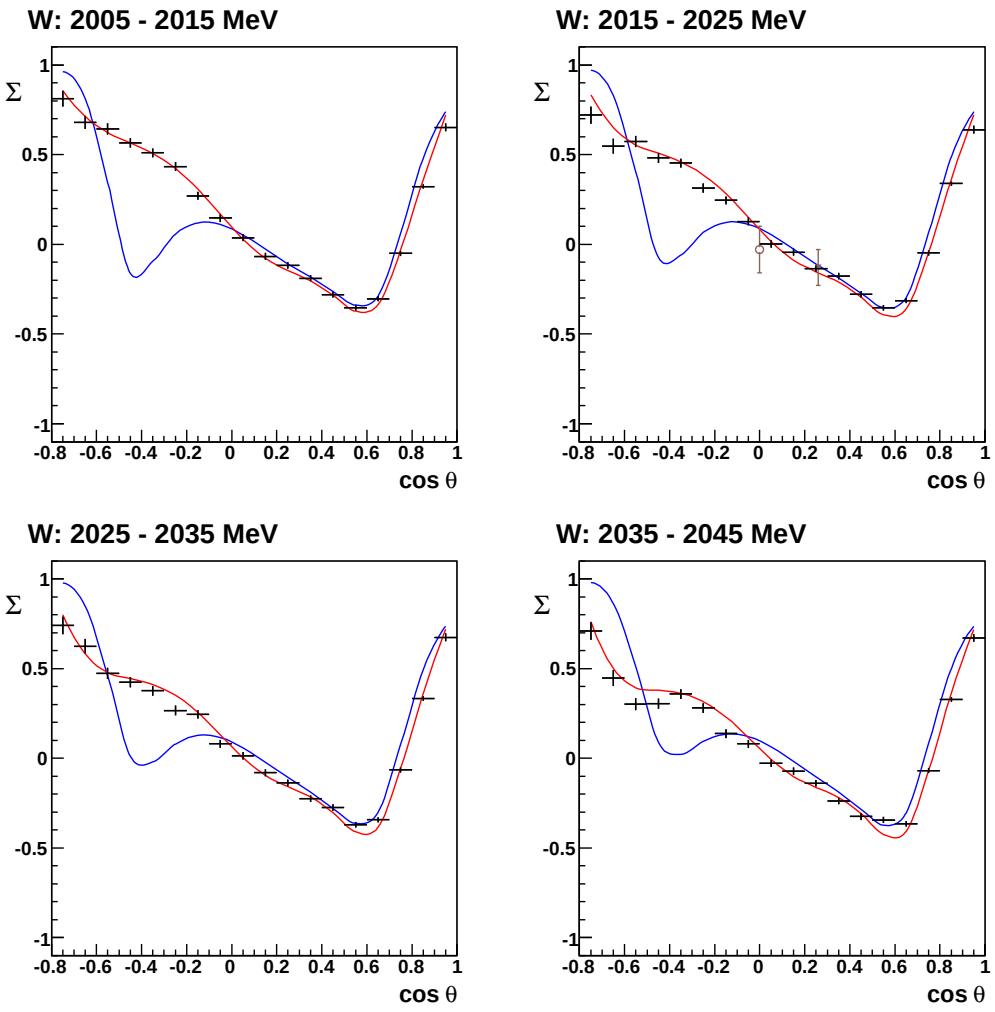

Figure 8.21: Beam asymmetry as a function of $\cos\theta$ for W 2005 – 2045 MeV, in 10 MeV wide bins, overlaid with SAID-09 (blue) and SAID-09-NEW (red) partial wave analysis solutions. Previous data from [97] and [99] shown with open circles and filled triangles respectively.

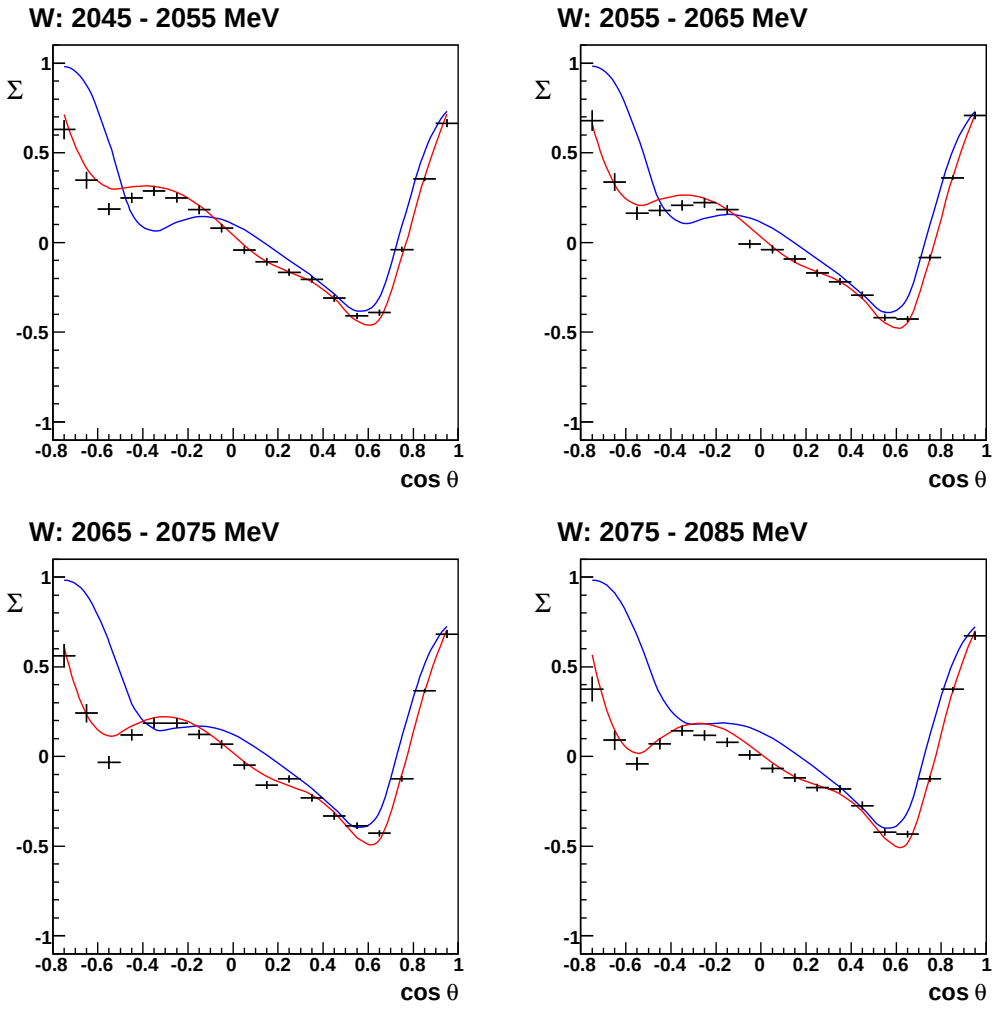

Figure 8.22: Beam asymmetry as a function of $\cos\theta$ for W 2045 – 2085 MeV, in 10 MeV wide bins, overlaid with SAID-09 (blue) and SAID-09-NEW (red) partial wave analysis solutions.

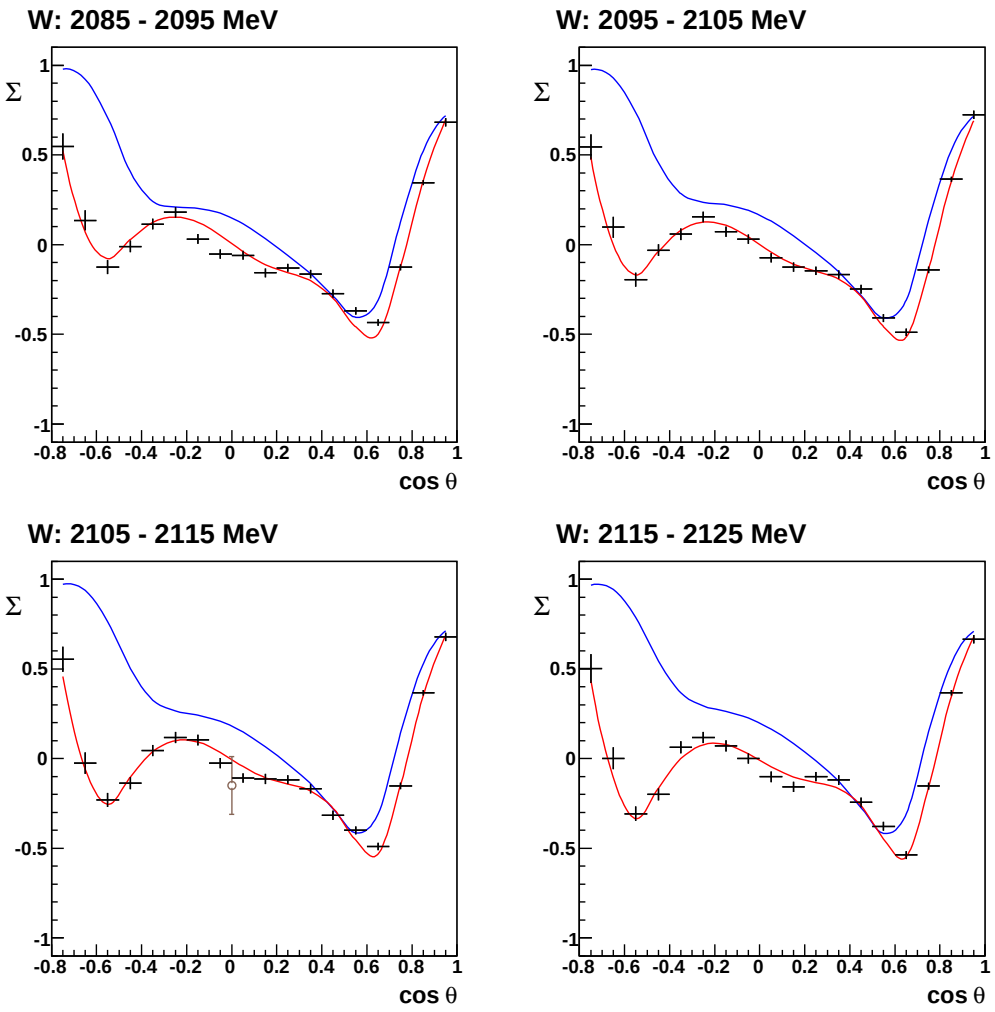

Figure 8.23: Beam asymmetry as a function of $\cos\theta$ for W 2085 – 2125 MeV, in 10 MeV wide bins, overlaid with SAID-09 (blue) and SAID-09-NEW (red) partial wave analysis solutions. Previous data from [97] shown with open circles.

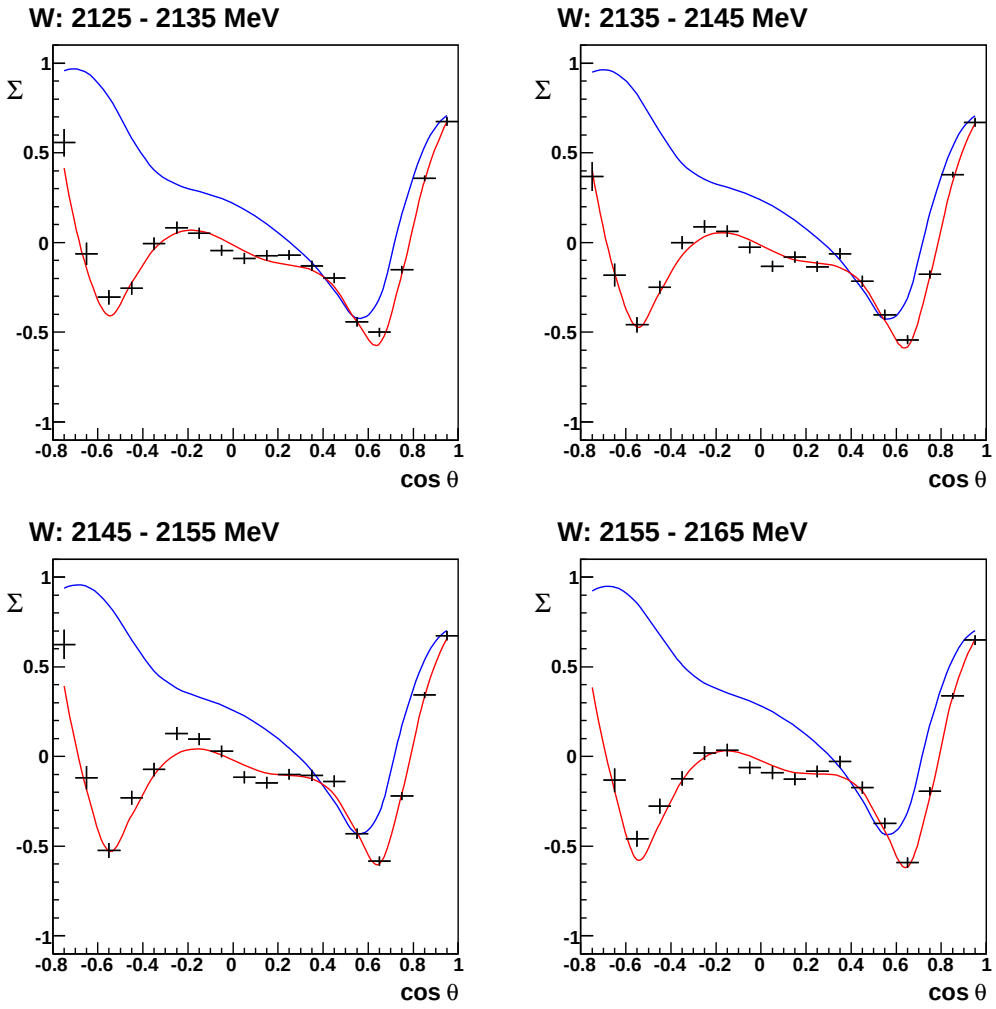

Figure 8.24: Beam asymmetry as a function of $\cos\theta$ for W 2125 – 2165 MeV, in 10 MeV wide bins, overlaid with SAID-09 (blue) and SAID-09-NEW (red) partial wave analysis solutions.

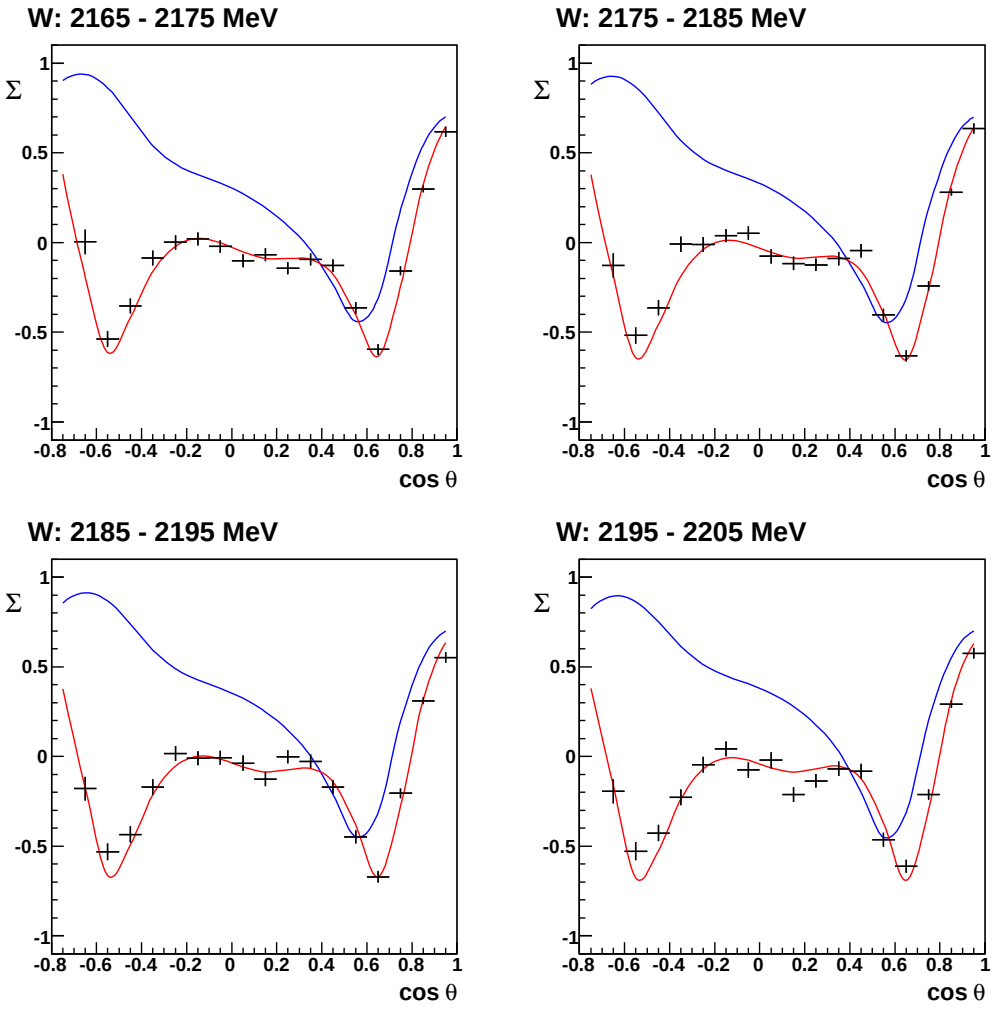

Figure 8.25: Beam asymmetry as a function of $\cos\theta$ for W 2165 – 2205 MeV, in 10 MeV wide bins, overlaid with SAID-09 (blue) and SAID-09-NEW (red) partial wave analysis solutions.

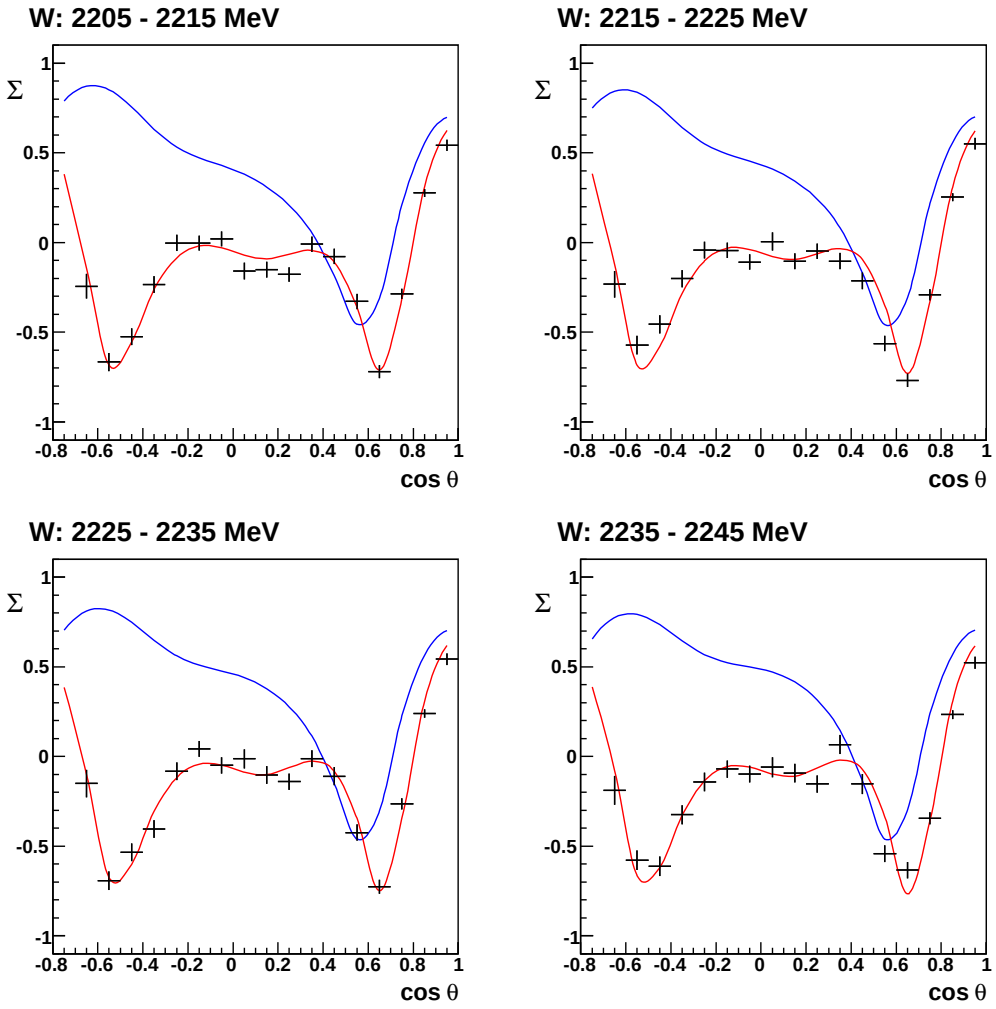

Figure 8.26: Beam asymmetry as a function of $\cos\theta$ for W 2205 – 2245 MeV, in 10 MeV wide bins, overlaid with SAID-09 (blue) and SAID-09-NEW (red) partial wave analysis solutions.

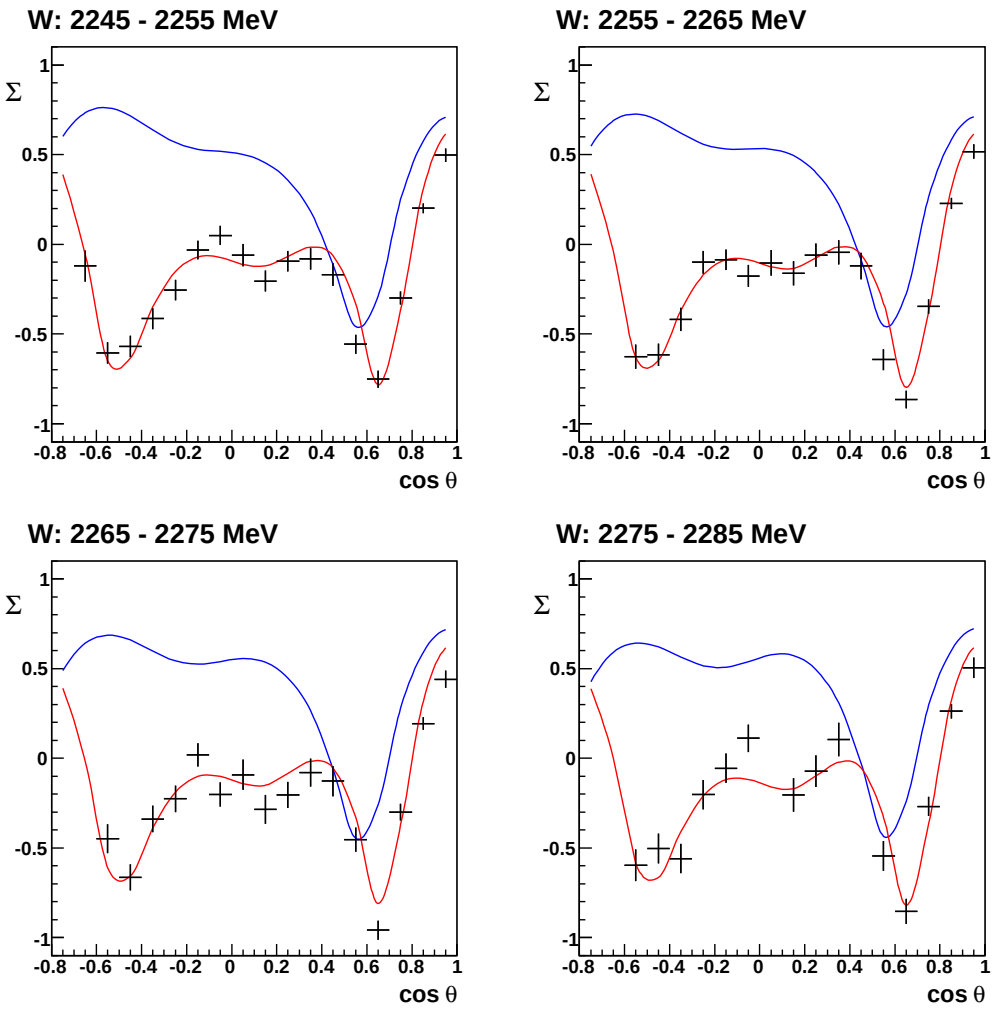

Figure 8.27: Beam asymmetry as a function of $\cos\theta$ for W 2245 – 2285 MeV, in 10 MeV wide bins, overlaid with SAID-09 (blue) and SAID-09-NEW (red) partial wave analysis solutions. Data points not available in the entire range of W due to limited statistics in several bins.

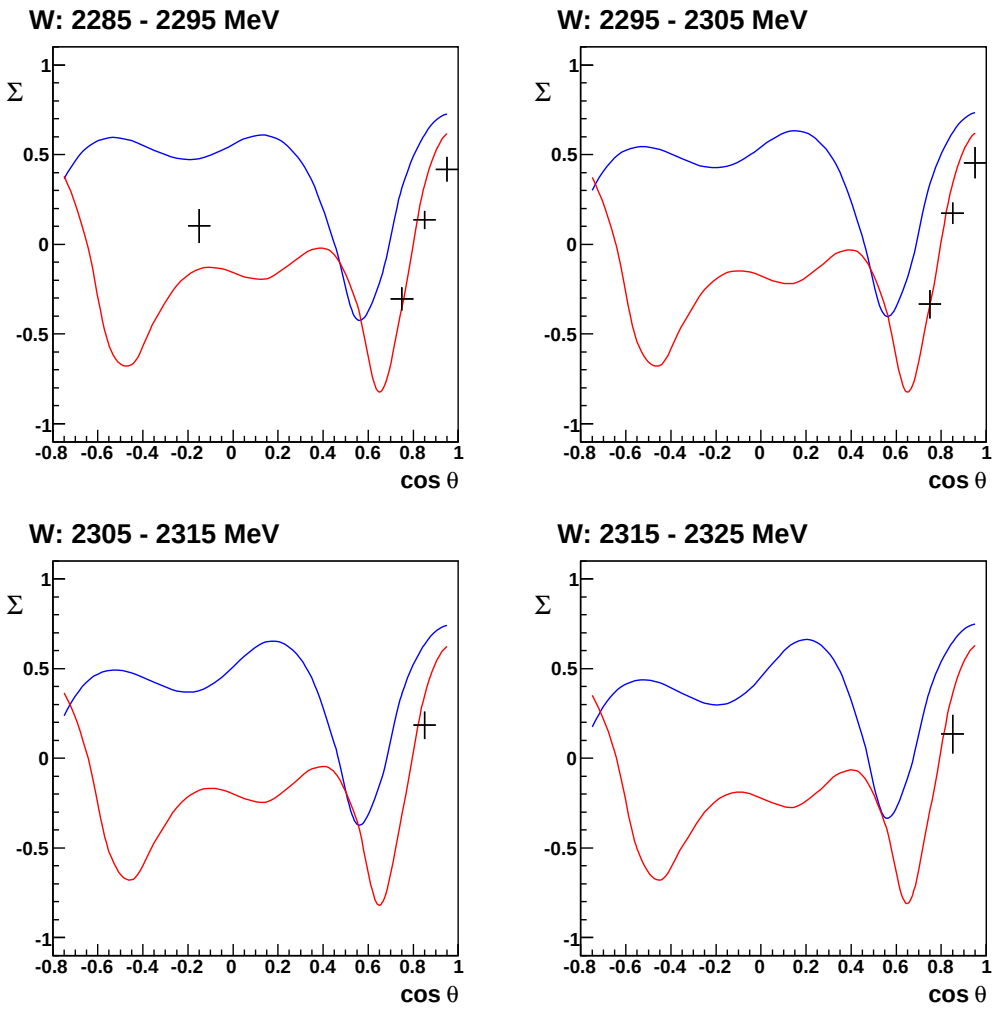

Figure 8.28: Beam asymmetry as a function of $\cos\theta$ for W 2285 – 2325 MeV, in 10 MeV wide bins, overlaid with SAID-09 (blue) and SAID-09-NEW (red) partial wave analysis solutions. Data points not available in the entire range of W due to limited statistics in the majority of bins.

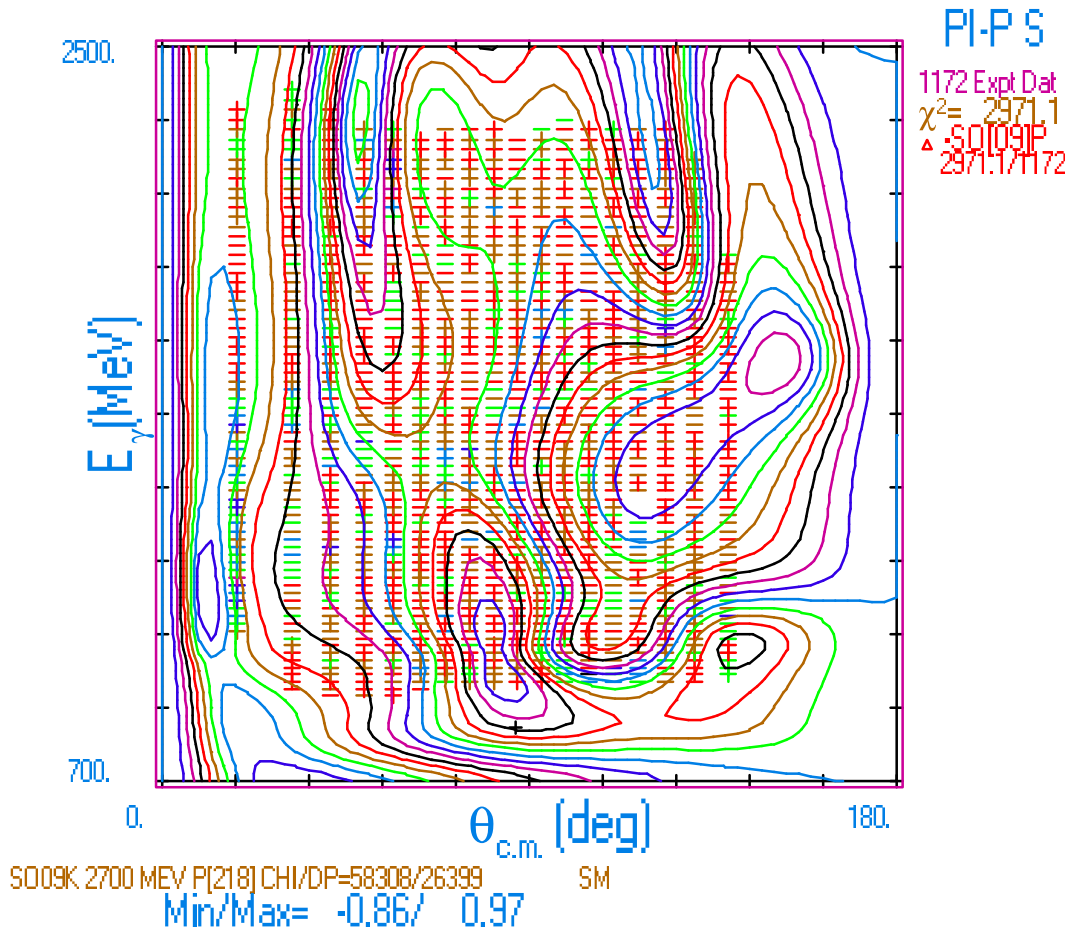

Figure 8.29: Contour plot of SAID-09-NEW beam asymmetry calculation carried out by [130] as a function of photon beam energy and θ overlaid over the grid of measured beam asymmetry points.

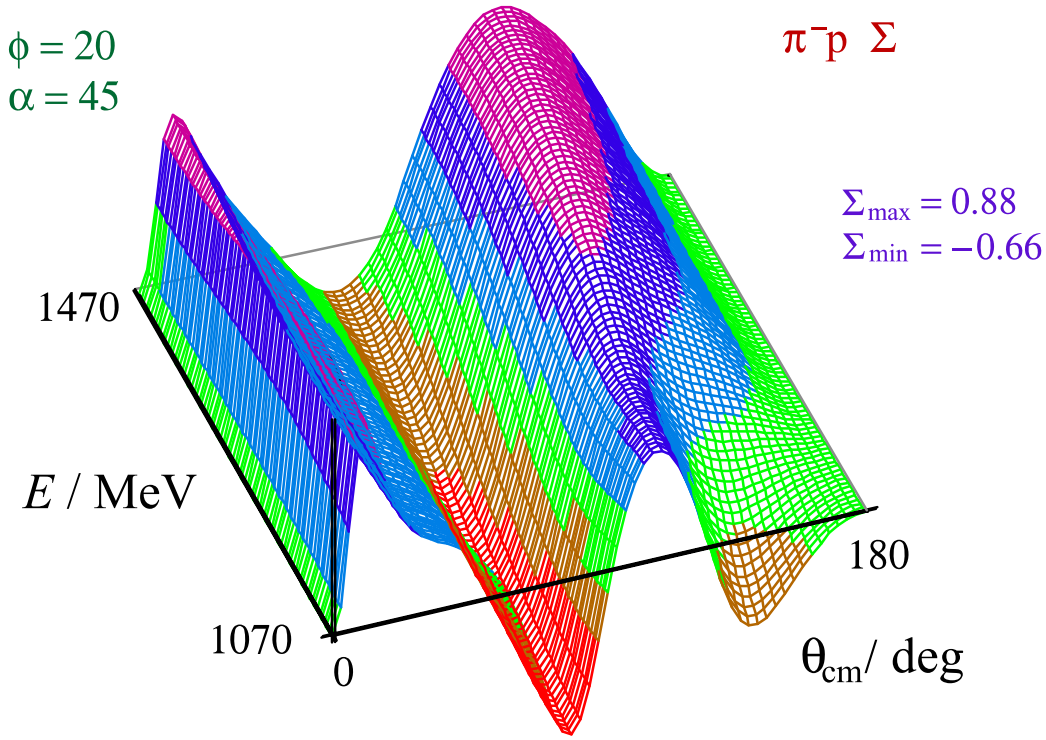

S009K 2700 MeV P[218] CHI/DP=58308/26399

Figure 8.30: Surface plot SAID-09-NEW beam asymmetry calculation carried out by [130] as a function of photon beam energy and θ.

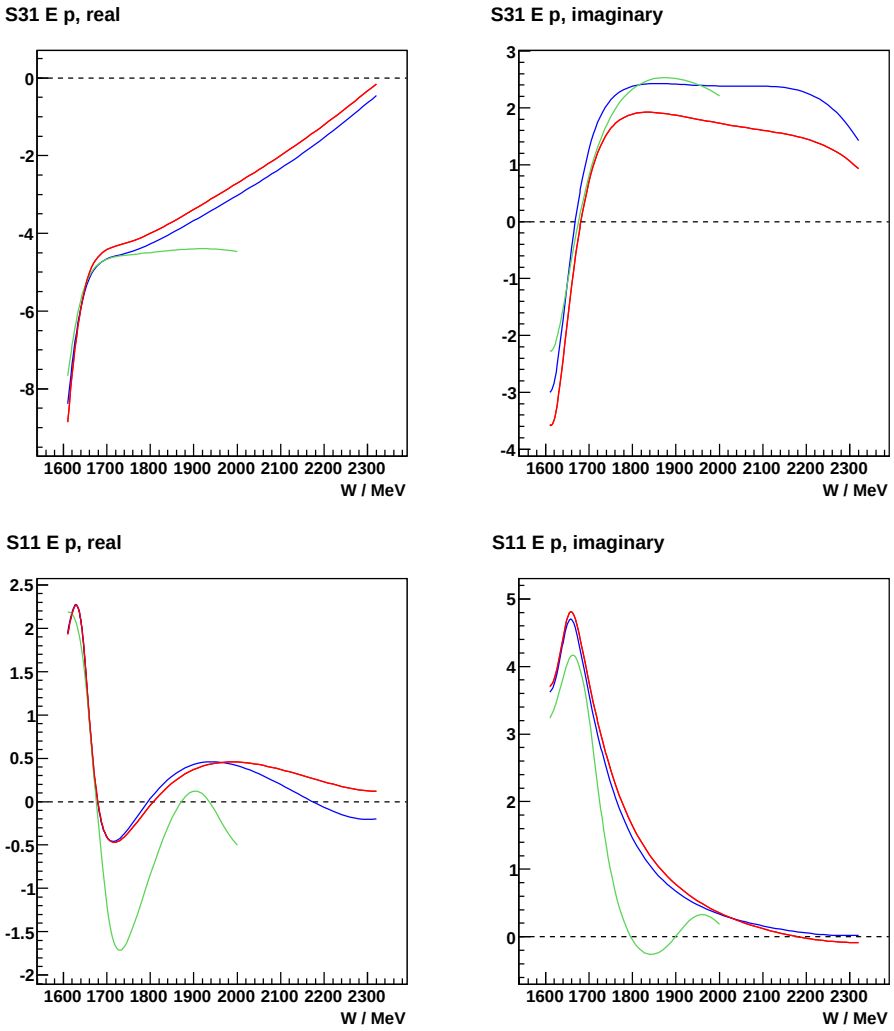

Figure 8.31: S_{31} and S_{11} electric multipoles for the proton, in units of am, extracted from the SAID-09 (blue), SAID-09-NEW (red) and MAID-07 (green) partial wave analyses by [130].

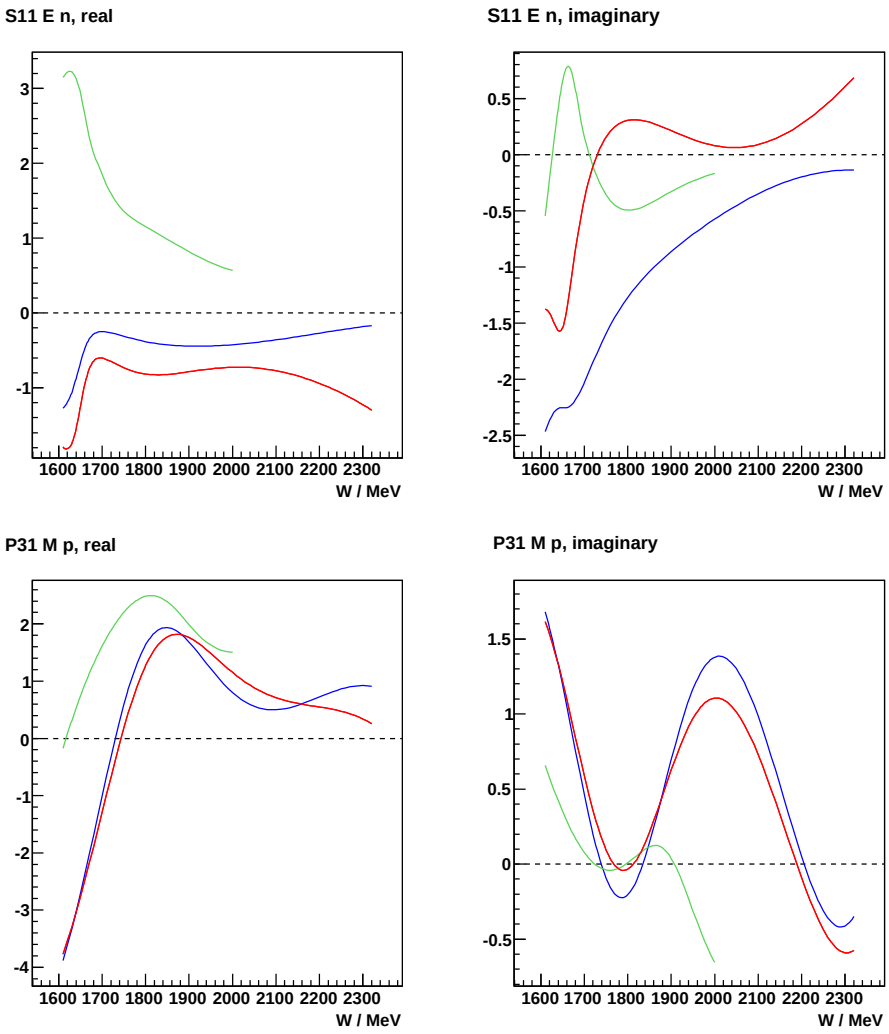

Figure 8.32: S_{11} electric multipoles for the neutron and P_{31} magnetic multipoles for the proton, in units of am, extracted from the SAID-09 (blue), SAID-09-NEW (red) and MAID-07 (green) partial wave analyses by [130].

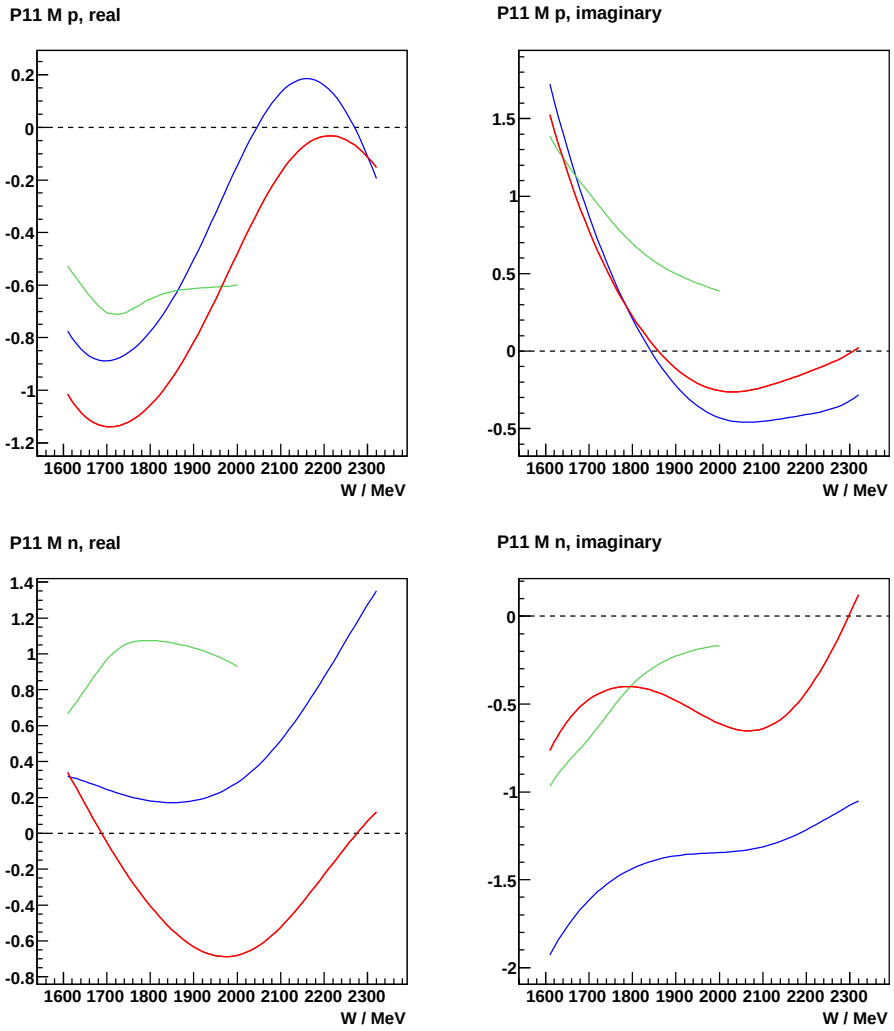

Figure 8.33: P_{11} magnetic multipoles for the proton and neutron, in units of am, extracted from the SAID-09 (blue), SAID-09-NEW (red) and MAID-07 (green) partial wave analyses by [130].

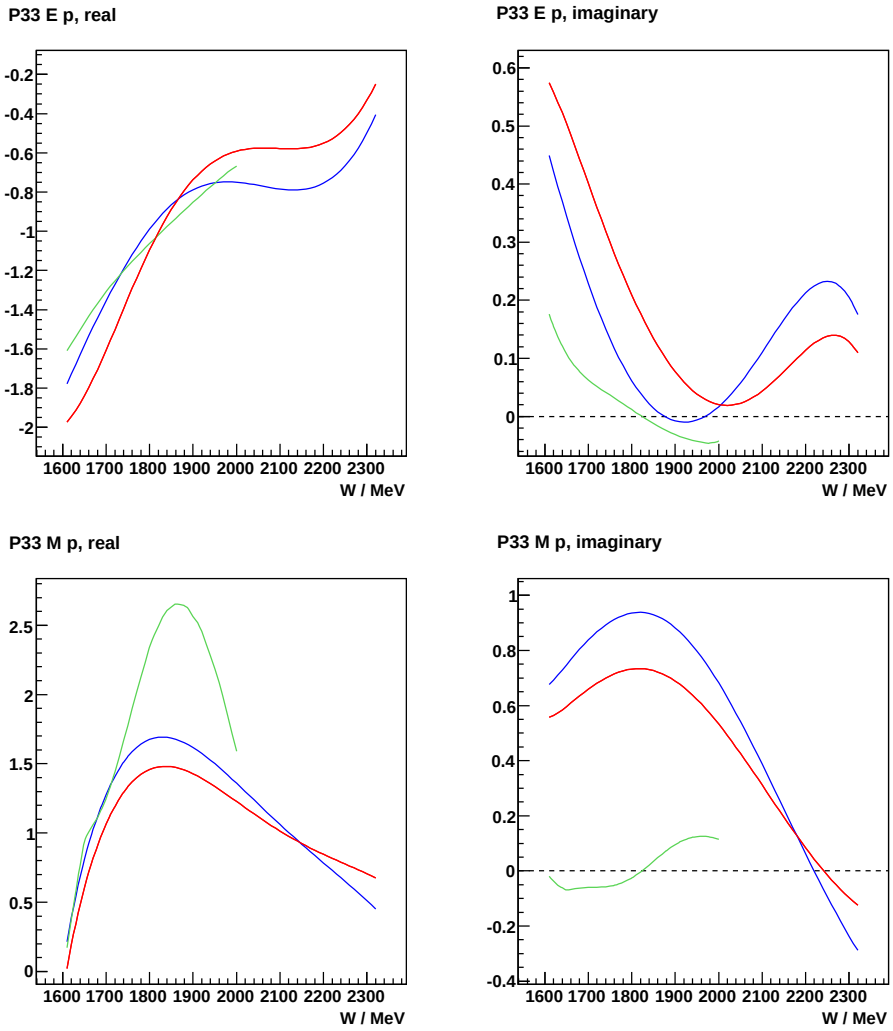

Figure 8.34: P_{33} electric and magnetic multipoles for the proton, in units of am, extracted from the SAID-09 (blue), SAID-09-NEW (red) and MAID-07 (green) partial wave analyses by [130].

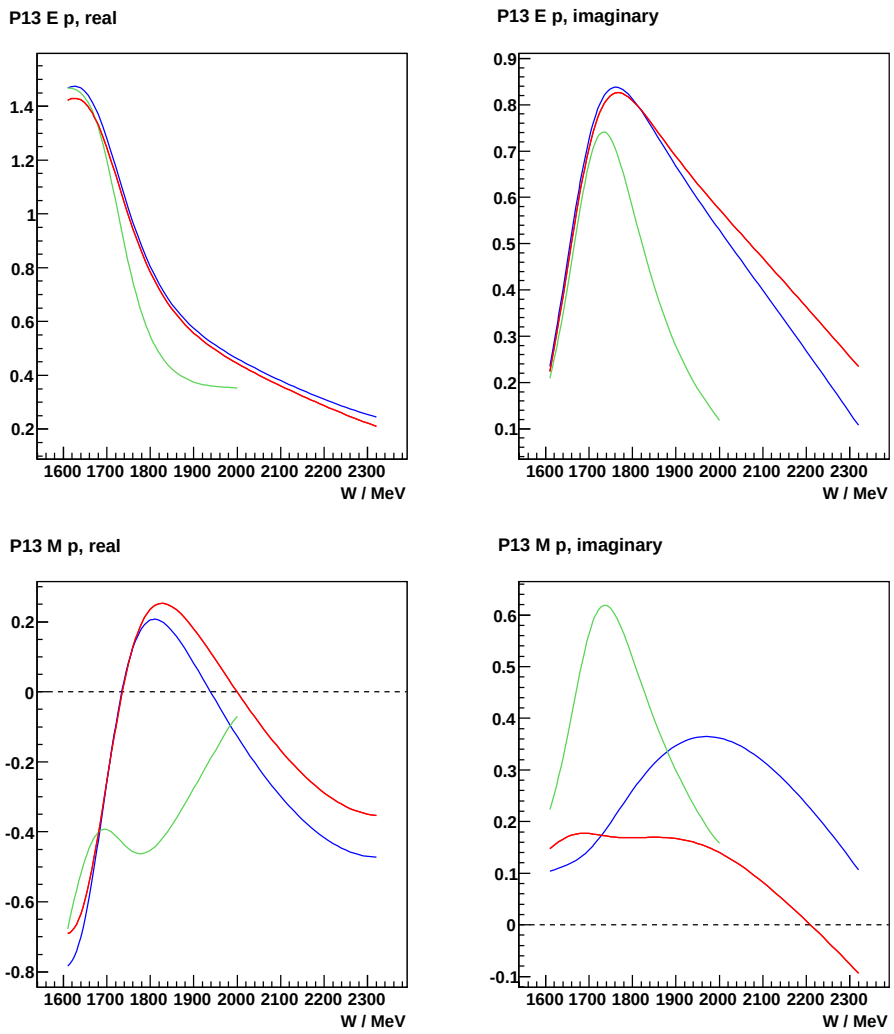

Figure 8.35: P_{13} electric and magnetic multipoles for the proton, in units of am, extracted from the SAID-09 (blue), SAID-09-NEW (red) and MAID-07 (green) partial wave analyses by [130].

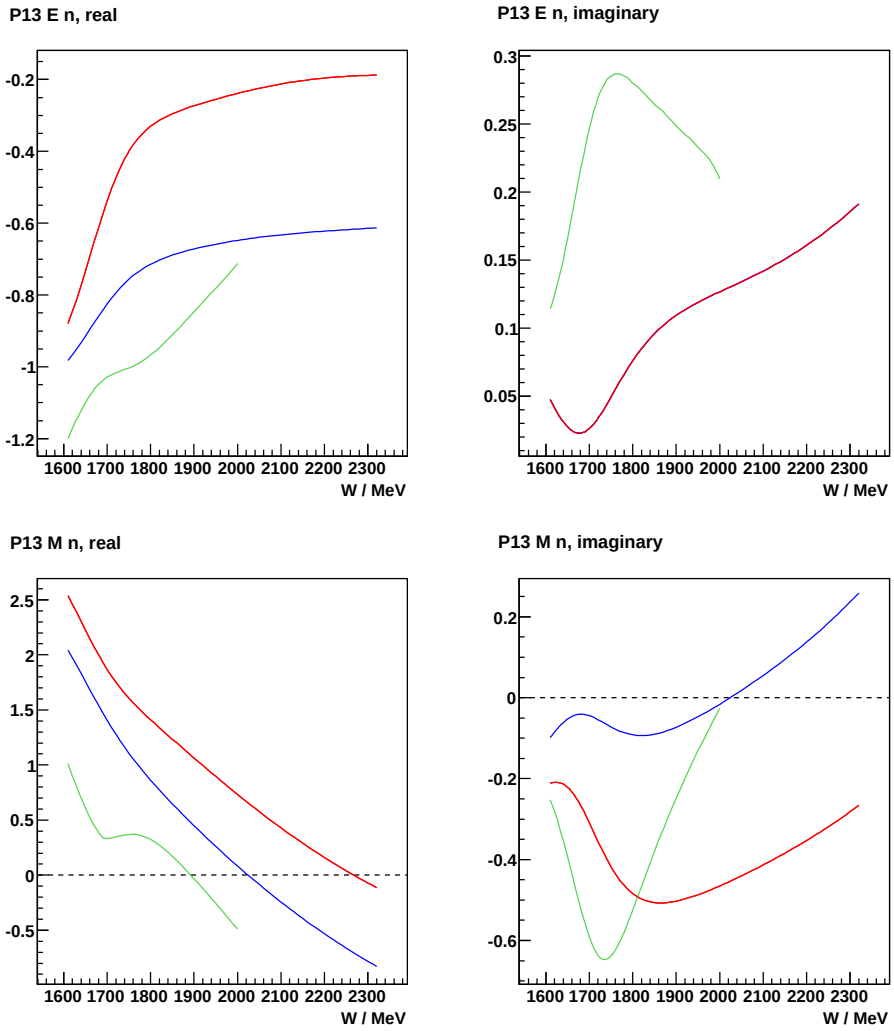

Figure 8.36: P_{13} electric and magnetic multipoles for the neutron, in units of am, extracted from the SAID-09 (blue), SAID-09-NEW (red) and MAID-07 (green) partial wave analyses by [130].

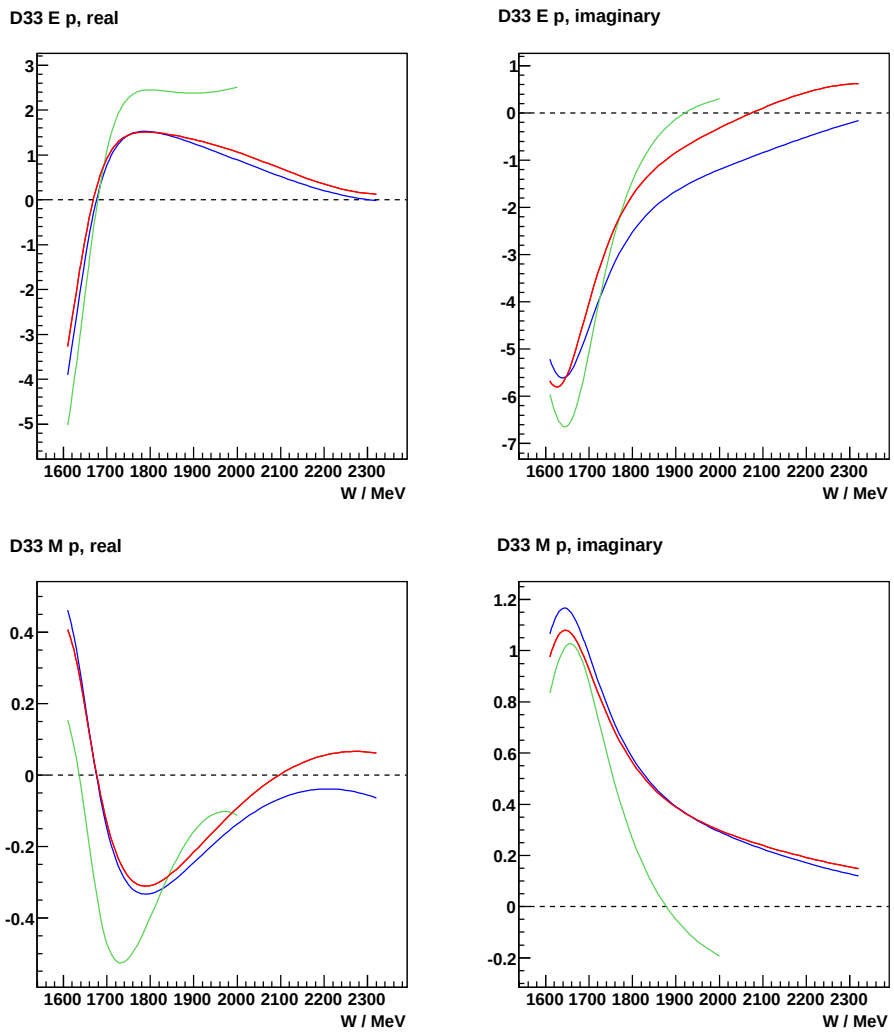

Figure 8.37: D_{33} electric and magnetic multipoles for the proton, in units of am, extracted from the SAID-09 (blue), SAID-09-NEW (red) and MAID-07 (green) partial wave analyses by [130].

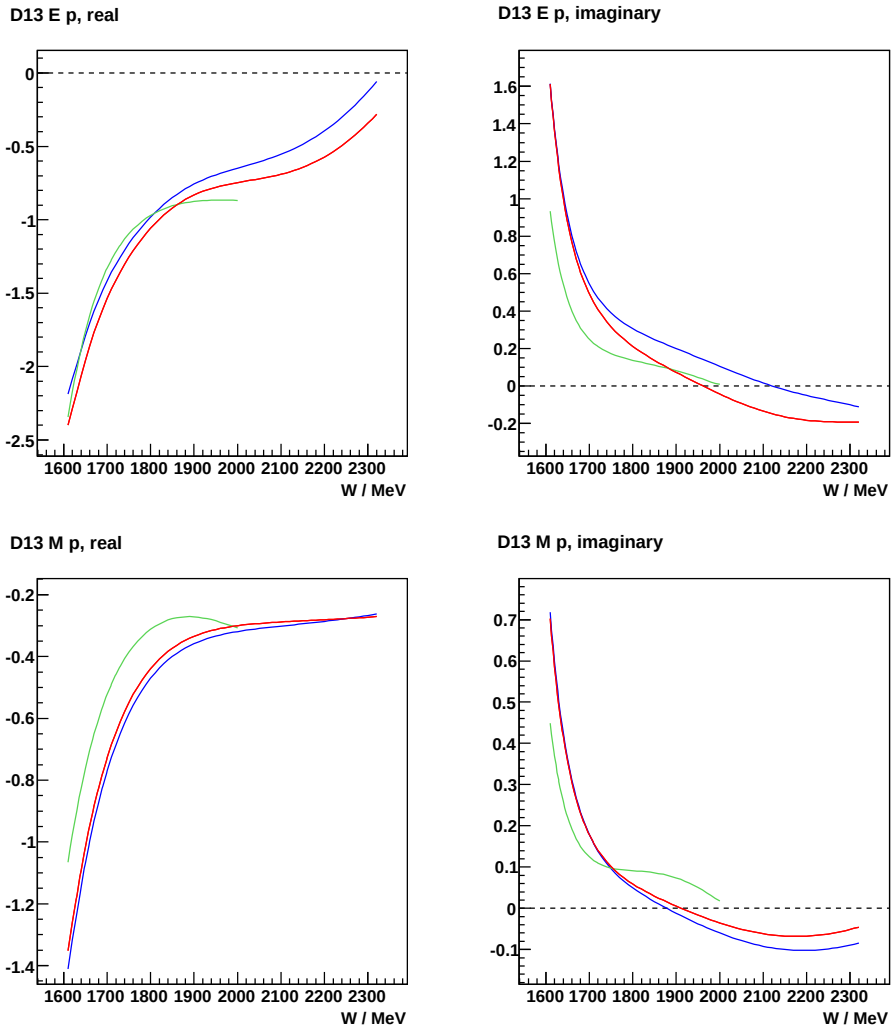

Figure 8.38: D_{13} electric and magnetic multipoles for the proton, in units of am, extracted from the SAID-09 (blue), SAID-09-NEW (red) and MAID-07 (green) partial wave analyses by [130].

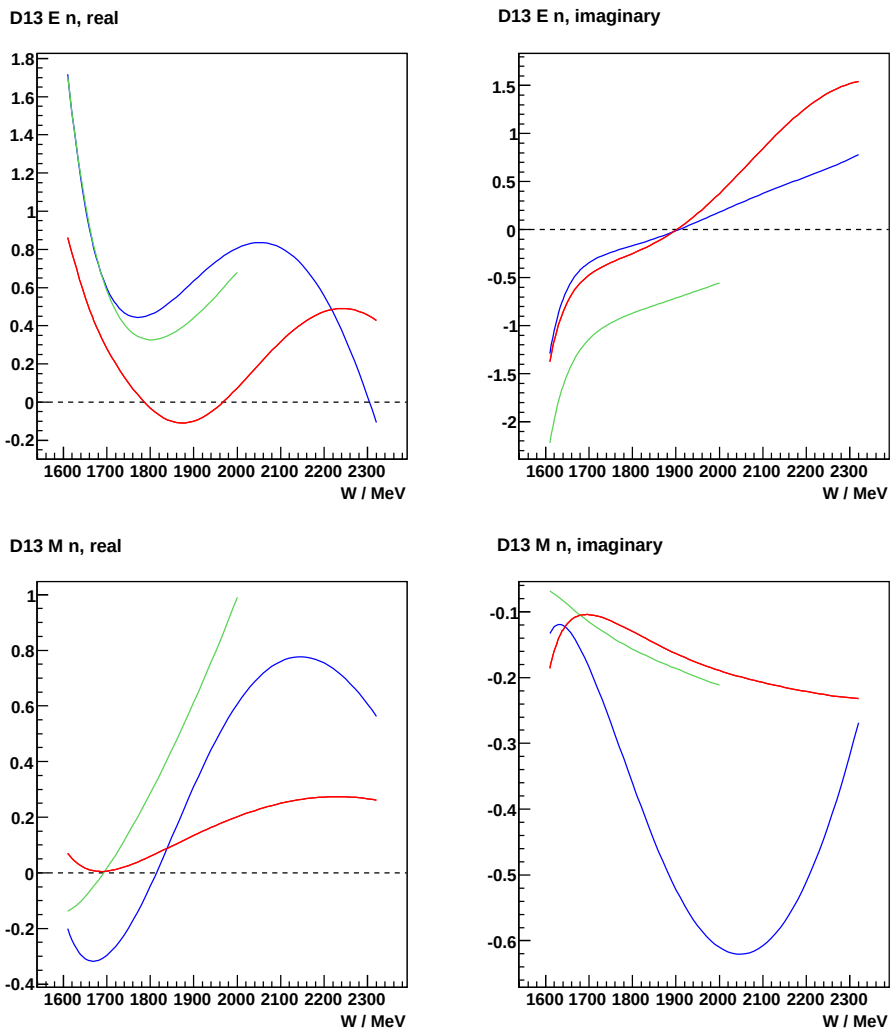

Figure 8.39: D_{13} electric and magnetic multipoles for the neutron, in units of am, extracted from the SAID-09 (blue), SAID-09-NEW (red) and MAID-07 (green) partial wave analyses by [130].

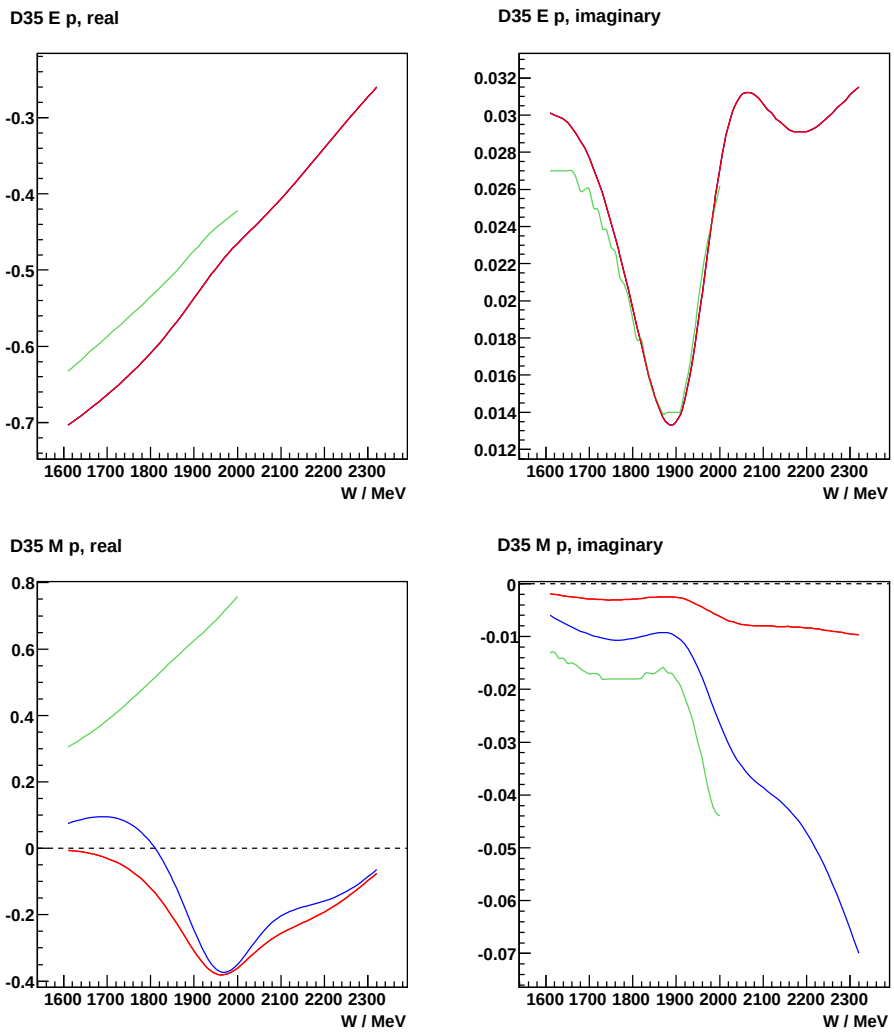

Figure 8.40: D_{35} electric and magnetic multipoles for the proton, in units of am, extracted from the SAID-09 (blue), SAID-09-NEW (red) and MAID-07 (green) partial wave analyses by [130].

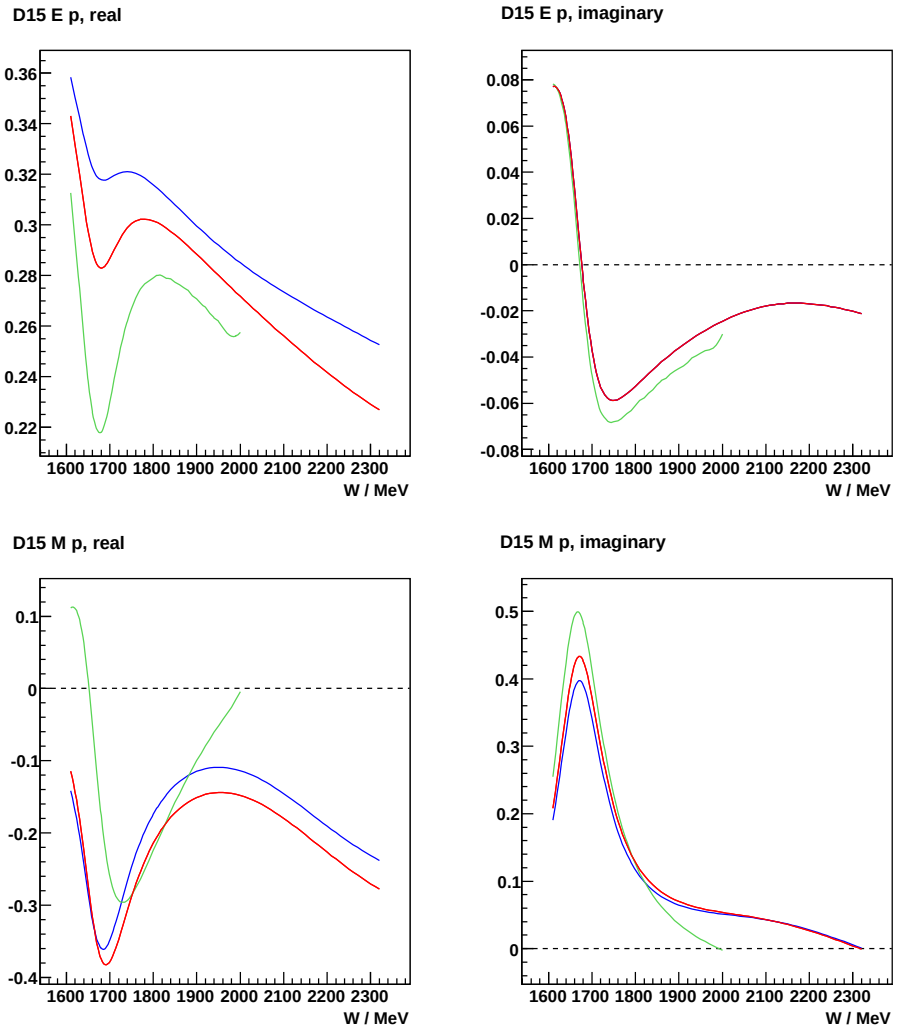

Figure 8.41: D_{15} electric and magnetic multipoles for the proton, in units of am, extracted from the SAID-09 (blue), SAID-09-NEW (red) and MAID-07 (green) partial wave analyses by [130].

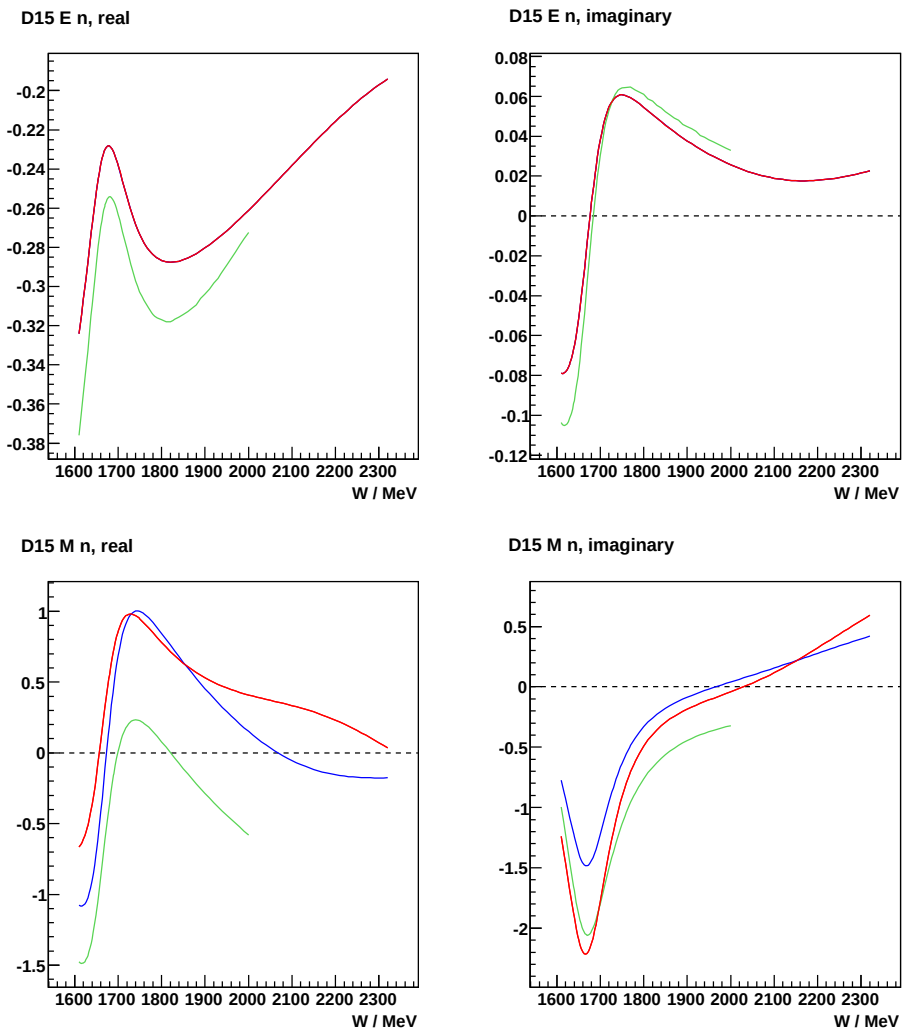

Figure 8.42: D_{15} electric and magnetic multipoles for the neutron, in units of am, extracted from the SAID-09 (blue), SAID-09-NEW (red) and MAID-07 (green) partial wave analyses by [130].

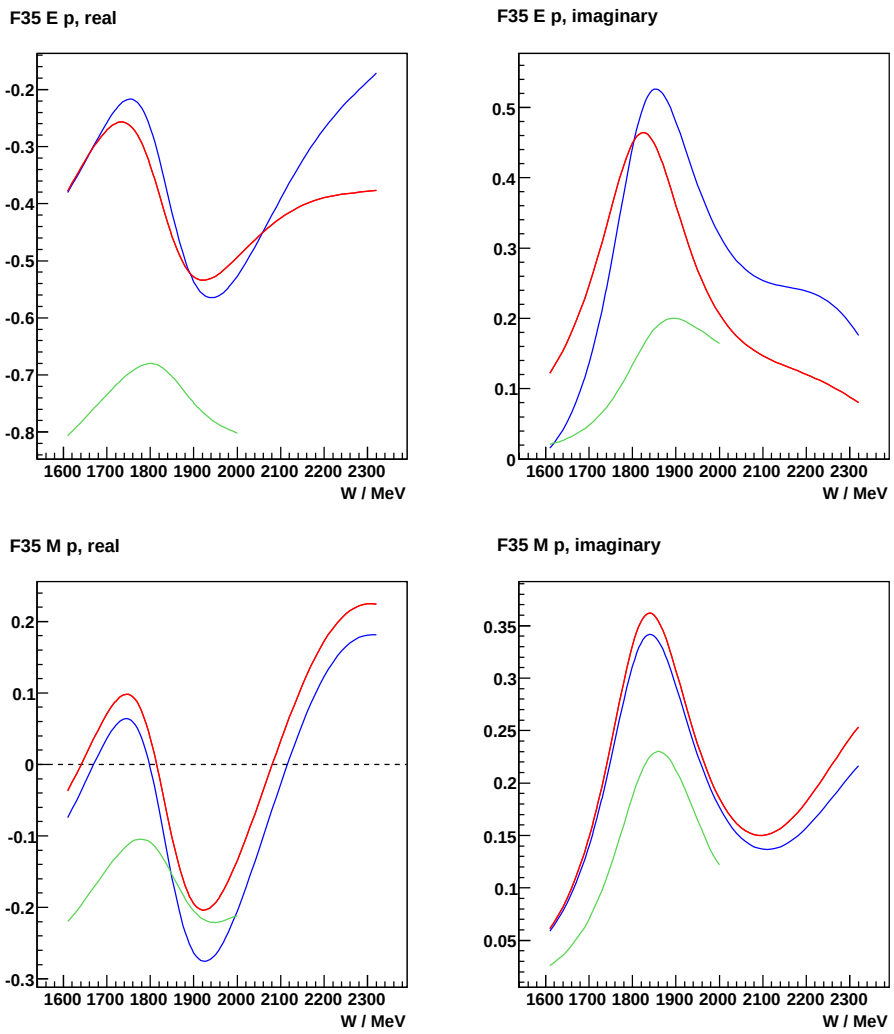

Figure 8.43: F_{35} electric and magnetic multipoles for the proton, in units of am, extracted from the SAID-09 (blue), SAID-09-NEW (red) and MAID-07 (green) partial wave analyses by [130].

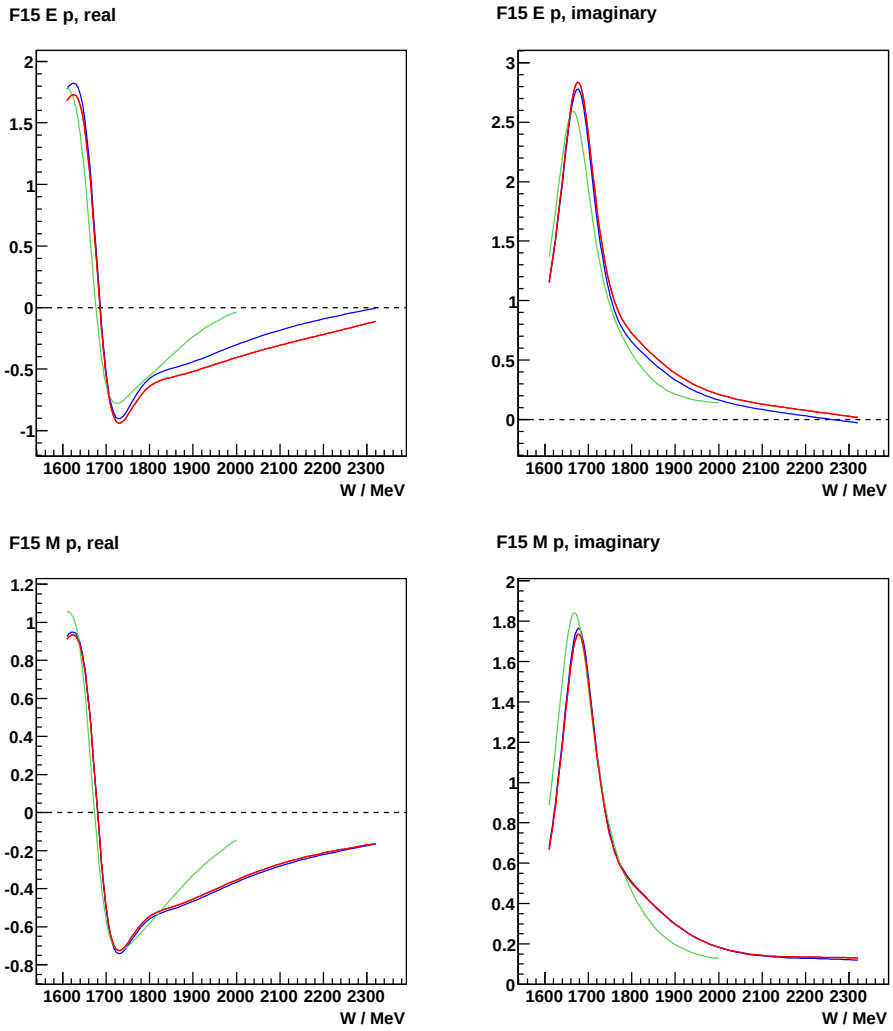

Figure 8.44: F_{15} electric and magnetic multipoles for the proton, in units of am, extracted from the SAID-09 (blue), SAID-09-NEW (red) and MAID-07 (green) partial wave analyses by [130].

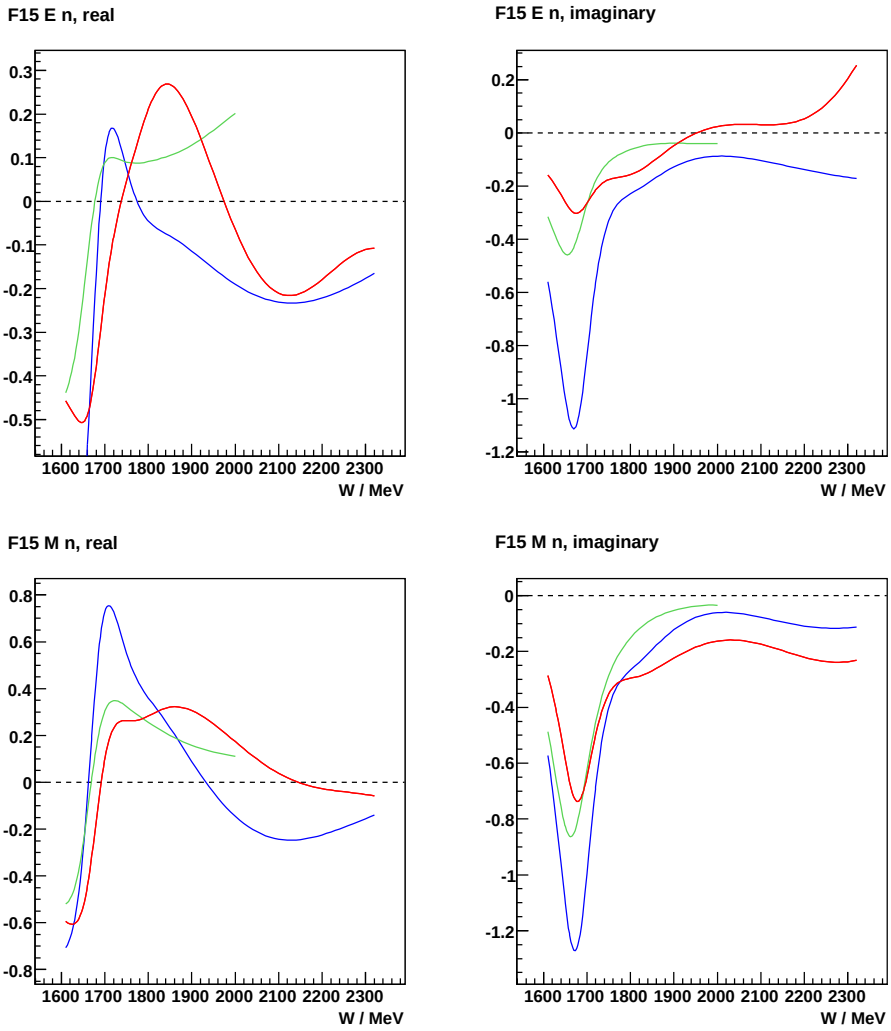

Figure 8.45: F_{15} electric and magnetic multipoles for the neutron, in units of am, extracted from the SAID-09 (blue), SAID-09-NEW (red) and MAID-07 (green) partial wave analyses by [130].

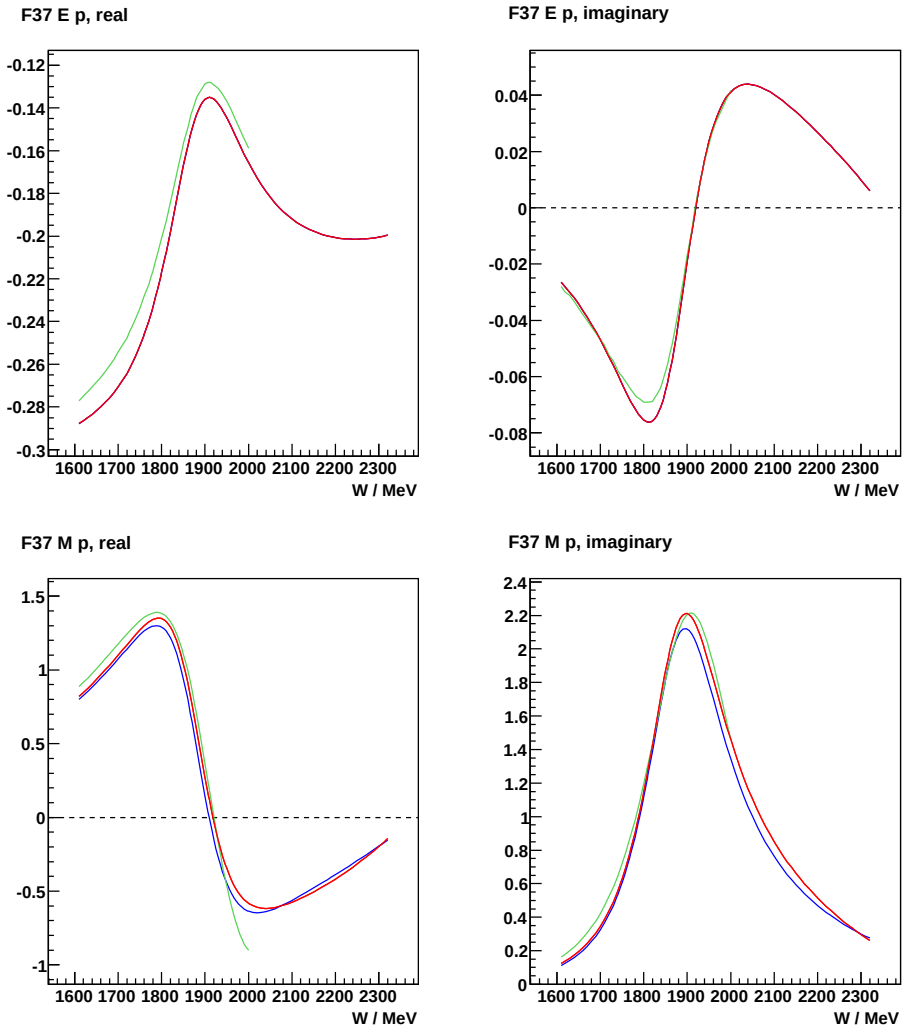

Figure 8.46: F_{37} electric and magnetic multipoles for the proton, in units of am, extracted from the SAID-09 (blue), SAID-09-NEW (red) and MAID-07 (green) partial wave analyses by [130].

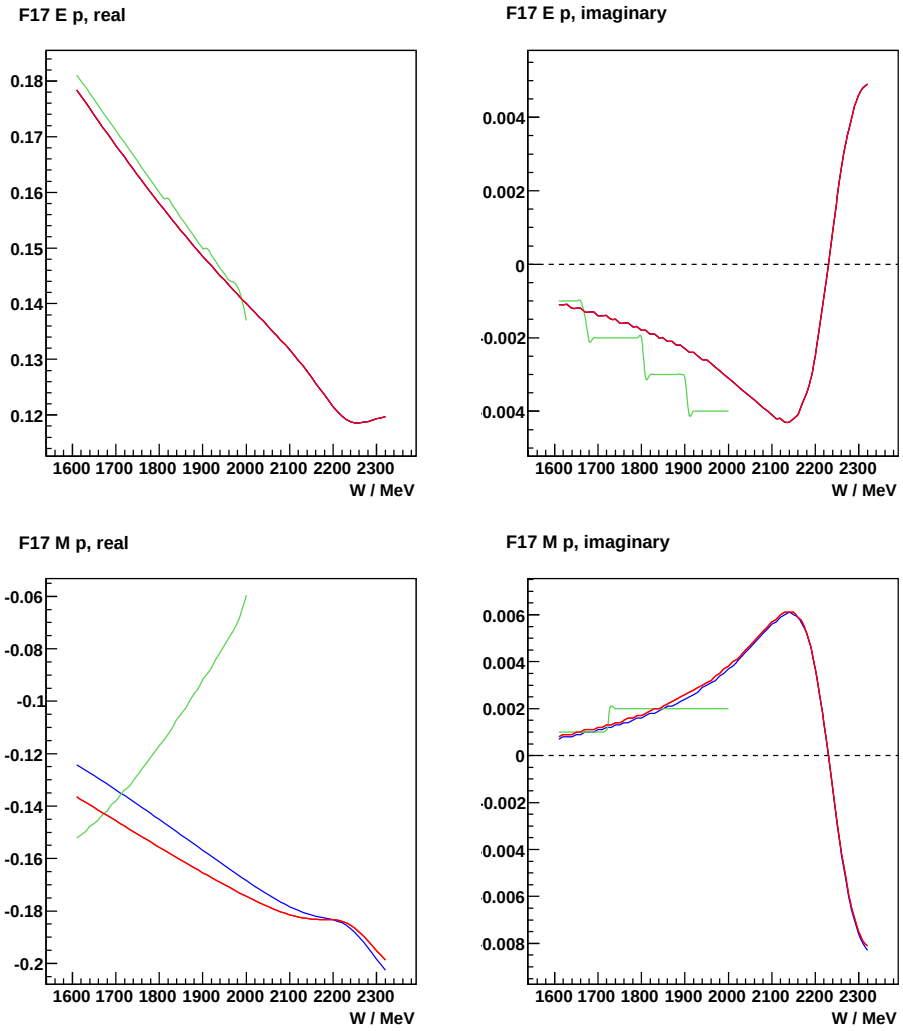

Figure 8.47: F_{17} electric and magnetic multipoles for the proton, in units of am, extracted from the SAID-09 (blue), SAID-09-NEW (red) and MAID-07 (green) partial wave analyses by [130].

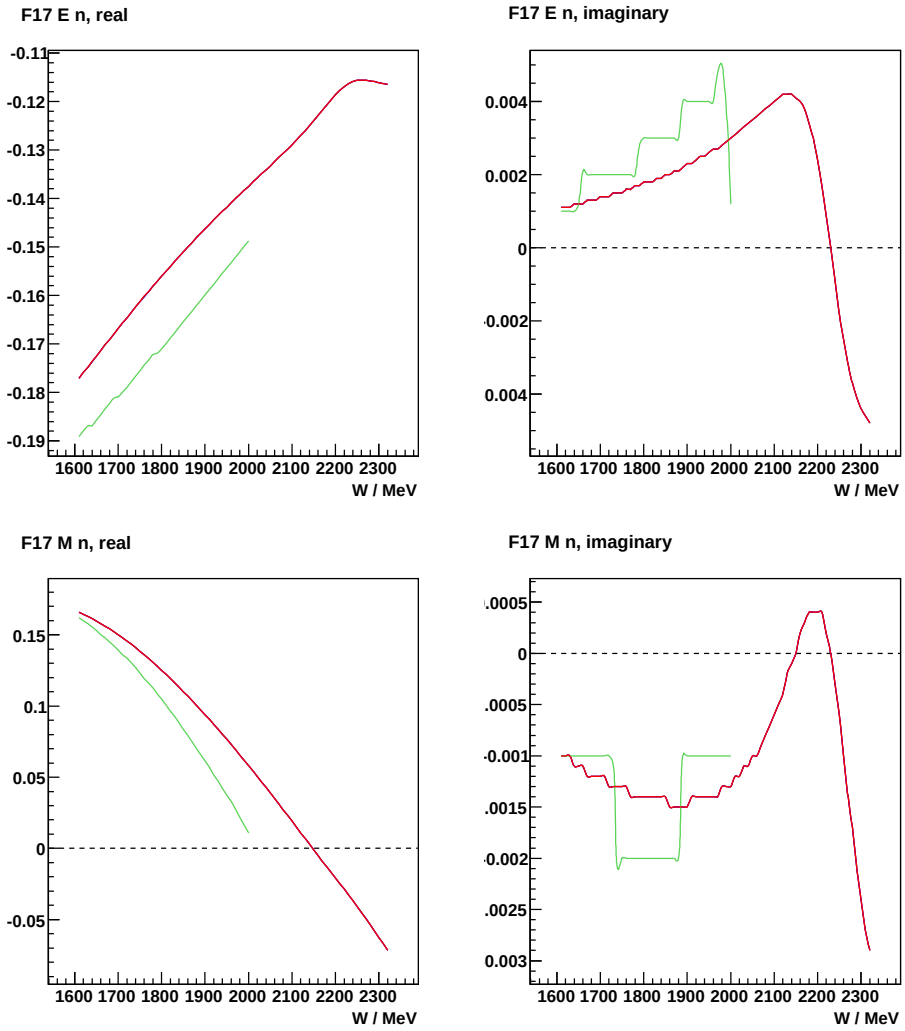

Figure 8.48: F_{17} electric and magnetic multipoles for the neutron, in units of am, extracted from the SAID-09 (blue), SAID-09-NEW (red) and MAID-07 (green) partial wave analyses by [130].

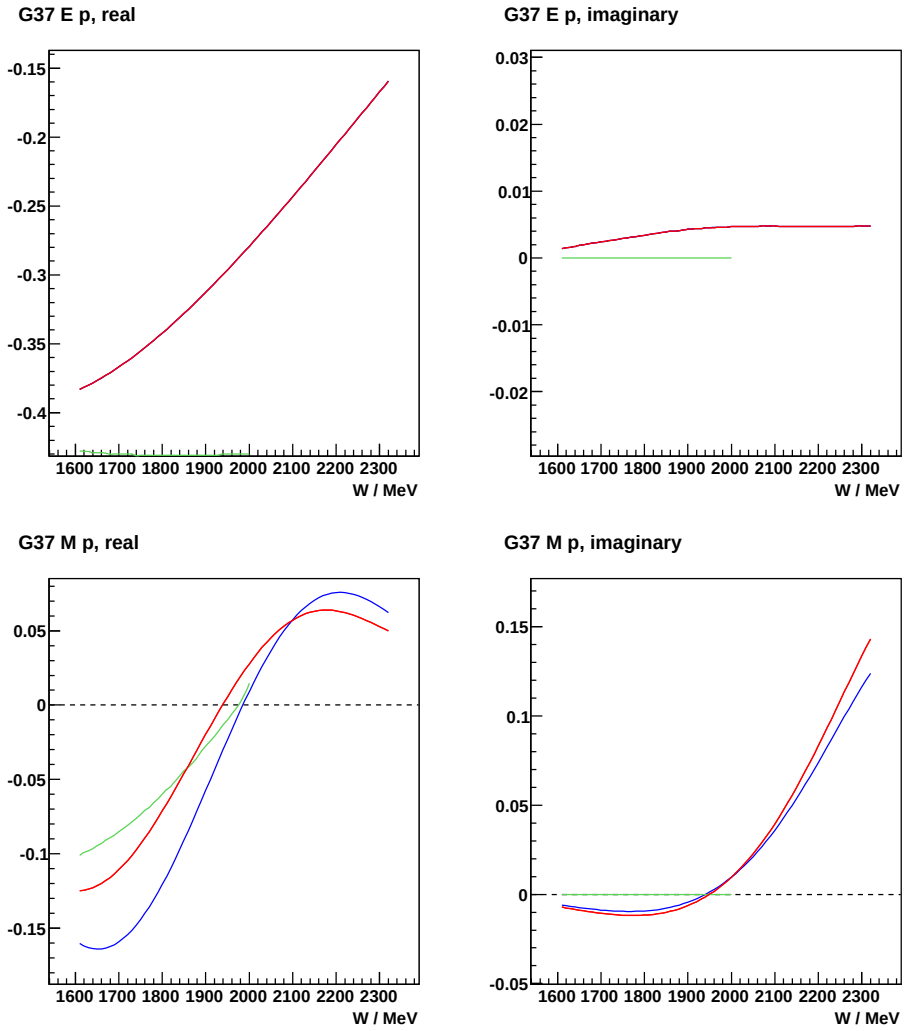

Figure 8.49: G_{37} electric and magnetic multipoles for the proton, in units of am, extracted from the SAID-09 (blue), SAID-09-NEW (red) and MAID-07 (green) partial wave analyses by [130].

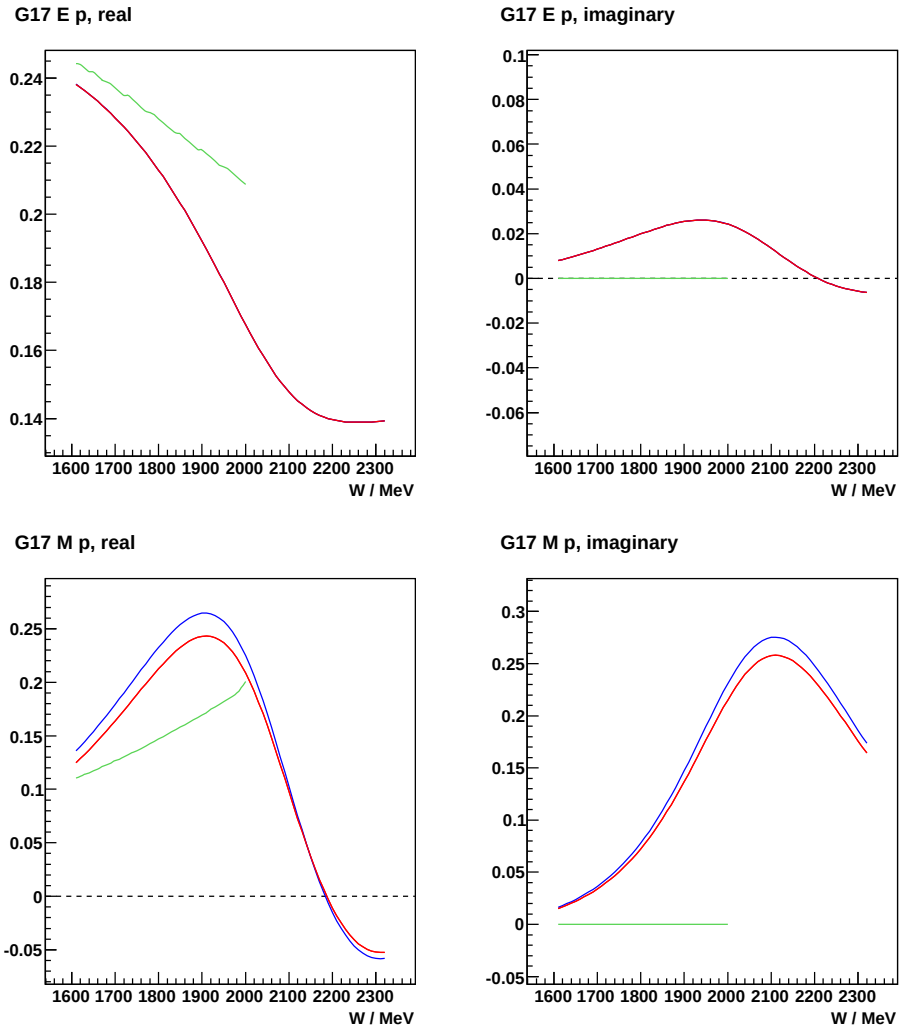

Figure 8.50: G_{17} electric and magnetic multipoles for the proton, in units of am, extracted from the SAID-09 (blue), SAID-09-NEW (red) and MAID-07 (green) partial wave analyses by [130].

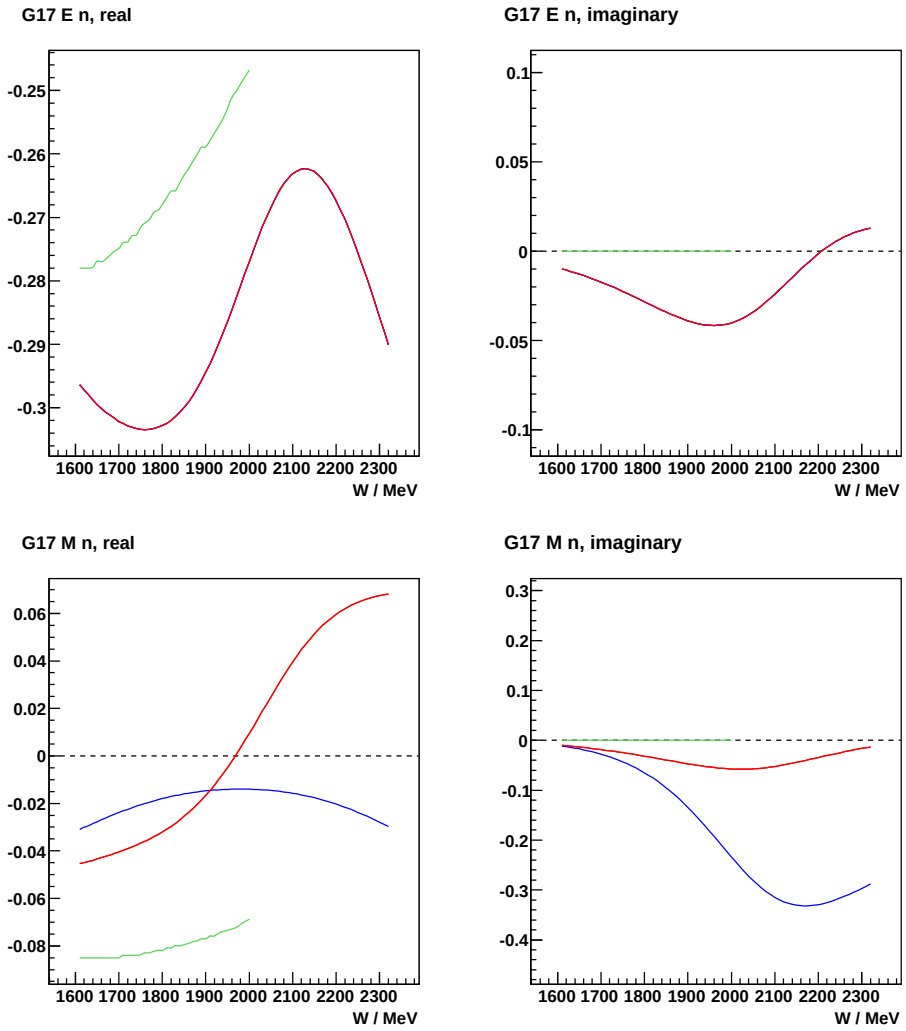

Figure 8.51: G_{17} electric and magnetic multipoles for the neutron, in units of am, extracted from the SAID-09 (blue), SAID-09-NEW (red) and MAID-07 (green) partial wave analyses by [130].

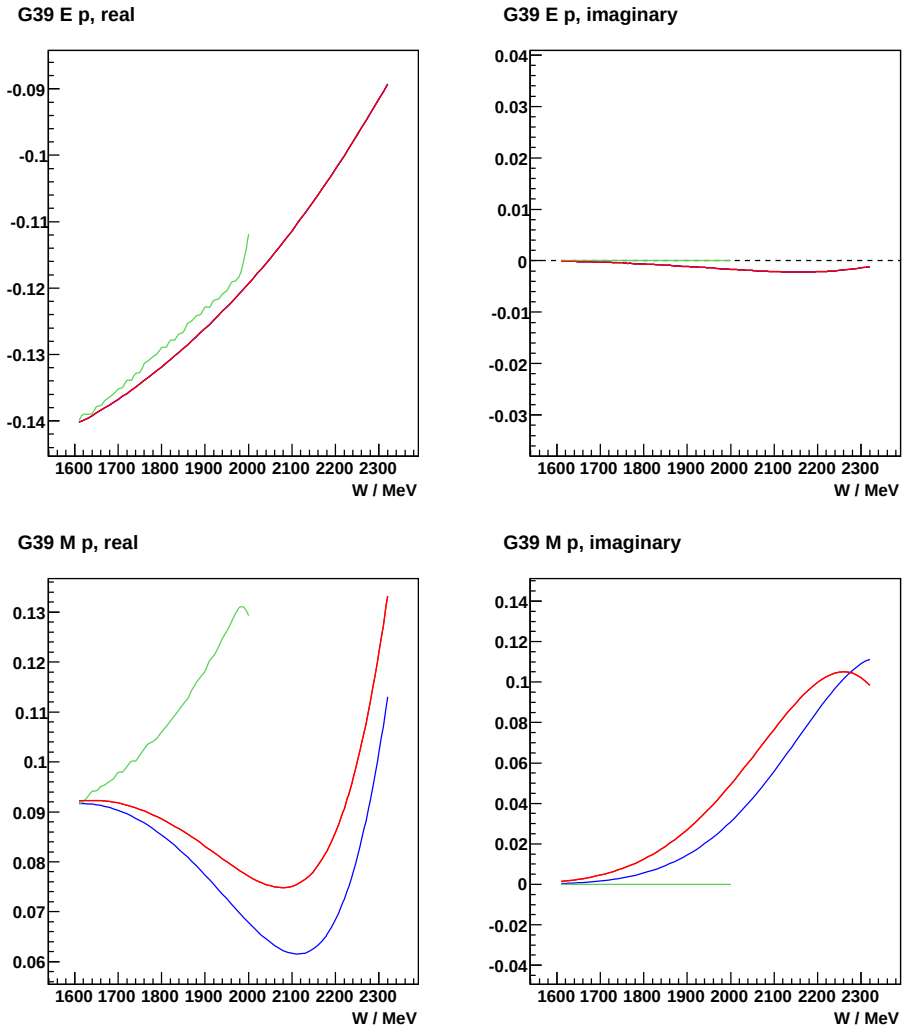

Figure 8.52: G_{39} electric and magnetic multipoles for the proton, in units of am, extracted from the SAID-09 (blue), SAID-09-NEW (red) and MAID-07 (green) partial wave analyses by [130].

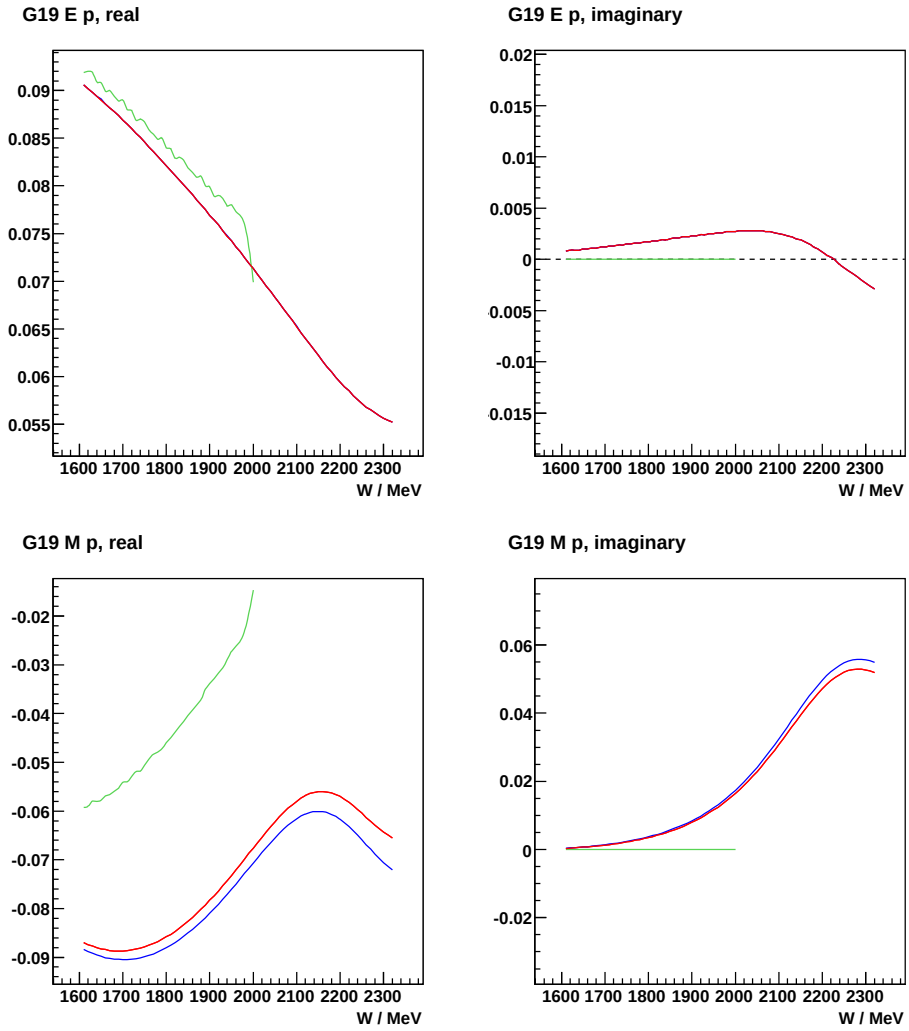

Figure 8.53: G_{19} electric and magnetic multipoles for the proton, in units of am, extracted from the SAID-09 (blue), SAID-09-NEW (red) and MAID-07 (green) partial wave analyses by [130].

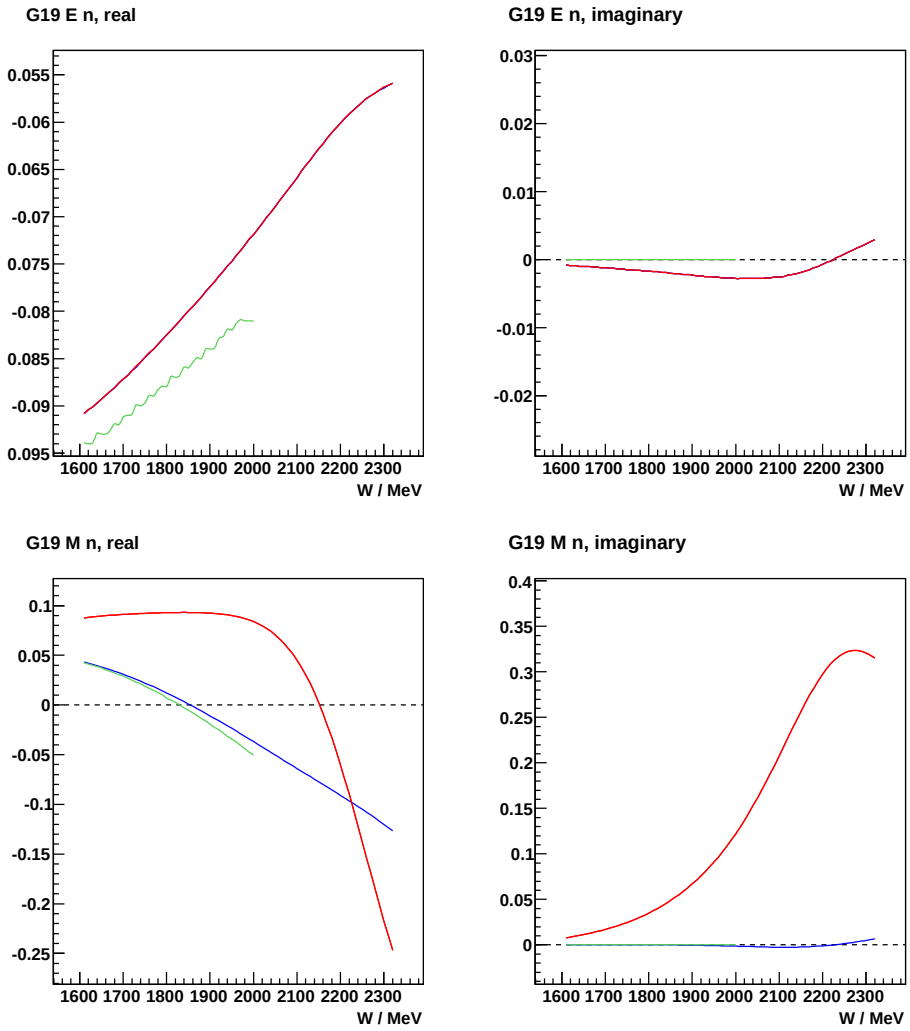

Figure 8.54: G_{19} electric and magnetic multipoles for the neutron, in units of am, extracted from the SAID-09 (blue), SAID-09-NEW (red) and MAID-07 (green) partial wave analyses by [130].

Chapter 9

Conclusions and Outlook

A very high statistics measurement of the beam asymmetry, Σ, in π^- photoproduction from the neutron has been obtained in the invariant mass range 1610 – 2320 MeV and in cosine of the meson production centre-of-mass angle ($\cos\theta$) in the range -0.8 – 1.0. The statistics and resolution of the measurement allowed a bin width of 10 MeV in the invariant mass and 0.1 in $\cos\theta$. This has greatly increased the world data set, adding 1179 new data points to the previously available 67.

The new data is in good general agreement with the previous measurements and has been compared to the latest partial wave analysis solutions based on fits constrained to the current world data set of meson photoproduction (MAID and SAID analyses). Both the MAID-07 and SAID-09 PWA solutions did not, however, give a good description of the new asymmetry data. A new partial wave analysis, SAID-09-NEW, was therefore performed, which included the new data set [130]. This analysis, as might be expected, provides a much better agreement with the new data. The quality of the SAID-09-NEW fit is good, having a χ^2 per degree of freedom of ~2.6.

The effect of the new data on the partial wave analysis was studied by comparison of the extracted multipoles from the MAID-07, SAID-09 and SAID-09-NEW solutions. The inclusion of the present measurement of the beam asymmetry into the SAID-09-NEW analysis has had a dramatic effect on the multipole amplitudes extracted, in particular for those from the neutron. Their comparison to the SAID-09 solution shows that the new data has resulted in the greatest changes to the P_{11}, P_{13}, D_{13}, D_{35}, F_{15}, G_{17} and G_{19} magnetic partial waves and so will be expected to have the biggest impact on the nucleon resonances contributing to them. Preliminary analysis

from the SAID PWA group indicates that very significant changes in the helicity amplitudes for a range of resonances can be expected. This analysis is underway by the SAID PWA group and will be included in the publication resulting from this work. The new data set will also be used to provide an updated partial wave analysis using the MAID framework. The comparison of these results with those of SAID are an important additional step because of the different approaches, including different treatment of background processes and of the inclusion of resonances in the two PWA frameworks.

As well as the electromagnetic properties of resonances the new data will also challenge the actual composition of the nucleon resonance spectrum. This will entail further investigation into the improvements of the PWA solution with the new data, for example by inclusion of missing or poorly established resonances into the MAID analysis. The investigations are currently underway by the PWA groups. However, it should be remarked that the current data set was taken in the context of a major world programme of measurements in meson photoproduction and that the most powerful statements on the nucleon resonance spectrum will be made when this data is combined with the other measurements of single- and double-polarisation observables in a combined PWA. The current data is a major step forward towards achieving this "complete" set of measurements to fully constrain the partial wave analyses for the first time.

Appendix A

Frames of measurement

The reconstruction of the photonuclear reaction starts in the laboratory frame of the detector, CLAS, and finishes in the invariant mass (CM) frame of the reaction, in which all quantities pertinent to the extraction of the beam asymmetry are calculated.

The axes of the lab frame follow standard nomenclature, where z is parallel to the beam-axis, x is perpendicular to it and parallel to the laboratory floor and y aligns along the last spatial dimension.

Transformation into the CM frame is achieved through a Lorentz boost into the frame moving with velocity (as a fraction of that of light, c)

$$\vec{\beta} = \frac{\vec{p_\gamma}}{E_\gamma + m_n} \tag{A.1}$$

where p_γ is the photon momentum, E_γ is the energy of the incoming photon and m_n is the nucleon mass. In this frame the co-ordinate axes are conventionally defined as follows:

- z'-axis parallel to the momentum transfer in the reaction. In the CM frame, this is equivalent to the photon direction
- y'-axis perpendicular to the reaction plane:

  $$\vec{y'} = \frac{\vec{p_\gamma} \times \vec{p_\pi}}{|\vec{p_\gamma}||\vec{p_\pi}|}$$

  where p represents the momentum of the photon or meson

- x'-axis chosen to complete a right-handed co-ordinate system:

$$\vec{x'} = \vec{y'} \times \vec{z'}$$

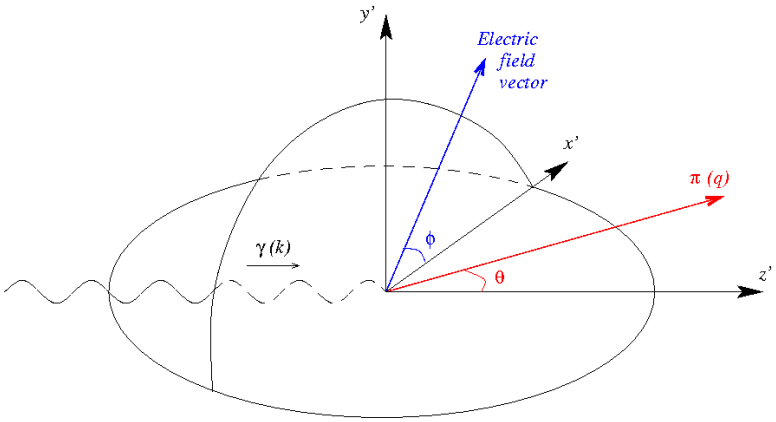

Figure A.1: Reaction axes convention

As can be seen in Fig. A.1, the ϕ angle from equations 2.21 and 7.1 is defined as the angle the photon electric field vector makes to the reaction plane in the CM. In order to extract this information more easily, a rotation matrix, **R**, was calculated for each event, which rotated the reaction axes to align them parallel to the lab orientation. The meson four-vector and the electric field vector of the photon in CM were then transformed under $\mathbf{R}^{-1}$, enabling easy extraction of angles.

References

[1] E. Rutherford, Philos. Mag. **37**, 537 (1919).

[2] J. Chadwick, Nature **129**, 312 (1932).

[3] W. Heisenberg, Z. Phys. **77**, 1 (1932).

[4] N. Bohr, Philos. Mag. **26**, 476 (1913).

[5] H. Yukawa, Proc. Phys. Math. Soc. Japan **17**, 48 (1935).

[6] C. Lattes *et al.*, Nature **159**, 694 (1947).

[7] E. Wilson, *An Introduction to Particle Accelerators* (Oxford University Press, Oxford, 2001).

[8] T. Kuhn, *The Structure of Scientific Revolutions* (University of Chicago Press, Chicago, 1996).

[9] D. Griffiths, *Introduction to Elementary Particles* (Wiley, USA, 1987).

[10] M. Gell-Mann, Phys. Rev. **92**, 833 (1953).

[11] T. Nakano and K. Nishijima, Prog. Theor. Phys **10**, 581 (1953).

[12] H. Kragh, *Quantum Generations: A History of Physics in the Twentieth Century* (Princeton University Press, Princeton, 1999).

[13] M. Gell-Mann and Y. Ne'eman, *The Eightfold Way* (Westview Press, Boulder, 2000).

[14] A. Pais, Prog. Theor. Phys. **10**, 457 (1953).

[15] V. Barnes *et al.*, Phys. Rev. Lett. **12**, 204 (1964).

[16] D. Lichtenberg and S. Rosen, *Developments in the Quark Theory of Hadrons* (Hadronic Press, Palm Harbor, USA, 1980).

[17] M. Gell-Mann, *The Quark and the Jaguar: Adventures in the Simple and the Complex* (Henry Holt and Co., New York, 1995).

[18] J. J. Aubert *et al.*, Phys. Rev. Lett. **33**, 1404 (1974).

[19] S. Herb *et al.*, Phys. Rev. Lett. **39**, 252 (1977).

[20] S. Abachi *et al.*, Phys. Rev. Lett. **74**, 2632 (1995).

[21] C. Amsler, *et al.* (Particle Data Group), Phys. Lett. B **667**, 1 (2008).

[22] O. W. Greenberg, Phys. Rev. Lett. **13**, 598 (1964).

[23] S. Bethke, Prog. Part. Nucl. Phys. **58**, 351 (2007).

[24] C. T. H. Davies *et al.*, Phys. Rev. Lett. **92**, 022001 (2004).

[25] S. Dürr *et al.*, Science **322**, 1224 (2008).

[26] P. Hägler, Proceedings of Science **LAT2007**, 013 (2007).

[27] F. X. Lee *et al.*, Nucl. Phys. B Proc. Suppl. **106-107**, 248 (2002).

[28] S. Sasaki, Nucl. Phys. B Proc. Suppl. **83-84**, 206 (2000).

[29] D. Brommel *et al.*, Eur. Phys. J. ST **162**, 63 (2008).

[30] J. Gasser and H. Leutwyler, Nucl. Phys. B **250**, 465 (1985).

[31] S. Scherer, in *Advances in Nuclear Physics*, edited by J. W. Nagele and E. W. Vogt (Springer-Verlag, New York, 2003), Vol. 27, pp. 277–538.

[32] G. Ecker, Proceedings of Science **Confinement 8**, 025 (2008).

[33] U.-G. Meißner, Proceedings of Science **Confinement 8**, 027 (2008).

[34] J. Erlich, Proceedings of Science **Confinement 8**, 032 (2008).

[35] J. Erlich *et al.*, Phys. Rev. Lett. **95**, 261602 (2005).

[36] S. Brodsky and G. de Teramond, Phys. Rev. Lett. **96**, 201601 (2006).

[37] M. Anselmino *et al.*, Phys. Rept. **261**, 1 (1995).

[38] S. Gerasimov, Sov. J. Nucl. Phys. **2**, 930 (1966).

[39] S. D. Drell and A. C. Hearn, Phys. Rev. Lett. **16**, 908 (1966).

[40] P. Grabmayr, Prog. Part. Nucl. Phys. **55**, 375 (2005).

[41] A. Thomas and W. Weise, *The Structure of the Nucleon* (Wiley, Berlin, 2001).

[42] L. Chang *et al.*, arXiv:0906.4304 [nucl-th] (2009).

[43] S. Capstick and W. Roberts, Prog. Part. Nucl. Phys. **45**, S241 (2000).

[44] A. de Rujula *et al.*, Phys. Rev. D **12**, 147 (1975).

[45] N. Isgur and G. Karl, Phys. Rev. D **19**, 2653 (1979).

[46] F. Wilczek, in *Deserfest: A Celebration of the Life and Works of Stanley Deser*, edited by J. T. Liu, M. J. Duff, K. S. Stelle, and R. P. Woodlard (World Scientific, Singapore, 2006), Chap. Diquarks as Inspiration and as Object, pp. 322–338, published earlier as arXiv:hep-ph/0409168 (2004).

[47] E. Santopinto, Phys. Rev. C **72**, 022201 (2005).

[48] P. N. Bogoliubov, Ann. Inst. Henri Poincare A **8**, 163 (1968).

[49] T. DeGrand *et al.*, Phys. Rev. D **12**, 2060 (1975).

[50] S. Théberge *et al.*, Phys. Rev. D **22**, 2838 (1980).

[51] G. Eckart and B. Schwesinger, Nucl. Phys. A **458**, 620 (1986).

[52] D. Diakonov *et al.*, Z. Phys. A **359**, 305 (1997).

[53] C. E. Carlson *et al.*, Phys. Lett. B **573**, 101 (2003).

[54] M. V. Polyakov and A. Rathke, Eur. Phys. J. A **18**, 691 (2003).

[55] D. G. Ireland *et al.*, Phys. Rev. Lett. **100**, 052001 (2008).

[56] V. Kuznetsov and M. V. Polyakov, JETP Lett. **88**, 347 (2008).

[57] P. Mergell *et al.*, Nucl. Phys. A **596**, 367 (1996).

[58] P. Weisenpacher, Czech. J. Phys. **51**, 785 (2001).

[59] M. Riordan, *The Hunting of the Quark: A True Story of Modern Physics* (Simon and Schuster, New York, 1987).

[60] H. W. Kendall, Rev. Mod. Phys. **63**, 597 (1991).

[61] D. Groom *et al.* (Particle Data Group), Eur. Phys. J. C **15**, 1 (2000).

[62] S. Boffi and B. Pasquini, Riv. Nuovo Cim. **30**, 387 (2007).

[63] T.-A. Shibata, J. Phys. G: Nucl. Phys. **29**, 1951 (2003).

[64] E. Klempt and J.-M. Richard, arXiv:0901.2055 [hep-ph] (2009).

[65] K. Hagiwara *et al.* (Particle Data Group), Phys. Rev. D **66**, 010001 (2002).

[66] T. Ericson and W. Weise, *Pions and Nuclei* (Clarendon Press, Oxford, 1988).

[67] F. Close, S. Donnachie, and G. Shaw, *Electromagnetic Interactions and Hadronic Structure* (Cambridge University Press, Cambridge, 2007).

[68] V. D. Burkert and T. S. H. Lee, Int. J. Mod. Phys. E **13**, 1035 (2004).

[69] I. Barker, A. Donnachie, and J. Storrow, Nucl. Phys. B **95**, 347 (1975).

[70] S. Amendolia *et al.*, Phys. Lett. B **138**, 454 (1984).

[71] D. Drechsel and L. Tiator, J. Phys. G: Nucl. Part. Phys. **18**, 449 (1992).

[72] S. Donnachie, G. Dosch, P. Landshoff, and O. Nachtmann, *Pomeron Physics and QCD* (Cambridge University Press, Cambridge, 2002).

[73] C. Bertulani, *Nuclear Physics in a Nutshell* (Princeton University Press, Princeton, 2007).

[74] J. Bjorken and S. Drell, *Relativistic Quantum Mechanics* (McGraw Hill, New York, 1964).

[75] A. Nagl *et al.*, *Springer Tracts in Modern Physics, Volume 120: Nuclear Pion Photoproduction* (Springer-Verlag, Berlin Heidelberg, 1991).

[76] F. Chew *et al.*, Phys. Rev. **106**, 1345 (1957).

[77] E. Amaldi *et al.*, *Springer Tracts in Modern Physics, Volume 83: Pion Electroproduction* (Springer-Verlag, Berlin, 1979).

[78] R. Walker, Phys. Rev. **182**, 1729 (1969).

[79] E. Leader, *Spin in Particle Physics* (Cambridge University Press, Cambridge, 2001).

[80] G. Goldstein *et al.*, Nucl. Phys. B **80**, 164 (1974).

[81] R. Worden, Nucl. Phys. B **37**, 253 (1972).

[82] B. Anderson, Nucl. Phys. **60**, 144 (1964).

[83] G. Keaton and R. Workman, Phys. Rev. C **53**, 1434 (1996).

[84] W.-T. Chiang and F. Tabakin, Phys. Rev. C **55**, 2054 (1997).

[85] T. Sato and T.-S. Lee, Phys. Rev. C **54**, 2660 (1996).

[86] E. Oset *et al.*, arXiv:0906.3801 [hep-ph] (2009).

[87] O. Hansteain, D. Drechsel, and L. Tiator, Nucl. Phys. A **632**, 561 (1998).

[88] D. Drechsel *et al.*, Nucl. Phys. A **645**, 145 (1999).

[89] I. Blomqvist and J. M. Laget, Nucl. Phys. A **280**, 405 (1977).

[90] D. Drechsel *et al.*, Eur. Phys. J. A **34**, 69 (2007).

[91] R. Arndt *et al.*, Phys. Rev. C **42**, 1853 (1990).

[92] F. F. Liu *et al.*, Phys. Rev. **136**, B1183 (1964).

[93] G. Knies *et al.*, Phys. Rev. D **10**, 2778 (1974).

[94] V. B. Ganenko *et al.*, Sov. J. Nucl. Phys. **23**, 511 (1976).

[95] K. Kondo *et al.*, J. Phys. Soc. Jap. **29**, 13 (1970).

[96] K. Kondo *et al.*, Phys. Rev. D **9**, 529 (1974).

[97] J. Alspector *et al.*, Phys. Rev. Lett. **28**, 1403 (1972).

[98] L. O. Abrahamian *et al.*, EFI-389-47-79-YEREVAN.

[99] F. V. Adamian *et al.*, J. Phys. G **15**, 1797 (1989).

[100] W. J. Metcalf and R. L. Walker, Nucl. Phys. B **76**, 253 (1974).

[101] B. A. Mecking, Prog. Part. Nucl. Phys. **34**, 53 (1995).

[102] J. Alcorn *et al.*, Nucl. Instr. and Meth. A **522**, 294 (2004).

[103] O. K. Baker *et al.*, Nucl. Instr. and Meth. A **367**, 92 (1995).

[104] B. A. Mecking *et al.*, Nucl. Instr. and Meth. A **503**, 513 (2003).

[105] R. Nasseripour *et al.*, Bull. Am. Phys. Soc **45**, 91 (2000).

[106] H. Olsen and L. C. Maximon, Phys. Rev. **114**, 887 (1959).

[107] K. Livingston, Nucl. Instr. and Meth. A **603**, 205 (2009).

[108] U. Timm, Fortschr. Phys. **17**, 765 (1969).

[109] F. A. Natter *et al.*, Nucl. Instr. and Meth. B **211**, 465 (2003).

[110] D. I. Sober *et al.*, Nucl. Instr. and Meth. A **440**, 263 (2000).

[111] Y. Sharabian *et al.*, Nucl. Instr. and Meth. A **556**, 246 (2006).

[112] F. Barbosa *et al.*, Nucl. Instr. and Meth. A **323**, 191 (1992).

[113] M. D. Mestayer *et al.*, Nucl. Instr. and Meth. A **449**, 81 (2000).

[114] G. Adams *et al.*, Nucl. Instr. and Meth. A **465**, 414 (2001).

[115] E. S. Smith *et al.*, Nucl. Instr. and Meth. A **432**, 265 (1999).

[116] M. Amarian *et al.*, Nucl. Instr. and Meth. A **460**, 239 (2001).

[117] M. Anghinolfi *et al.*, Nucl. Instr. and Meth. A **537**, 562 (2005).

[118] D. Cords *et al.*, CLAS Note 94-012, Jefferson Laboratory.

[119] P. Nadel-Turonski *et al.*, *Kaon Production on the Deuteron Using Polarised Photons*, CLAS proposal PR-06-103, Jefferson Laboratory (2006).

[120] E. S. Smith *et al.*, CLAS Note 1999-011, Jefferson Laboratory.

[121] J. Li *et al.*, CLAS Note 2003-04, Jefferson Laboratory.

[122] E. Anciant *et al.*, CLAS Note 1999-04, Jefferson Laboratory.

[123] E. S. Smith *et al.*, CLAS Note 2002-007, Jefferson Laboratory.

[124] D. Lawrence and M. Mestayer, CLAS Note 1999-018, Jefferson Laboratory.

[125] R. Brun, ROOT, http://root.cern.ch.

[126] K. Livingston, ROOTBEER.

[127] J. B. Cladis *et al.*, Phys. Rev. **87**, 425 (1952).

[128] V. Vegna *et al.*, Chin. Phys. C **33**, 1249 (2009), *Proceedings of NSTAR 2009*.

[129] K. Livingston, *Private Communication* (2009).

[130] I. Strakovski, *Private Communication* (2009).

[131] D. Diakonov and V. Petrov, Phys. Rev. D **69**, 094011 (2004).